Improving Particle Confinement in Inertial Electrostatic Fusion for Spacecraft Power and Propulsion

By

Carl C. Dietrich

S.B. Aeronautics and Astronautics, MIT 1999
S.M. Aeronautics and Astronautics, MIT 2003

SUBMITTED TO THE DEPARTMENT OF AERONAUTICS AND ASTRONAUTICS IN PARTIAL FULFILLMENT OF THE REQUIREMENTS FOR THE DEGREE OF DOCTOR OF PHILOSOPHY IN AERONAUTICS AND ASTRONAUTICS AT THE MASSACHUSETTS INSTITUTE OF TECHNOLOGY

FEBRUARY 2007

Signature of author: _____
Department of Aeronautics and Astronautics
February 28, 2007

Certified by: _____
Manuel Martinez-Sanchez
Professor, Aeronautics and Astronautics
Thesis Committee Chairman

Certified by: _____
Raymond J. Sedwick
Principal Research Scientist
Thesis Advisor

Certified by: _____
Ian Hutchinson
Professor, Nuclear Science and Engineering

Certified by: _____
Oleg Batishchev
Principal Research Scientist

Accepted by: _____
Jaime Peraire
Professor, Aeronautics and Astronautics
Chairman, Committee for Graduate Students

(This page intentionally left blank)

Abstract

Improving Particle Confinement in Inertial Electrostatic Fusion for Spacecraft Power and Propulsion

By

Carl C. Dietrich

Fusion energy is attractive for use in future spacecraft because of improved fuel energy density and reduced radioactivity compared with fission power. Unfortunately, the most promising means of generating fusion power on the ground (Tokamak based reactors like ITER and inertial confinement reactors like NIF) require very large and heavy structures for power supplies and magnets, in the case of magnetic confinement, or capacitors and lasers in the case of inertial confinement. The mass of these reactors and support equipment is sufficiently large that no existing or planned heavy-lift vehicle could launch such a reactor, thereby necessitating in-space construction which would substantially increase the cost of the endeavor. The scaling of Inertial Electrostatic Confinement (IEC) is such that high power densities might be achievable in small, light-weight reactors, potentially enabling more rapid, lower cost development of fusion power and propulsion systems for space applications.

The primary focus of the research into improving particle and energy confinement in IEC systems is based on the idea of electrostatic ion focusing in a spherically symmetric gridded IEC system. Improved ion confinement in this system is achieved by the insertion of multiple concentric grids with appropriately tailored potentials to focus ion beams away from the grid wires. In order to reduce the occurrence of charge exchange and streaming electron power losses, the system is run at high vacuum. This modification to the usual approach was conceived of by Dr. Ray Sedwick and computational modeling has been conducted by Tom McGuire using a variety of custom and commercial codes.

In this thesis, a semi-analytic model of the potential structure around a multi-grid IEC device is developed. A 1-D paraxial ray ion beam envelope approximation is then used along an equatorial beamline and the assumed beam density is gradually increased until an effective beam space charge limit is reached at which point the potential fusion output is calculated. Significant use of the commercial particle-in-cell code OOPIC was made, and its ability to predict multi-grid IEC confinement properties is evaluated. An experiment was built to confirm the effectiveness of the multiple-grid structure to improve ion confinement times. It is shown that the multi-grid IEC can improve ion confinement time over the conventional, 2-grid IEC device. The PIC predicted ion bunching mode is also seen in experiment.

Acknowledgements

There are so many people who have helped guide and support me in my (extended) time at MIT. I would like to take this opportunity to thank a few of them.

First, to my parents, MaryAnn and Charles Dietrich, who gave me the amazing opportunity to study at MIT and focus on exactly what I wanted to do. Thank you for your continual support of me in all my endeavors.

To the members of my thesis committee, Prof. Manuel Martinez-Sanchez, Prof. Ian Hutchinson, Dr. Oleg Batishev, and to my thesis readers, Professor Paulo Lozano and Professor Jack Kerrebrock: thank you all for your invaluable guidance and insight over the years.

To Paul Bauer, thank you for your many hours of help in the lab.

To my coworkers, Tom McGuire, Noah Warner, Simon Nolet, and Dr. Sam, thank you all for your friendship and support.

To my wife, Anna, thank you for being part of my life, and encouraging me in all ways. I love you.

Finally, I want to particularly thank my thesis advisor, Dr. Raymond Sedwick. Without Ray's unwavering support and willingness to put up with my occasional stubbornness, this work would never have been done. Thank you for all of your help and guidance over the past six years.

Table of Contents

Table of Figures

1. Introduction

1.1. Background

Inertial electrostatic confinement (IEC) fusion is often credited as being conceived of by Philo T. Farnsworth, the inventor of television [20]. In IEC devices, fusion ions are electrostatically accelerated through a (nearly) spherically symmetric central focus point. At the focus point they are at sufficiently high energy to overcome their mutual electrostatic repulsion that some small fraction of the ions will fuse and release energy in the form of high energy fusion products. Figure 1 illustrates the practical simplicity of IEC fusion.
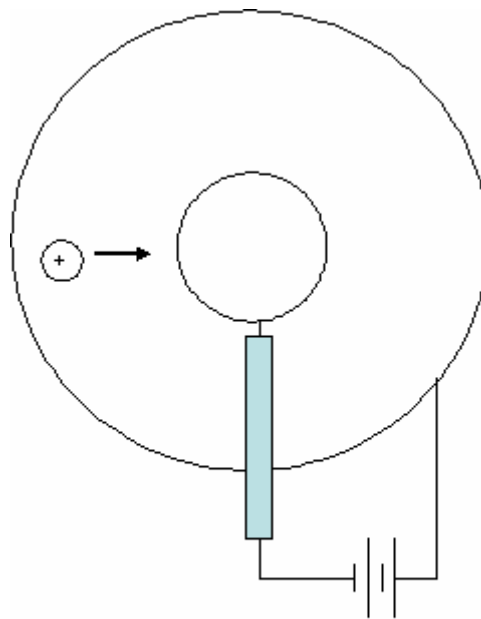
Simple IEC Device

Figure 1: Schematic drawing of conventional, 2-grid IEC device

The earliest published work on the concept was done by Salisbury in 1949 [1], then expanded by Elmore, Tuck and Watson in the late 1950s[2, 3]. There has been sporadic work on IEC fusion for the past 50 years [4-350]. Experimental programs are relatively cheap to develop, and they have been shown to be a detectable neutron source given sufficient input power. The largest fusion output to date was achieved by Hirsch in 1967 with an output of nearly 10^{10} neutrons/second with Deuterium and Tritium [18]. It is widely accepted that it is not difficult to make fusion reactions in an IEC reactor, but the best efficiency to date as measured by the fusion power out divided by the electrical power in (Q) is approximately 10^{-5}. Because of its poor efficiency, IEC has never been a priority in the quest for a fusion energy source.

However, IEC is appealing in its simplicity, and it has consequently gained a substantial amateur following from people who enjoy the idea of having a fusion reactor in their garage.
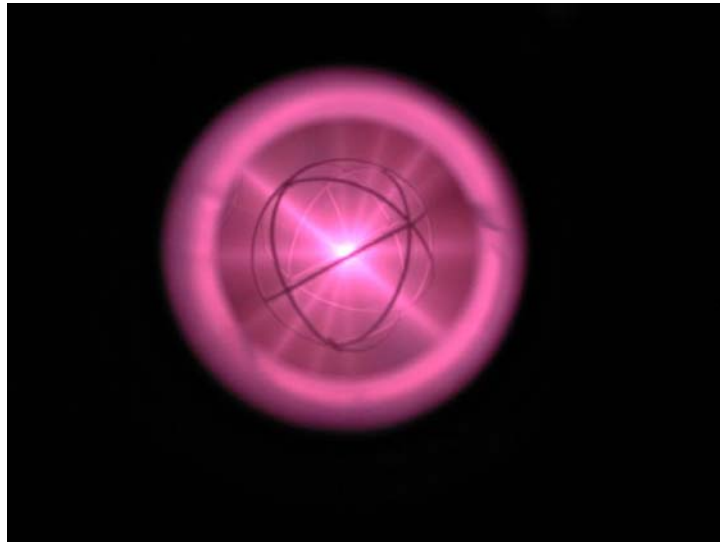
Figure 2: IEC "Fusor" built by high-school student Brian McDermott (photo credit: Brian McDermott, reproduced with permission)

These devices have developed a strong following in online forums and bulletin boards. Figure 2 is a photograph of an operating IEC fusion reactor built by high school student, Brian McDermott. Many other amateur scientists have built similar "fusor reactors" [361].

Theoretical systems studies have identified significant barriers to the practical implementation of IEC fusion systems for power production [175], but significant interest remains because of the simplicity, the attractive scaling, and the low mass of the IEC fusion reactor system. This low mass is particularly of interest for space-based power and propulsion systems. While there are designs for many types of magnetically confined and inertial fusion reactors that are much closer to achieving net power output, these concepts are sufficiently massive that tremendous monetary resources would need to be allocated for development of that type of reactor in space. The scale of such an undertaking would likely surpass the scale of the International Space Station (ISS) – requiring multiple launches and in-space assembly. It is therefore valuable to work on the challenges associated with making IEC fusion more efficient because of the potential to put an entire reactor in space with a single launch. The potential for a more practical, small-scale, implementation of fusion power for spacecraft systems is the fundamental driver for this research.

The primary limiter of the efficiency of IEC fusion systems is the extremely short energy confinement time, the embodiment of which is the short charged particle confinement time in the system. Under typical IEC operating parameters, electrons stream out from

the central cathode and are collected on the outer anode, and ions typically make only 10 passes through the cathode before being lost by either impacting one of the grid wires or undergoing a charge-exchange reaction with background gas in the system [357]. In a typical system, the probability that any given ion will be lost to a process other than fusion is approximately 100,000 times more likely than losing an ion to a fusion reaction.

Previous work [357] identified the need to operate an IEC fusion device in a regime where the ion loss probability is within the fusion energy gain to input power ratio of ion fusion probability (a factor of order 10) in order to approach Q=1. The improvement of charged particle confinement in IEC systems is therefore of paramount interest. Sedwick and McGuire proposed a method of improving ion confinement times by electrostatically focusing ion beams to keep them away from cathode grid wires. McGuire also identified the need to operate the system in the ultra-high-vacuum (UHV) regime in order to avoid charge-exchange and collisional scattering losses with background gas. With an appropriately hard vacuum and a properly focused recirculating ion beam, typical ion confinement times were computationally shown to be improvable by three orders of magnitude – from 10 passes to 10,000 passes dependent on the background pressure. This improved ion confinement has the potential to yield dramatic improvements in system efficiency [357].

The practical implementation of this type of improved confinement requires the development of an IEC reactor with 3 or more independently biased, concentric spherical grids (multi-grid). The potentials on these grids would be set so as to provide a confining electrostatic field. By minimizing the rate of ion-grid impact, the electron current will

also be reduced because the majority of streaming electrons are emitted as secondary electrons when ions collide with the cathode. Electrostatic ion confinement thereby has the potential to reduce the two largest energy sinks in IEC systems.

While focusing ion beams is nothing new to physicists, and there are many tools to predict ion beam behavior in the presence of focusing fields, the development of new models was required in order to predict the behavior of ions in this type of recirculating ion trap. The development of some of those new models and the construction and experimental evaluation of the first multi-grid IEC confinement experiment is the subject of this thesis.

1.2. Rationale Behind Current Investigations

Previous work computationally identified the potential to improve ion confinement in IEC devices by implementing a multiple-grid configuration, but hardware based tests were needed to experimentally validate the predicted improvement.

1.2.1. Ion Confinement

The goal of this research is to compare a conventional, 2-grid IEC device with a 5-grid IEC device to evaluate the potential of the multi-grid approach to improve ion confinement. Based on the computational modeling, significant increases in ion confinement were expected with properly tailored potentials in the 5-grid device. The major ion loss mechanisms in a conventional, 2-grid IEC device are chaotic ion trajectories and background gas interactions. Operating the 5-grid device at very low background gas pressure and with a focusing field structure is expected to improve ion confinement.

1.2.1.1. Unconfined ion trajectories

Particle-In-Cell (PIC) simulations conducted by McGuire and repeated with modification by the author indicated that the typical 2-Grid IEC device would be subject to chaotic ion trajectories due to both field asymmetries from the presence of a feed through and the highly defocusing nature of the vacuum electrostatic field structure surrounding the cathode. This defocusing field curvature in the region of the cathode grid wires could cause a recirculating ion beam to either disperse resulting in spatially chaotic ion trajectories or impact a cathode grid wire after only 2-3 passes through the device core.
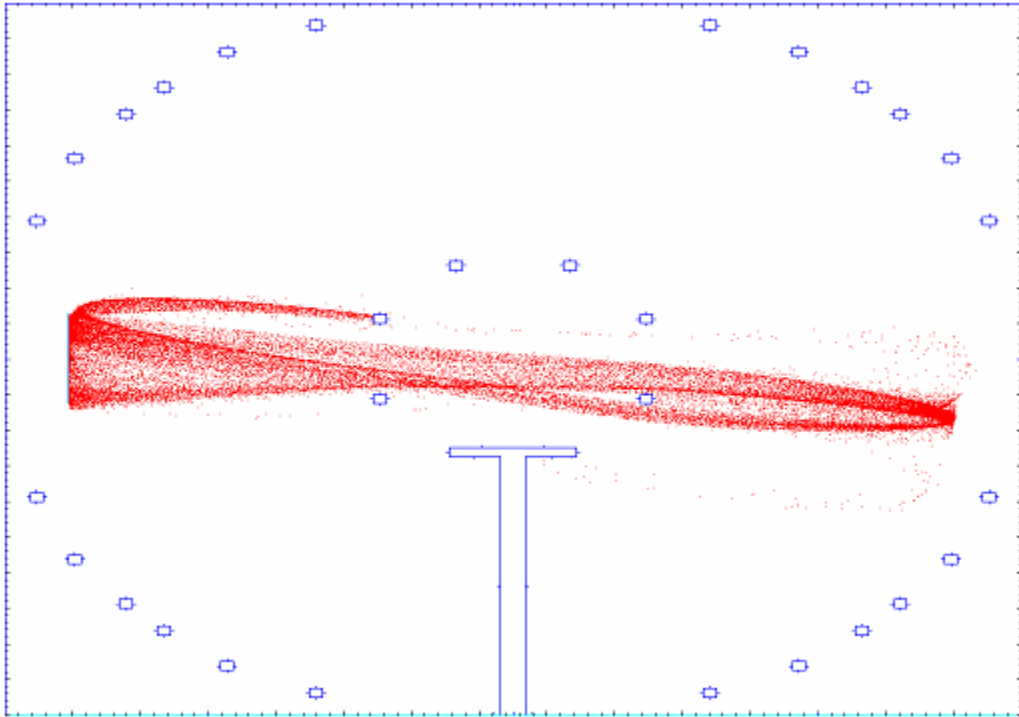
Figure 3: OOPIC model of 2-grid ion trajectories with field asymmetry due to the feed-through

Figure 3 shows a particle in cell model of ions in a 2-grid IEC device with a feed-through field asymmetry. When multiple, concentric, independently biased wire grids are used as shown in figure 4, the vacuum electrostatic field structure was shown to be capable of

confining the ions away from the cathode grid wires for many more passes through the core than in the conventional, 2-grid design simulated above. With the confining field structure of the multi-grid configuration, significant improvements in ion confinement were shown to be possible even with a small, off-axis ion injector that would act as an ion sink as well as a source.
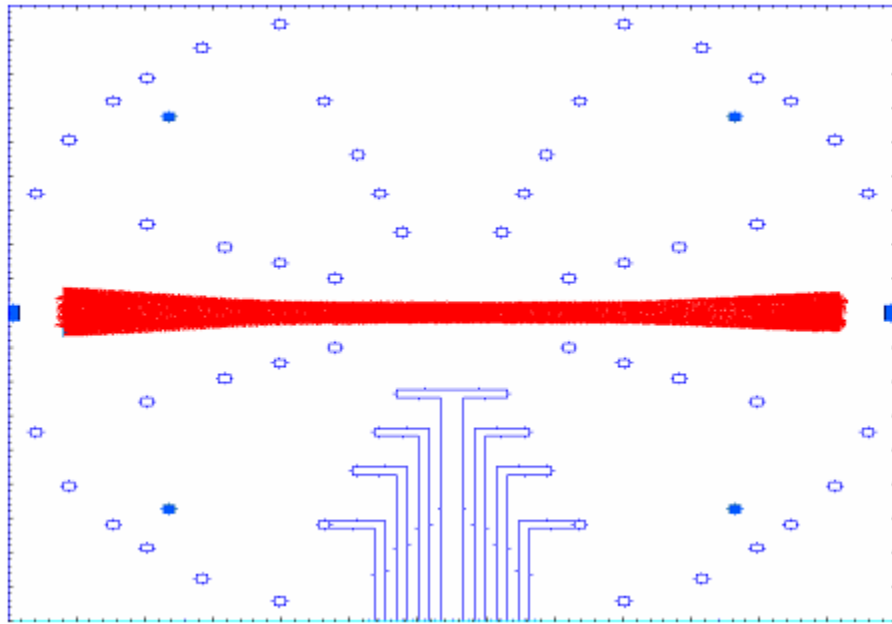
Figure 4: Multi-grid with asymmetric feed-through and off-axis, absorbing ion injector

These early studies strongly indicated that uncontrolled ion trajectories in conventional, 2-grid IEC devices could be a major ion (and energy) loss mechanism and supported the hypothesis that the use of multiple grids could significantly improve ion (and energy) confinement times in IEC devices.

1.2.1.2. Scattering and charge exchange with background

In the regime where most conventional IEC devices are operated for maximum measured reaction rates, uncontrolled ion trajectories are not a significant concern because the background gas pressure is typically so high (1e-3 < p < 1e-1 mbar typical) that the mean free path of ions in the IEC devices is less than twice the diameter of the device. Most ions in these systems are lost to the grid wires via scattering collisions or through charge exchange with the background gas [357]. The spatial representation of ions in these high pressure systems wind up resembling ion clouds, as opposed to well defined ion beams.
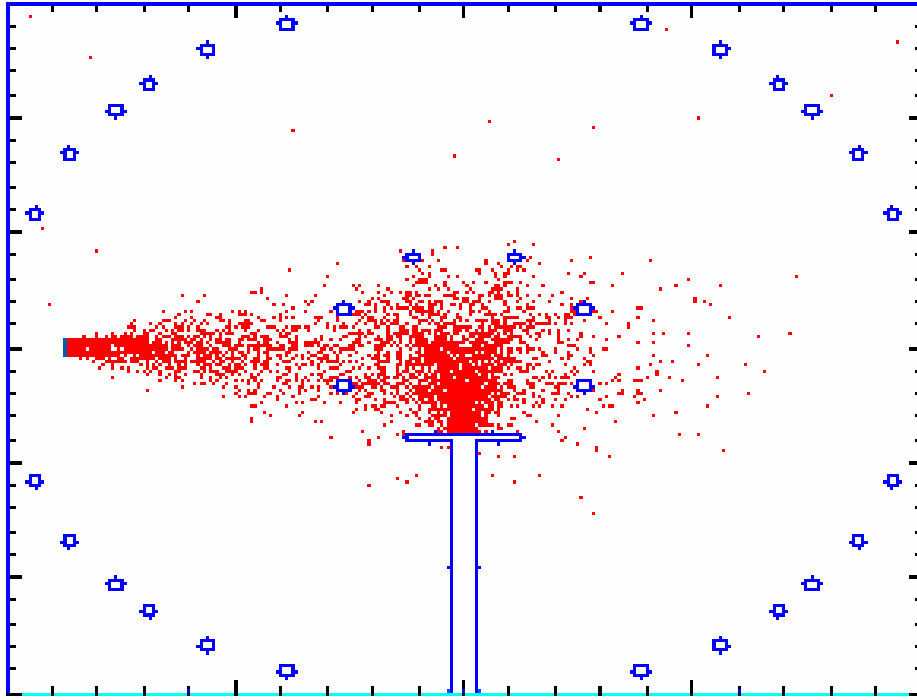
Figure 5: OOPIC simulation of typical high pressure IEC discharge (p = 3e-3 mbar, Argon)

Figure 5 shows a high-pressure (3e-3 mbar) discharge that is typical of most of the experimentation that is done [361]. The effect of scattering collisions is clear when

compared to the hard vacuum of figure 2. In this high pressure regime, the majority of fusion reactions are between ions and the neutral background gas. While the measurable neutron output is highest in this pressure regime, the scattering and charge exchange interactions of the ions with the background gas limits the ion confinement time. The maximum measured Q of IEC devices in this high pressure regime approached 10^{-5} with deuterium and tritium (DT reaction) gas [18]. IEC operation in most experiments uses only deuterium (DD reaction). The average Q is of the order 10^{-9}.

1.2.2. OOPIC Modeling

A Particle-In-Cell (PIC) modeling tool has been developed using a commercial-off-the-shelf (COTS) code called OOPIC. The OOPIC physics kernel was originally developed by UC Berkeley's computational physics group [359, 360]. It is a 2-D code that has a wide range of built in functionality including a Monte Carlo Collision (MCC) model, simulated ion sources, realistic electron and ion bombardment ionization models for Argon, Helium and a number of other gases, and simple user definable geometries.

PIC modeling informed much of the original investigations into improving ion confinement. It has been particularly useful for predicting ion bounce times, simulating the effects of multiple grids, and evaluating the development of the ion-ion counter-streaming instability in these low-pressure, non-neutral IEC systems with good particle confinement.

1.3.   Scaling of UHV IEC Devices

One of the particularly interesting characteristics of a non-neutral IEC system is the scaling. Contrary to the physical intuition of most power production systems where the power produced is proportional to the size of the device (for similar device types), a non-neutral IEC reactor has inverse scaling because achievable particle densities are limited by space charge effects.

1.3.1.   Derivation

The physics of a non-neutral IEC device are dominated by the Poisson equation.

$$\nabla^2 \Phi = \frac{-\rho_{ch}}{\varepsilon_o}$$ **Equation 1.1**

We will define a dimensionless number from the Poisson equation that relates the maximum curvature due to particle space charge effects to the curvature of the vacuum potential structure which is just the Laplacian of the potential. We characterize the curvature of this Laplacian imposed by the boundary conditions on the grid wires with a typical radius, R_{typ} and a typical potential difference, Φ_{typ}. We can then define our non-dimensional "IEC" number as follows:

$$IEC \equiv \frac{\rho_{ch} R_{typ}^2}{\varepsilon_o \Phi_{typ}}$$ **Equation 1.2**

It is convenient to make a number of assumptions for the purposes of comparison. We will first assume that R_{typ} is the radius of the outermost grid (or the largest radius of the device), and we will assume Φ_{typ} to be the maximum potential difference between the anode and cathode grids in the device. We will also assume that any electrons generated

19

inside the IEC device will be lost on a time scale much faster than the ions, so the number density of electrons in the system is effectively 0. The charge density term can then be replaced by the maximum number density of ions in the system times Z_{eff} times the elementary charge, e. We will differentiate this number from the above number by using lower-case letters.

$$iec \equiv \frac{eZ_{eff}n_{i_{max}}R_{anode}^2}{\varepsilon_o\left(\Phi_{anode} - \Phi_{cathode}\right)}$$
Equation 1.3

In order to maximize power density for a given system, it is always desirable to maximize the iec number, but space charge effects will limit the maximum achievable iec number in any non-neutral device. If we therefore assume that the iec number is constant for any system operating near the maximum space charge limit, the fundamental scaling relationships emerge. For two IEC devices with the same iec number, Z_{eff}, and grid potentials:

$$n_{i_{max}} \propto 1 \Big/ R_{anode}^2$$
Equation 1.4

$$PowerDensity \propto 1 \Big/ R_{anode}^4$$
Equation 1.5

$$Power \propto 1 \Big/ R_{anode}$$
Equation 1.6

1.3.2. Numerical Validation of Scaling

This very simple scaling argument stands up to test by detailed numerical simulation. The maximum ion density achievable in a system the size of our experiment (0.5 m diameter) at fusion-relevant cathode potentials (-100kV) is approximately 2e-14 m^{-3} or an iec number of approximately 9. The simple scaling relationship indicates that in order to

achieve ion densities that are comparable to those in a Tokamak, the radius of the device

must be decreased by a factor of 1000.
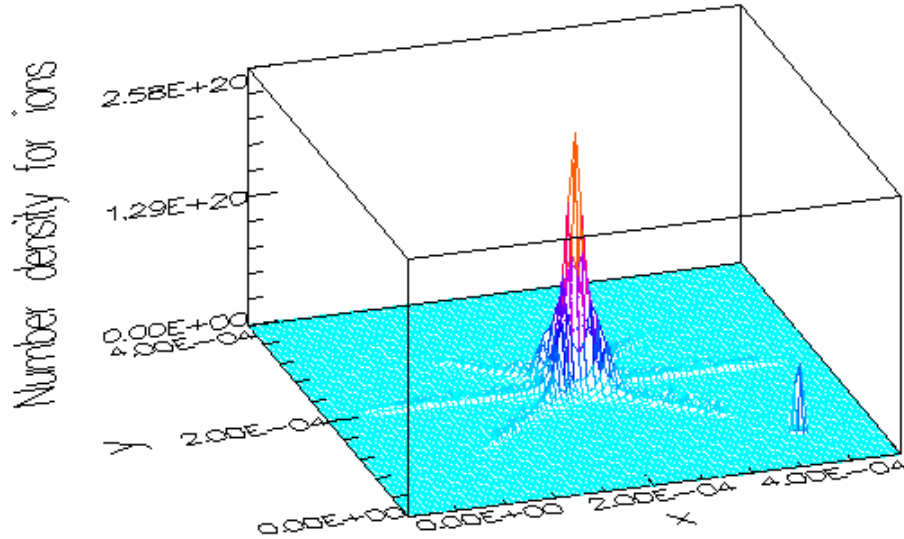
Figure 6: Particle-In-Cell simulation showing ni 2.5e20m-3 at 0.5mm diameter device size

When a geometrically similar OOPIC model was created with a diameter of 0.4 mm and

the same -100kV potential was applied to the cathode, the peak ion densities were seen to

top 2.5e20 m^{-3} (an iec number of 7.4) as predicted by the simple scaling derivation in the

previous section.

Although the maximum iec number for a given size system does depend on the details of

the design and implementation, for a system with good ion confinement that approaches

its own space charge limits, the iec numbers are not expected to vary by more than one

order of magnitude because fundamental space charge limits cannot be designed around

in non-neutral systems.

2. Experiment Development

Experimental validation of the hypothesis that ion confinement time in IEC devices could be improved by the addition of wire focusing grids was sought. It was decided at an early stage that this experimental validation would come from the simple geometric reconfiguration of the wire grids in a single experiment at high vacuum. The experiment would first be built in a conventional 2-grid geometry with a single cathode grid near the center of a much larger anode grid such as the geometries represented in figures 3 and 5. The ion confinement times for this system would be inferred from measured data. Additional focusing grids would then be added to the system (similar to figure 4), and ion confinement times would again be inferred from the new, "Multi-grid" data. These two data sets would then be compared to reveal whether they support the core hypothesis.

A number of design and modeling techniques were employed to facilitate the design of the experiment. These models are detailed in the following chapter. The net result of the modeling effort was to confirm assertions that were inferred from the basic scaling given in chapter one and, more importantly, to quantify and predict the expected ion densities and confinement times of the system.

The geometry of the experiment was largely dictated by experimental convenience – available equipment, measurement access, and ease of grid construction with available tools and techniques. This section discusses four critical aspects of the development of the experiment: confinement time detection techniques, sources of error, selection of primary diagnostic, and hardware development.

2.1.   Confinement Time Detection Techniques

There are many ways to measure the confinement time of ions in an IEC system. This

section will give an overview of the concepts that were considered for this experiment.

All of the techniques presented require that the source of ions have either a well

calibrated injection rate or a rapid on/off switching time. If neither of these conditions

can be met, accurate measurement of the ion confinement time is not possible.

2.1.1.   Measurement of current to the grid wires

As ions are injected into an IEC system where wire grids are used to establish the

background potential structure, they will occasionally adopt a trajectory that will

intercept one of the grid wires. When an ion impacts a grid wire it is rapidly decelerated

and neutralized by the "sea" of electrons in the wire. In the process, the energy of the ion

goes into heating the grid wire and potentially liberating secondary electrons from the

surface of the wire. Because the ion is neutralized on the surface, the impact of an ion on

a grid wire will draw an electric current which can be detected. The current drawn will

be proportional to, but not identical to the ion current (defined by the rate of ion loss

times the charge per ion). This discrepancy is due to the emission of secondary electrons

from the surface of the wire which will cause the detected current to exceed the ion loss

current by the average secondary electron yield factor.

$$I_{grid} = I_{ions}\left(1 + \gamma_{ie}\right)$$
<div align="right">**Equation 2.1**</div>

Early particle-in-cell (PIC) experiments showed that the number of ions lost to grid wires

per unit time is roughly proportional to the number of ions trapped in the system at that

time, particularly under high vacuum conditions where confinement limits are imposed

by collisions with background gas. Once the source of ions in turned off, this relationship will cause the rate of ion loss to follow an exponential decay curve. One method of estimating the confinement time of ions in the system is to numerically evaluate the time-constant of the assumed exponential decay. This can be done by measuring the time between the maximum loss rate and 1/e times that loss rate after the ion source has been turned off. In this manner, ion confinement time can be inferred from the measurement of the current to the grid wires as a function of time.

2.1.2. Destructive Beam Dump

Ion confinement time can be directly measured by a destructive count of the number of ions remaining in the trap a certain period of time after ion injection is turned off. This technique is referred to as a destructive beam dump (DBD). The DBD hardware would consist of an ion collector plate mounted in the beam path near the anode opposite the ion source. The collector plate would be held at or near ground so that ions could not impact the plate without substantial upscatter or thermalization of the distribution function. Then, when a measurement of the trapped ion population is desired, the potential of the plate would be rapidly lowered so that all of the ions would be energetically capable of impacting the collector plate. The location of the plate inline with the beam will cause all of the ions in the trap to be rapidly evacuated and neutralized on the surface of the collector. If the gradient of the electrostatic potential at the surface of the plate is such that it suppresses any net secondary electron emission, the time integral of the current that is drawn to the plate will be equal to the net charge that had been contained in the trap. When this measurement is made in conjunction with assumptions about the relative fraction of singly and doubly ions, the total population of ions in the trap at the dump time could be inferred with a high level of confidence.

DBD is appealing because it has the potential to be a direct measurement of the total trapped ion population at a given time. By taking many of these measurements with different delays from the termination of ion injection, a decay curve can be extracted of the actual ion population in the trap. Although many more measurements are required to perform this analysis, it is appealing in that the actual number of ions is measured as opposed to a signal that is simply proportional to the actual number of ions (as in the previous technique).

The primary disadvantage of the DBD technique is that it is more expensive and time intensive to implement than the previous technique. In order to get a measurement of the ion population in the trap at a given time, the collector potential is rapidly lowered on the order of 1kV for this experiment. Ideally, this change in potential would be instantaneous, but since the collector and its feed wires have a finite capacitance, an instantaneous change is not possible. The question then becomes, "how fast does it have to be?" This question can be answered by looking at the dynamics of the ions in the system and assuming something about the loss rate of ions from the trap. It is desirable to have the measurement of ions in the trap be "effectively instantaneous" – meaning that there is a negligible change in the trapped ion population during the time it takes to drop the collector potential from ground to the collecting potential. Mathematically speaking the condition is

$$\tau_{collector\_drop} << \frac{N_{Trap}}{\dot{N}_{Trap}} \qquad\qquad \textbf{Equation 2.2}$$

PIC modeling of the system suggests that the confinement time of a 2-grid system is O(10) passes. Since it is desirable to compare the 2-grid system with the multi-grid system using the same diagnostic, the characteristic time for the collector potential drop ($\tau_{collector\_drop}$) should be less than half of the bounce time in order for accurate measurements of the 2 grid confinement time with a DBD technique.

$$\tau_{collector\_drop} < \frac{\tau_b}{2}$$ **Equation 2.3**

In addition, there is concern that the 2-grid beamline is not robust to minor asymmetries in the potential structure which could cause the beam to intersect the collector plate near the edge or miss the plate entirely. Clearly, if the plate is missed entirely, an accurate measurement cannot be made with this technique, but even if the beam impacts the collector near the edge, secondary electrons could be emitted from the collector to the ground which would introduce error into the "direct" measurement of trapped ions.

There are other practical difficulties with implementing this type of detection scheme. The current required to change the potential of the plate due to its finite capacitance would need to be subtracted from the signal, and the need to rapidly pulse the potential of the collector over the very short dump time requires special power supplies.

2.1.3. Capacitive Detection of Trapped Charge

A probe or plate like the one used as a collector in the DBD technique can be similarly used to detect the trapped ions capacitively. Not only is this a direct measurement of the ions in the trap, it is also a non-destructive measurement so the entire decay can be

monitored with each injection without the need to take multiple measurements with different destructive delays on different injections as in the DBD.

Capacitive detection of ions in the trap relies on the detection of the very small "image charge" currents that are induced in the probe or detector plate by nearby ions. In effect, the detector becomes one half of a capacitor and the trapped ions become the other half. The minor perturbation of the electric field in vacuum caused by the presence of nearby ions induces a small current in the wire leading to the plate if that wire is connected to ground (or some constant potential). Since there can be no electric field inside the conductor, the charges will rearrange to shield the field perturbation at the surface. That small current can be detected with an ammeter circuit.

A primary difficulty in the use of a capacitive detector is that the measurement relies on an assumed location of the ion beam in order to estimate the effective capacitance of the detector. Based on the PIC models of the 2-grid device, the geometry of the beamline in this configuration is not at all well understood, so the effective "capacitance" of this detector is uncertain. It is therefore difficult to determine absolute magnitude of trapped charge using this technique, but temporal resolution should be excellent when using a small probe with <1pF capacitance.

2.1.4. Laser Induced Fluorescence

Laser induced fluorescence (LIF) of the trapped ion population could, in theory be used to measure the density of ions trapped in the system. LIF is appealing because it is a non-destructive direct measurement of the trapped ion density and it has the potential to directly show the spatial variation of the beam density. In LIF a laser beam is projected

through a measurement region that is anticipated to contain an ion population. The laser

is tuned to excite a particular electron transition. The decay of that excited ion releases a

photon in any direction. An aperture/filter arrangement in conjunction with a

photomultiplier tube is then used to detect some small fraction of these photons. That

signal is then assumed to be proportional to the density of ions in the region of space that

is intersected by the beam and the field of view of the detector. By monitoring the density

as a function of time (which may need to be done statistically with multiple

measurements because of the small signal) it is theoretically possible to back out the

trapped ion decay curve and hence the confinement time.

Due to the expense associated with the development of a LIF detector, LIF was never

seriously considered as a practical detection option for this experiment. It is mentioned

here because it has substantial promise to reveal the shape of the actual beam envelope

which could powerfully inform future investigations by validating or invalidating much

of the PIC modeling that has been done.

2.2.   Sources of Error

Every experiment has many potential sources of error which at best introduce inaccuracy

or noise into the data and at worst cause the experiment to completely fail to measure

what it is attempting to measure. This section details a number of the potential sources of

error in what is anticipated to be levels of increasing significance.

2.2.1.   Earth's Magnetic Field

Charged particles will experience accelerations due to electric and magnetic fields.

$$\vec{a} = \frac{q}{m}\left[\vec{E} + \vec{v} \times \vec{B}\right]$$ **Equation 2.4**

While typical electric fields in the experiment are $O(10^4$ V/m), the v-cross-B term is only of order 10. This thousand-fold difference in the terms of the equation of motion is the justification for ignoring the effects of the Earth's magnetic field in the PIC modeling. However, the effect is real and will result in the very slight broadening of an ion trajectory that would otherwise turn back directly upon itself in a linear trajectory. This skew in the trajectory that is introduced can be estimated by integrating the acceleration perpendicular to the nominal, radial ion trajectory over the period of one pass (or one half of the bounce time). This method implicitly assumes small angle deviations.

Although in the actual experiment, the ion beam is out of alignment with Earth's field lines by only 40 degrees (+/-10 degrees as measured with a compass on the device), in order to be conservative I will assume that the beamline is perpendicular to the local field. The average ion velocity is given approximately by:

$$\bar{v} = \frac{1}{2}\sqrt{\frac{2q\Delta\phi}{m}}$$ **Equation 2.5**

and the total trajectory skew per pass is approximately given by:

$$\Delta x_{B-skew} \cong \int_0^{\tau_b/2}\int_0^{\tau_b/2} \frac{q}{m}\bar{v}|B|dtdt$$ **Equation 2.6**

With a bounce time of 24 microseconds and a local field strength of approximately 55 microTesla, this expression evaluates to a total skew of roughly 733 microns per pass for Ar 1+. Due to their faster average velocity, singly charged Helium ions, could be skewed by up to 2.3mm per pass, but these distances are arguably negligible since they are small

29

with respect to the grid openings at the anode (~18cm). It would require approximately 123 passes (or about 2.9 milliseconds) for a singly charged argon ion to move from the center of the beam to an anode grid wire based solely upon this magnetic drift. A singly charged Helium ion would require 39 passes or approximately 147 microseconds to drift the same distance. Since confinement times have generally been limited to approximately 10 passes, the effect of this magnetic drift will be ignored. Asymmetries in the electric field are far more likely to cause significant perturbations of the ion trajectories than magnetic drift.

While the impact on ion trajectories is negligible, the Earth's magnetic field could substantially alter the trajectories of secondary electrons. But since all magnetic lines intersect the anode, even very low energy electrons with Larmor radii much smaller than the device scale will wind up impacting the anode. Due to the broad energy spectrum of secondary electrons, and the fast dynamics compared to the ions, electron confinement was not modeled. It is expected to be poor.

In addition to directly impacting the particle trajectories in the experiment, the Earth's field could also produce a Hall-effect current in the voltage divider resistors which could result in a local corona and flashover effect on the surface of the resistors. In order to protect the voltage dividers from corona and flashover and to prevent unwanted leak currents, the voltage dividers are potted in Silicon RTV. There is no evidence from the experiment that suggests that this phenomenon is occurring.

Overall, the Earth's magnetic field is not expected to introduce substantial error into the measurement of the ion confinement time.

2.2.2. Secondary Electron Emission

In the commercial PIC code OOPIC, the Vaughn model is used to predict secondary electron emission from the surface of the grid wires [353]. There is large uncertainty, however, in how much of the energy of impacting ions results in secondary electrons versus surface heating versus sputtering. A thorough literature search was conducted, and the work of Szapiro and Rocca [355] was determined to be a good basis for our estimates of secondary electron production.

Due to the possibility of a current cascade where secondary electrons from one grid wire are accelerated and impact other focusing wires at high energy which then produce their own secondary electrons, only the measurement of the current to the cathode grid will be used as being truly proportional to the ion flux.

Since the cathode will be held at -10kV for both the 2-grid and multi-grid cases, Szapiro and Rocca would estimate our secondary electron yield at roughly 3 electrons/ion for 10keV argon ions impacting a stainless steel wire. Our stainless steel longitude wires are annealed in the atmosphere, however, there is an oxide layer covering the stainless steel wire which is likely to substantially enhance the secondary electron current. The 304 stainless steel from which our wires are made is composed of Iron (66-74%), Chrome (18-20%), and Nickel (8-10%) with trace amounts of other elements. Based on the research of Allen, Dyke, Harris, and Morris [356] it is likely that the majority of the oxide on the wire surface is iron oxide. Direct data for argon ions impacting oxidized

31

iron at relevant energies were not located, but secondary electron yield from other oxides with 10keV argon ions could be as high as 6 to 9 electrons/ion (for Aluminum oxide and magnesium oxide respectively)[355].

These yields are in stark contrast to the yields of secondary electrons off of clean, pure metal surfaces which are typically less than 1 electron/ion and depend substantially on ion incidence angle as well as energy and crystallographic orientation of the base metal [354].

While there is a large amount of uncertainty in the actual yield of secondary electrons, the secondaries will actually increase the measured current to the grid in proportion to the ion flux (for the cathode). Therefore secondary emission will be simultaneously a source of increased signal strength and increased signal noise. Due to the statistical nature of the process and the high frequency of grid impacts and secondary emission, the signal strength is expected to increase much more than the noise. Of course, the oxide layer on the grids may sputter off which could cause the signal/noise to degrade with time as the grids are sputtered clean. The time of this variation will undoubtedly be a function of the depth of the oxide layer on the grids and the conditions at which the system is run (background pressure, applied voltage, injected beam current, etc.).

2.2.3. Modeling Uncertainties

Ions can be lost via undetectable pathways: recombination, or ion neutralization on the ion source itself. These loss mechanisms have not been modeled because they are assumed to be negligible compared to the primary loss mechanisms already discussed. If

confinement is worse than expected, it may be worthwhile to model these other possible loss mechanisms.

2.2.4. Equipment Limitations

The experiment described in this thesis was conducted in a vacuum chamber that was consistently capable of a high vacuum base pressure on the order of 5e-7 mbar. The lowest pressure achieved in the chamber after extensive cleaning and a 3 day pump-down was 8e-8 mbar. The facility does not have provisions for bake-out or an ion pump for UHV operation. While these base pressures should allow the demonstration of improved confinement in the multi-grid configuration, the chamber is not currently capable of achieving the base pressures identified [357] as necessary for ion-ion collision limited confinement.
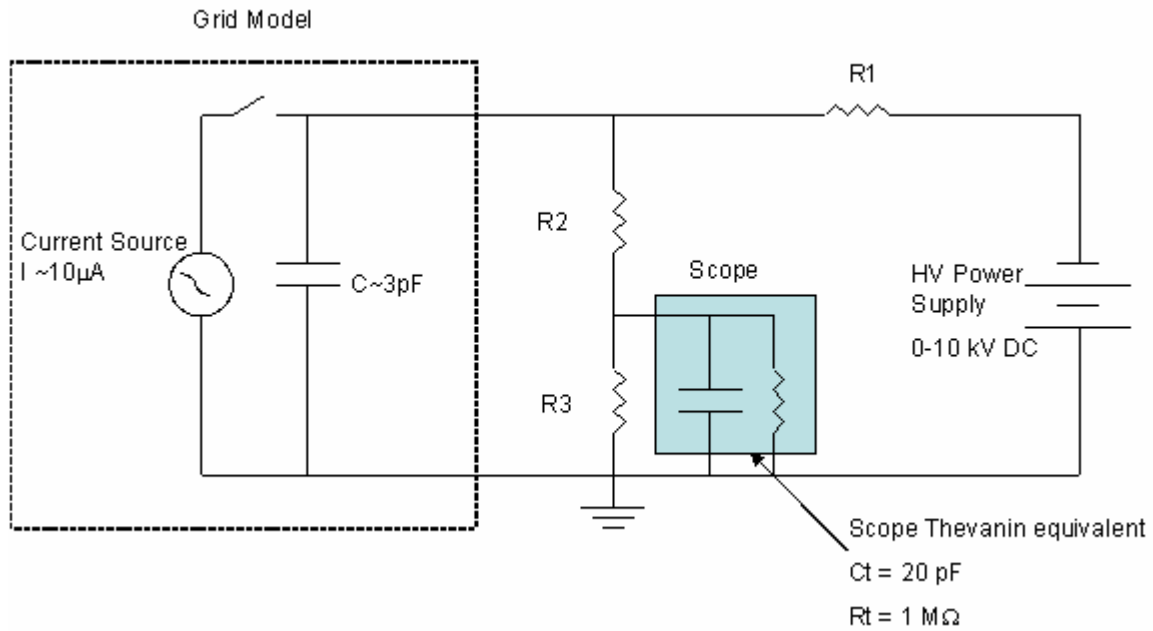
Figure 7: Schematic model of one high-voltage grid circuit

The four high voltage power supplies that control the grid potentials are also each limited to a maximum current of approximately 425 µA and a potential of -10 kV. The

maximum power output of each of the four independent supplies is approximately 4W.

The geometry of the HV feed-through and the wire grids resulted in a built-in capacitance

of approximately 3pF as shown in figure 7. Because 1/e ion confinement times could be

as low as half the bounce time (or a minimum of around 3μs for Helium ions and a -10kV

cathode), the resistance between the grids and ground (R2+R3 in figure 7) could be at

most 1MΩ in order for the RC decay time constant to be lower than the decay time we

are trying to measure using the direct measurement of current to the grid wires. This

resistance limitation combined with the power/current limitations on the HV supplies

resulted in a minimum cathode voltage of only -400V for the grid-current diagnostic.

It should be noted that by floating (isolating) the potential of either the power supply

itself or a difference amplifier across R1 in figure 7 the current could be measured

without this restriction on the grid voltage. Due to practical constraints on isolating these

components in the existing laboratory environment, these options were not pursued.

The use of the destructive beam-dump diagnostic was prevented by the unavailability of a

second functional fast-switching HV supply. One is necessary to control the injection of

ions, and another would be required to dump the trap after a certain amount of time.

Only one functional fast-switch was available for the present investigations. A second

switch was on hand, but it stopped working before useful measurements could be made.

Differential pumping was not available, so it was not practical to maintain a substantial

pressure differential between the ion production region and the bulk of the chamber

volume. Therefore, the strength (current out) of the ion source is proportional to the

background gas pressure in the chamber. When the pressure is reduced to levels where multiple order-of-magnitude improvements in 1/e confinement time are predicted by the particle in cell models, the ion source is so weak that the signal to noise ratio is too low to discern the 1/e confinement time from the data.

A final, and potentially quite important source of error arises from the construction of the ion source itself. The ion source is contains a thoriated tungsten filament which serves as an electron source. The filament is located outside the anode grid. A fine (~1cm spacing) wire mesh screen covers the equatorial section of the anode. See figure 18 in the next section for a schematic drawing of the ion source. The filament potential is rapidly (<1μs) switched from the ground (anode) potential to -150V. Electrons emitted by the filament are then accelerated toward the anode screen. Because the screen is 87% transparent, the Hirsch formula [21] suggests that electrons will make 3.58 passes back and forth through the screen before impacting one of the wires. Background gas in the region is ionized via electron bombardment. Ions that are generated inside the anode grid fall into the potential well of the device, while ions that are created outside the anode grid are accelerated towards the filament and are expected to generally result in the production of more secondary electrons. When the ion source is turned off the filament potential is rapidly (<1μs) raised to ground. The electrons that are now "boiled off" the surface thermionically do not have sufficient energy to ionize the background gas. The ion source is effectively turned off. The possible source of error arises from ions that were generated on the outside of the anode just before the filament potential was grounded. Those ions may be extracted from their location outside the anode screen into the potential well by field penetration from the inner grids through the screen. This situation

could result in a "slug" of ions born outside the anode entering the well after the filament potential is raised to ground. This transient slug of ions could result in an increase in the measured 1/e confinement time. There is evidence to suggest that this happens in the experiment.

2.3. Selection of Primary Diagnostic

Although it was originally anticipated that the measurement of the current to the grid wires would be the primary diagnostic for the experiment, the limitations described in the previous section resulted in a change in primary diagnostic.

2.3.1. Diagnostic Comparison

The candidates for the primary diagnostic were: the measurement of the current to the grid wires, the measurement of the current to a probe near the anode held at a potential lower than the anode, and the capacitive pickup on the probe near the anode held at a potential above the anode. As previously mentioned, DBD and LIF had been discounted due to equipment limitations.

The measurement of the current to the grid wires is limited to cathode voltages of -400 V. There was concern that with this relatively high cathode voltage and correspondingly shallow potential well, electrons born on the filament at -150V could penetrate quite far down into the potential well. The ions born in the well from the electron bombardment of the background gas would then have a relatively broad energy spectrum compared to the well depth. This sort of "spread ion source" was shown in OOPIC simulation to

result in less well confined ions. The birth location and potential of the ions was

observed to have an impact on the ion confinement time in the OOPIC simulation, so this

detection technique was not selected as a primary diagnostic. It is useful for purposes of

comparison however.

A probe inserted into the ion beam opposite the ion injector was used to make two other

types of diagnostics (see figure 19).   When the probe is biased at a potential lower than -

150V, all ions in the system are energetically capable of being neutralized on the surface

of the probe. The probe at this potential can act like a separate "collector grid" and allow

the direct measurement of lost ion current similar to the measurement of the current to the

grid wires. This type of diagnostic is appealing due to the ability to disconnect the grid

voltages from the collector voltage. The cathode grid can be biased to a potential much

lower than the -400V limit of the previous diagnostic, and the time resolution on the

detector can be improved by the use of a diagnostic with a smaller inherent capacitance

(<1pF) and a lower resistance (<1MΩ). The very presence of the probe, however,

significantly perturbs the potential structure around it because the Debye length of the

system at the operating densities is significantly larger than the diameter of the device.

This situation is true for any non-neutral IEC device. The perturbation of the potential

field around the probe results in an asymmetry which has the ability to change the

confinement properties. The biggest disadvantage of the use of the probe in this manner

is that it introduces an intentional ion sink into the ion beam that would not exist in an

operating device.   Due to the 2-D nature of the OOPIC code, the effect of the probe at

this potential could not be realistically modeled because in the simulation, every ion that

approached the probe would neutralize on the surface. While this scenario is not

physical, there is not a good way of quantifying the error with the existing tools.

When the same probe is biased slightly above the anode potential (+0.3V, figure 20), ions

born in the system are energetically incapable of impacting the probe. The ion sink is

removed. A significant asymmetry in the potential structure still exists, but OOPIC

modeling (which could be used in this case since no ions are lost to the probe) suggested

that a potential structure with good confinement would still tend to have good

confinement with the probe in the system on one side. The probe at this potential acts as

a capacitive pickup. Although the currents to the probe will be lower, the probe should

not significantly reduce the confinement time of ions in the system. This diagnostic was

therefore chosen as the primary diagnostic for these experiments.

2.4. *Hardware Development*

Significant effort went into the development of the facilities necessary to show the

potential for multiple grids to improve the ion confinement time in IEC systems. This

section details some of the important work should it need to be recreated in the future.

2.4.1. Vacuum Chamber Retrofitting

A stainless steel vacuum tank was acquired from another university where it had been

used for sputtering materials. The inside of the tank was blasted clean and a hinged door

was retrofitted. An additional port was added to the tank to accommodate the 1000 L/s

turbopump used for all high vacuum operation. A leaded-glass window was added to one

of the ports. A 10kV electrical feedthrough was added to supply the grids, along with a

combined gas and electrical feedthrough structure for the ion source and a 700V

diagnostic feedthrough opposite the ion source. Finally, a stand was constructed that

would allow the chamber to be transported and supported horizontally for easy access.

Figure 8 shows the chamber in its final configuration. A combined pirani and ion gage

pressure sensor was mounted to another port on the chamber allowing pressure

measurement from 1 atmosphere to 10^{-10} mbar.

Power supplies and diagnostic hardware are visible in the rack on the right. A 2 GHz

Tektronix 2014 Digital Oscilloscope was used for data acquisition. Output was through

an RS-232 serial cable to the computer (monitor visible on the bench at the far right).
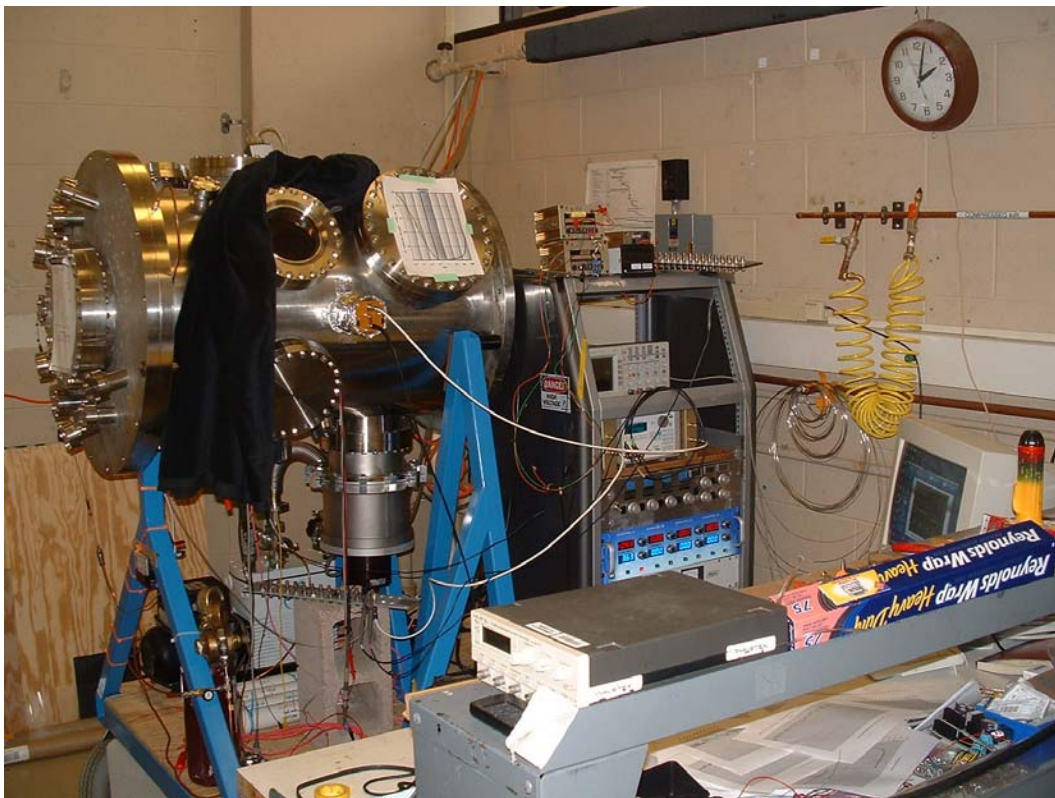
Figure 8: Vacuum chamber

2.4.2.   Grid Fabrication

Since the decision had been made to construct the multi-grid portion of the experiment with five concentric spherical wire grids, it was necessary to develop a standard methodology for constructing the grids. The final solution that was arrived at is reported in this section.

After considering many different options for grid wire materials, 1mm diameter 304 stainless steel wire was chosen for all grids so the structures would have sufficient rigidity to survive normal handling, and so conventional, spot-welding techniques could be implemented with ease. It is expected that a more detailed analysis of the material choice will be required for future devices.

Figure 9: Fabrication of grid wire jig

A jig to hold the 304 stainless wire in place at the proper curvature for spot welding was machined from a piece of polycarbonate as shown in figure 9. The wire was laid in the trough and spot-welded to the desired diameters. It was then removed from the jig. The wires that were to become longitude lines were then annealed so they could be cut and still maintain the desired radius of curvature. After some limited experimentation shown in figure 10, it was discovered that running a current of 35 A through the hoops for 1 minute would give the desired effect.
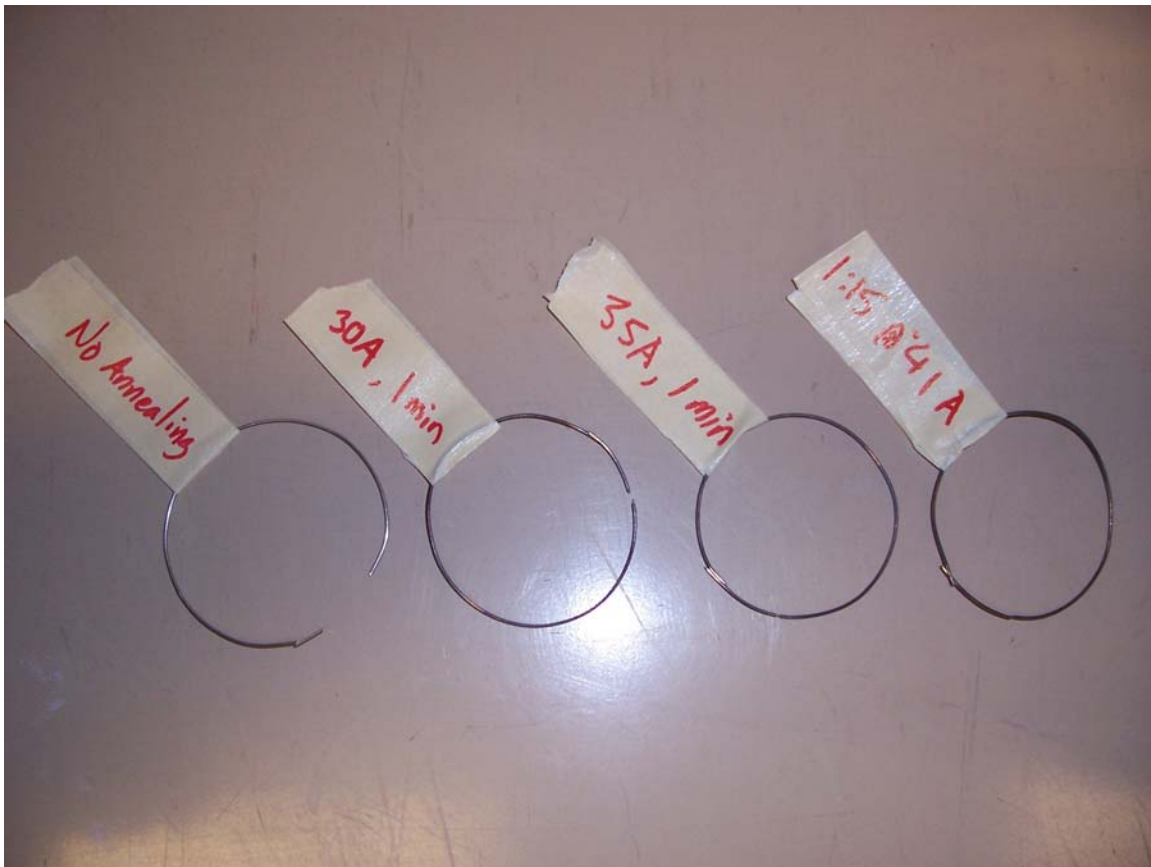
Figure 10: Grid wire annealing tests

When less current was used for less time, the wire would show some residual "spring-back," but if more current was used for much more time, the wire would tend to deform significantly under its own weight and the forces applied by the alligator clips used to supply the current.
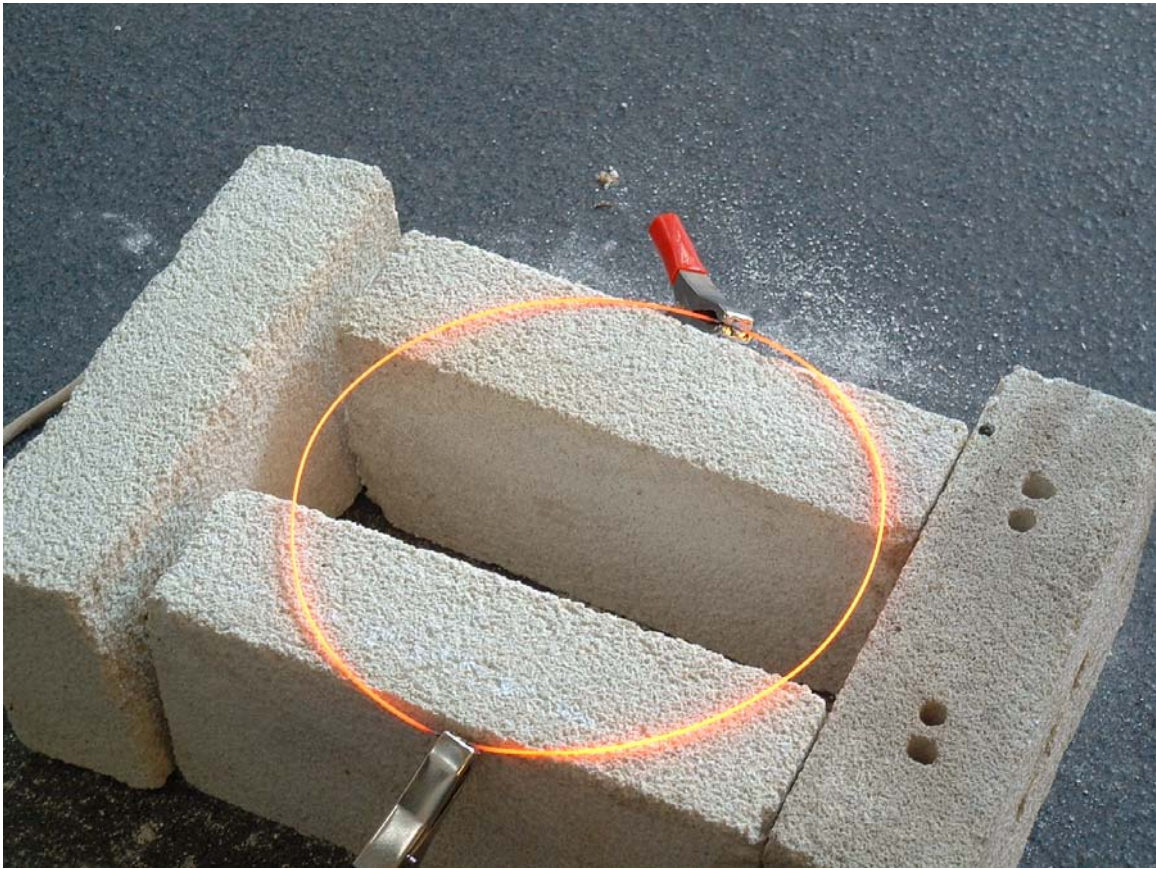
Figure 11: Atmospheric annealing of longitude wires

Figure 11 shows the atmospheric annealing of one of the grid wires. Once the annealing of the longitude lines was complete, they could be cut in sections and maintain the desired radius of curvature. The latitude lines were not annealed because they did not need to be cut during the assembly procedure. The longitude lines had to be cut so the feed-throughs supplying the inner grids could pass through the pole and introduce the minimum possible field asymmetry.

In order to attach the longitude wires to the polar feed-through, special stainless steel rings were fabricated from 1/16" plate using an OMAX waterjet cutter. These rings provided structural support and an electrical connection for the grids.

Figure 12: Spot welding longitude wires to retaining rings

The eight longitude wires were spot-welded to the support rings as shown in figure 12. The support rings were designed to fit onto custom machined aluminum parts that were held onto the alumina feed-through stalk at the appropriate radius by a set screw.

After the longitude lines were welded to the retainer rings, the latitude lines would be spot welded onto the outside of the longitude lines at the appropriate position. A simple wire spacer was used to locate the hoops concentrically around the poles. Errors in the actual location of the longitude lines could result in a slight perturbation of the latitude line position. In general, this construction error was measured to be less than 5%.
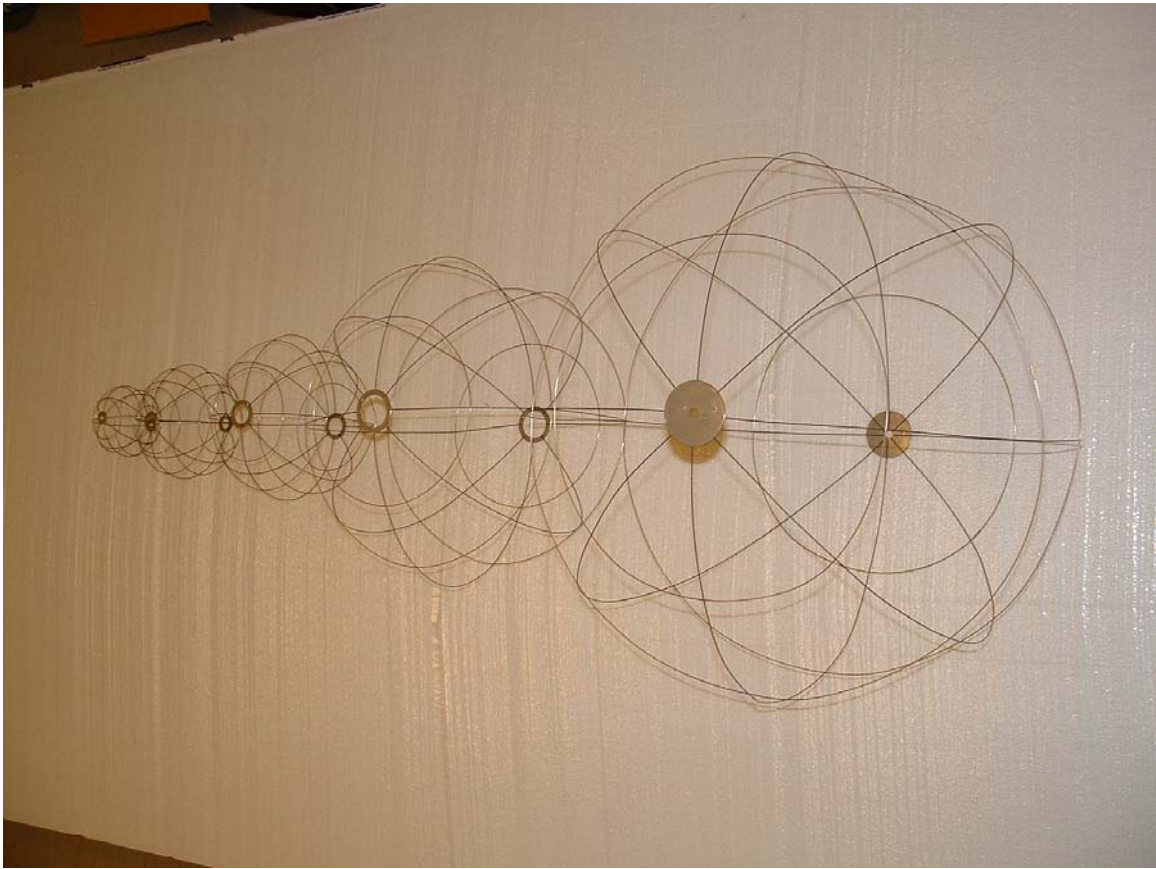
Figure 13: All finished grids

Figure 13 shows all of the completed wire grids. Slight asymmetries in the grid wires are visible to the naked eye, but position errors of the latitude line locations were all measured to be less than 8% of the respective radius. Longitude line errors were significantly less than that.

In order to install the grids in the final multi-grid system, they had to nest one inside the other. This was accomplished by again cutting the longitude lines near the equator this time. The cut was made actually just "south" of the equator – right above the southern "tropic" latitude line. This asymmetric cut was used to improve the ease of re-assembly. It was desired to have one well-located, stiff wire end, and one more easily manipulated,

less well-located wire end that would be moved to align with the stiff end. This was

assumed to be easier than lining up to wire ends of moderate stiffness.
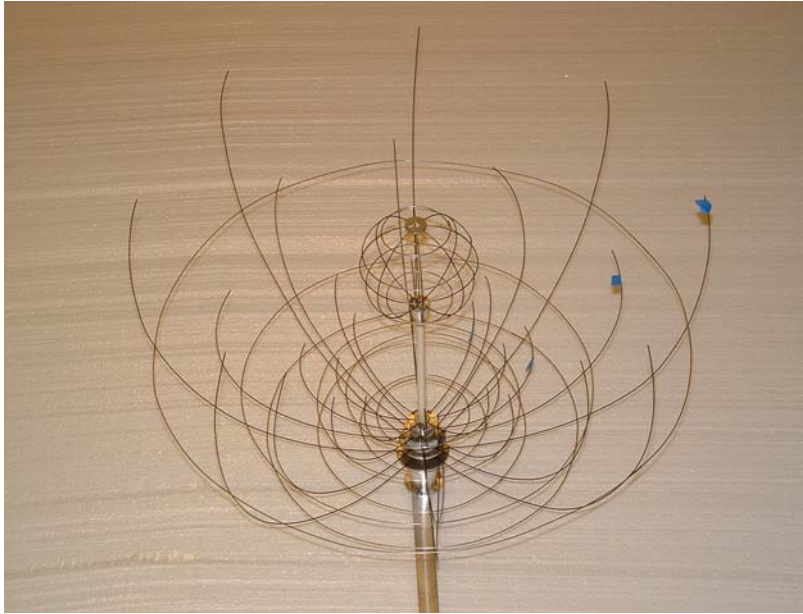
Figure 14: The "Awesome Blossom"

The resulting "half-grids" resemble a flower blossom as shown in figure 14 and a radar

dish or directed listening device as shown in figure 15.
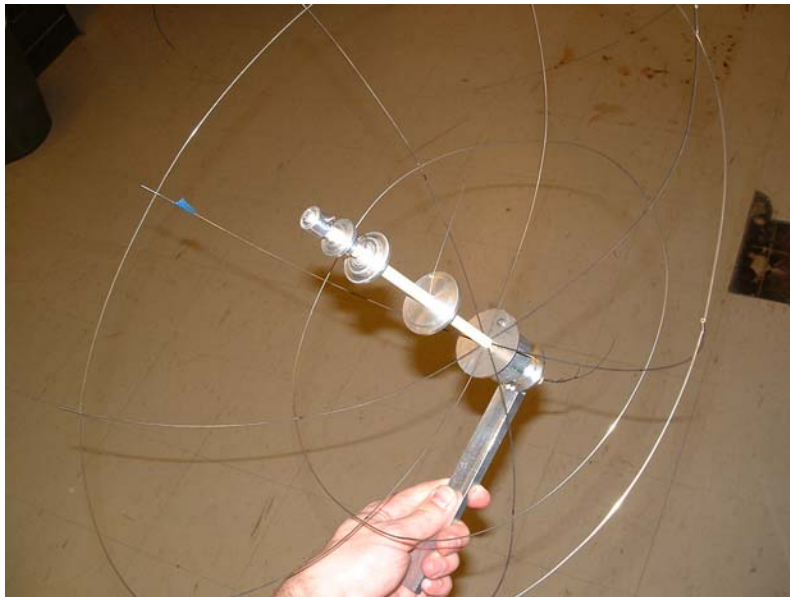
Figure 15: The "radar" with alumina feed-through and aluminum ring supports

When the grids are assembled in the chamber, 1" sections of 1/16" diameter stainless steel tubing are crimped onto the longitude wire ends on the "radar" half, which allow the insertion and perfect alignment of the longitude lines on the upper, "blossom" half. Figure 16 shows the completed multi-grid IEC assembly inside the vacuum chamber.
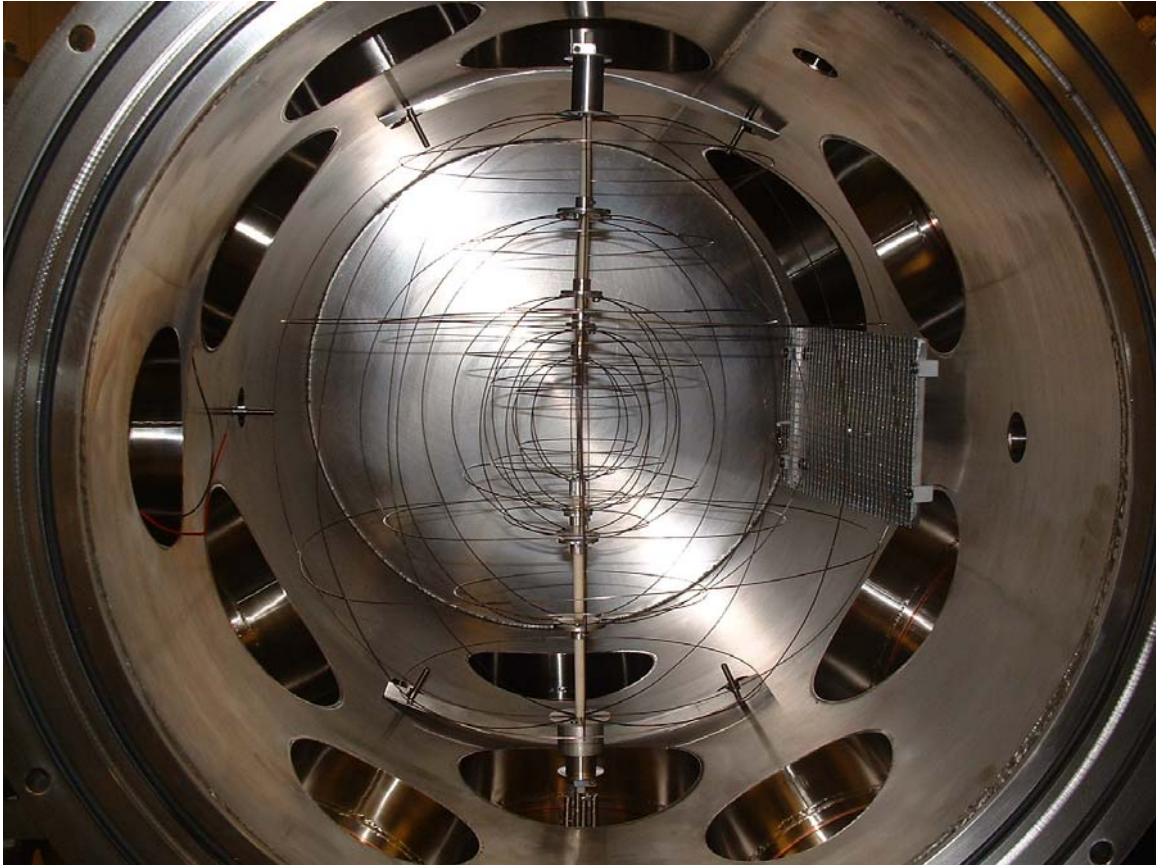
Figure 16: Multi-grid IEC in the vacuum chamber

2.4.3. Ion Source

During the course of these investigations a number of different ion source geometries were tried. The final ion source used for all of the experiments reported in this thesis was designed to have a minimal impact on the potential structure inside the anode grid.
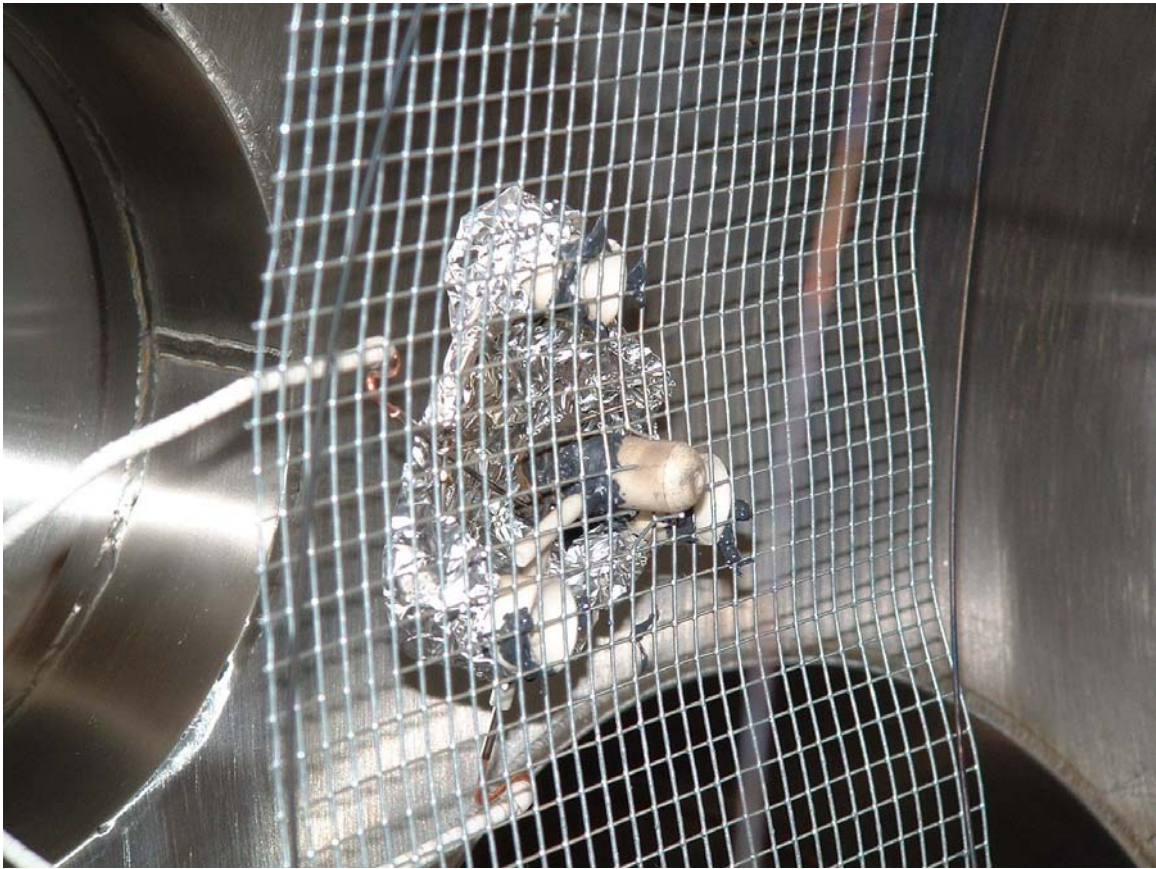
Figure 17: Ion source used in experiment

Figure 17 shows a picture of the ion source used for all experiments reported herein. Ions are generated by electron bombardment of the background gas in the chamber. The electron source is a thoriated tungsten wire filament located outside the anode grid. The filament continually emits electrons thermionically. The filament is powered by an isolated variac that is always on. When ion generation is desired, the filament potential is reduced from ground to -150 V by a fast amplifier capable of driving the filament circuit to the desired potential within 3 μs. Electrons emitted from the filament at the lower potential are accelerated towards an 87% transparent screen mesh which is held at ground. Figure 18 shows a schematic of this ion source.

The peak of the electron bombardment ionization cross-sections for both Argon and Helium lie in the range of 100-150eV electron energy. Ions are therefore generated all around the screen mesh which is positioned such that it is tangent to the surface of the spherical anode grid. Those ions which are generated inside the anode grid fall into the well, while those generated outside are accelerated towards the filament and aluminum foil "neutralizer" which is electrically connected to one of the filament leads.
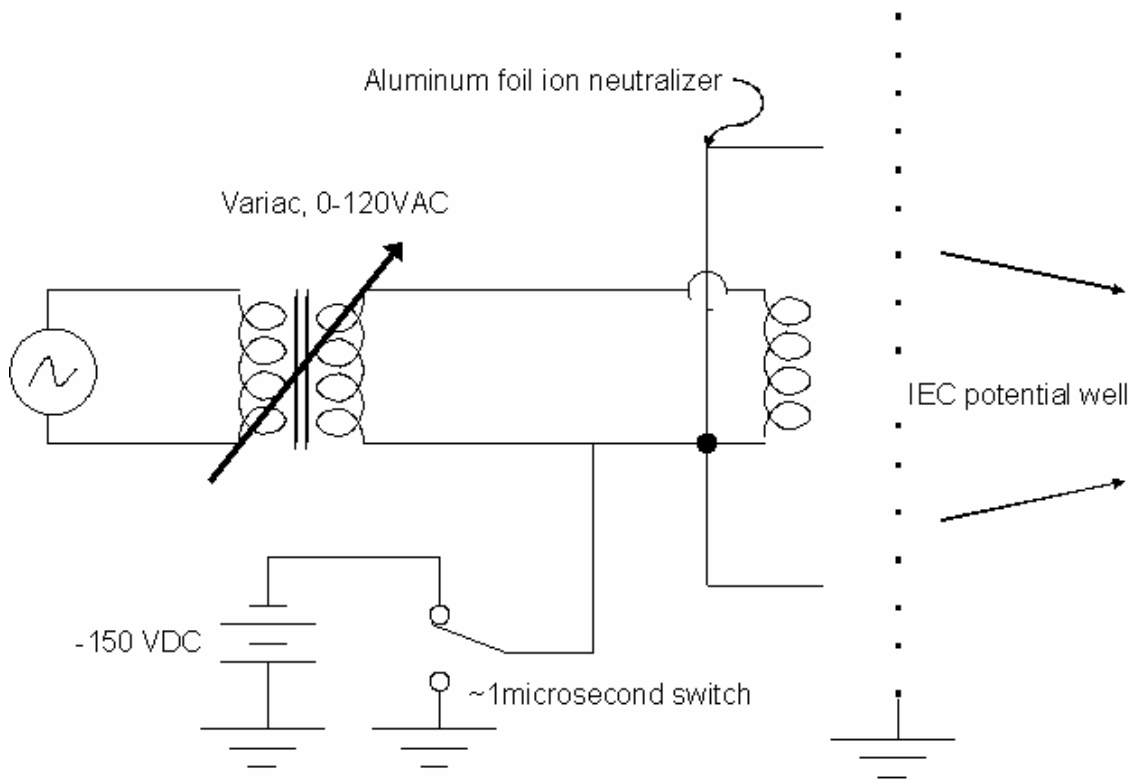
Figure 18: Schematic representation of ion source

This design results in the quick removal of ions generated outside the anode while allowing the ions generated inside the anode to fall unobstructed into the IEC potential well.

48

One drawback of this source is that after the filament potential is returned to ground, there are ions that were generated between the filament and the screen which now are not attracted to the neutralizer and are slowly extracted into the IEC potential well by field penetration through the grid mesh. Due to the high electron density in this region, there exists a large number of these ions relative to the ions generated on the other side of the screen. This results in a "slug" of ions at shutdown which can be seen clearly in the data when the potential structure has good confinement.

2.4.4.   Ion Detector

The capacitive probe was the primary ion detector used in these experiments, although measurements of the current directly to the grid wires were also made at grid potentials near ground (down to -400V).   Figure 19 shows a picture of the capacitive probe wire poking through the center of the anode mesh.
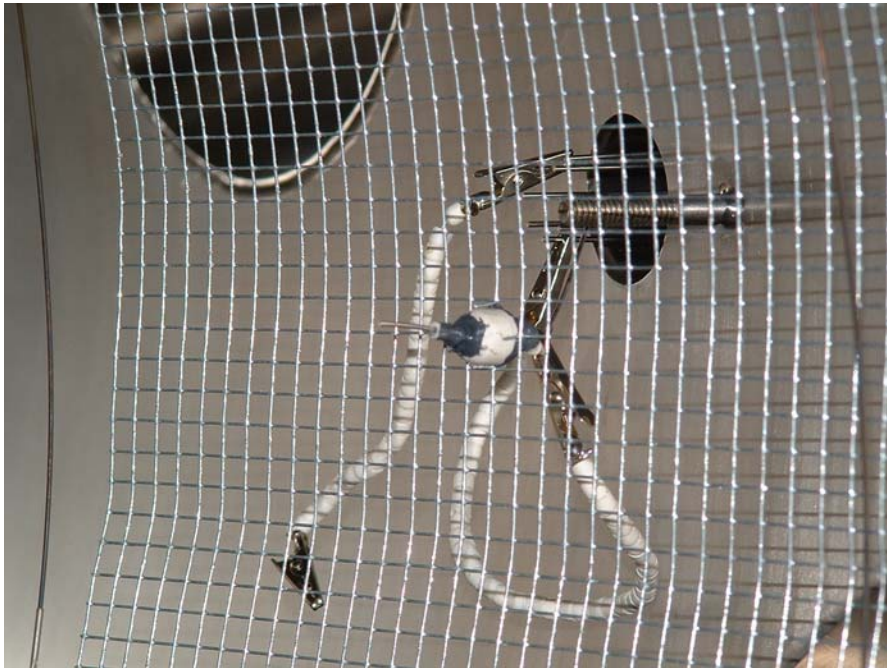
Figure 19: Wire probe

The detector circuit is a simple 1/100 voltage divider on a 30V DC power supply which held the probe at a nominal potential of around 0.3V (actually 0.28 V due to resistor tolerances).   A schematic of the detector is shown in figure 20.

Since the maximum birth potential of any ion in the system is 0V, this 0.3V offset would ensure that a negligible number of ions will be neutralized on the probe due to the thermal spread of the ion energy at birth (assumed ~.03eV). Most ions should be born at lower potentials (an average of around -25V based on the Argon cross-section). Of course, collective effects such as the two-stream instability have the potential to spread the ion distribution function on a much faster time-scale than the collisional thermalization time which could result in some ions impacting the probe, but due to its small area compared with the anode grid and screen, it is highly unlikely that the probe will be a significant ion sink.
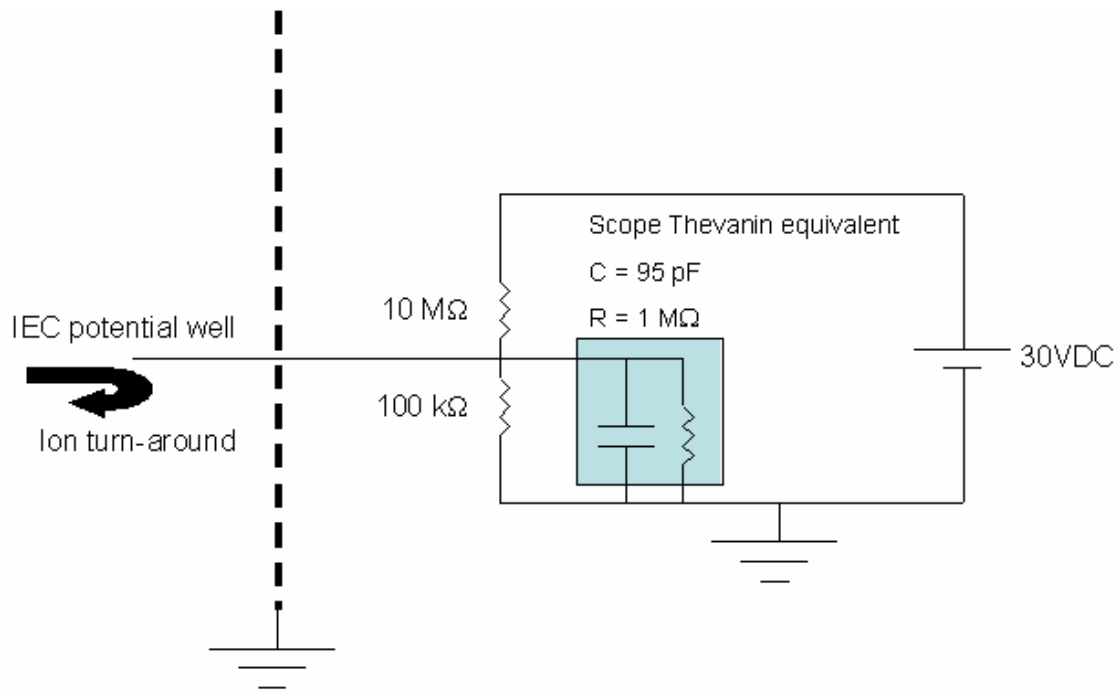
Figure 20: Schematic of capacitive detection circuit

The Tektronix TDS 2014 scope was attached to the wire probe on the middle of the divider via a 1X scope probe. With these resistors, the estimated maximum bandwidth of this detector is around 100kHz which is about at the limit for Argon (with a bounce time of ~23 μs). Lower value resistors were used to search for the predicted two-stream instability in Helium due to Helium's 8 μs bounce time, but lower value resistors reduce the strength of the signal as well as increase the bandwidth, and Helium had a much weaker signal to begin with due to its lower ionization cross-section.

The following chapter presents some of the computational modeling that was done prior to and concurrent with the design and operation of the experiment.

3. Computational Modeling for Design

In order to estimate IEC device performance, two independent computer codes were used to predict ion behavior. The commercial PIC code called OOPIC was introduced in chapter 1. In addition, a custom code was written in MATLAB to approximate the true, 3-D potential structure. The potential variation along the center of the beamline was then used in conjunction with the 1-D paraxial ray approximation to solve for the beam envelope and the maximum confined core ion density. This chapter explains these computational tools in greater depth.

3.1. Semi-analytic potential model for a multi-grid IEC device

A means of solving for the full, three-dimensional potential structure around a multi-grid IEC device was desired. Conventional finite difference approaches are not convenient. The small wire size and the large volume and wire spacing make for a computationally inefficient solution. Finite element methods with adaptive grid spacing were not seriously considered due to the scope of the computational problem. Instead, a semi-analytic approach was adopted with a truncated series potential representation.

3.1.1. Derivation

First the space charge of the trapped ions in neglected, so the potential structure is assumed to be a solution to the Laplace equation.

$$\nabla^2 \Phi = 0 \qquad\qquad \textbf{Equation 3.1}$$

We choose to represent the potential in spherical coordinates where $\theta \equiv$ longitude and $\phi \equiv$ co-latitude. The potential and its derivatives can then be represented by a summation of orthogonal spherical harmonics

$$\Phi_i(r,\phi,\theta) = \sum_{k=0}^{\infty} \sum_{m=-k}^{k} \left[A_{km}^i r^k + B_{km}^i r^{-(k+1)} \right] P_k^m(\cos\phi) \cos m\theta + F_i \qquad \textbf{Equation 3.2}$$

and

$$\frac{\partial \Phi_i}{\partial r}(r,\phi,\theta) = \sum_{k=0}^{\infty} \sum_{m=-k}^{k} \left[k A_{km}^i r^{(k-1)} - (k+1) B_{km}^i r^{-(k+2)} \right] P_k^m(\cos\phi) \cos m\theta \qquad \textbf{Equation 3.3}$$

where P_k^m is the associated Legendre function of the first kind and the index "i" is an integer from 1 to $n+1$ where $n = $ # of concentric spherical wire grids. The coefficients A and B (and the constant offset F) uniquely determine the potential. It can be inferred from equation 3.2 that for a finite potential solution, all $A^{n+1} = 0$, and similarly, all $B^1 = 0$. A finite potential solution also requires $A \to 0$ and $B \to 0$ as $k \to \infty$. Therefore a truncated series with sufficiently large "k" should closely approximate the exact solution. The problem becomes one of solving for the A and B coefficients for the finite series given the appropriate boundary conditions. With this type of representation, the boundary conditions become trivial to impose. From continuity we get:

$$F_{i+1} = F_i \qquad \textbf{Equation 3.4}$$

$$B_{km}^{i-1} - B_{km}^i = \left(A_{km}^{i-1} - A_{km}^i \right) r_i^{(2k+1)} \qquad \textbf{Equation 3.5}$$

where r_i is the radius of the ith grid. We then define an angular delta function such that

$$r_i \int_0^{\alpha} \delta(\theta - \beta) d\theta \equiv 1, \quad \int_0^{\alpha} f(\theta) \delta(\theta - \beta) d\theta = \frac{f(\beta)}{r_i}, \quad 0 < \beta < \alpha \qquad \textbf{Equation 3.6}$$

Poisson's equation (the flux condition) at the grid wires can then be expressed as

$$\left[\frac{\partial \Phi^i}{\partial r} - \frac{\partial \Phi^{i-1}}{\partial r}\right]_{r=r_i} = \frac{-1}{\varepsilon_o}\left[\sum_{j=1}^{t} q_i \delta(\phi - \frac{j\pi}{t+1}) + \sum_{j=1}^{l} q_i \delta(\theta - \frac{j2\pi}{l})\right] \qquad \textbf{Equation 3.7}$$

where q_i is the charge per unit length on the grid wires, $t \equiv \#$ of latitude wires, and

$l \equiv \#$ of longitude wires. Note the form of this equation assumes an even angular

distribution of both longitude and latitude lines. From this point forward, the expression

on the right hand side of equation 3.7 will be referred to simply as RHS and the

expression on the left will be referred to as LHS. Substituting $\dfrac{\partial \Phi}{\partial r}$ on the LHS we get

$$\sum_{k=0}^{\infty}\sum_{m=-k}^{k}\left[kr_i^{(k-1)}\left(A_{km}^i - A_{km}^{i-1}\right) - (k+1)r_i^{-(k+2)}\left(B_{km}^i - B_{km}^{i-1}\right)\right]P_k^m(\cos\phi)\cos m\theta = RHS \quad \textbf{Equation 3.8}$$

Then using continuity as expressed in equation 3.5, this expression can be simplified to

$$\sum_{k=0}^{\infty}\sum_{m=-k}^{k}(2k+1)r_i^{(k-1)}\left(A_{km}^i - A_{km}^{i-1}\right)P_k^m(\cos\phi)\cos m\theta = RHS \qquad \textbf{Equation 3.9}$$

or

$$\sum_{k=0}^{\infty}\sum_{m=-k}^{k}-(2k+1)r_i^{-(k+2)}\left(B_{km}^i - B_{km}^{i-1}\right)P_k^m(\cos\phi)\cos m\theta = RHS \qquad \textbf{Equation 3.10}$$

It can be clearly seen that the RHS expression uniquely determines the relationship

between the A^i and A^{i-1} coefficients, and similarly B^{i+1} and B^i coefficients. Because we

know that all the B_{km}^1 and A_{km}^{n+1} coefficients must be zero in order for the series to

converge at $r = 0$ and $r = \infty$ respectively, all of the A and B coefficients can be solved

based upon the RHS expression. These coefficients can be extracted from the

summations because of their respective orthogonality. In particular, cosine orthogonality

can be used to simplify the expression. This step will eliminate the sum over m.

$$\int_0^{2\pi} (LHS) \cos m'\theta d\theta = \int_0^{2\pi} (RHS) \cos m'\theta d\theta \qquad \textbf{Equation 3.11}$$

This picks out *m=m'* and gives a factor of pi. Similarly, the orthogonality of Legendre polynomials can be used to eliminate the sum over *k*. When complete, equation 3.9 becomes

$$2\pi r_i^{(k-1)} \frac{(k+m)!}{(k-m)!}\left(A_{km}^i - A_{km}^{i-1}\right) = \int_0^\pi \int_0^{2\pi} (RHS) P_k^{m''}(\cos\phi)\sin\phi\cos m'\theta d\theta d\phi \qquad \textbf{Equation 3.12}$$

Substituting in the RHS term and integrating reveals the simplified relationship between the coefficients.

$$2\pi r_i^{(k-1)} \frac{(k+m)!}{(k-m)!}\left(A_{km}^i - A_{km}^{i-1}\right) = \frac{-q_i}{\varepsilon_o r_i}\left[\delta_{m0} 2\pi \sum_{j=1}^t P_k^m\left(\cos\tfrac{j\pi}{t+1}\right) + \delta_{m(zl)} l \int_0^\pi P_k^m(\cos\phi)\sin\phi d\phi\right]$$

$$\textbf{Equation 3.13}$$

where $\delta_{ab} \equiv \begin{cases} 1, a = b \\ 0, a \neq b \end{cases}$ and *z* is any positive integer. So to solve for any coefficient,

simply start with $A_{km}^{n+1} = B_{km}^1 = 0$ and use.

$$A_{km}^{i-1} = \frac{q_i}{2\pi\varepsilon_o r_i^k}\frac{(k-m)!}{(k+m)!} X + A_{km}^i \qquad \textbf{Equation 3.14}$$

$$B_{km}^i = \frac{q_i}{2\pi\varepsilon_o r_i^{-(k+1)}}\frac{(k-m)!}{(k+m)!} X + B_{km}^{i-1} \qquad \textbf{Equation 3.15}$$

where $X = \delta_{m0} 2\pi \sum_{j=1}^t P_k^m\left(\cos\tfrac{j\pi}{t+1}\right) + \delta_{m(zl)} l \int_0^\pi P_k^m(\cos\phi)\sin\phi d\phi$.

In this manner the vacuum potential structure around an arbitrary number of independently charged concentric, spherical wire grids can be modeled in three-dimensions.

The charge q_i on the wires is approximated from a simple spherical capacitive relationship multiplied by a factor to account for the high transparency of the "spheres" and the distribution of charge over the surface area (proportional to r^2).

$$q_i = 4\pi\varepsilon_o \frac{\%A\left(\Phi_i - \Phi_{i+1}\right)}{r_i^2 \left(\dfrac{1}{r_i} - \dfrac{1}{r_{i+1}}\right)}$$

Equation 3.16

In the coded implementation of this model, Gaussian distributions of charge in ϕ and θ were used instead of delta functions to limit the bandwidth of the spatial representation of the wires to allow for faster convergence with a smaller truncation value of k. More information about the details of the modeling can be found in the code contained in the appendix.

Because a representation of the potential in all three dimensions is difficult to plot, sample cross-sections are presented in this chapter either at constant $r, \phi,$ or θ. In general a *kmax* of 32 yielded smooth partial derivatives in r which were required for paraxial ray beam envelope approximations. Figures 21, 22 and 23 show the modeling results for a typical potential variation on a plane through the equator.
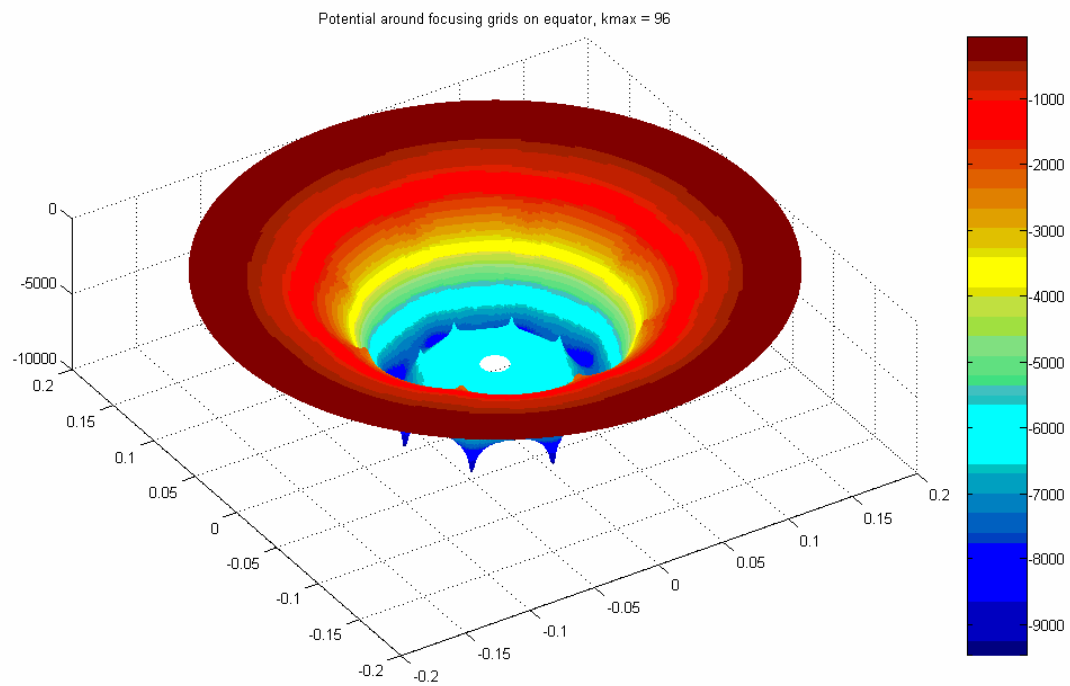
Figure 21: Potential map of equatorial cross-section ($\phi=\pi/2$) of a multi-grid IEC device.
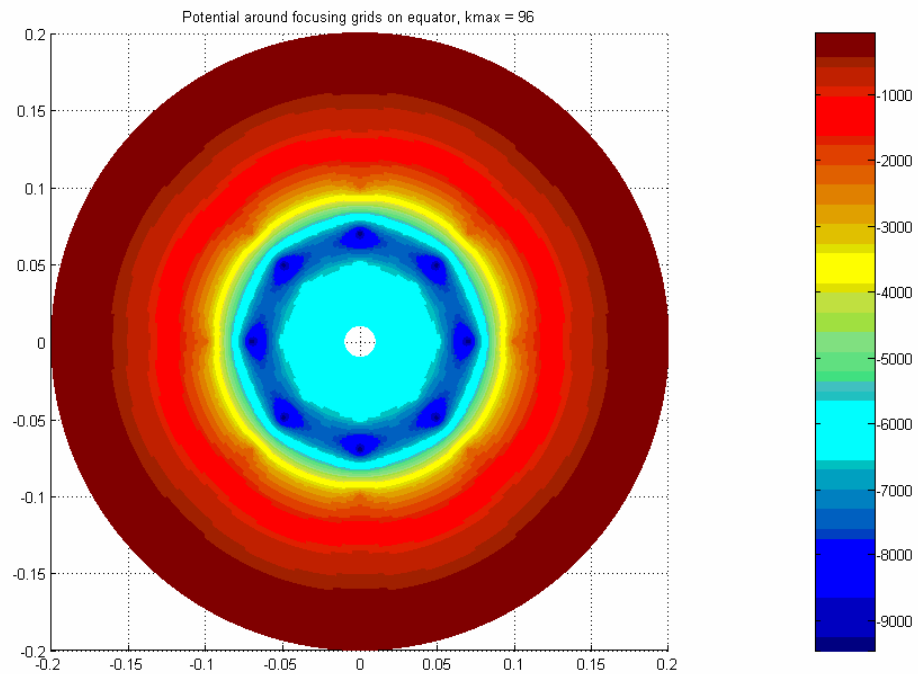
Figure 22: Different view of same potential map
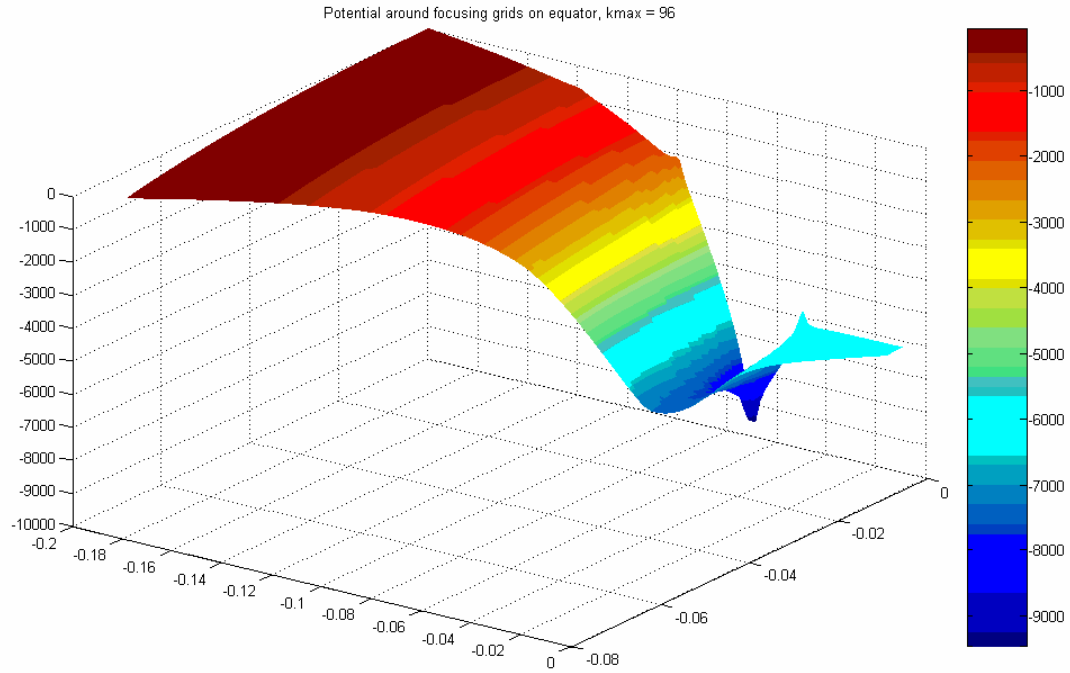
Figure 23: Same potential model, "pie" section from beamline to grid wires

3.1.2. Limitations and Inaccuracies

As with any model, there are limitations to the range of applicability of the model described in the previous section. In particular, the model has two fundamental inaccuracies which impose strict limitations on its range of validity:

1) Truncation of the infinite series results in unrealistic high frequency "noise" in the potential representation – especially when approximating field gradients over very short distances without applying any type of spatial potential smoothing near the cut-off frequency.

2) The assumption of constant charge density on the grid wires in wrong. In fact, the charge density varies significantly from the equator to the poles and in regions where wires overlap. The proper boundary condition is a constant potential on the grid wires. Unfortunately, that type of B.C. cannot easily be

implemented with this modeling approach. Plots of equipotential surfaces in figure 24 allow assessment of the significance of this inaccuracy.
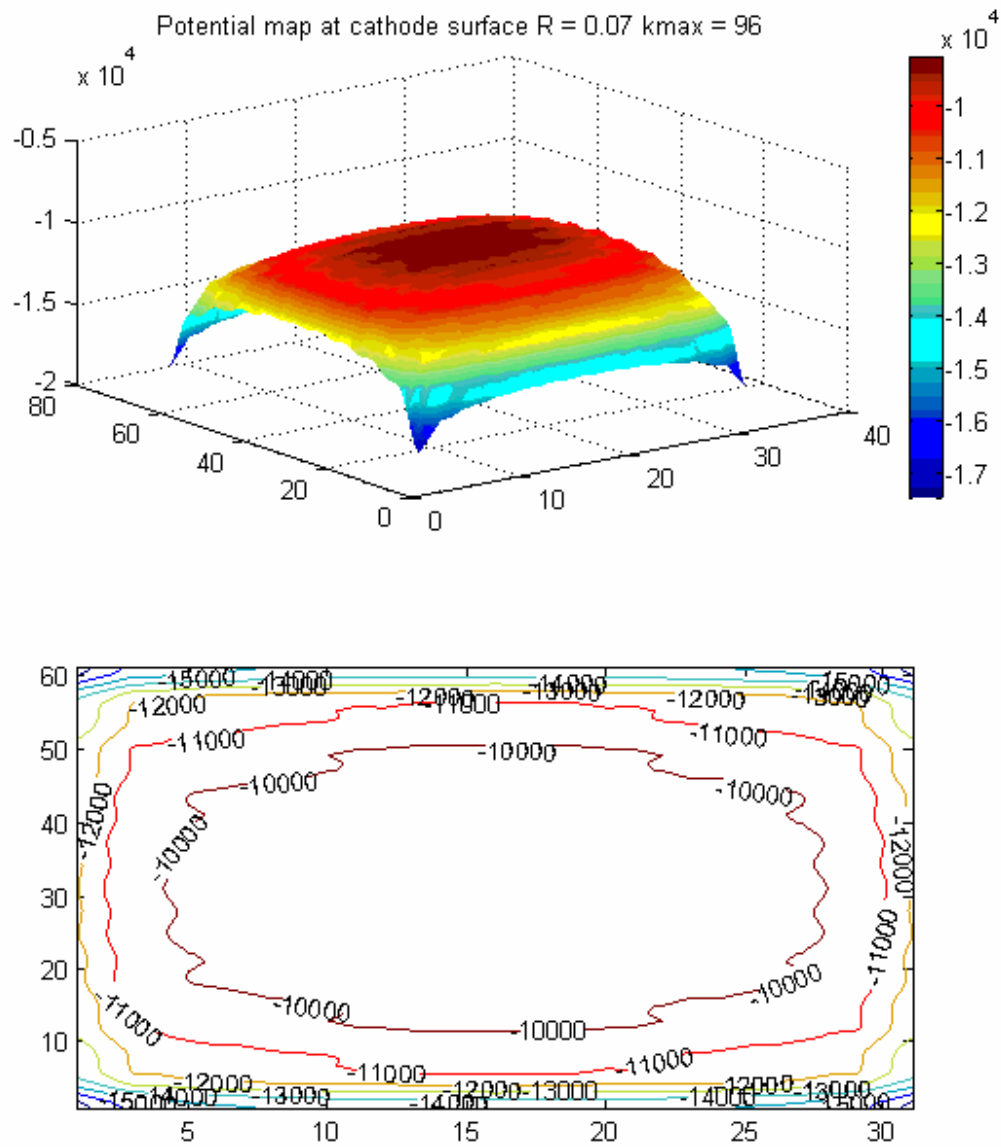
Figure 24: Spatial maps of the potential at a constant radius in between latitude and longitude wires on the equator, note unrealistic high frequency noise in the equipotential representation and potential deviation at wire overlap at the corners of the figures.

Figure 24 illustrates these inaccuracies clearly. An exact model would show no difference in the potential between the corners and the middle of the wires (along the edges of the figures). An exact model would also have smooth equipotential surfaces instead of the ripples introduced by the truncated series approximation.

These inaccuracies, together with the assumptions in the model itself result in the following limitations:

1) If resolution of the potential and derivatives of the potential are required at a given spatial frequency, the chosen value of kmax must not only satisfy the Nyquist condition, it must be twice the typical Nyquist criterion (at least 4 times the frequency) to allow the spatially smoothed signal to satisfy the Nyquist criterion i.e. the smoothing window should correspond to ½ the size of the minimum detail desired, and kmax must be ½ the wavelength of the smoothing window.

2) The potential model should not be used at all within the minimum resolution (as defined in #1 above) of the grid wire locations.

3) The potential model should not be used within the range of the inaccurate boundary conditions. This range of inaccuracy can be seen in the equipotential plots. When the equipotentials do not resemble the bulk shape of the grid wires (e.g. near the wire overlaps), the model will not give an accurate potential.

Fortunately, this model is to be used only for the purposes of preliminary experiment design, and for that reason, the only potential that is of significance is that along the

center of the beam line. This model should yield reasonable estimates of the potential for these crude purposes.
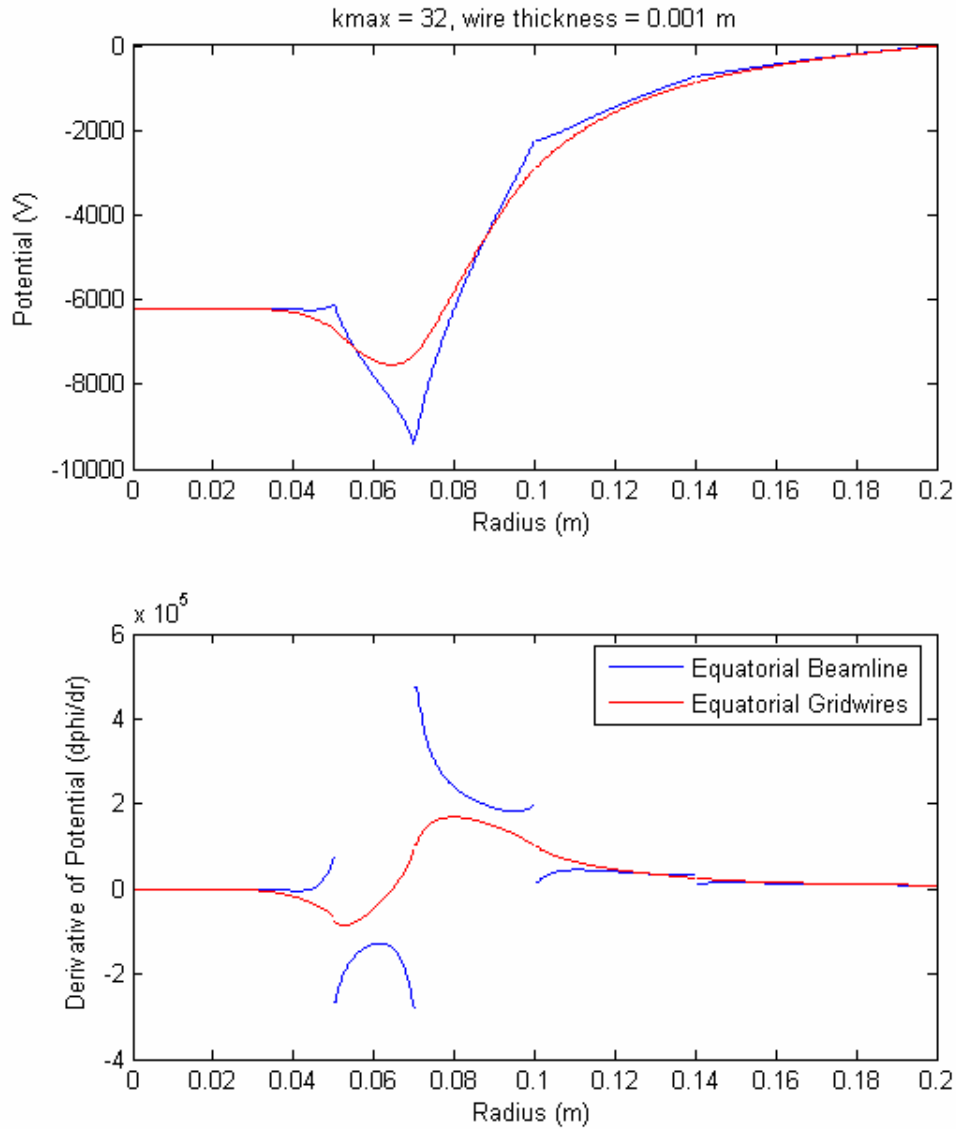
Figure 25: Constant θ cross section plots of potential structure of a multi-grid IEC device on a grid wire v. on the beam path

Figure 25 illustrates the continuous potential (upper plot) and derivative of the potential (lower plot) along the beam line and the discontinuous derivative of the potential at the grid wire locations as a result of the charge located there. The upper plot also shows the

regions where the potential structure is "confining" to ions and where it is "unconfining" i.e. near the lowest potential grid.

3.2. 1-D Paraxial Ray Equation Approximation

In order to estimate the maximum confined non-neutral ion density achievable in a multi-grid IEC device, a simple model of the variation of the radius of an ion beam based on the paraxial ray equation was developed.

3.2.1. Model Description

The output from the semi-analytic potential model described in section 2.1 was used to approximate the potential and the derivatives of the potential along an equatorial beam path in the multi-grid IEC device. The paraxial ray equation was used to predict the evolution of the ion beam envelope based upon that variation in the axial potential. This model was derived primarily from the work of Humphries [362]. Since there are no magnetic fields in an IEC device, the general form of the paraxial ray equation reduces to

$$R'' = -\frac{\Phi' R'}{2\Phi} - \frac{\Phi'' R}{4\Phi} + \frac{\varepsilon^2}{R^3} + \frac{K}{R}$$

Equation 3.17

where R is the radius of the beam envelope (perpendicular to the beam line and the r vector in the IEC device). ε in this equation is the beam emittance, and K is the generalized perveance defined relativistically as

$$K = \frac{eI_o}{2\pi\varepsilon_o m_o (\beta\gamma c)^3}$$

Equation 3.18

In this equation, $\gamma = \dfrac{1}{\sqrt{1 - v^2/c^2}}$, c is the speed of light and β=v/c the ratio of the ion

velocity to the velocity of light. The generalized perveance is proportional to the number

density of ions, and it is the term that accounts for the space charge of the beam in this

simple model. Although it is inaccurate, zero emittance (the laminar beam

approximation) is assumed because the goal of this model is to predict the maximum

space-charge limited confined ion density in the core of the device, not to predict a

particular beam envelope.

3.2.2.   Numerical Integration of Beam Envelope

Symmetry of the ion beam in the core of the device (a zero slope condition) is assumed

along with a core radius. These assumptions provide the initial boundary conditions from

which the paraxial ray equation can be integrated. MATLAB's "ode45" routine is then

used to integrate the paraxial ray equation from the core out to the radius of the injector.

In order to verify convergence of the integration, the numerical integration is repeated in

reverse, this time the initial conditions are the final conditions of the 1st integration and

the beam envelope is integrated on the way in. The deviation of the final radius and slope

of the beam envelope is compared to the assumed initial radius to verify convergence of

the routine.

Figure 26 shows an example of a beam envelop that did not converge, while figure 27

shows a converged beam envelope.
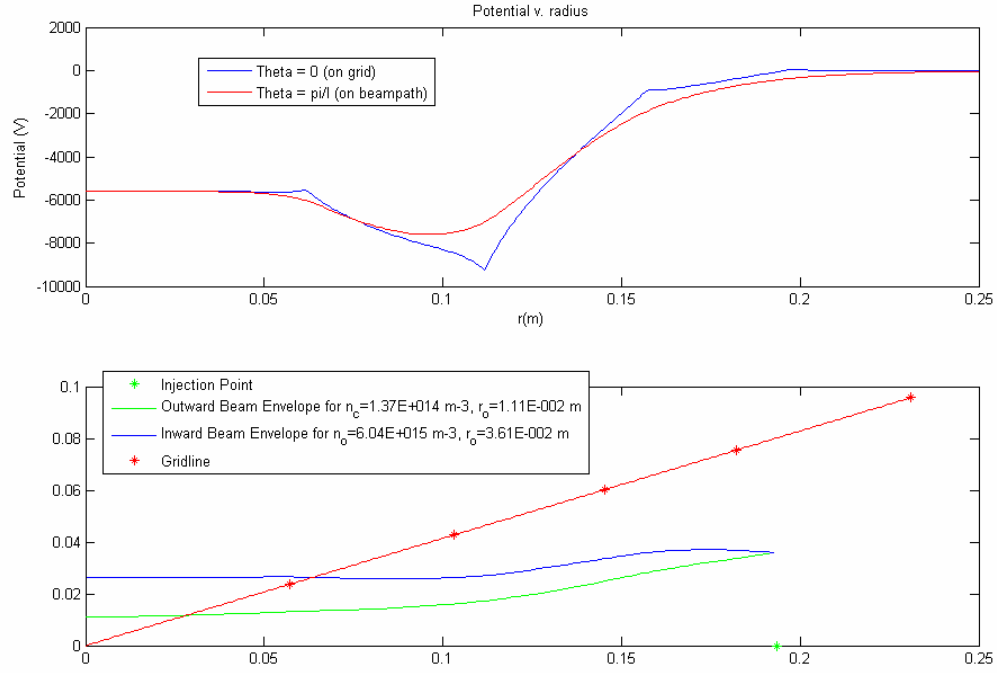
Figure 26: Improperly converged integration example

3.2.3. Iterative Solution to Maximum Beam Density

A maximum acceptance window which defines how close the modeled beam is allowed to come to the grid wires is assumed (typically 70-90% of the height of the grid wire from the beam axis). The initial beam current (ion density) is assumed to be two orders of magnitude lower than the density at which space charge effects are expected to be seen based on PIC modeling and simple back-of-the-envelope Child-Langmuir calculations for this size device. The beam envelop is then solved out to the injector radius. Near the injector radius the paraxial ray equation loses all validity because the implicit linearization assumes beam-like behavior which is not the case near the ion injection potential. If the beam envelope does not exceed the acceptance window at the grid-wire locations, the core density is increased by a factor of two, and the integration is repeated.

64

This iterative process is repeated until the space charge effects of the beam force the

beam envelope outside the acceptance window of one of the grids at which point the

routine is stopped. The maximum confinable ion density is thereby found to within a

factor of two.
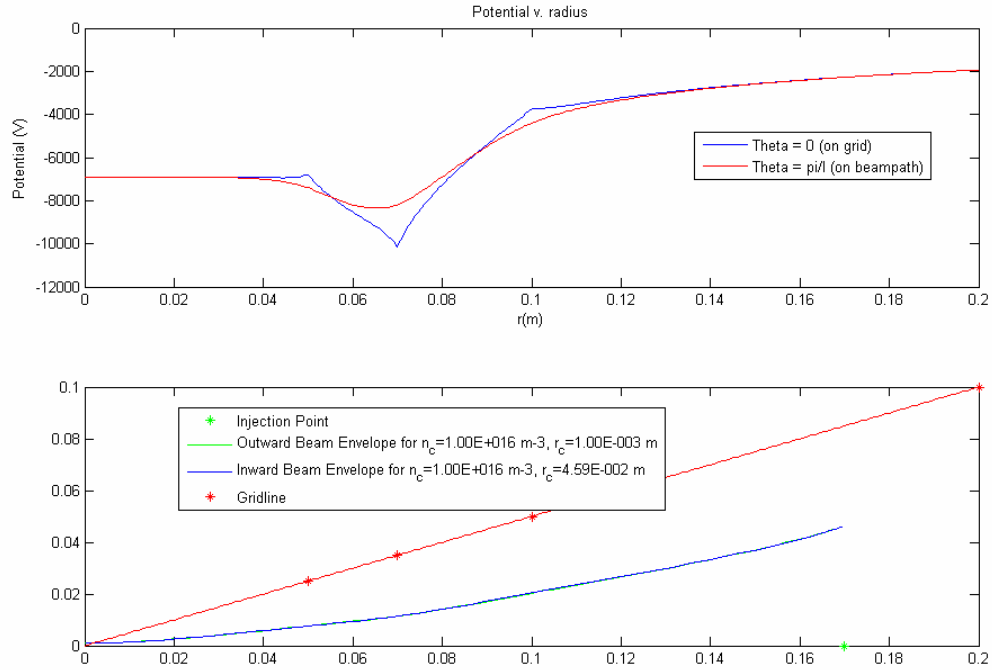
Figure 27: Potential map (top) and beam envelope (bottom) versus beam-line position for very small core focus and high core ion density (not reproducible in OOPIC)

Given the assumptions implicit in this method, it was expected to yield results only

accurate to within an order of magnitude of the actual space charge limit, and when

exceedingly small core radii were assumed, the maximum predicted density differed from

the PIC model by more than an order of magnitude. When the assumed core radius was a

significant percentage of the innermost grid radius, comparison to OOPIC modeling

revealed agreement to within a factor of 2. Figures 28 and 29 show the similarities in

the predicted beam envelopes from the modeling described above and the OOPIC

simulation. It is worth noting that OOPIC has only a 2-dimensional model of the

potential, so minor deviations between the two codes should be expected.
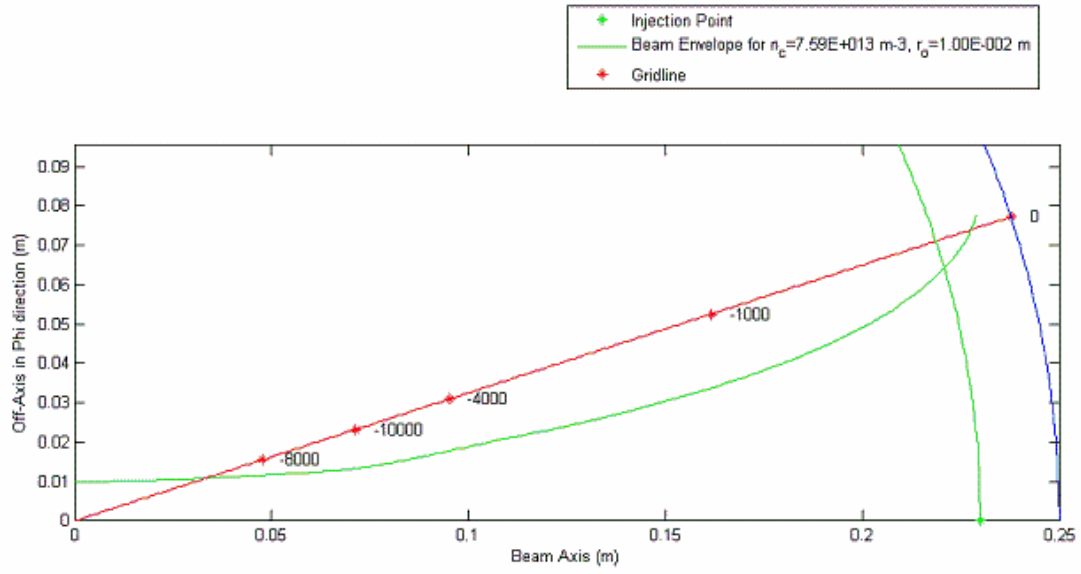
Figure 28: Model with large assumed core size that matches OOPIC results to within a factor of 2
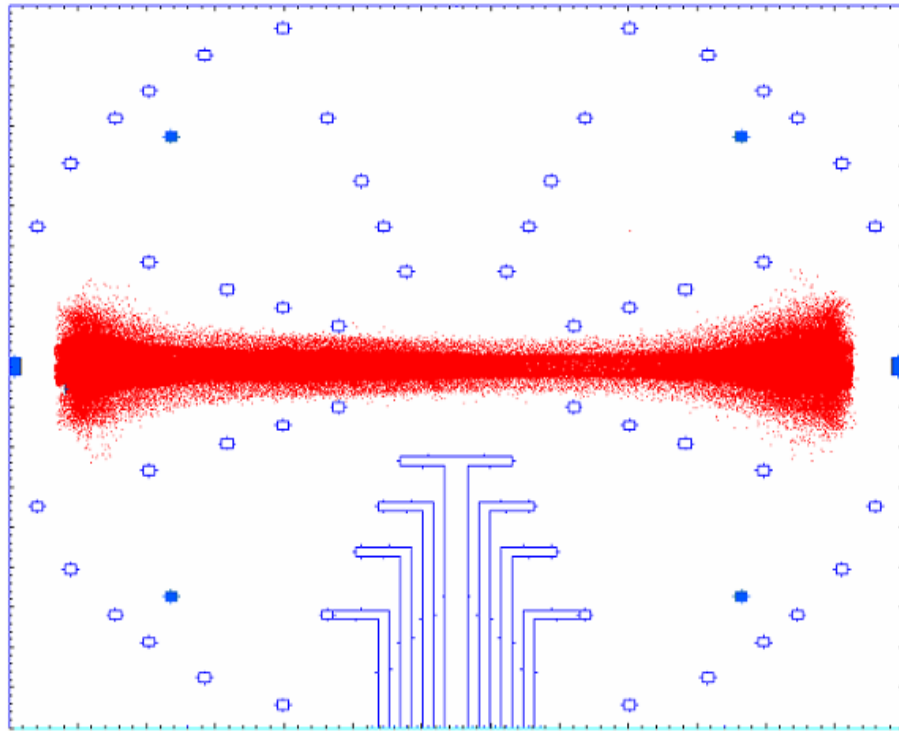
Figure 29: OOPIC model showing similar beam envelope for similar grid voltages and ion mass

3.3. Simulated Annealing IEC Design

Due to the large number of independent variables involved in the design of a multi-grid IEC experiment, a code was developed based upon the beam modeling in the prior section to help find an optimal or near optimal design for a multi-grid IEC reactor given the limited resources of our group. Simulated Annealing (SA) is a design methodology for complex systems which depend on multiple independent design variables. SA is an active area of research in complex systems, and it has been shown to be an effective optimization tool for the design of complicated systems.   Because of the large number of independent design variables (grid positions and potentials) in a multi-grid IEC, simulated annealing design was explored.

The premise of simulated annealing design is that while there can be a very large number of independent design variables, the quality of any design can be quantified by a singular metric known as an energy function. The lower the energy function, the better the design. Because the overall design space can be very complex, there can be many local minima which could fool a gradient-search based design code. An SA approach initially resembles a Monte-Carlo method in that design variables are changed at random and even if a given change results in a higher value of the energy function, at the beginning that change is kept and another change to the design is made. The best design found is always kept in memory. As the code progresses, the bounds of whether a new design change is kept are gradually reduced until the code simulates a traditional gradient search method. This approach which gradually transforms itself from a Monte-Carlo design tool to a gradient search method has been shown to be quite good at finding designs at or near the global minimum energy function. The gradual decrease in the accepted bounds of

energy resembles the physical process of cooling (hence "simulated annealing") – if it is
done sufficiently slowly, the global minimum energy (single crystal) state will emerge.

3.3.1. Energy Function

For the multi-grid IEC design problem, an energy function was desired which would give
a design with the maximum fusion energy output given the constraints on the design
variables. The energy function was therefore set as proportional to the inverse of the
estimated fusion power output from the device.

$$EnergyFunction = \frac{1}{n_{core}^2 \left(\Phi_{inj} - \Phi_{core} \right)^2 R_{core}^3}$$

Equation 3.19

The fusion reaction rate is proportional to the square of the ion density in the core and the
cube of the core size. The key implicit assumption here is that the fusion cross section is
proportional to the square of the core ion energy, this assumption is only valid up to a
certain fraction of the energy of the maximum fusion cross section for a given reaction
(~50keV for deuterium). Since the grids in our experiment are limited to -10kV
potentials by the power supplies available, this assumption should be good for the current
application. If future experiments are to use the same code, an energy function which
incorporates the actual variation of the fusion cross-section for the desired fuel would be
better.

3.3.2. Design Variables and Limitations

The radius and potential of each grid are all independent design variables. In addition,
the radial location of the injector could be moved. The anode radius and the number of
latitude and longitude wires were fixed, and the core radius was assumed to be a constant

fraction of the innermost grid radius. The innermost grid radius was limited to 10 cm

maximum, and the grids were not allowed to be positioned within 2 cm radially of one

another. These constraints were imposed for ease of fabrication, diagnostic access, and

assembly.

3.3.3. Summary of SA Results

The simulated annealing design code converged on an optimal solution after 1600

independent and random design perturbations.
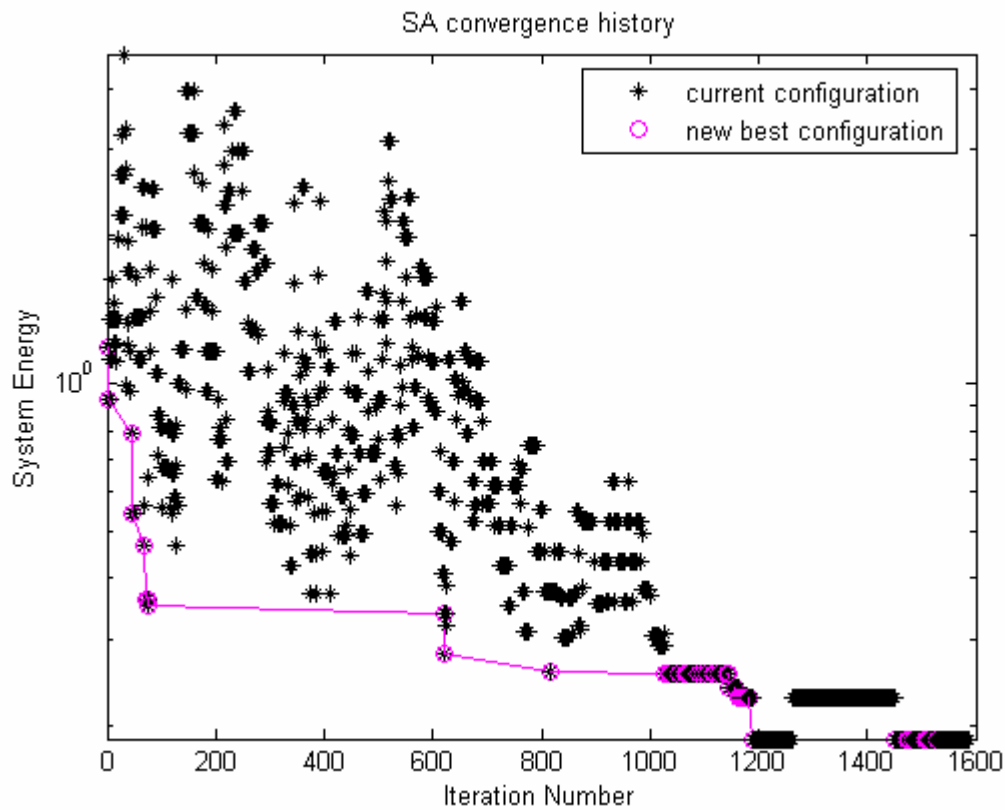
Figure 30: Final Convergence History for Simulated Annealing Design

The initial design guess had an energy function that was nearly an order of magnitude

higher than the final solution. Figure 30 shows the progression of the design with each

successive iterative perturbation. The code successfully resulted in a grid design and a

recommended potential structure that would result in a significantly higher fusion power

output than the initial guess.
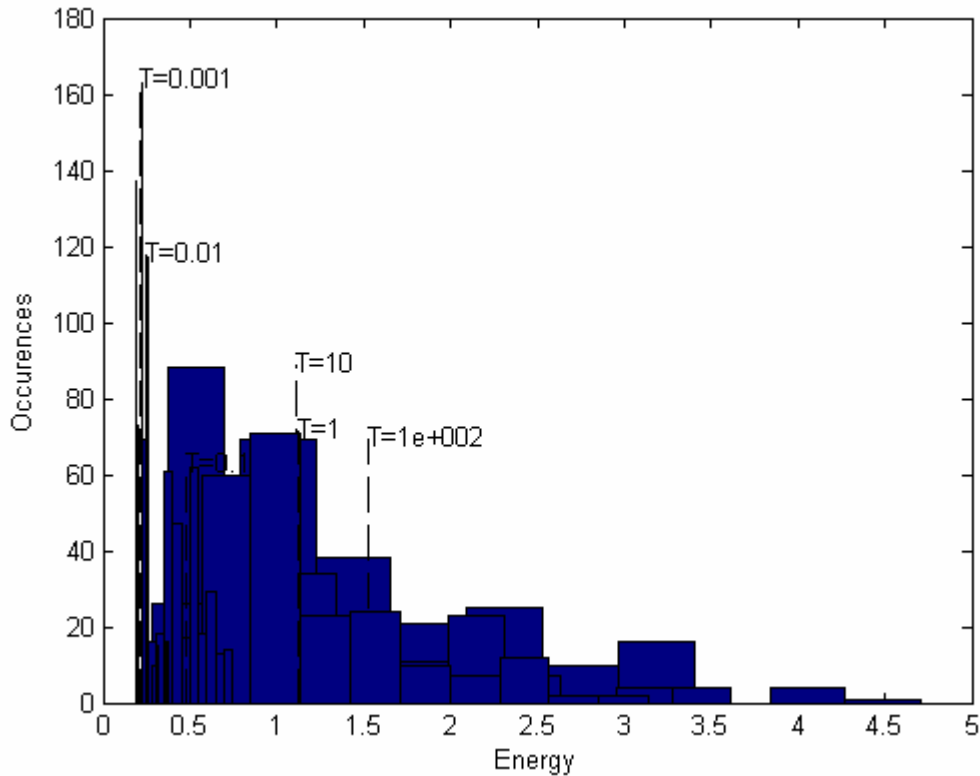
Figure 31: Number of occurrences v. energy in final SA run

The progression of the "cooling" of the design can be viewed either by plotting the

energy v. the iteration number, or by looking at the number of occurrences at different

energy levels and the average energy level for all iterations at a particular pseudo-

temperature as shown in figure 31.

The "freezing" of the design can be seen by the drop in the "entropy" and the rapid rise in

the "specific heat" of the design as illustrated in figure 32.
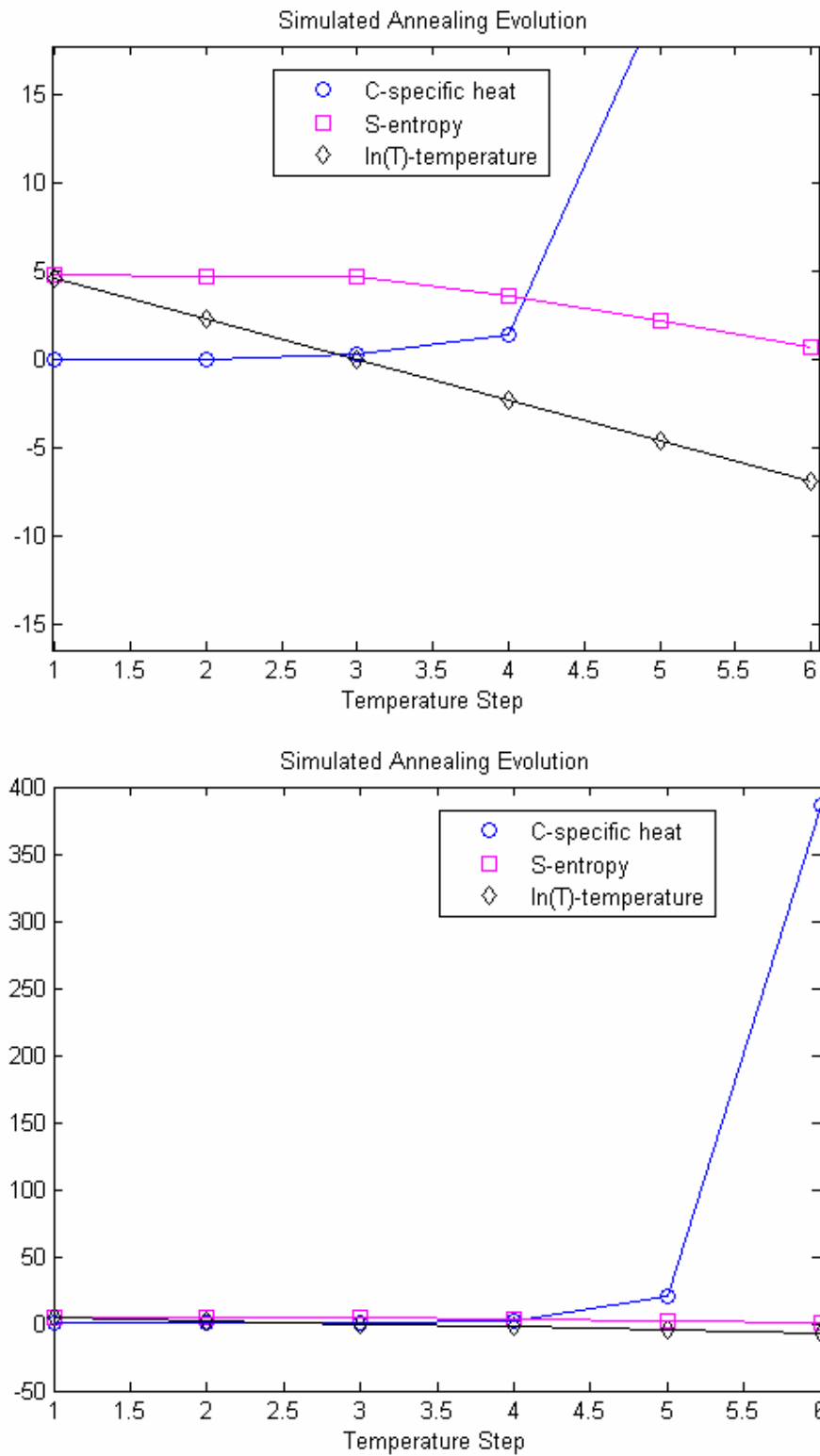
Figure 32: Evolution of the SA design showing the freezing of the configuration

71

The final output of the SA code gave the potential structure and beam envelope shown in figure 33.
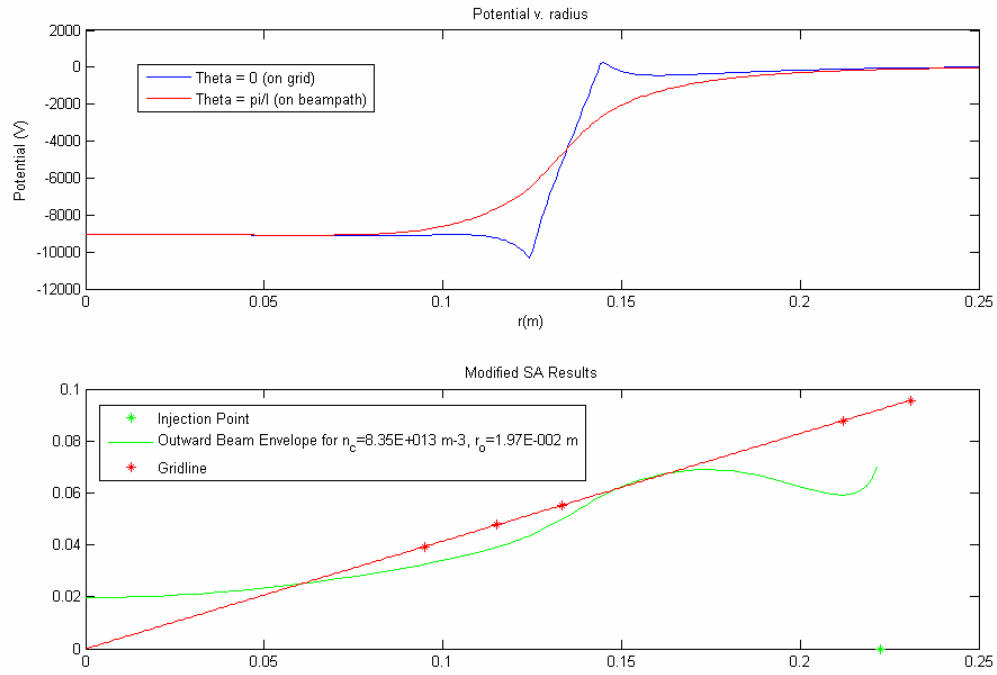
Figure 33: Final Output of SA design showing largest allowed inner grid and bunching of accelerating grids at coded limit of 2 cm.

As can be seen in figure 33 above, the SA design code pushed the inner-most grid out to the coded limit of 10 cm. It also bunched the inner grid and the two accelerating grids to the minimum coded spacing limit of 2 cm. These can be explained by simply maximizing the size of the fusing volume and minimizing the spacing between the accelerating grids to reduce the space charge effects by maximizing the local field curvature near the accelerating grids. The injector potential is very close to ground, and the core potential is very close to the minimum of -10kV. In fact the second and third grids out from the center are at -10kV and 0V respectively – the maximum possible potential difference and the minimum spacing. It is interesting to note that neither the

72

first grid nor the fourth grid have any significant role to play in shaping the potential structure. This suggests that the optimum number of grids may be 3 (not 5). It is interesting to note that the while the energy function did change substantially, little of that change was due to a difference in density. In fact, the energy function showed the most sensitivity to the size of the innermost grid (and hence the assumed core size) and the difference between the core potential and the injection potential. The maximum density for Argon ions in the system was always seen to be around $8e13$ m^{-3}.

While this tool may be useful for future investigations of actual fusion reactors, it was less useful than anticipated for informing the design of the present experiment. This was partly due to relating the energy function to possible fusion output instead of relating it to a measurement of the confinement experiment. Because most of the signals in the experiment will be proportional to the number of trapped ions, and that number does not seem to vary substantially given the maximum potential difference and fixed dimensions desired for experimental access, the actual hardware design was based off of experimental convenience instead of the results of this analysis. The code is included in the appendix of this thesis for future reference.

3.4. *Modeling with commercial OOPIC Pro code*

Throughout these investigations, extensive use of the OOPIC Pro code was made in order to gain insight into the detailed physics of the multi-grid IEC device. OOPIC Pro is a 2D planar particle in cell model with Monte Carlo collisions [358]. This section details some

of the predictions that were made prior to experiment operation based upon this useful tool.

3.4.1. 2-Grid Modeling and Confinement Estimations

Initial computational investigations explored the conventional, 2-grid IEC configuration. As illustrated in the first chapter, at the pressures which yield the highest neutron rates in the literature (4.0 microns) [18], the mean free path of ions in the system is less than the typical device diameter. The majority of these reactions were shown to be beam-background reactions [357]. As the pressure is reduced, the reaction rate peaks at approximately 0.1 microns and then is also reduced, but the ion confinement time is increased. In the limit of a perfect vacuum, the only means of ion loss from the IEC system are:

1) Ion neutralization on a grid wire via unconfined/chaotic trajectory or ion-ion collisional scattering

2) Ion neutralization on the anode via ion-ion collisional energy spread

3) Fusion

Hirsch estimated the average number of passes through the center of a 2-grid device in this hard vacuum regime with a simple grid transparency argument [21].

$$\delta = \frac{v}{1-v^2}$$ **Equation 3.20**

In this simple model, v is the grid transparency (typically 0.9 to 0.98) and δ is the expected number of passes through the center of the device. The sole loss mechanism implicit in this model is number 1) in previous list, i.e. loss to the grid wires.

OOPIC was used to check the validity of this assumption. A simple 2-grid model was developed which did not contain any of the realistic field asymmetries which had already been shown to be capable of reducing the ion confinement time to 1-5 passes. Due to the finite grid size the grid wires are larger than they typically are experimentally which limits the modeled transparency. In this model the grid transparency is 88% which should yield 4 passes through the center on average according to the Hirsch model. The OOPIC model presented here assumes that the ions are Ar^{+1} and the cathode potential is -7500 V resulting in an ion bounce time of approximately 8 μs or a single pass time of 4 μs. The average confinement time is therefore expected to be 16 μs.
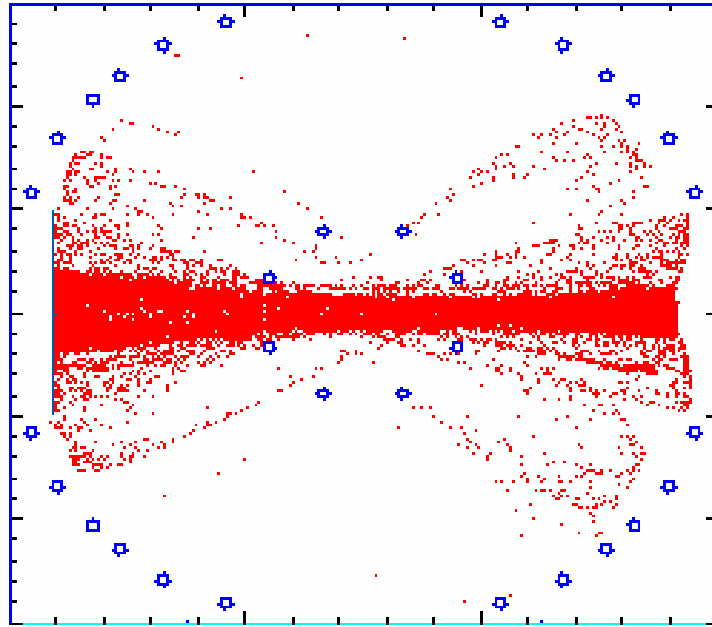
Figure 34: Low pressure, 2-grid OOPIC simulation, ion injector on

Figure 34 shows a 2-grid OOPIC model with no electric field asymmetries and no neutral background gas. When the simulated ion injector is turned off, the number of ions in the system will decrease as ions are lost. The 1/e time of the decay curve can be compared to the expected confinement time based on the Hirsch formula.
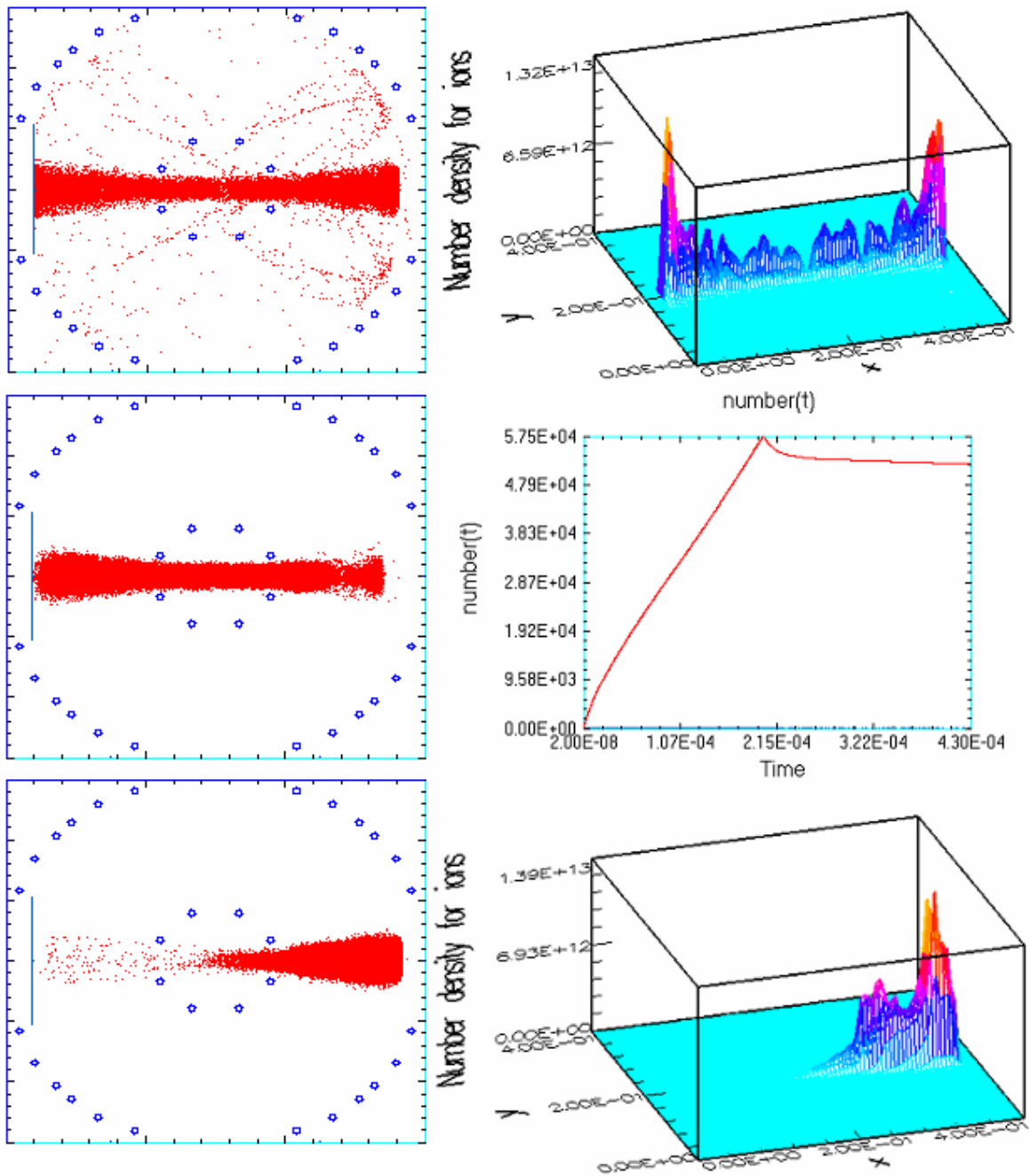
Figure 35: Time evolution of Argon +1 ions in the simplest 2-grid OOPIC model (no background gas)

Figure 35 shows the time evolution of ions in this model under these idealized conditions.

Not surprisingly, when injection is turned off at 200 μs (top two images is figure 35),

there is a rapid loss of ions on the order of the Hirsch confinement time. The top two

images in figure 35 show the spatial location of the ions on the left and the spatial density of the ions on the right.   The rapid loss of ions appears to be localized in space – it is only the ions outside of what may be considered a "grid acceptance window" which are lost on this rapid 16 μs timescale.

The middle two images in figure 35 show the ions in the system 230 μs after termination of injection. The image on the right is the same spatial representation of the location of the ions, while the image on the left shows the time history of the total number of ions in the system. It is clear that the rate of decay of ions in the trap has changed in such a way that it is no longer proportional to the number of ions in the trap as would be expected if confinement were either limited by statistical grid wire interception or collisions with background gas.   In fact, the 1/e decay time of those ions inside the grid acceptance window is approximately 40ms -- orders of magnitude longer than the 16 μs predicted from the transparency model.   Even though the local field around the cathode is nominally defocusing, the overall ion confinement is good enough in this idealized simulation that the two-stream instability has time to develop and bunch the ions as seen in the bottom two images of the figure 35 at a time of approximately 1ms after termination of injection.   This bunching was first identified by McGuire [357] in computational modeling of IEC devices and is a saturated mode of the well-known streaming instability in this type of device.

When asymmetries in the field structure are modeled by introducing the realistic effects of a stalk or feed-through, however, the Hirsch model does much better at predicting ion confinement in a 2-grid IEC device.
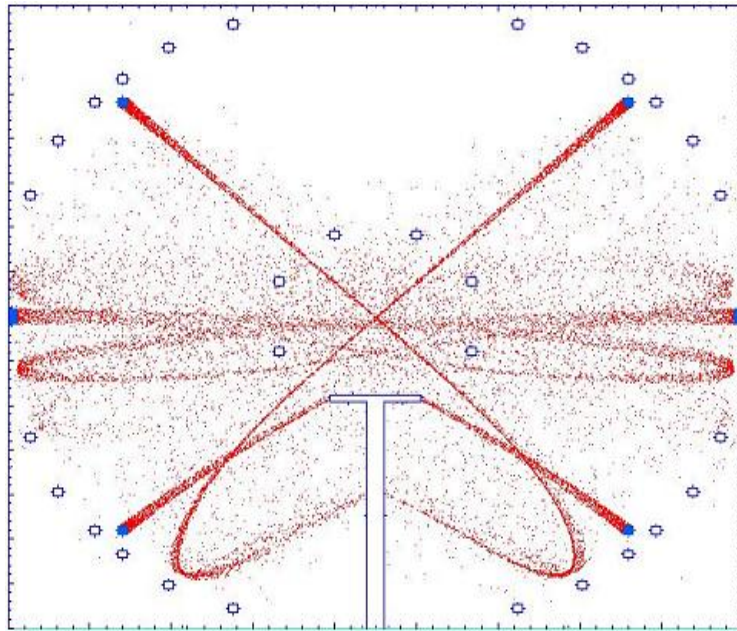
Figure 36: 2-Grid OOPIC model showing ions impacting cathode after 1/2 to 5 passes

Figure 36 shows how the field asymmetries caused by the cathode feed stalk result in

very short ion lifetimes of 1-5 passes through the inner cathode grid -- dependent upon

the location of the ion injector(s).

These simple simulations suggest that the "transparency" model developed by Hirsch

may not be a good means of estimating the confinement time in a 2-grid IEC device if the

device is carefully constructed to minimize the effects of asymmetric background fields,

but it should be reasonable for most 2-grid devices with realistic field asymmetries due to

feed through stalks.

3.4.2.   Multi-Grid Modeling and Confinement Estimations

One very effective way of shielding the effects of feed-through asymmetry and

improving ion confinement is by carefully tailoring the field structure with multiple

independently biased grids.   The efficacy of this approach was clearly illustrated using

OOPIC in chapter 1 figures 3 and 4. McGuire has conducted extensive investigations into this technique using OOPIC [357]. His original code was used as the basis for all OOPIC modeling of multi-grid IEC devices contained in this thesis.

If we assume that the multiple grid configurations are capable achieving the highly confined ion trajectories observed in the simulations, the primary limiter on ion confinement is scattering due to collisions. Scattering with background gas and other ions and thermalization become the primary loss mechanisms. Therefore it should become possible in UHV conditions to push the theoretical limits proposed by Rider [175].

In order to achieve these theoretical improvements, an experiment was designed with the goal of demonstrating the potential to significantly improve confinement time using multiple grids. This experiment is operated under high vacuum conditions; lower than the pressures at which most IEC experiments are run, but above the UHV pressures that would be required to push the limits of thermalization. At these pressures, collisions with the background gas are the biggest limiter to confinement. OOPIC was used to estimate the effects of background gas on ion confinement times in the multi-grid experiments. Figure 37 shows a typical, multi-grid simulation geometry in OOPIC.
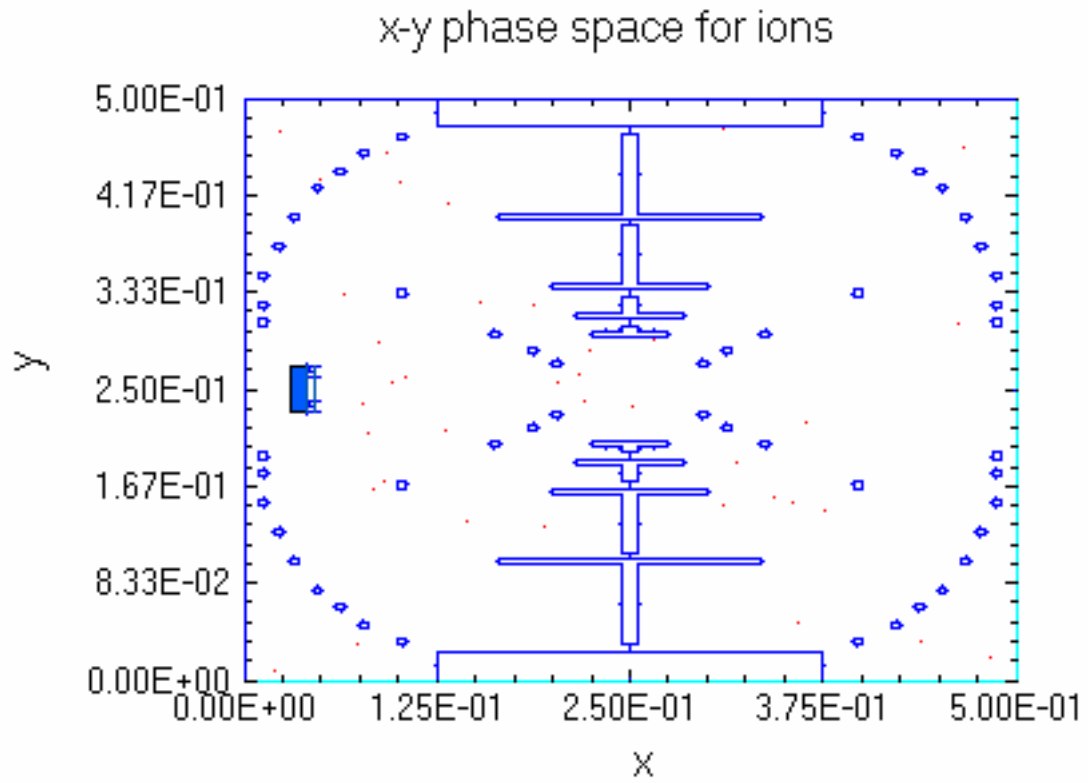
Figure 37: Typical simulated multi-grid geometry, x and y dimensions are meters, grid locations and ion injector geometry are based upon the physical experiment

In order to facilitate evaluation of the 1/e time, the ion signal is normalized to the level at the time when the injection is turned off. This practice will be used throughout the thesis. The complete, un-normalized curves typically resemble the curve shown in figure 38:
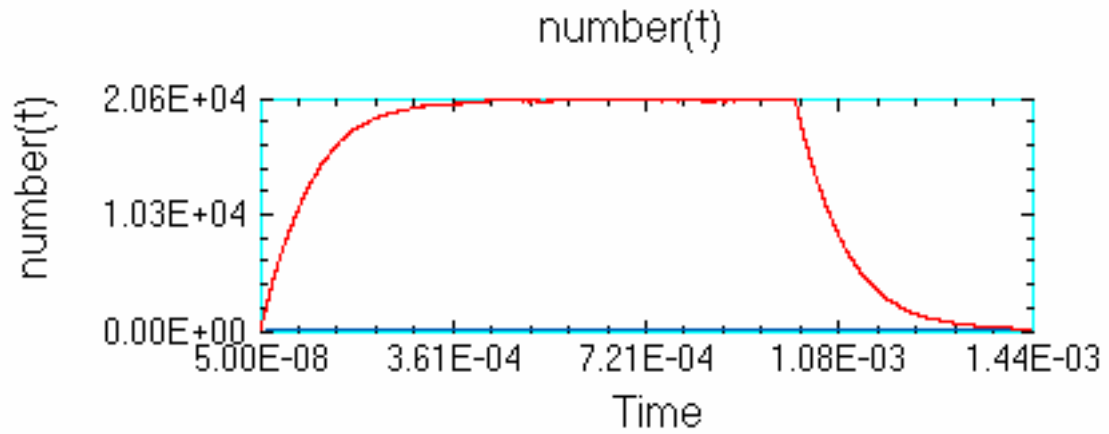
Figure 38: Typical plot of number of macroparticles in an OOPIC simulation

80

The standard practice that was adopted for both computational experiment and physical experiment was to inject ions for 1ms then turn off the injector and observe only the decay portion of the curve. While the maximum number of ions in the system (and hence the signal strength) can vary with the strength of the source, the decay curve will only be a function of the sink. Comparing the 1/e times of the normalized decay curves will therefore give the best indication of actual confinement time of ions in the device. Figure 39 shows a map of the potential structure in a typical multi-grid OOPIC simulation which illustrates the ability of the multiple grids to "shield out" the effects of the feed-through stalks.
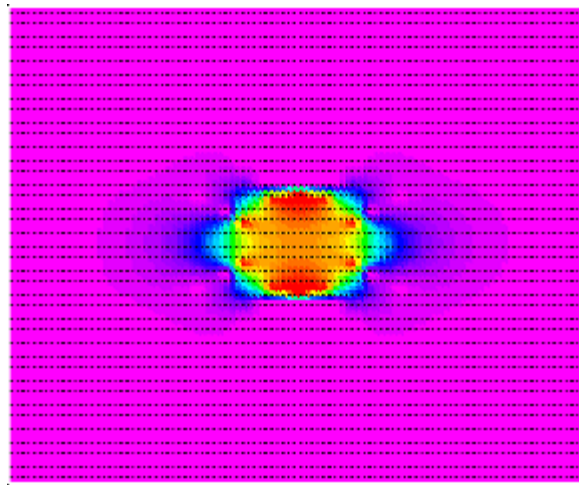
Figure 39: OOPIC multi-grid potential model for a scenario with good ion confinement

Not all multi-grid scenarios showed improved confinement. In fact the ion confinement was expected to be quite sensitive to the particular grid potentials based upon OOPIC modeling.
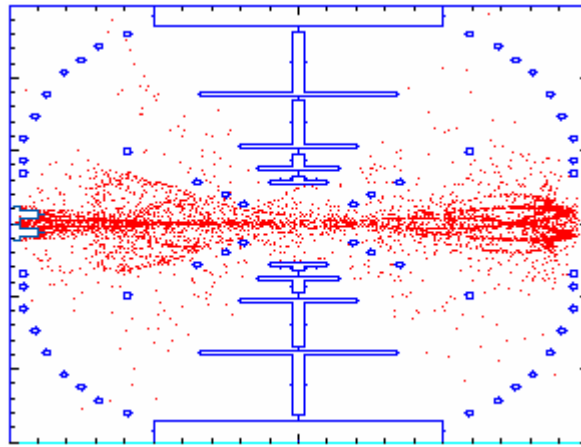
Figure 40: Symmetric multi-grid field with poorly confined ions

In the figure 40 above, the field structure is symmetrical, but the ions are not well confined due to a field structure that prematurely focuses the ion beam. The beam then freely expands in the core region where there is little confining field curvature. On the opposite side of the device, the over-focused field again skews the trajectory of the beam which results in a wider beam envelope. Ions are quickly lost to the grid wires, and the overall confinement is very poor. It is clear from this one example that the specific potential structure imposed by the grids can be quite important in determining the ion confinement time even in the absence of field asymmetries.

When a small asymmetry in one of the grid wires is introduced (a one grid space perturbation which corresponds to a 2.5% change in position of one grid wire), the poor confinement is even more pronounced. Figure 41 shows the effect of an unperturbed (left) and perturbed (right) wire in the multi-grid simulation. The perturbation introduces field asymmetries which tend to skew the ion beam
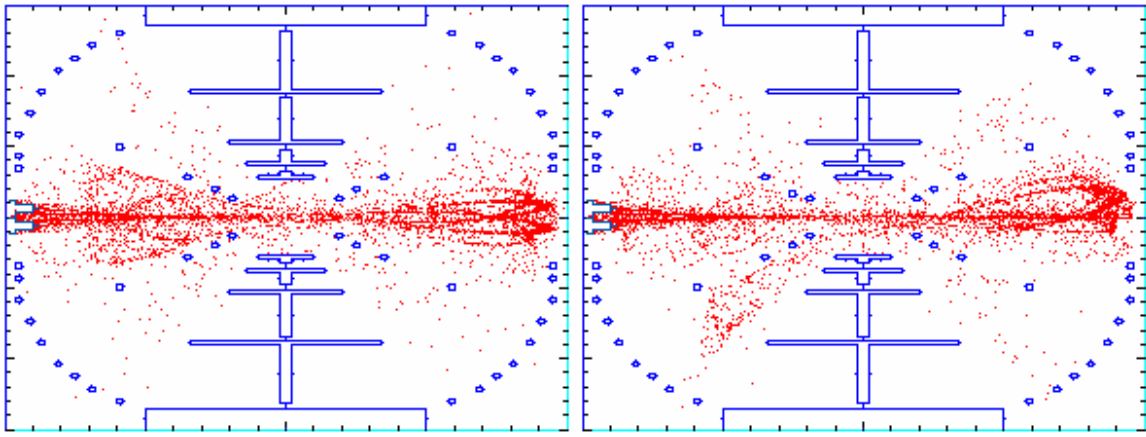
Figure 41: Comparison of perfectly symmetric field (left) with a 2.5% location perturbation on one wire (right). The perturbed wire is the second grid from the center in the upper left hand quandrant.

If the imposed potential structure results in a well confined ion beam (figure 42), however, there is much less sensitivity in the overall shape of the beam envelope to geometric perturbation in either the grid wires or the ion source.
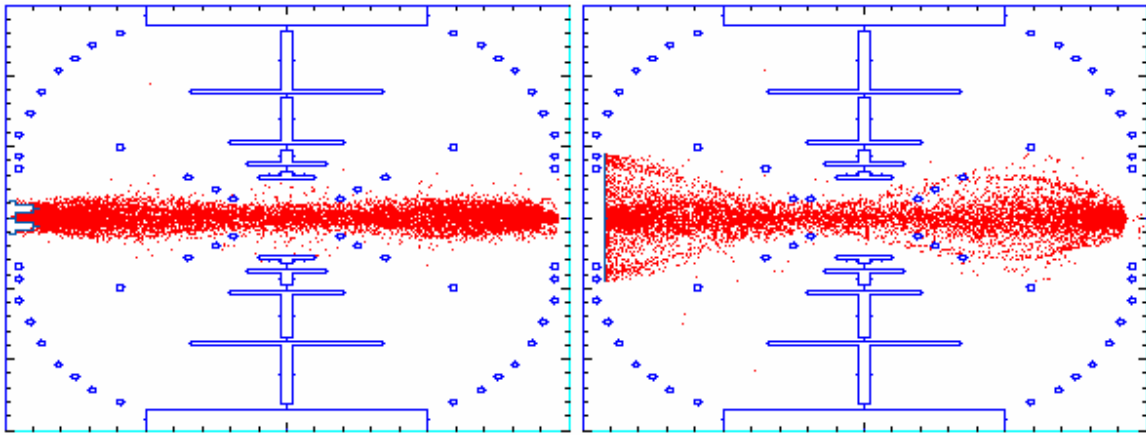
Figure 42: Good multi-grid confinement with unperturbed grids and concentrated ion source (left), and highly perturbed grids (5% on 2nd grid and 2.5% on 3rd grid) with diffuse ion source (right), same grid potentials

The geometry on the right hand side of figure 42 above is representative of the worst case scenario for the experiment as designed at an achievable pressure of 8e-5 torr. For this model with Helium gas, He^{+1} ions and a cathode potential of -5000 V, the predicted 1/e confinement time is 8 µs or approximately 2 passes as shown in figure 43.
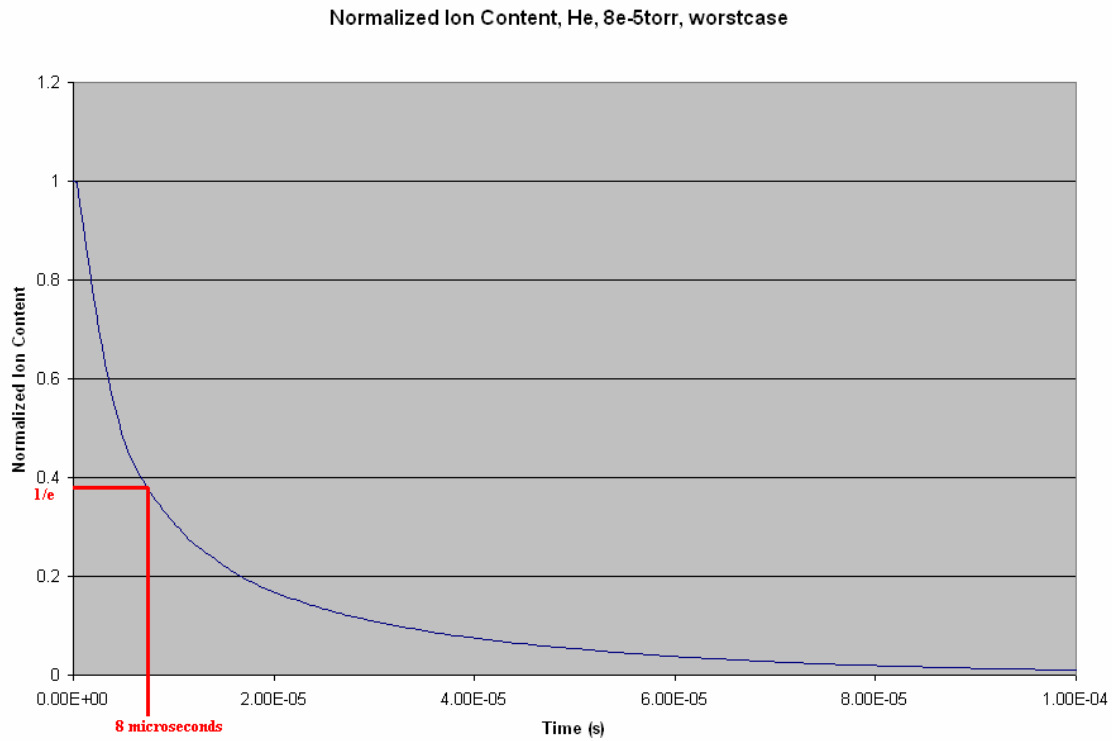
Figure 43: Normalized plot of the decay of the number of ions in the "worst case" OOPIC simulation for 8e-5 mbar He.

Once the experiment was completed and data with various diagnostics was taken, it became clear that for Helium, the pressure range with the highest S/N was 1e-4 mbar or 8e-5 torr. A comparison of best expected confinement time at this pressure was then conducted to evaluate how close to the best simulated confinement we had achieved in the actual experiment.   The worst case scenario is presented in figure 43 above. Although the worst case 1/e confinement time of 8μs is quite bad, it is still better than the perfect vacuum 2-grid simulation (5.4 μs) with the stalk assymmetry.

The decay for the best case scenario (left side of figure 42) is shown in figure 44 below. The grid potentials from anode to cathode for both of these runs are [0, 0, -1000, -1500, -5000]. It is worth noting that the geometry of the ion source combined with large

84

(though not unreasonable) asymmetries in the grid wires have the potential to alter the 1/e confinement time of the system by a factor of 5. This change is purely geometrical as a result of the induced field asymmetries, i.e. the pressure, the gas, and the grid potentials are all the same in these two scenarios.
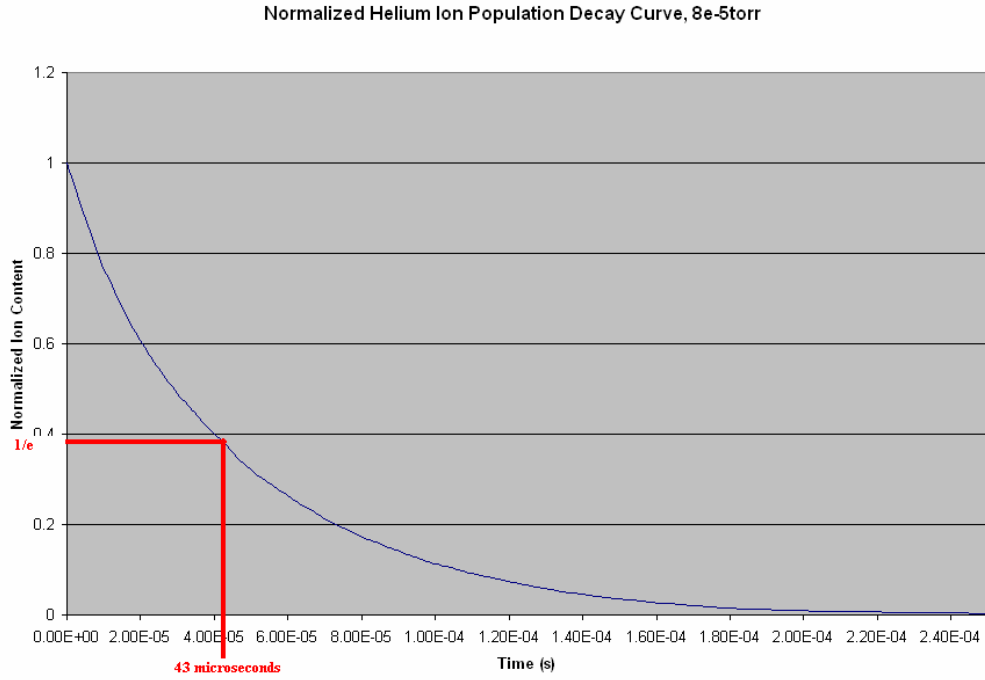
Figure 44: Normalized decay curve of best case, Helium at 8e-5 torr

These results can also be compared with estimations of the mean free path for collision and charge exchange at this mean ion energy and device pressure.

$$\lambda_{mfp} = \frac{1}{n\sigma} = \frac{kT}{P\sigma}$$ **Equation 3.21**

Assuming a room temperature background gas at 1e-4 mbar, the mean free path for charge exchange at this pressure and average energy is only 4.1 m corresponding to 8 passes or 32 μs based on the charge exchange cross-sections given by Hegerberg [352].

The OOPIC simulation in conjunction with these simple calculations suggests that the dominant loss of ions at this pressure is due to charge exchange collisions with the background gas. While all charge exchange reactions will result in some loss of energy (via the fast neutral), not all charge exchange reactions result in direct loss of an ion from the system (especially those ions that undergo charge exchange near the edge of the potential well), it is therefore possible that confinement times longer than the mean time until charge exchange could be expected.

The effects of changing the background gas pressure were simulated. For all of these multi-grid runs, the same confining potentials were applied to the grids [0, 0, -1000, -1500, -5000] volts, and the corresponding grid radii are [.25, .17, .10, .075, .05] meters. As expected, the 1/e confinement time is proportional to 1/p for multi-grid experiments. 1/e confinement time for 2-grid experiments shows a general insensitivity to pressure in the regimes explored. Figure 45 clearly shows the expected difference between 2-grid and multi-grid confinement times based on OOPIC modeling.

1/e Confinement Time v. 1/Pressure

$y = 0.0042x + 1.759$
$R^2 = 0.9957$

$y = 3E-05x + 4.4544$
$R^2 = 0.3654$
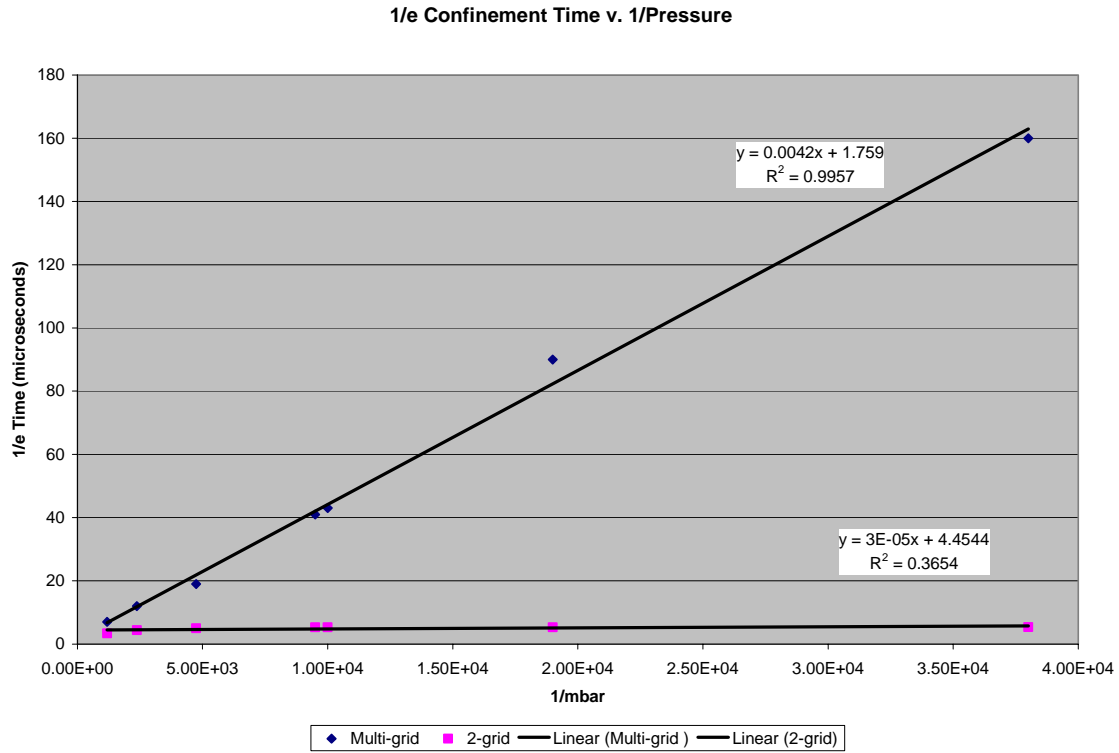
Figure 45: OOPIC simulated effect of pressure on 1/e confinement time for 2-grid and multi-grid IEC systems

It is worth noting that the simulated 2-grid confinement times are implicitly worst case scenarios. The 2-dimensional simulation results in a loss of all particles that pass by the stalk. In the real system, not all ions with "low" trajectories will impact the stalk on their first pass. Unfortunately full 3D PIC modeling of this system was not available for these investigations.

Figure 46 clearly shows the expected difference in the ion trajectories in the multi-grid (left) and 2-grid (right) geometries.
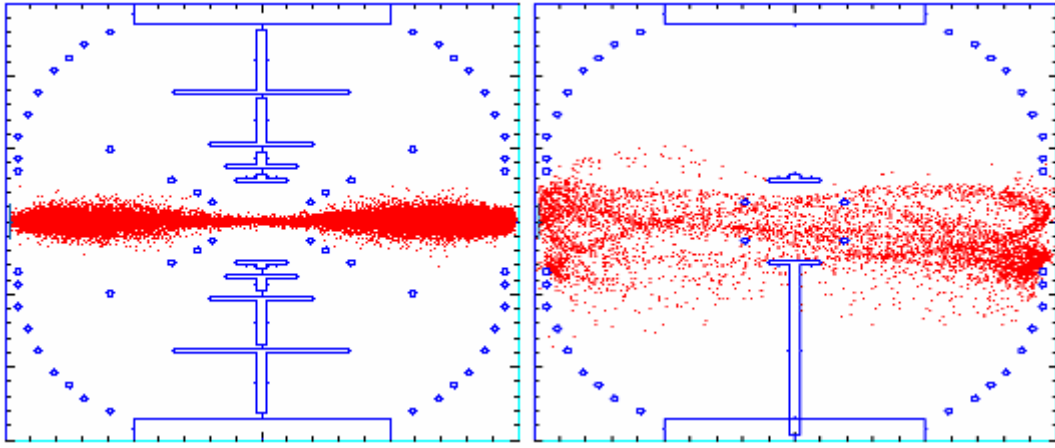
Figure 46: Multi-grid (left) and 2-grid (right) OOPIC simulations

Simulated runs at zero background pressure were also conducted for the multi-grid and 2-grid scenarios above. At zero pressure, the 2-grid 1/e confinement time was 5.4 µs (still limited to ~1pass), and the multi-grid 1/e confinement time was 2640 µs (2.6 ms). In the zero pressure limit, the loss rate of ions from the multi-grid system should go as n^2 not simply n, so it may be desirable to characterize confinement times with a different metric than the 1/e time used in this work. This is due to ion-ion collisional effects as opposed to ion-background collisions which dominate in the current experiment. A difference in the shape of the decay curve was noted in the simulation (figure 47), which would suggest this relationship. Due to the very long confinement times and hence the very long simulation run times, this relationship was not thoroughly explored.
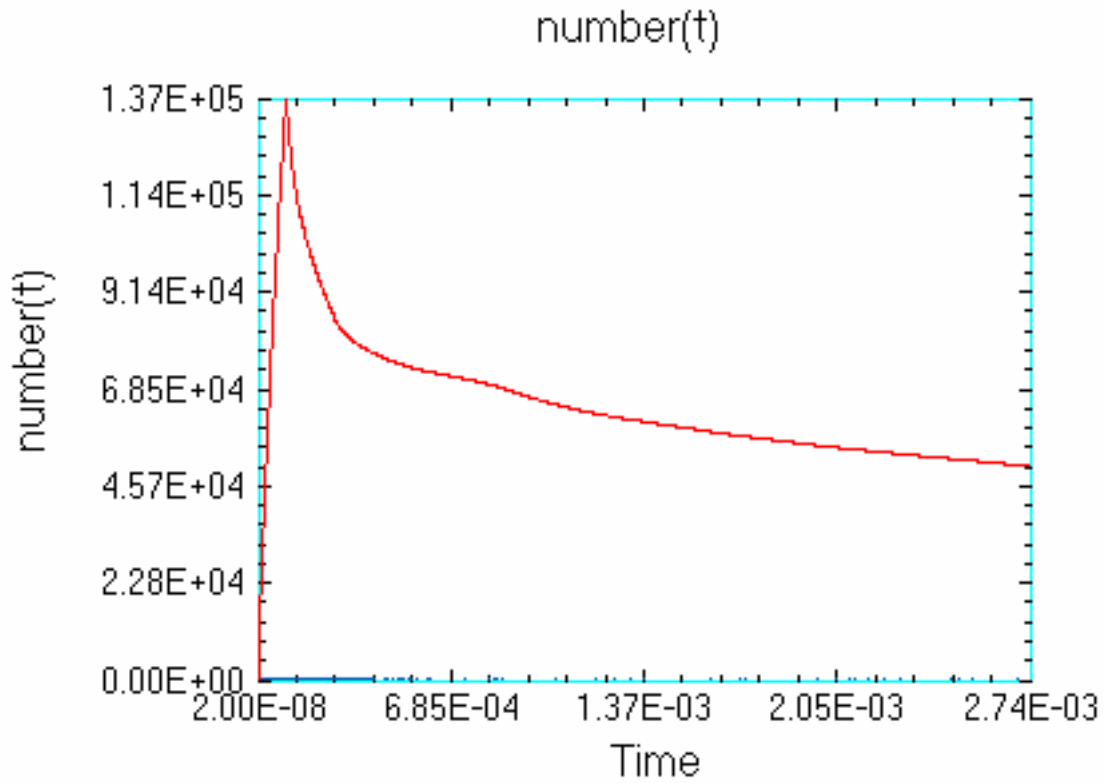
Figure 47: Non-exponential decay shape of multi-grid in perfect vacuum

In order to achieve this different confinement regime in an experiment of this size where the density of ions is greater than or on par with the background gas density assuming a comparable strength ion source, base pressures on the order of 10^{-11}mbar would need to be achieved. This n^2 confinement relationship cannot be explored in experiments at this time due to the limitations of the existing vacuum equipment and ion sources. The multi-grid UHV regime exploration is left to future students.

In addition to the pressure sweeps shown in figure 45, a simulated voltage sweep of the 3rd grid was also conducted in order to evaluate the sensitivity of the 1/e confinement time to the potential structure. The potential on the third grid was varied from 0 (the potential of the 4th grid) to -1500 V (the potential of the second grid).
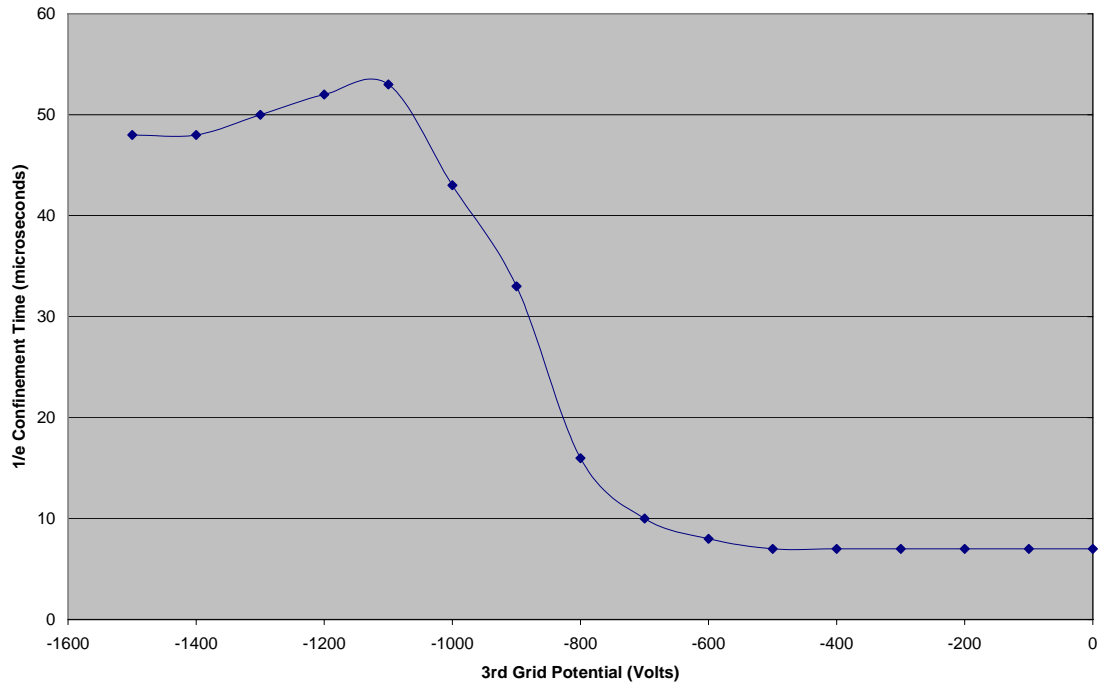
Figure 48: Predicted sensitivity of 1/e confinement time to 3rd grid potential (1e-4 mbar)

It can be seen in figure 48 that the particular grid potential can have a significant impact

on the confinement time of ions in the system. The purpose of this sweep is to compare

the OOPIC modeling to the experiment so the effectiveness of the 2-D PIC model can be

determined for predicting confinement behavior. Experimental results will be presented

in the next chapter.

3.4.3.   Summary of Expectations Based on Modeling

Due to the presence of field asymmetries, all 2-grid experiments are expected to have ion

confinement times roughly predictable by the Hirsh transparency model. The accuracy of

that model is questionable, but in general, 2-grid experiments are not expected to show a

significant dependence of confinement time on pressure because confinement will be

limited by skewed trajectories resulting from asymmetric potential fields. At a -5000 V

cathode potential with Helium ions, the expected 1/e confinement time is 28 μs (7 passes) while Argon ions should be confined for approximately 84 μs.

Multi-grid experiments with proper tuning of the grid potentials, however, are expected to show a pressure dependant confinement time because of their ability to shield out field asymmetries. It is expected that the multi-grid design will result in a significant improvement in 1/e confinement time over the conventional 2-grid IEC configuration. OOPIC modeling has suggested that at a pressure of 8e-5 torr (He), with a -5000V cathode, the 1/e time of ions in the system could be 43 μs – significantly better than the best 2-grid estimate at these potentials.

If improved confinement is achieved, there may be signs of the saturated two-stream instability as has been seen in the idealized OOPIC simulations.

4. Experimental Results and Discussion

This section gives an overview of the data collected on the MIT SSL IEC experiment. Initial testing was done with only the 10 cm diameter cathode grid and the 50 cm diameter anode grid. The three intermediate grids (15, 20, and 35 cm diameters) were then added for multi-grid testing. Due to changes in the ion source and confinement diagnostic during the multi-grid testing, a final round of 2-grid testing was done to have a more direct comparison.

For both configurations, testing was conducted under low and high vacuum conditions. The low vacuum testing (higher pressure) was conducted in air while the high vacuum data used a backfill of Helium or Argon gas depending upon the type of ion desired. All low vacuum data acquisition was done with a 6 megapixel digital camera. High vacuum data acquisition was done with a 2 GHz Tektronix TDS 2014 Oscilloscope.

4.1. The 2-Grid Configuration

Data was first collected in a traditional 2-grid device. The simple anode-cathode structure (as shown in figure 1) is the most abundant IEC Fusion reactor design and has been extensively studied by Farnsworth, Hirsch, Miley and many others. The data taken in this configuration would serve as a baseline for purposes of comparison. Figure 49 shows a picture of the 2-grid device in the vacuum chamber. (Note: the cylindrical structure in the port on the left of the image is an old ion source that was not used).
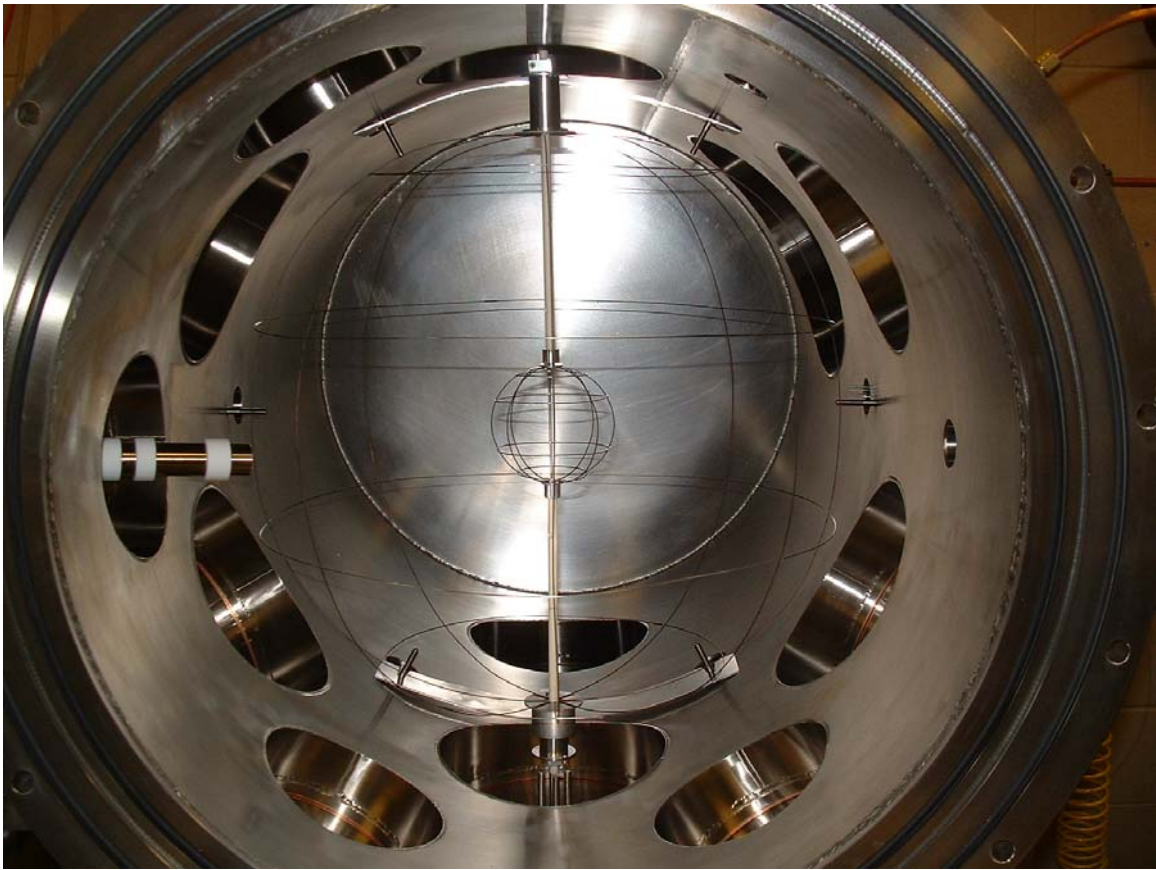
Figure 49: 2-Grid assembly in the vacuum chamber

4.1.1.　Low Vacuum Operation

Early experiments were done in the low vacuum regime in order to satisfy our curiosity about the optical discharge that would appear.

The background pressures during these discharges are sufficiently high that ion-electron cascading results in a rapid change in discharge impedance. As more ions are generated, the impedance decreases and the current rapidly begins to grow as secondary electrons liberated from the grid wires by ion impact cause more ionization of the background gas. The power and current limits of the high-voltage power supplies connected to the grid

93

imposed by the built-in protection circuitry result in a highly irregular pulsing of the voltage and current on a time scale of a few milliseconds. Because these voltage and current fluctuations are driven by the power supply protection circuitry instead of the actual physics of the plasma discharge, the shape of the voltage and current pulses are not worthy of study. A consequence of this cascading phenomenon is that the most interesting "real" data are the measurements of the optical discharges in the various pressure regimes as captured by digital camera.

Figure 50: Jet-mode in 2-grid configuration

It was found that all of the reported modes of operation of high pressure IEC devices could be successfully recreated. Namely, there was evidence of both the jet-mode plasma

94

configuration as shown in figure 50, and the star-mode plasma as shown in figure 51. These modes have been previously reported by Miley et. al.[155].

Figure 51: Star mode (1.7e-3 mbar) in 2-grid configuration

4.1.2.   HV Operation

The low vacuum operations were interesting from an aesthetic point of view and to confirm results reported by others, but the primary interest was increasing the ion confinement time which could only be done in high vacuum. For most of these experiments, a base pressure of approximately 1e-6 mbar was reached, and the chamber was then back-filled with the gas of choice for ionization.

4.1.2.1. Measurements of current to the grid wires

Early experimentation was done in the two grid configuration at low voltage (-400V cathode) to evaluate the possibility of using the measurement of the currents to the grid wires as a measurement of ion confinement time. A simple voltage divider circuit was used to measure the small fluctuations in grid potential that indicate the ion flux to the grid wires. The detection limits of the circuit were tested by simulating a high impedance pure current source using a high voltage square wave signal generator in series with a 10MOhm resistor attached to the cathode grid. The RC decay of the detection circuit can be seen in figure 52 to be approximately 3 microseconds, much shorter than the shortest measurable confinement time in the system (Helium ions with an obstruction).

He Decay and Detection Limits
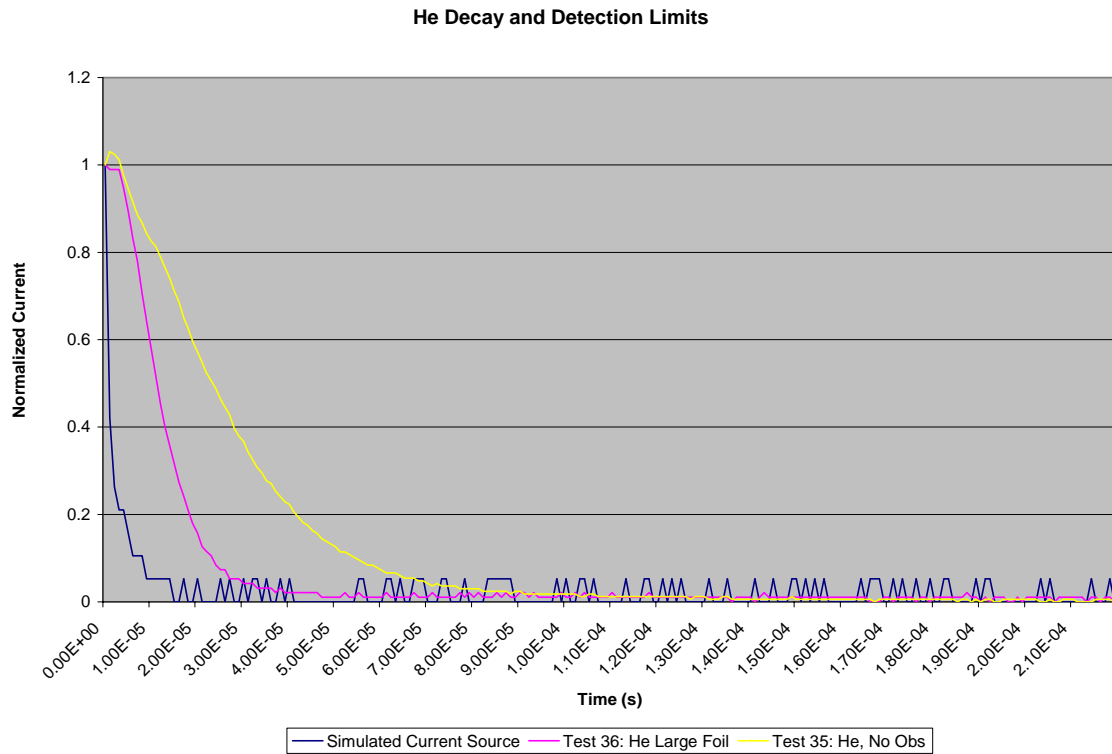
Figure 52: Detection limits of sensing circuit due to RC smoothing

Helium Decay Current, Varying Voltages
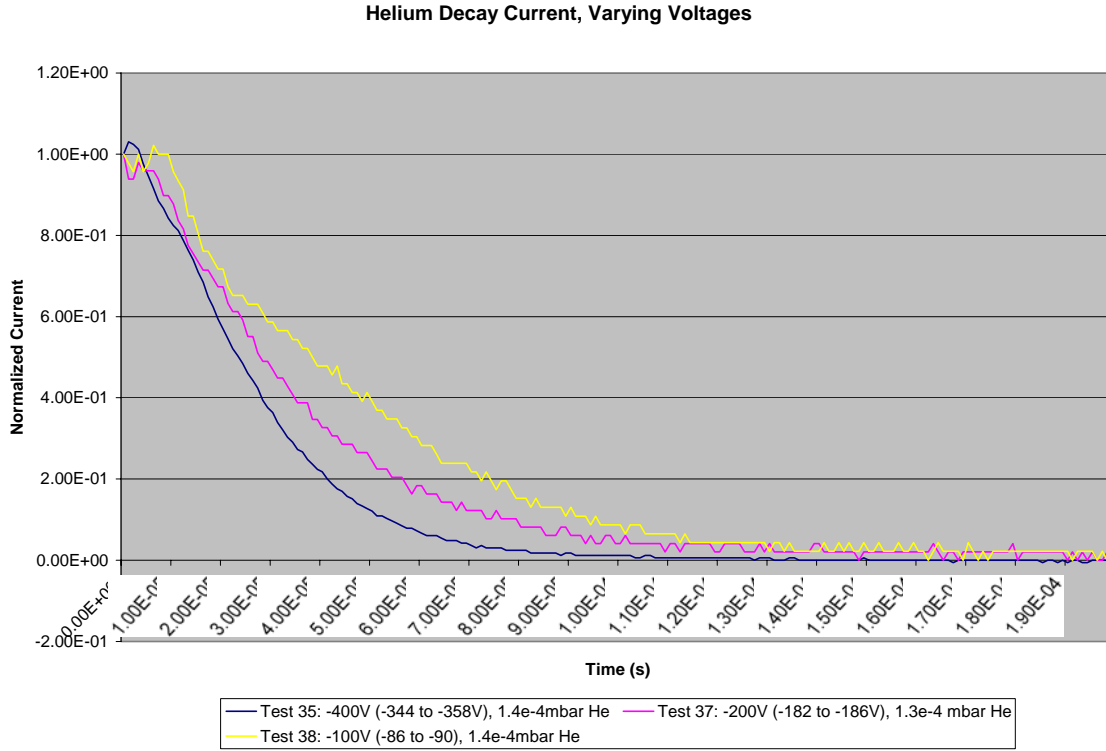
Figure 53: Effect of varying cathode voltages on Helium ion confinement time

Figure 53 shows that when the cathode potential was varied, there was an effect on the

confinement time. In fact these data confirmed that reducing the cathode potential has

the expected effect of reducing the 1/e confinement time varying roughly with the inverse

of the square root of the absolute magnitude of the cathode potential. This supported the

argument that the ion confinement was limited to a certain number of passes through the

system. Due to the experimental limitations on this detection technique discussed in

chapter 2, this technique will not be discussed further.

4.1.2.2.   Measurements with the capacitive probe

While measurements of current to the grid wires gave a good initial grounding to these

investigations, the capacitive probe allowed much lower cathode potentials to be

achieved. The advantages of this measurement technique were expounded upon in

chapter 2.   This section presents the data collected in the 2-grid configuration with the capacitive probe under a wide range of pressure conditions.

2-Grid, Helium, Pressure Effect

$y = 0.0019x + 32.651$
$R^2 = 0.8586$
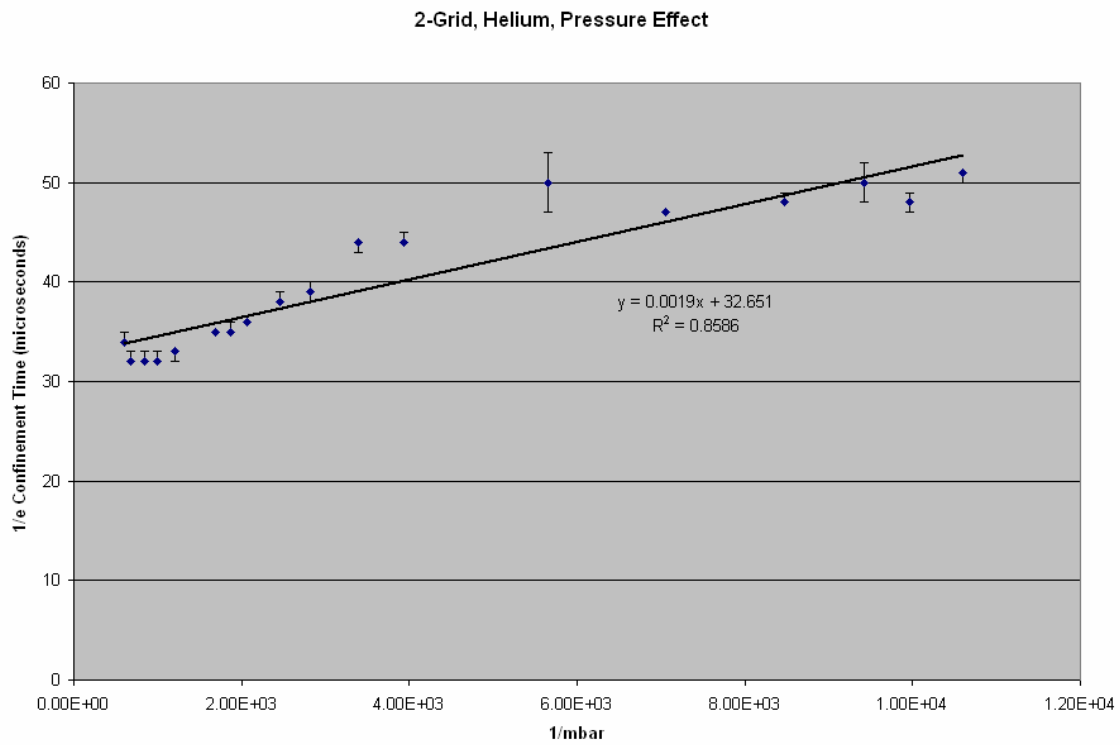
Figure 54: Effect of pressure on 2-grid confinement, Helium

Figure 54 shows the 2-grid helium confinement time plotted against the inverse of pressure. These data clearly indicate that pressure does effect confinement time in 2-grid IEC devices. They also show what appears to be two distinct confinement regimes, a high pressure regime and a low pressure regime. The dividing inverse pressure is around 5000 mbar^{-1} or 2e-4 mbar. At pressures higher than this dividing pressure, the confinement appears reasonably linear with 1/P as shown in figure 55. The slope of the linear regression is similar although slightly lower than the slope of the predicted multi-grid confinement, and the regression fit is quite good.

At pressures lower than this dividing pressure (figure 56), there is no clear relationship between confinement time and pressure and the regression fit is very poor but it shows that the confinement time is does not increase as the pressure is further reduced.

2-Grid, Helium, High Pressure Regime
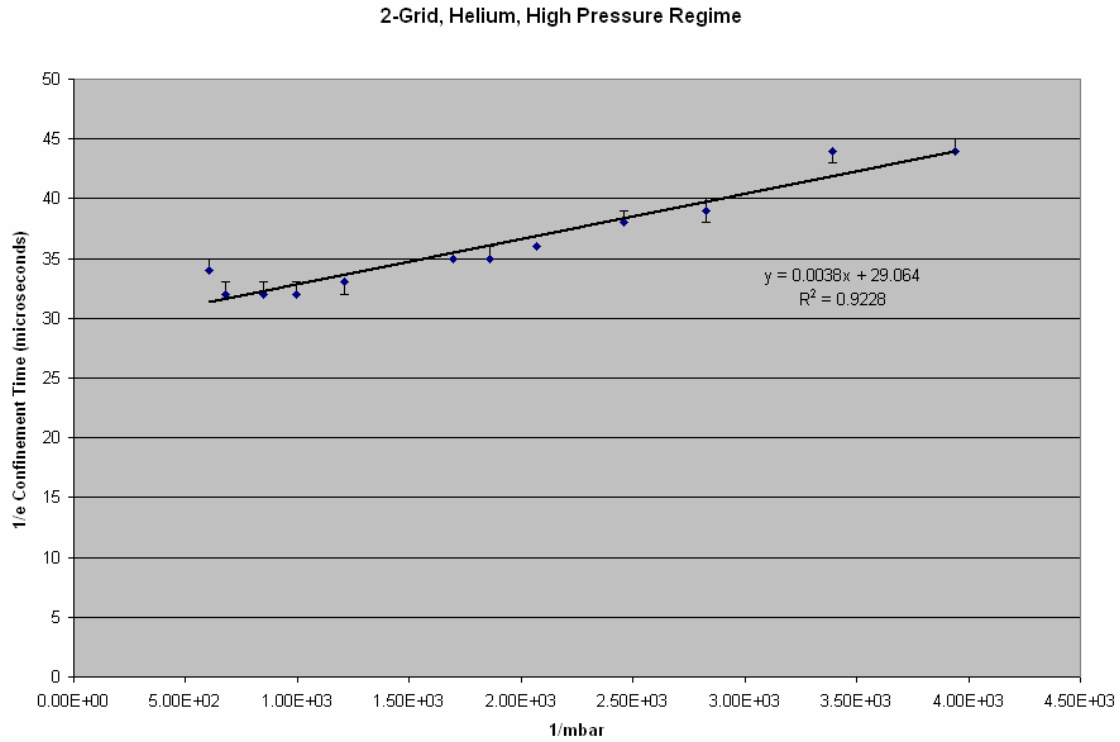
Figure 55: 2-Grid confinement, high pressure regime, Helium
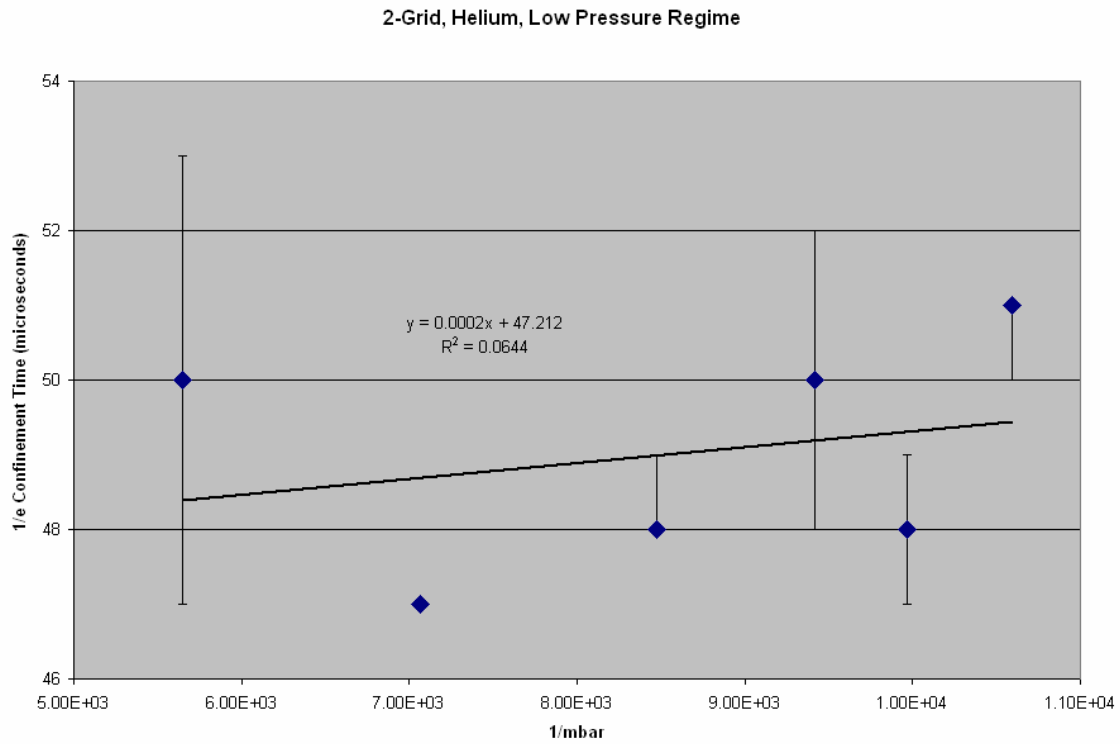
Figure 56: 2-Grid confinement, low pressure regime, Helium

This insensitivity of confinement time to pressure is similar to what was predicted with the OOPIC modeling, although the OOPIC modeling showed a much lower confinement time than is measured in experiment. Possible reasons for this discrepancy include the 2-dimensional nature of the OOPIC model and the lower simulated transparency of the grid and stalks. The ion slug at injection termination also artificially increases all of these numbers equally by approximately 7-9 μs for helium.

The 2-grid Argon data (figure 57) show a similar 2-regime effect, although the critical pressure for Argon appears to be around 1e-4 mbar. The ion slug artificially increases these measured confinement times by approximately 10-12 μs for argon.

2-Grid Argon

y = 11.535Ln(x) - 28.62
$R^2 = 0.9176$
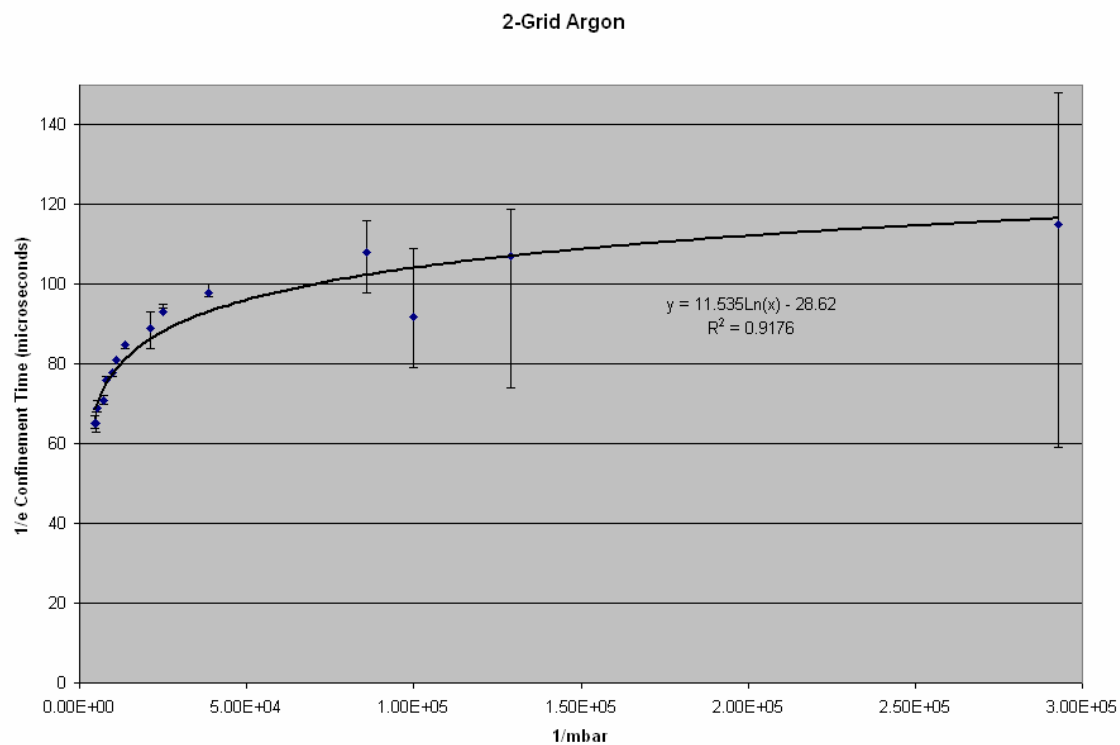
Figure 57: 2-Grid confinement time pressure sensitivity, Argon

The Argon data indicate that there may be a very slight effect of pressure in the very low pressure regimes, but it is clearly not as strong as it is at high pressure; the slopes differ by a factor of 22 between the two regimes as shown in figures 58 and 59.
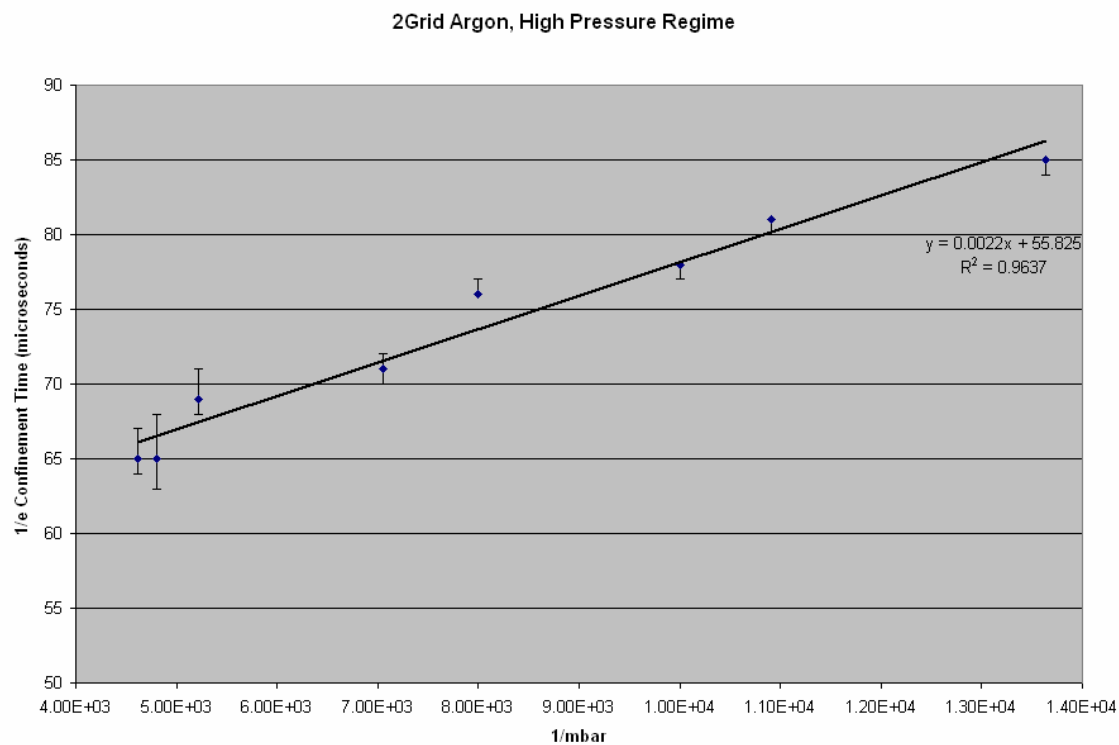
Figure 58: 2-Grid high pressure regime, Argon
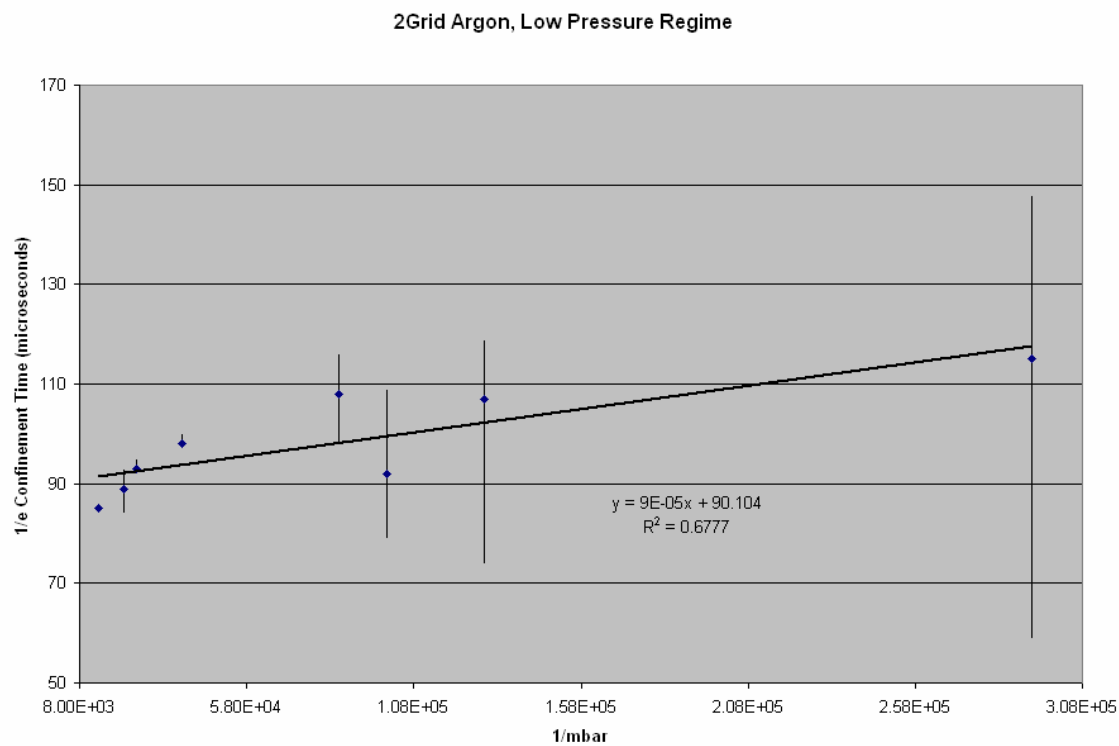
Figure 59: 2-Grid low pressure regime, Argon

The experimental data collected in the 2-grid configuration with both Helium and Argon gas indicate that the 2D OOPIC model does not yield an accurate prediction of ion confinement time in a 2-grid IEC device.

A simple analysis shows that the relative 1/e confinement time trends of Helium and Argon in their respective high pressure regimes are consistent with a model in which the primary loss mechanism is due to charge exchange with background gas.

$$1/e\_ConfinementTime \propto \frac{n_i}{IonLossRate} \qquad \textbf{Equation 4.1}$$

$$IonLossRate \propto n_i n_b \sigma_{cx} v_i \qquad \textbf{Equation 4.2}$$

$$1/e\_ConfinementTime \propto \frac{1}{n_b \sigma_{cx} v_i} \qquad \textbf{Equation 4.3}$$

Therefore, at the same pressure (background density),

$$\frac{1/e\_Ar}{1/e\_He} \approx \frac{\sigma_{cxHe} v_{He}}{\sigma_{cxAr} v_{Ar}} \qquad \textbf{Equation 4.4}$$

The charge exchange cross-section of Argon at the energies of interest is approximately 2.6 times the cross-section of Helium [372], but the 10:1 mass ratio for the two species results in a theoretical 1/e confinement time ratio of 1.21 for Ar/He. The data presented in this section shows a 1/e confinement time ratio of 1.38 at a pressure of 2.2e-4 mbar (the low end of the Helium high pressure regime and the high end of the Argon high pressure regime data). This 14% deviation can be explained by a combination of the inaccuracy of the data collected here due to the "slug effect" and imprecision in the literature on charge exchange cross-sections (~5-10% spread in the data), the assumptions of the energy at which most charge exchange occurs that results in ion loss, and finally (and perhaps most importantly) the influence of the presence of the grids with a finite

transparency. Since Argon is more massive, the ions will have ~1/3rd the "passes"
through the system in a given amount of time as Helium. Helium consequently has many
more opportunities to hit a grid wire. This could help explain the larger measured spread
of confinement time than predicted by the pure charge exchange model. It could also
help explain why the dividing pressure for Helium is much higher than the dividing
pressure for Argon.

The flattening of the trends at lower pressure indicates that the ion lifetime is limited
substantially by a mechanism other than charge exchange such as direct grid impact of
primary ions. This would be consistent with the flat confinement time predictions from
OOPIC or the Hirsch model – a statistical model in which on average ions are lost by
cathode impact after a certain number of passes through the system. In the zero pressure
limit, one would expect ratio of 1/e confinement times of Argon/Helium to approach the
square root of the mass ratio (3.16). These data indicate a ratio of 1.5 to 3 in confinement
time at the lowest measured pressures (the error bars are large at the lowest pressures).
These data also suggest that the number of passes at the lowest pressures is limited to
approximately 10 ion-core transits, quite a few more than predicted by the Hirsh
transparency model.

4.2. Multi-grid Configuration

The core hypothesis of this thesis is that ion confinement times can be increased by the use of multiple (>2) independently biased grids.   This section reports on the first known multi-grid IEC experiment.

4.2.1.   Low Vacuum Operation

Again, the device was first tested at low vacuum in order to see the optical discharge. Interesting plasmas were generated. They are presented here for purposes of completeness and qualitative comparison with the 2-grid pictures.
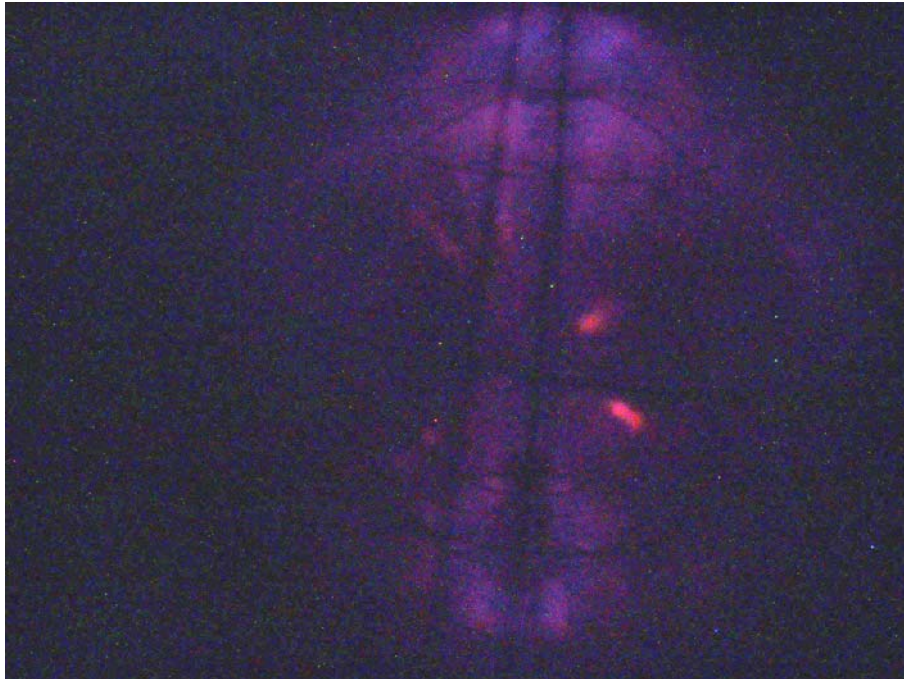
Figure 60: Multi-grid discharge 2e-2 mbar, air

At very high pressures, the discharge occurred at the feed through. As the pressure is dropped, the discharge appeared at the polar regions as in figure 60. As the pressure continued to drop, distinct jets became visible (figures 61 and 62) and gradually grew more pronounced at the equator.
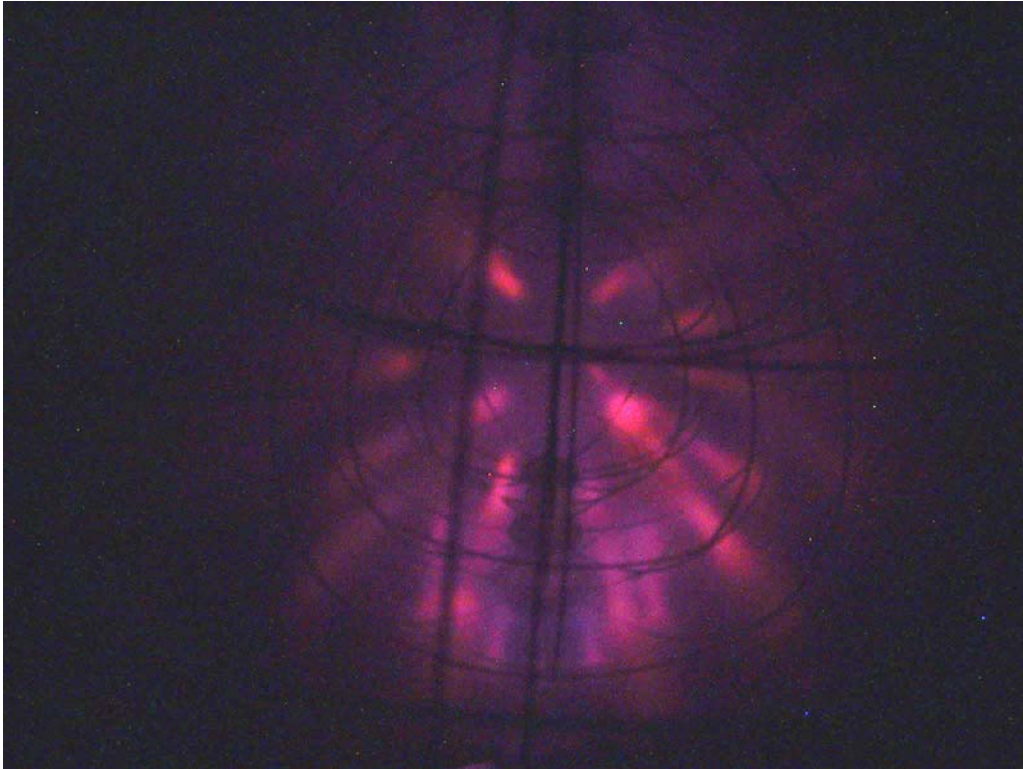
Figure 61: Many jets (~1.5e-2 mbar)
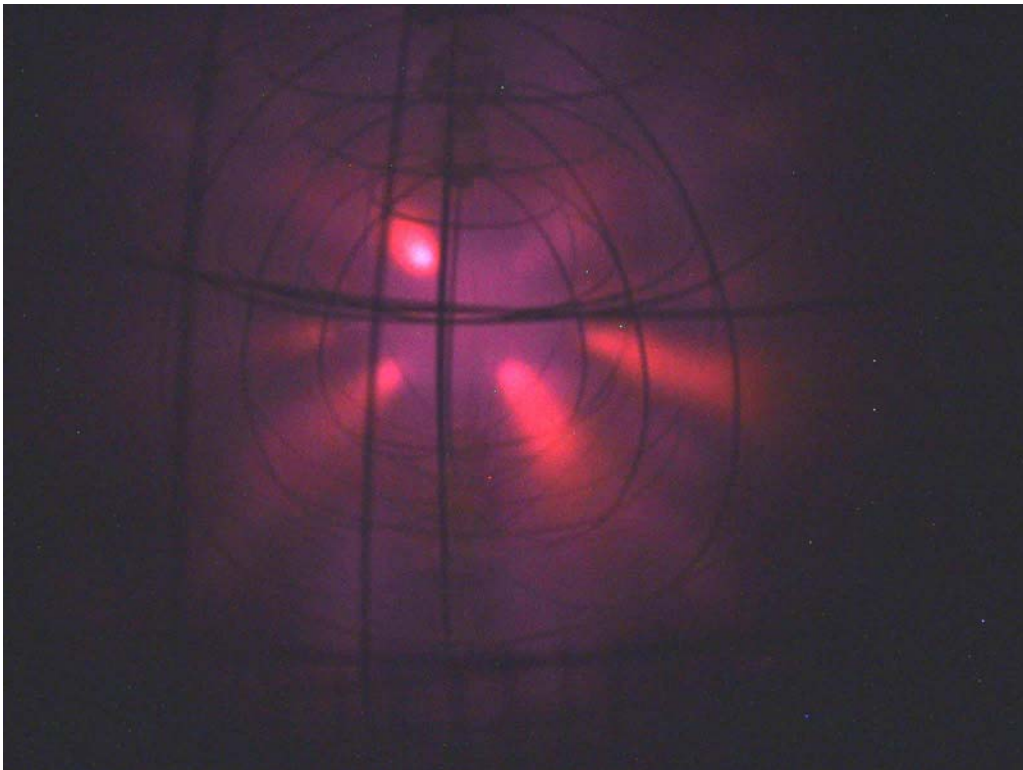
Figure 62: Multi-grid air discharge 1e-2 mbar
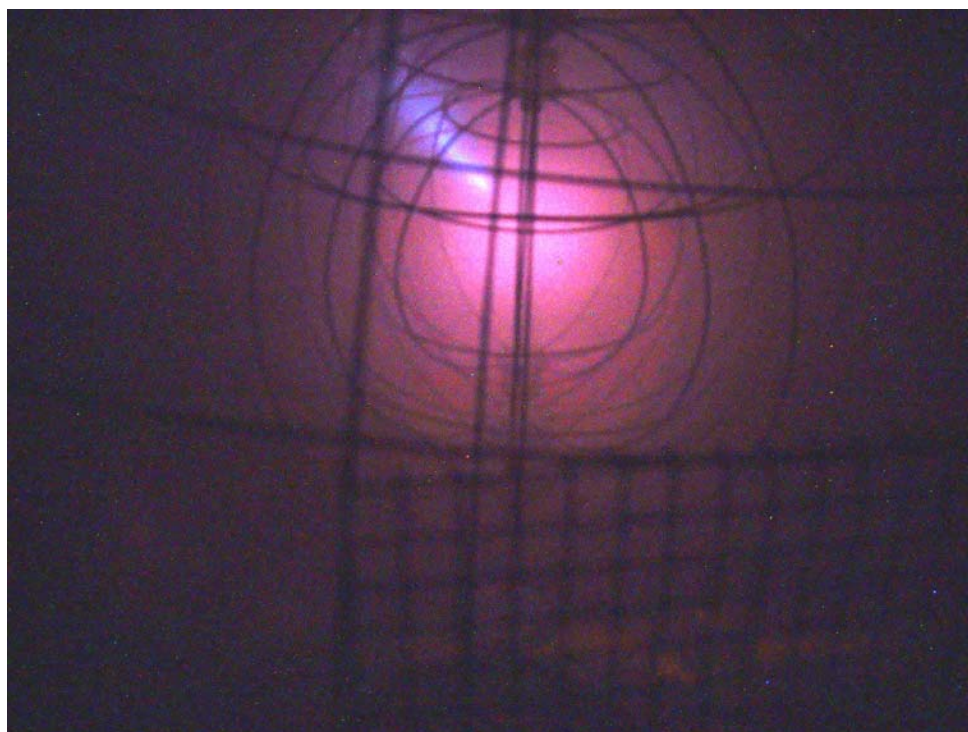
Figure 63: Multi-grid jet-mode (7e-3 mbar)
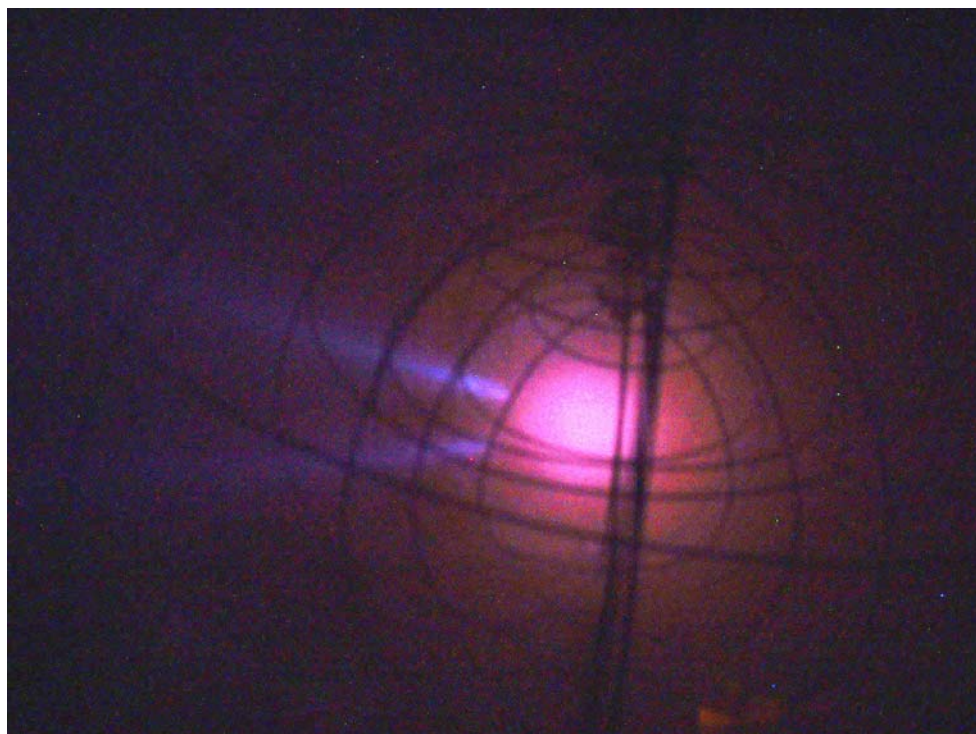
Figure 64: Multi-grid "jumping" jet exposure

Lower pressures resulted in a single primary jet that would move between equatorial longitude lines as shown in figures 63 and 64. These jets were a more bluish color than the higher pressure pink jets. Eventually, as the pressure was lowered still more, the optical discharge would reduce in intensity and the star-mode (figure 65) with its characteristic multiple beams and small core focus was developed (although at a slightly higher pressure than in the 2-grid runs). The discharge also terminated at a higher pressure (2.7e-3 mbar) than it had in the 2-grid runs (1.5e-3).

Figure 65: Multi-grid, star-mode 3e-3 mbar, air

It is worth noting that during these high pressure discharges, the potentials on the grids are not held constant. The HV power supplies on the grids have current limiting circuitry which limits the potential and the discharge on a 1ms time-scale. The photon capture time for the CCD on the camera used to take these pictures is up to 0.6 seconds, so these rapid pulses are not seen. In fact, the "double-jet" image in figure 64 is somewhat deceiving; the jet moved between those two locations while the electronic shutter of the

camera was open. There was only one jet at any given time in that regime. In the star-mode regime, the jets appear to be simultaneous to the resolution of the naked eye (<~0.1s).

4.2.2. High Vacuum Operation

Base pressures of 5e-7 mbar to 1.5e-6 mbar were typically reached for the multi-grid high vacuum experiments.

.

4.2.2.1. Effect of Pressure on 1/e Confinement Time

In Chapter 2 interactions of ions with the background gas was identified as the primary limiter on ion confinement time in multi-grid systems with good confining potential structures. It was therefore desirable to experimentally evaluate the effect of pressure on 1/e ion confinement time. For the following data, a potential structure with good confinement was imposed by setting the grid potentials at [-5000, -1500, -1000, 0, 0]. The background pressure was varied using a fill gas of Helium and Argon. Since confinement time is expected to increase linearly when plotted against the inverse of pressure, that is the format that has been adopted herein.

Effect of Pressure on Confinement

$y = 0.0044x + 19.798$
$R^2 = 0.998$
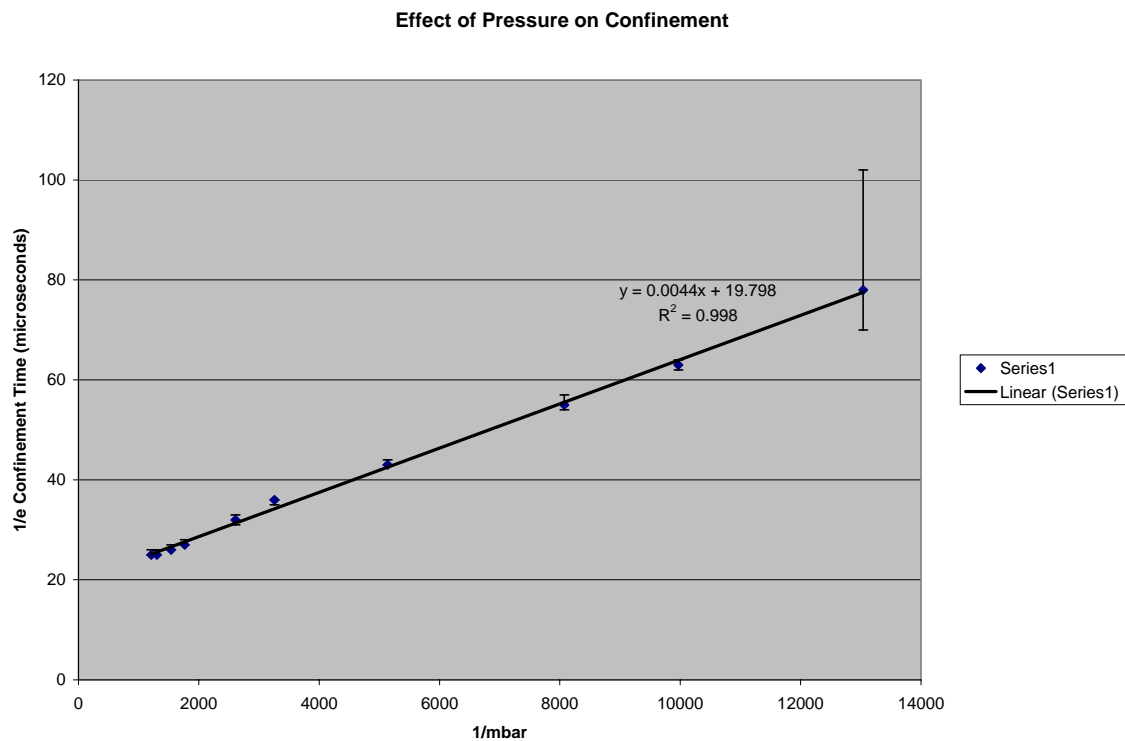
Figure 66: 1/e Confinement time v. 1/Pressure, Helium

Pressure Effect: Comparison of Experiment to OOPIC

$y = 0.0044x + 19.798$
$R^2 = 0.998$

$y = 0.0046x - 0.9409$
$R^2 = 0.9931$
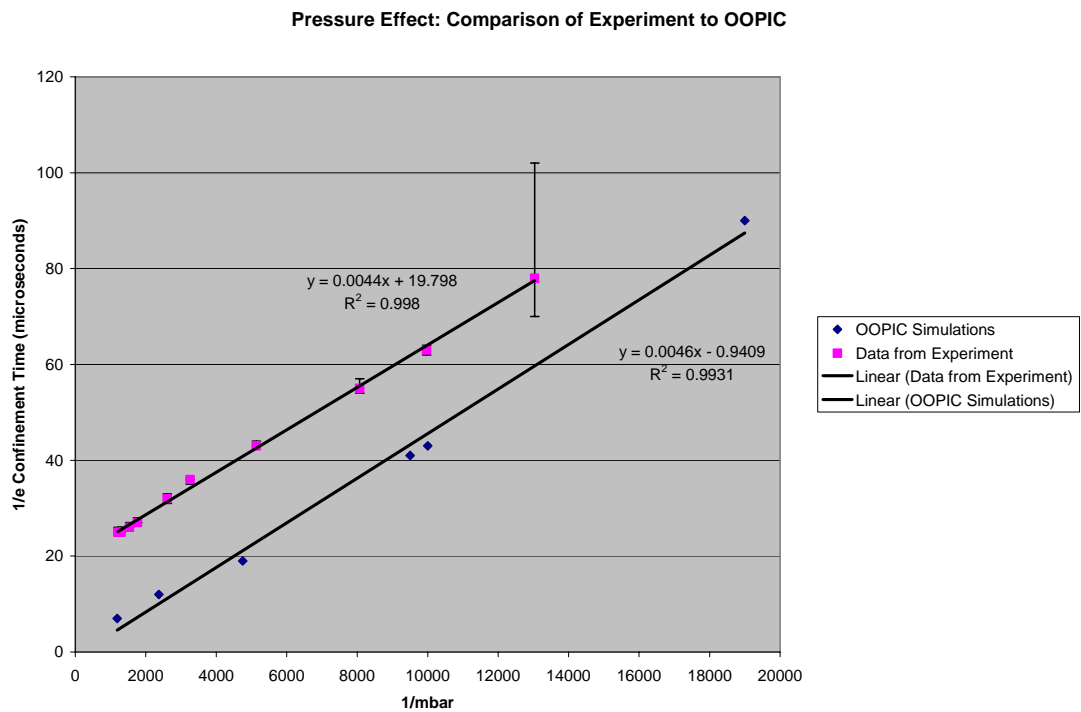
Figure 67: Pressure effect: comparing experimental results to OOPIC, Helium

Figure 66 shows the Helium confinement time plotted against the inverse of pressure. Figure 67 compares those data to the OOPIC predictions for the same potential structure over a similar range of background pressures. It is interesting to note that the slopes of both the physical and computational experiments are the same, but the data from the physical experiments show a longer confinement time than predicted by the OOPIC modeling. This constant 20 μs offset can be explained by a combination of three differences between the OOPIC model and the experiment.

1) The modeled transparency of the grid wires in the OOPIC simulation is only 87% due to computational grid limitations but the actual, physical transparency is 93%.

2) The leakage of the slug of ions from the ion source outside the anode is not modeled in the OOPIC simulations.

3) The OOPIC model measures the total number of particles in the system which starts decaying immediately when the ion injection is stopped whereas the physical experiment detects the ion density near the probe (opposite the ion source), so there is a delay corresponding to the ion transit time across the system (~4 μs for He +1 and 12 μs for Ar +1 for a -5000 V cathode)

Of the unaccounted for 20 μs, 4 μs is clearly explained by the delay due to the location of the probe, the remaining 16 μs can easily be accounted for by a combination of the transparency factor and the ion slug. It is not clear how much of the remaining discrepancy is due to which factor since the velocity and birth location of the average ion in the slug can vary significantly, and the magnitude of the field penetration from the cathode cannot be accurately predicted with the tools at hand, but the data consistently indicate that there is a peak in the ion signal 16-17μs (figure 68) after termination of injection in these multi-grid tests.
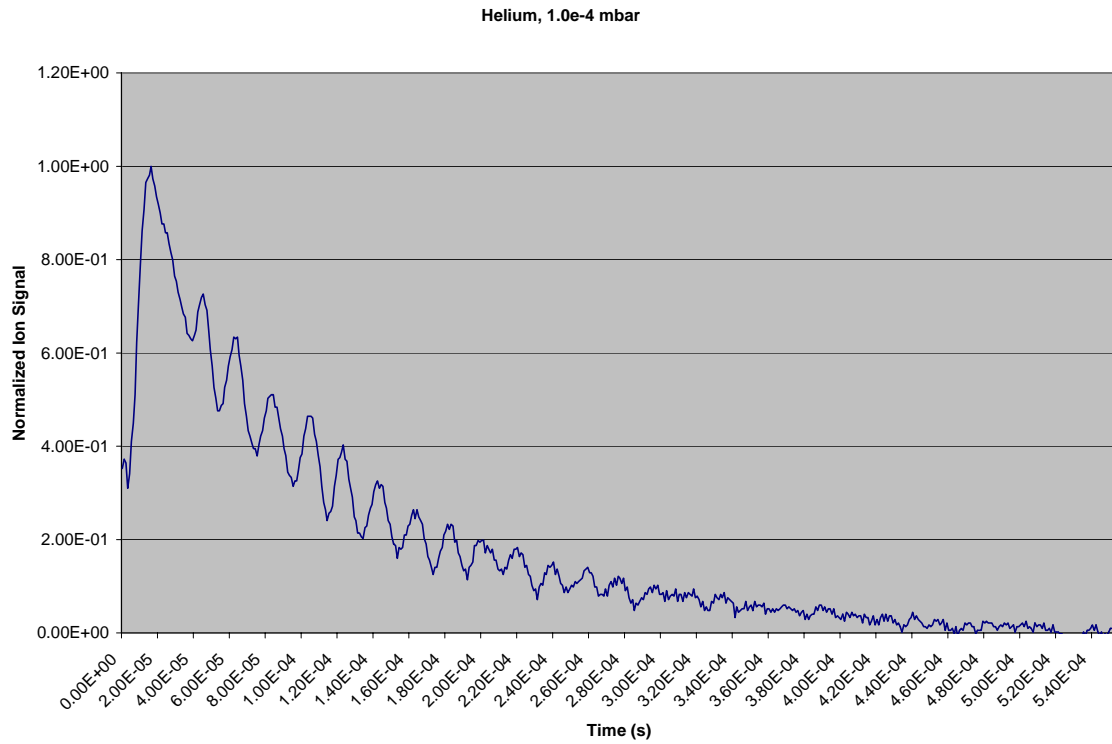
Figure 68: Multi-grid Helium ion decay curve, 1e-4 mbar

Compensating for this 16-17 μs lag in combination with the 4 μs ion transit time would

result in an exact overlap of the two curves in figure 67 to within 1μs over the entire

range.   This would result in the linear data fit of figure 67 passing through the 0,0 point

as would be expected.

Figure 69 shows a similar peak in the ion slug for Argon ions. It is interesting to note

that the initial magnitude of the "slug effect" is comparable between Argon and Helium,

but the dampening of the slug signal is faster at the same background pressure with

Argon than with Helium (likely due to Argon's higher charge exchange cross-section).
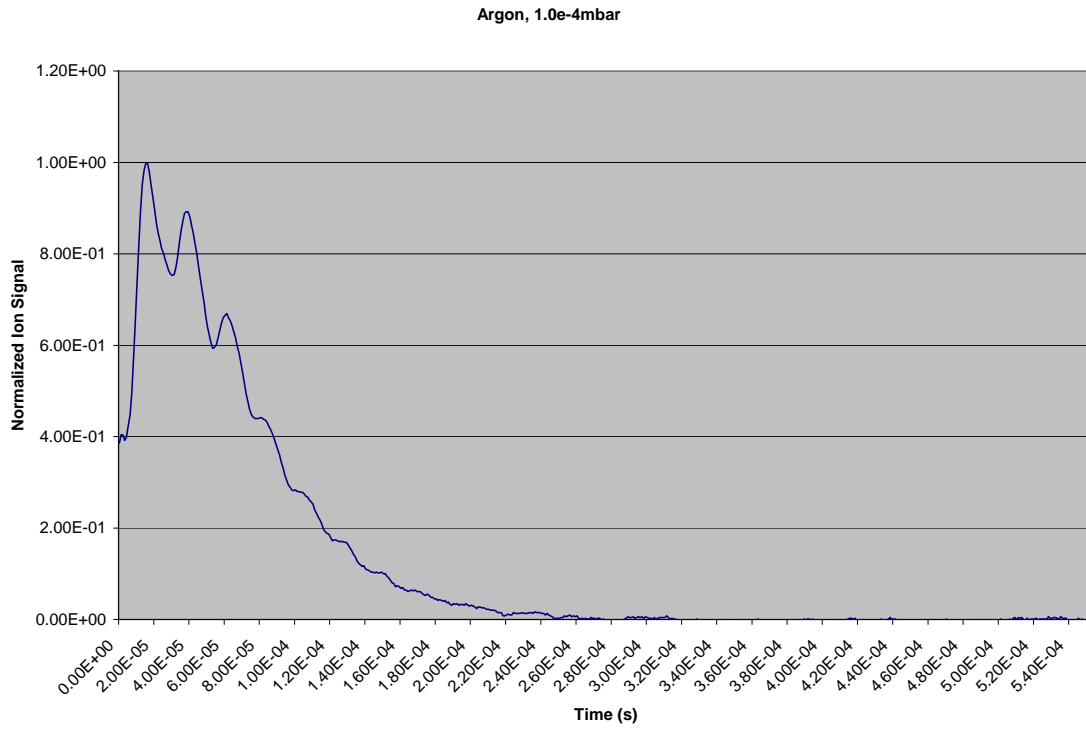
Argon, 1.0e-4mbar

Figure 69: Multi-grid Argon ion decay curve, 1.0e-4 mbar

The OOPIC model in combination with these simple data analyses is thereby shown to give a reasonable approximation of the effect of pressure on the confinement time of ions in a multi-grid IEC device. Although exact numerical prediction was not achieved due to the transit time and the slug effect, the slope of the variation of the 1/e confinement time with the inverse of the pressure was shown to be within 5% of the OOPIC prediction for Helium. The Argon data is even more interesting.
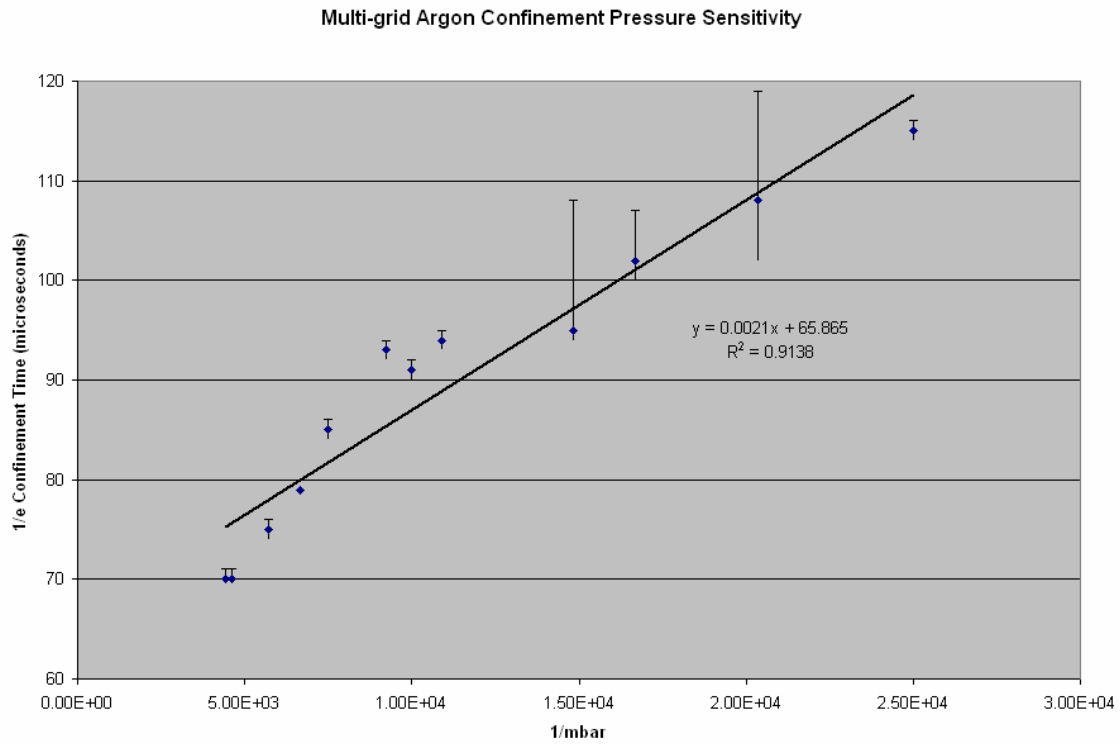
Figure 70: Multi-grid Argon Confinement Pressure Sensitivity

It can be seen in the figure 70 above that the data for argon do not provide as good a linear fit as the Helium data. The slope of the fit is also nearly half of the slope of the Helium data. Due to Argon's much larger electron-impact ionization cross-section (a factor of ~ 8), an acceptable signal to noise ratio is maintained at much lower pressures with Argon than with Helium. Note the inverse pressure range for Helium is 1000-13,000 mbar[-1] in figure 67 while the range for Argon in figure 70 is 5000-25,000 mbar[-1]. It was desirable to expand this range as much as possible given the available equipment.

An interesting phenomenon began to occur around 1e-4 mbar in the experiments with Argon: the slug of ions that is emitted when the ion source is turned off results in an underdamped ringing at pressures lower than around 1e-4 (figure 72). At pressures higher than 1e-4, this ringing is damped within a few cycles (figure 71).
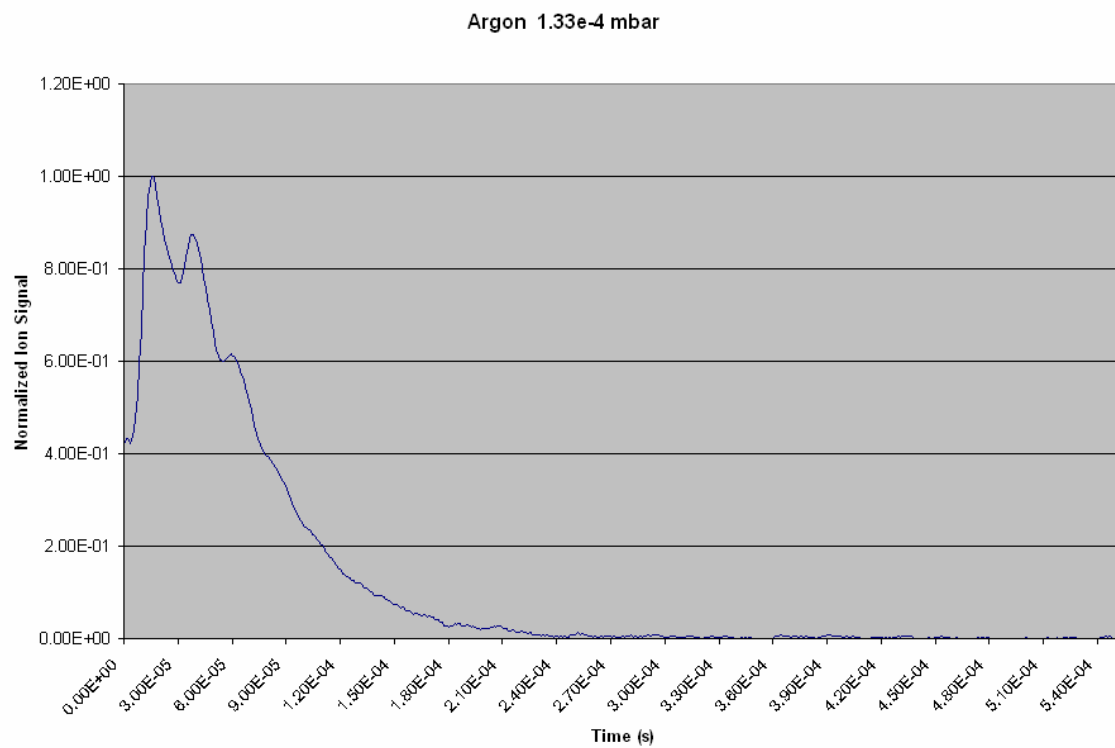
Figure 71: Higher pressure regime decay example
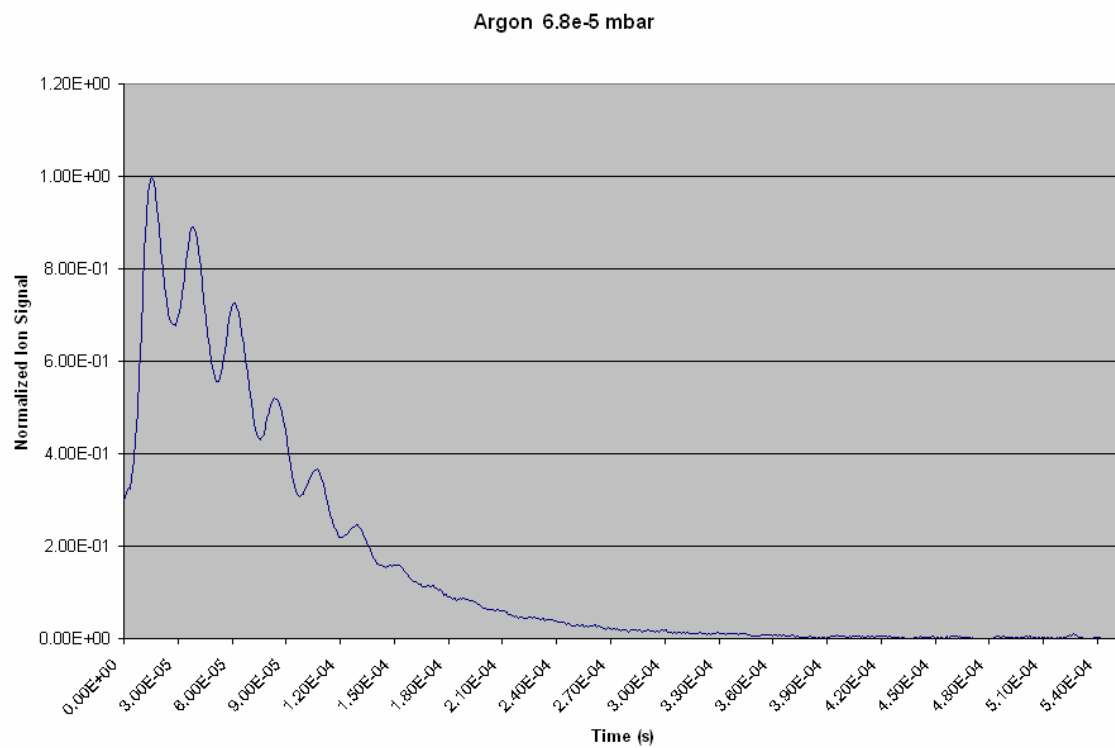
Figure 72: Lower pressure regime decay example

115

While this ringing signal appears similar to the ringing one would expect from the two-stream instability, it is a direct result of the ion slug emitted at injector shut-down, and should not be interpreted as direct evidence of the instability. It appears, however, that when this "ringing" is present, the ion confinement does not follow the same trend as is established at higher pressures when the "ringing" is damped out within a few cycles. Indeed, if the data in figure 70 is split into two separate regimes, one at higher pressures where the ringing is damped, and one at lower pressures where the ringing is highly underdamped, linear fits in both regimes are much better.

ArgonPressureEffect_highpressregime
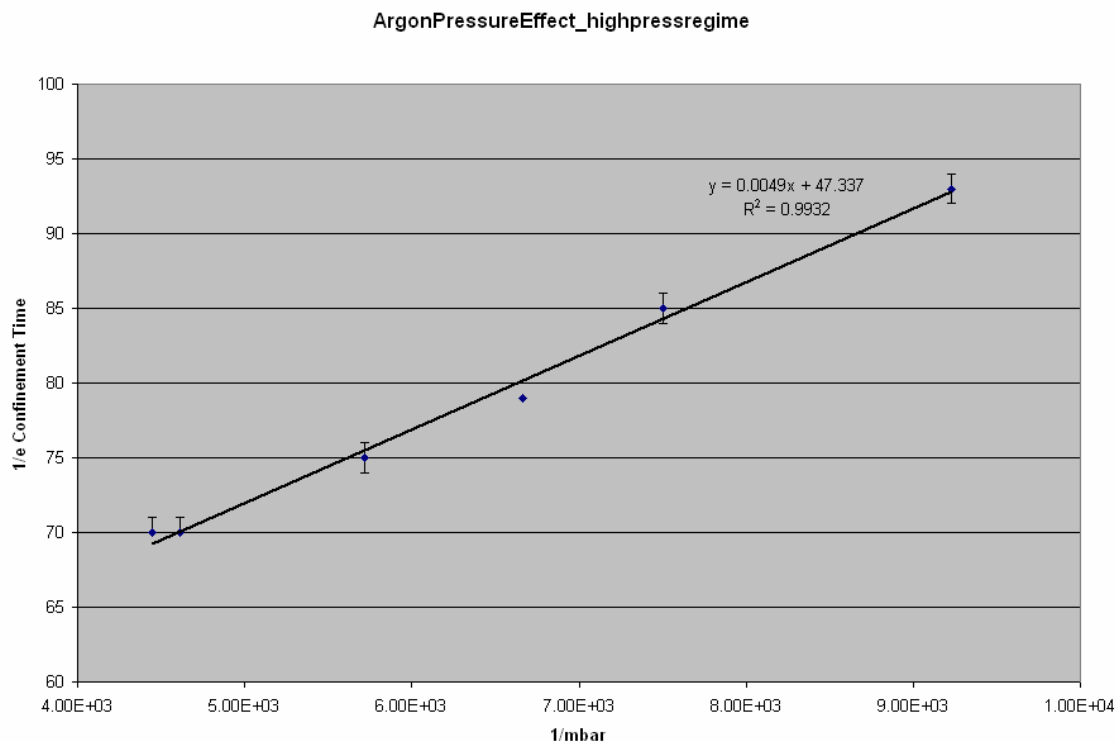
Figure 73: High pressure confinement regime, Argon

In the high pressure regime (figure 73), the slope of the linear fit is similar to the Helium data to within 12%. The linear fit as measured by R^2 is also quite good -- comparable to the fit of the Helium data in the similar pressure regime.

116
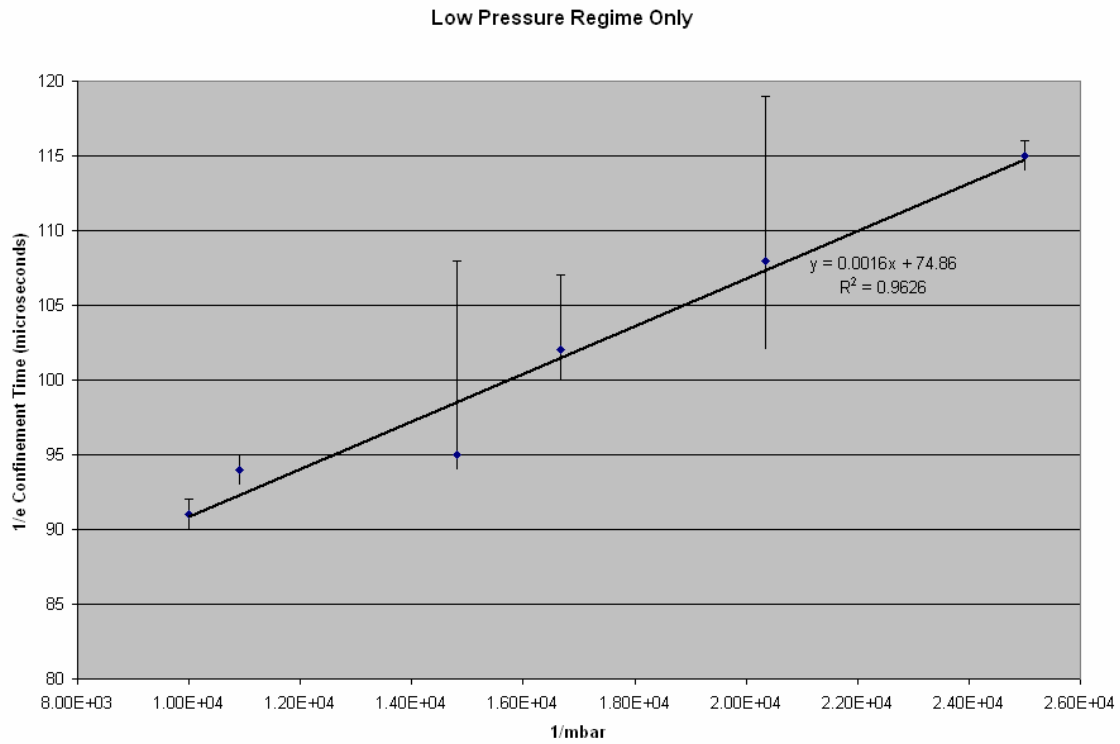
Figure 74: Low pressure confinement regime, Argon

The data in figure 74 suggest that the presence of an underdamped, "ringing" bunch of ions could significantly reduce the confinement time based upon the comparison of the slopes of the linear reductions in the two regimes. The error bars in the lower pressure regime are much larger due to the difficulty in ascertaining the exact 1/e time in the presence of a proportionally large amplitude oscillation.

4.2.2.2.   Intermediate Grid Voltage Sweeps

It was desirable to evaluate the sensitivity of the ion confinement to the potential structure. For all of the tests reported in this section, the 5cm radius (1st) grid is held at a potential of -5000 V, and the 25cm radius anode grid is held at ground.

The baseline grid potentials are [-5000, -1500, -1000, 0, 0]. The second, third, and fourth grid potentials were varied individually from this baseline condition in the experiment to evaluate the effect on ion confinement time.

3rd Grid Voltage Sweep, P = 1e-4 mbar, He
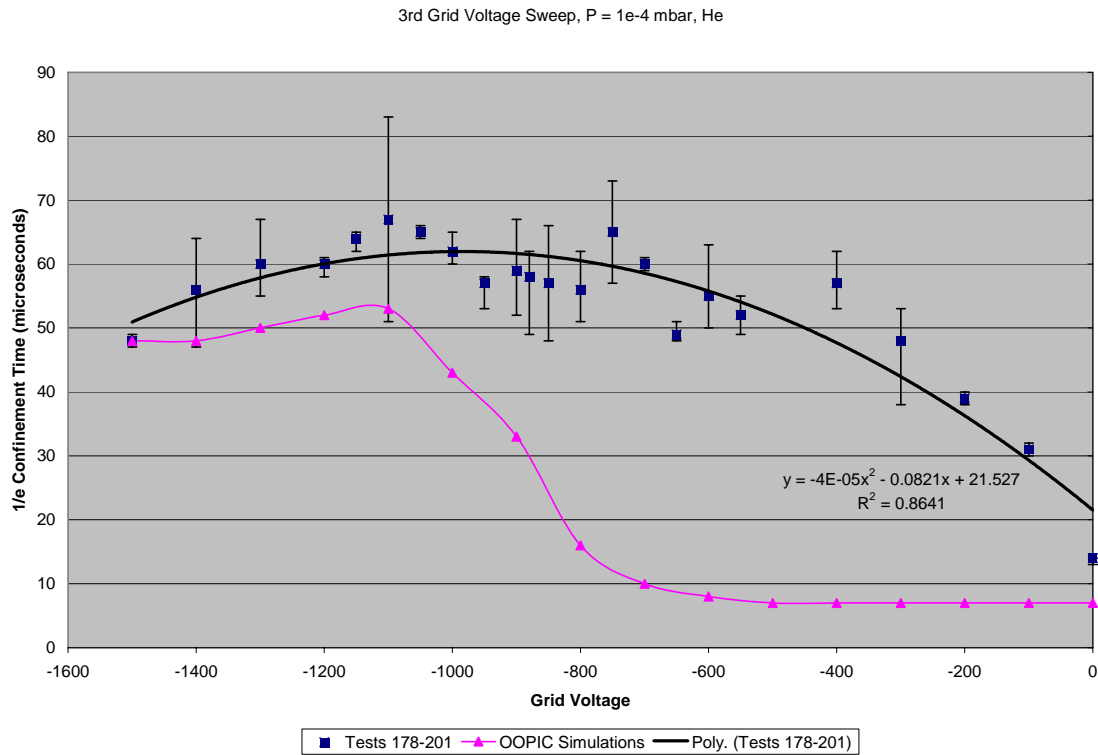
Figure 75: Voltage sweep comparison to OOPIC simulation

The 3rd grid or middle grid (20 cm diameter) was expected to have less of an effect on the confinement of ions in a multi-grid system than either the 2nd or the 4th grids based upon extensive computational and physical testing. It was therefore desired to use a sweep of the potential of this grid to evaluate the ability of the 2D particle-in-cell code, OOPIC, to predict the confinement of ions in a 3D physical experiment. As shown in figure 75, The ability of OOPIC to predict the effect of the variation of grid potential on the ion confinement time was shown to be quite poor based on these data. OOPIC predicted that in the range of -600 to -1200 volts, there would be a substantial change in the

118

confinement time. No such significant change was visible in the data until the 0 to -400 volt range was examined. It is clear based upon these data that the 2D OOPIC code does not give an accurate prediction of the effect of the 3rd grid potential on the confinement properties of the multi-grid IEC system in the experiment.

The only conclusion that can be reasonably drawn from these data is that OOPIC consistently seems to under predict the real, measured confinement times, and as the 3rd grid potential approaches the potential of the next grid in, the ability to predict the confinement seems to improve. Some possible reasons for this under prediction were expounded upon earlier in this section. One possible reason that was not explained before is the slight difference in the field structures due to the 2D Poisson solver versus the real, 3D scenario. This slight difference can affect the confining properties of the potential structure. The additional degree of freedom in experiment also can allow particles to move around things like feed-through stalks in the real world whereas in the 2D simulation, all particles going "past" the stalk, hit the stalk. It would be quite informative to compare the experiment to a full 3D PIC code.

Due to its inability to accurately predict the sensitivity of ion confinement to intermediate grid potentials, OOPIC modeling is not presented with the following grid sweep data. Figures 76 and 77 show the effect of 2nd grid voltage (15 cm diameter) on the confinement time for Helium ions and Argon ions respectively, Figures 78 and 79 show the effect of 3rd grid voltage (20 cm diameter) on the confinement time of Helium and Argon ions respectively. And figures 80 and 81 show the effect of 4th grid voltage (35 cm diameter) on the confinement time of Helium ions and Argon ions respectively.
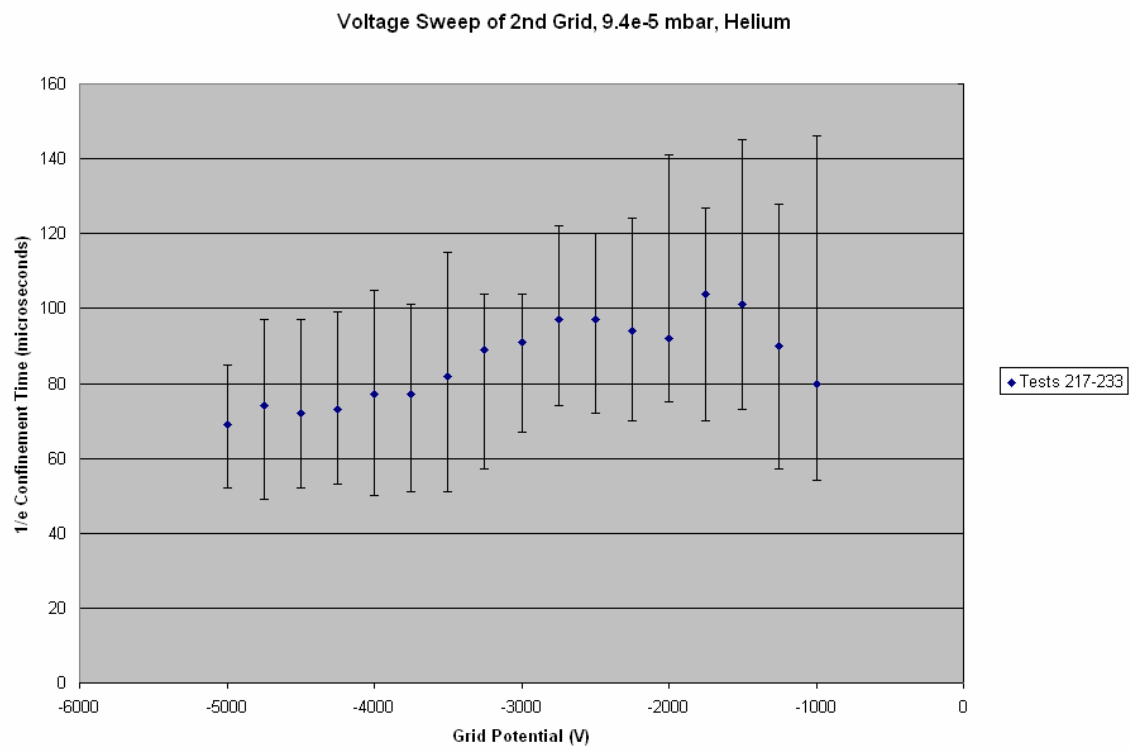
Figure 76: 2nd Grid voltage sweep, Helium
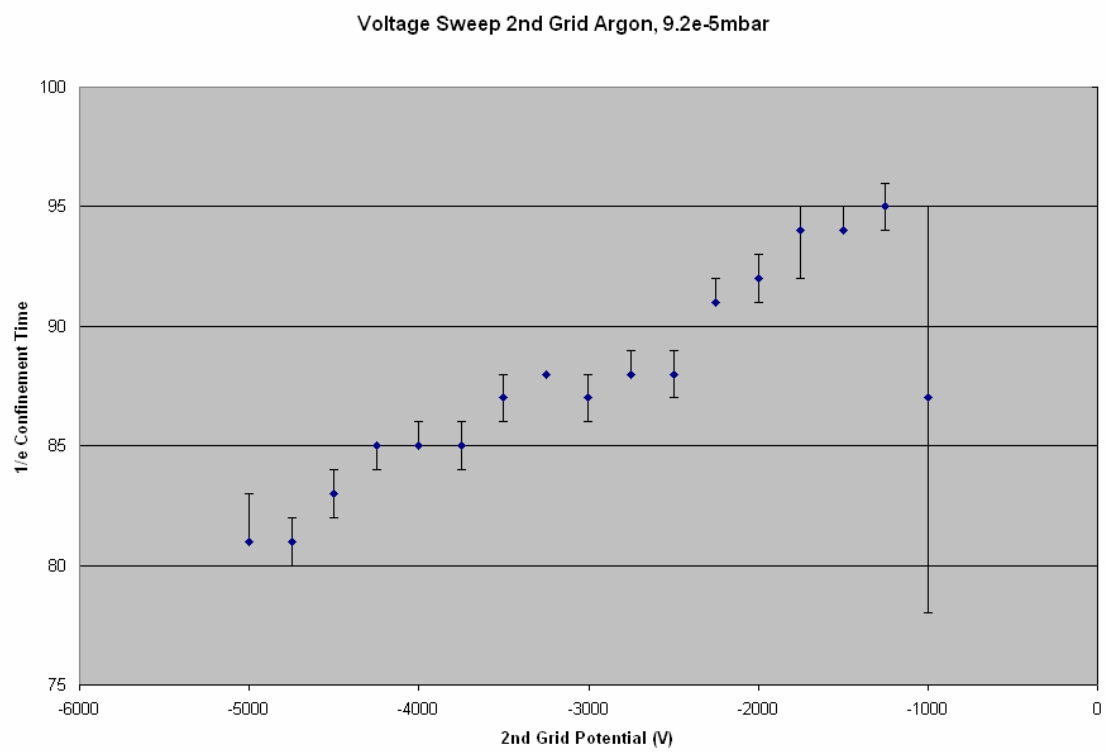
Figure 77: 2nd Grid voltage sweep, Argon

120

Voltage Sweep of 3rd Grid, 1e-4 mbar Helium
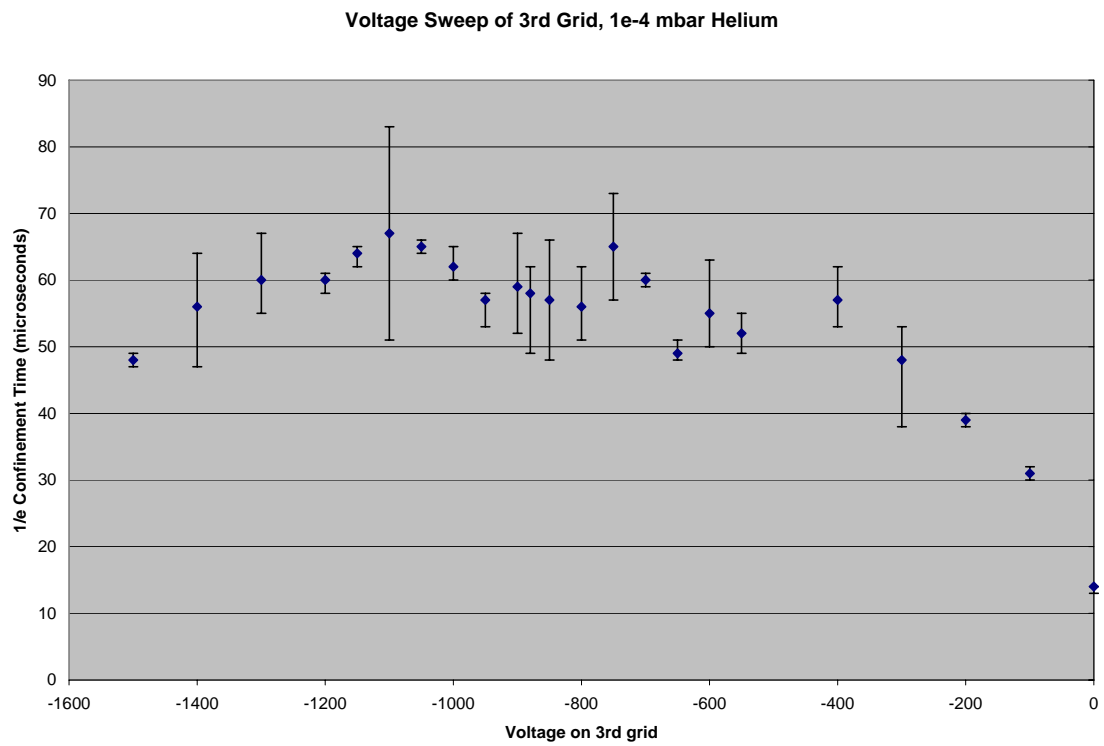
Figure 78: 3rd grid voltage sweep, Helium

3rd Grid Voltage Sweep, Argon, 1.0e-4 mbar
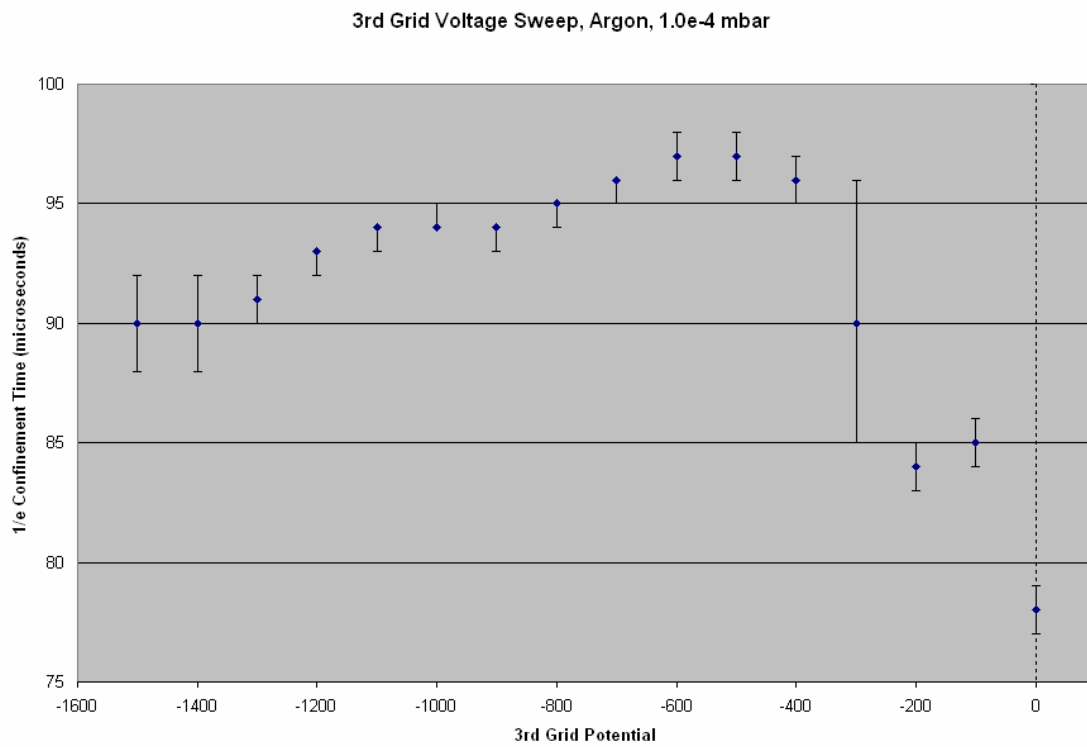
Figure 79: 3rd grid voltage sweep, Argon

121

Voltage Sweep 4th Grid, 7.7e-5 mbar Helium
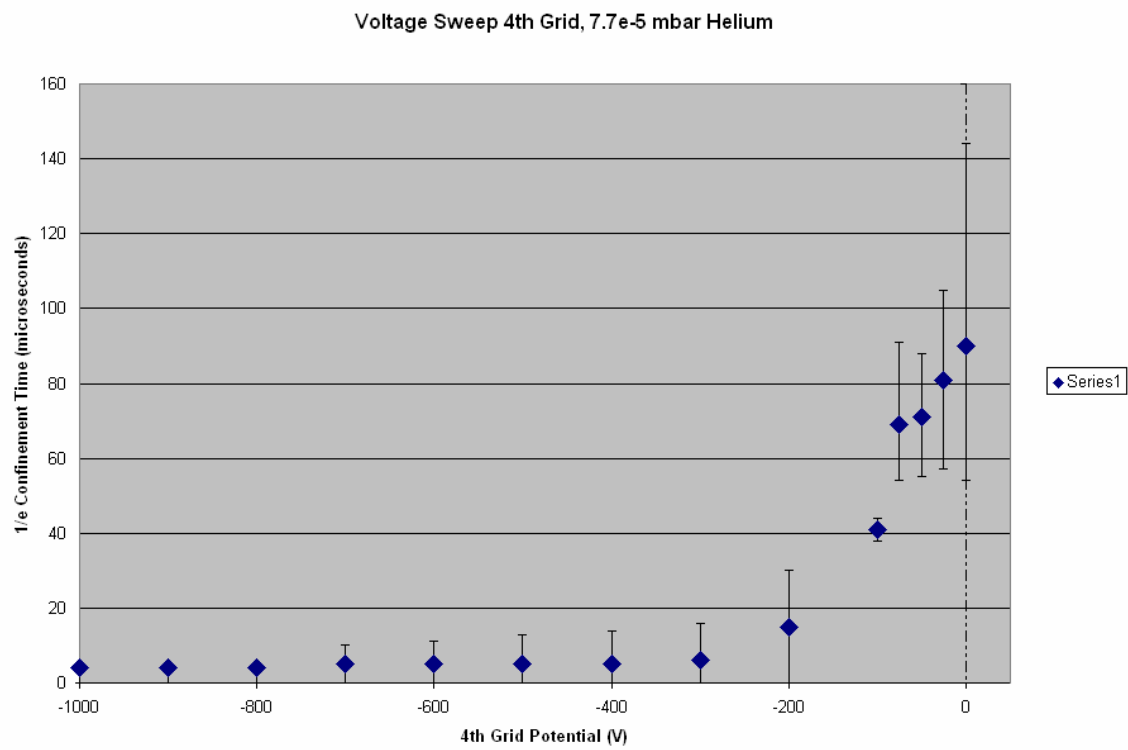
Figure 80: 4th grid sweep, Helium

4th Grid Voltage Sweep, Argon 1.1e-4 mbar
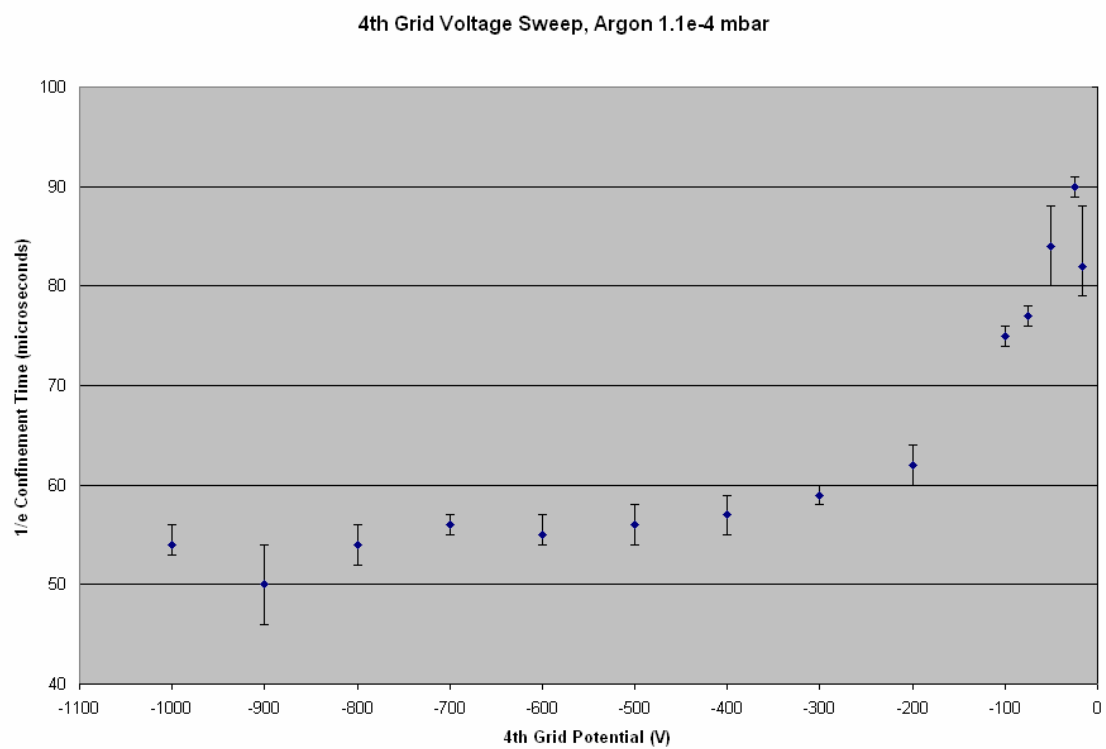
Figure 81: 4th grid sweep, Argon

122

The data on the previous pages clearly show that the sensitivity of ion confinement to grid potential is not strongly dependent on the type of ion. While argon confinement times were all generally longer than Helium confinement times as expected, the sensitivities to grid potentials were consistent between the two ion species. It can also be concluded from these data that ion confinement is most sensitive to the outermost grid potentials i.e. those near the ion "turn-around" potential. The fourth grid clearly exhibits the most sensitivity to grid potential.

4.3. Summary of Data

This section summarizes the most important results obtained from the experiment. Each data point represents an individual experiment. For brevity, the raw data is not included in this thesis except in a few instances for purposes of extreme examples at very low pressures.

4.3.1.   Comparison of 2-grid to multi-grid data

The primary goal of this research was to show that multiple independently biased concentric spherical grids could be used to improve ion confinement times in IEC systems.   The following pages present the comparison of all of the data collected that can be used as a basis for this comparison.   These data were all collected with the capacitive probe detector under high vacuum conditions with both Helium and Argon ions in a background of neutral Helium and Argon respectively. The ion source and detector probe were identical for all of these experiments. The multi-grid data were collected with five concentric spherical grids of radii 5cm, 7.5cm, 10cm, 17cm, and 25cm, and grid potentials of -5000V, -1500V, -1000V, 0V and 0V respectively. For the 2-grid tests, the three intermediate grids were removed and the 5cm grid was held at -5000V while the 25cm grid was held at ground. The probe potential was held at 0.3V above ground, and the ion source was turned on and off by rapidly (~2µs) changing the filament potential from ground to -150V (on) and back to ground.
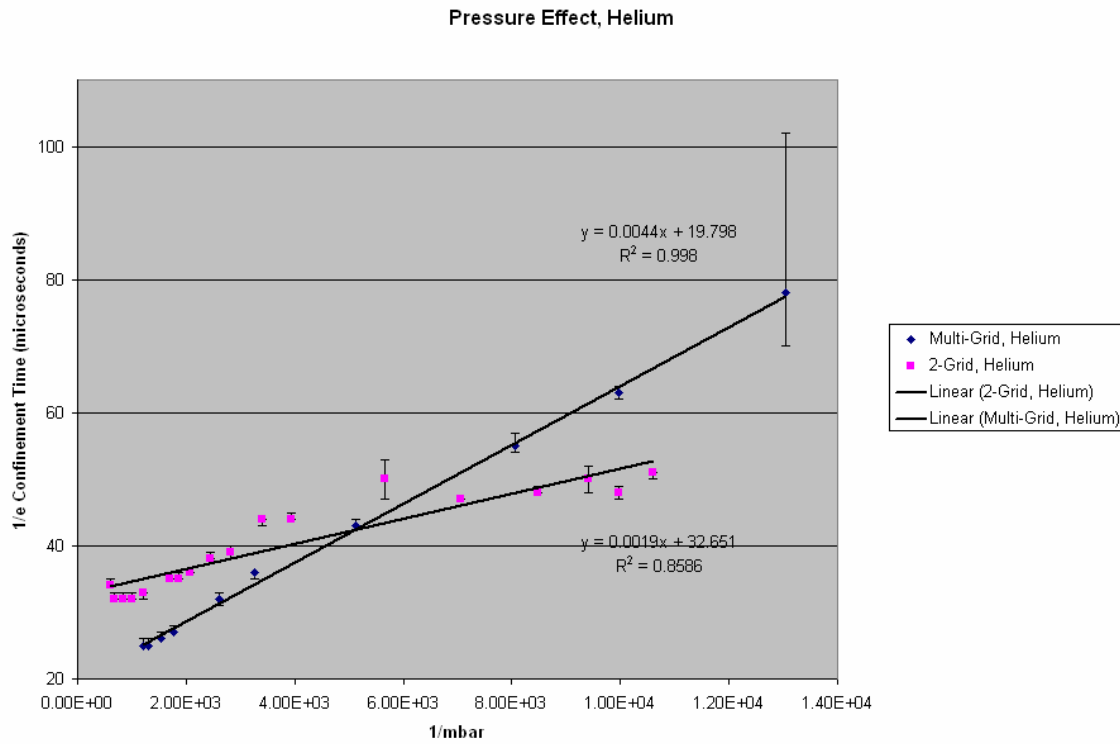
Figure 82: Helium, Multi-grid v. 2-grid confinement

Figure 82 compares the 2-grid and multi-grid data for all of the experiments conducted with Helium ions and Helium background gas. At high pressures, the 2-grid device has better confinement than the multi-grid device. This is likely due to the short mean-free-path of Helium ions relative to the size of the device and the larger ion sink surface area present in the multi-grid tests. As the pressure is lowered, below 1e-4 mbar, the multi-grid confinement time is seen to exceed the 2-grid confinement time by a significant margin. These data strongly suggest that a multi-grid IEC operating at very low pressure could have a significantly longer confinement time than a 2-grid IEC device.

Multi-grid v. 2-Grid, Pressure Effect, Argon

$$y = 0.0021x + 65.865$$
$$R^2 = 0.9138$$

$$y = 0.0013x + 63.219$$
$$R^2 = 0.8519$$

Legend: Multi-Grid Data; 2-Grid Data; Linear (Multi-Grid Data); Linear (2-Grid Data)

Axes: 1/e Confinement Time (microseconds) vs 1/mbar
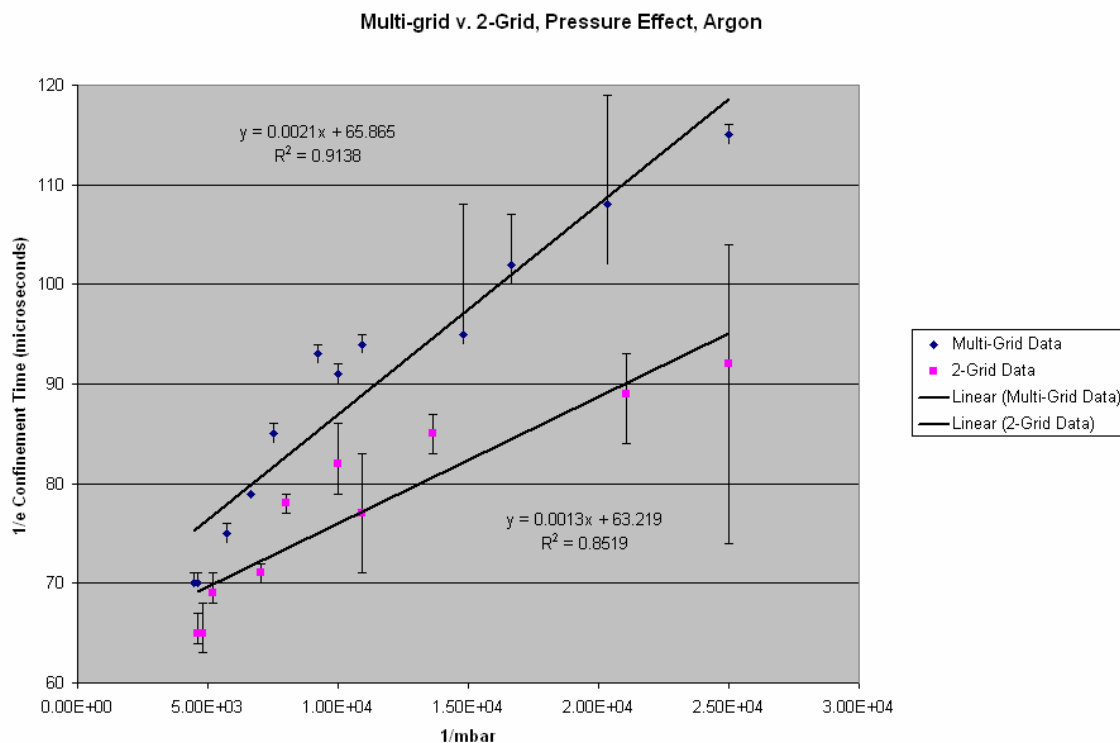
Figure 83: Argon, Multi-grid v. 2-grid confinement

Figure 83 compares the 2-grid and multi-grid data for all of the experiments conducted with Argon ions in Argon background gas. Again, it can be inferred from these data that a multi-grid IEC operating at very low pressure (below 1e-4 mbar) will have a much longer confinement time than a 2-grid device.

It is worth noting, that although there exists both a high pressure regime and a low pressure regime in these multi-grid tests with Argon, similar to the 2-grid experiments, the slope of the low pressure confinement is a factor of 16 higher in the multi-grid data than in the 2-grid data. These data clearly indicate that a significant improvement in the ion confinement can be achieved at low pressures with a multi-grid IEC experiment.

126

It is clear that improved confinement has been achieved in experiment and the trends

indicate that as pressure is reduced, the confinement will improve faster with multiple

grids than with the conventional 2-grid device.   Lower pressures were also explored

particularly with Argon where the higher ionization cross-section allowed a discernable

signal down to pressures as low as 1.9e-6 mbar.
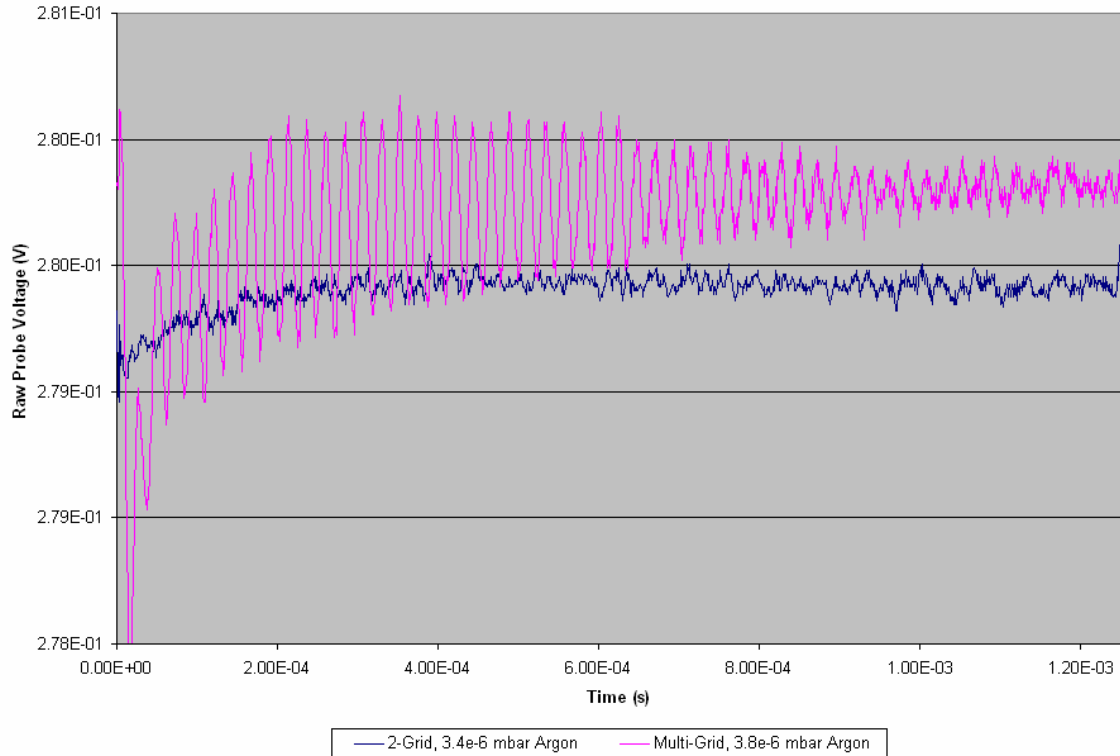
Figure 84: Comparison of Argon ion signals at very low pressures

At these very low pressures, the error bars on the 1/e confinement time are very

significant, and although the S/N is reasonable, the interpretation of the signal is difficult

in the multi-grid system due to the presence of the ion bunching as seen in figure 84

above. If instead of trying to discern the 1/e confinement time, we look for the time at

which the S/N ratio is approximately equal to 1 (the time at which ions can't be detected),

the above raw data clearly show the potential of multi-grid IEC to improve ion

confinement in that a clear ion signal is visible 1ms after termination of injection in the

127

multi-grid case, while the ion signal can only be seen over the background noise for 0.2 to 0.3 ms in the two grid case. It should be noted that the data in figure 84 is raw, un-normalized probe voltage data which is why the signal is seen to "decay" in a positive voltage direction.

4.3.2.   Detection of two-stream instability

A secondary goal of this work was to look for evidence of the two-stream instability that McGuire had seen in computational experiments with good confinement [357]. The saturated mode of this instability was generally seen to be either a single or double bunching of the ions as they "ring" in the well of the IEC system. This growth can be seen in the raw data of figure 84 and more clearly in figure 85 below.
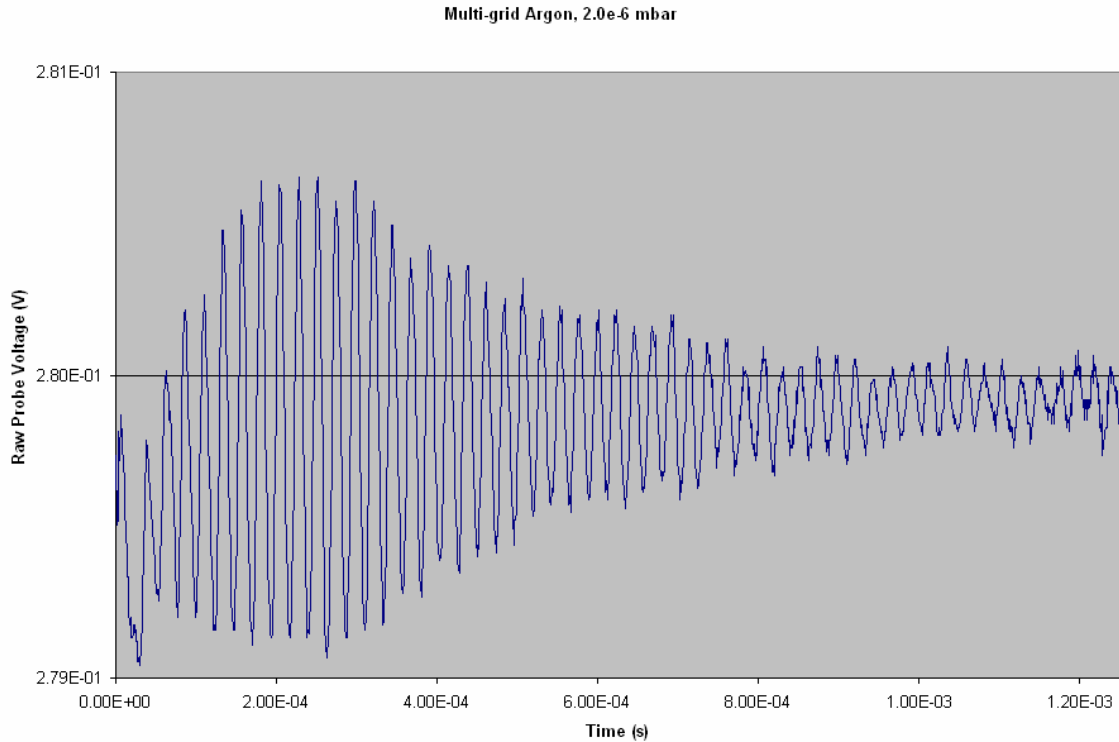
Figure 85: Evidence of two-stream instability at the bounce frequency, Argon 1.9e-6 mbar

128

Figure 85 shows very clear evidence of the presence of instability. The detection of this single bunched mode was not difficult to achieve with the capacitive probe due to its sensitivity to the local ion density at the reflection point. Figure 85 above clearly illustrates the growth in amplitude of the oscillating signal after the ion injection is terminated (time 0). While a slug of ions is expected after the ion source is shut down, this bunching would gradually spread out (decay) over time or stay at roughly the same amplitude in the worst case, unless there is a collective mode instability. The only mechanism for an actual amplitude increase after all ion sources have been terminated is a collective instability. No doubt this instability is excited by the perturbation caused by the slug of ions as the phase of the signal matches the slug quite well.

The instability was only clearly observed with Argon ions. This is believed to be due to Argon's much larger electron bombardment ionization cross section. While a distictive S/N with Helium was only possible down to pressures of 4e-5 mbar, Argon signals could be resolved at pressures as low as 1.9e-6 mbar (figure 85). The instability was seen in argon from this lowest pressure up to 3.4e-5 mbar when the ion source was operating.

As can be seen from the preceding figure, the bunching is very long-lived. In the test presented above at 1.9e-6 mbar, the ion signal can still be seen clearly 1.25ms after the termination of injection – indicating much better confinement than any other reported test, as would be expected at this low pressure. The data show 52 full cycles of the ion bunch or 104 passes of ions through the core of the device over a period of 1200 microseconds. The corresponding cycle time of 23 µs is quite close to the bounce time predicted in OOPIC (~24 µs) for Argon ions. It can be clearly inferred from these data

that this is an Argon ion bunch oscillating at the bounce frequency.   It is worth noting that the number of passes indicated by these data suggests that other effects such as the previously discounted magnetic drift may begin to have a significant impact on the ion confinement time in this long-confinement time operating regime.

Normalized Oscillation Envelope
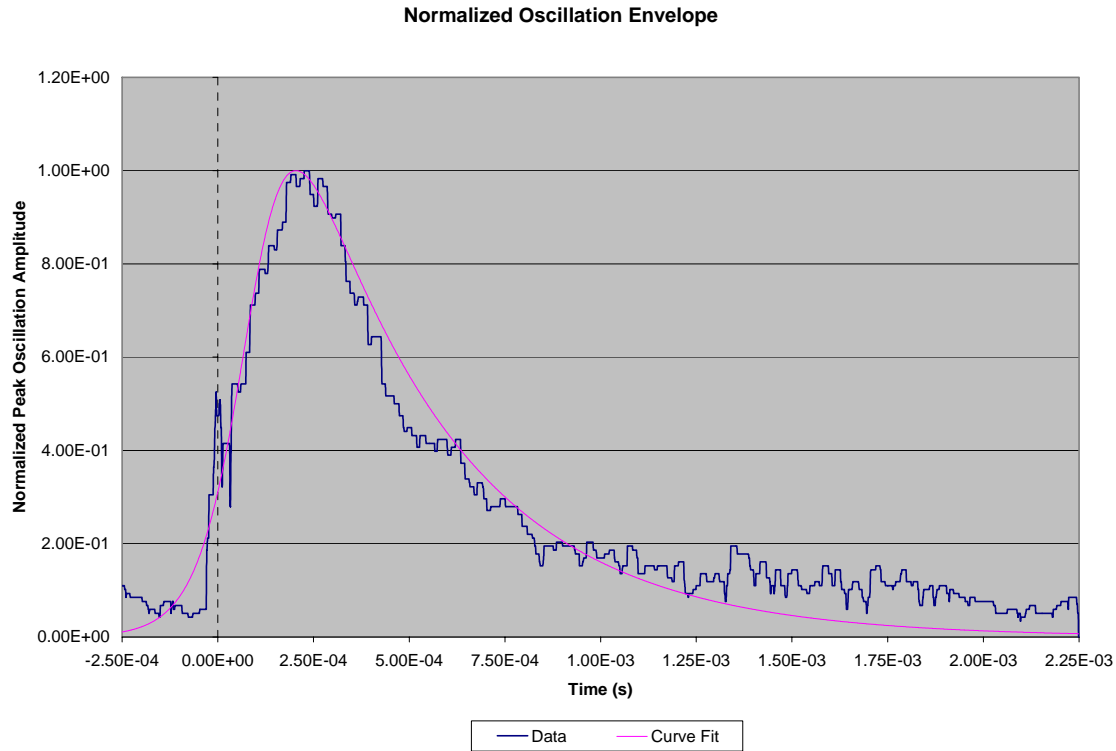
Figure 86: Normalized oscillation envelope and exponential-sigmoid curve fit for the test plotted in figure 85 (Argon, 1.9e-6 mbar)

If we attempt to extrapolate the 1/e confinement time from figure 85 based on the amplitude of the oscillation envelope in the signal (figure 86), it can be seen in that the 1/e time is approximately 400 or 33 passes. It is interesting to note that if the trend in figure 74 were to be extrapolated to this low pressure, the predicted confinement time would be 875 μs, so it is clear that the actual confinement time does not follow that linear extrapolation under these circumstances. It may be that the presence of the instability causes a more rapid loss of ions than would otherwise be expected.

The curve fit shown in figure 86 is a decaying exponential multiplied by a sigmoid function. The decaying exponential represents the continuous loss of ions from the system at a rate proportional to the number of ions in the system. The sigmoid function is used to represent the growth and saturation of the streaming instability which causes bunching that increases the amplitude of the detected ion signal. The specific function that is normalized and plotted in figure 85 is

$$Envelope(t) = \frac{\exp\left(-t/0.0004\right)}{\left(1 + \exp\left(-(t - 0.0001)/0.00006\right)\right)}$$

<div align="right">**Equation 4.5**</div>

Note the 100 μs time shift of the sigmoid to align the growth with the time axis of the data. Based on this model, the growth and saturation of the instability happens on a much faster time scale (60 μs) than the loss of ions from the system (400 μs). The growth of the instability in these data may be artificially accelerated, however, by the injection of the ion slug (an artificially large perturbation) at ion-source shut-off.

Due to this different method of evaluation of confinement time in the presence of the instability at these lower pressures, these confinement time data are not included in the earlier presentations of confinement time data. There is also no good measurement of the two grid confinement time at this lowest pressure for purposes of comparison. If the trend at the lowest pressures is extrapolated from figure 59, the 2-grid confinement would be approximately 135μs at this pressure – a factor of 3 lower than the measured 400μs multi-grid time.

The specific conditions and mechanism for this instability are investigated in depth in the Ph.D. thesis of Tom McGuire. Experimentally, in the grid geometry tested, the instability was seen with a number of different confining potential structures. The best signal (most bunching) at all pressures was achieved with grids at the following potentials: [-5000, -2400, -830, -14, 0]. Double bunching was never seen in experiment although McGuire sees it in computational modeling. The detailed investigation of this phenomenon is beyond the scope of this work.

5. Conclusions and Future Work

Computational and experimental investigations into improving ion confinement in inertial electrostatic confinement systems were conducted. The baseline 2-grid system was compared to a multi-grid system and it was found that the shaping of the electrostatic background field could improve ion confinement in the high vacuum operating regime. The PIC predicted ion bunching mode which is believed to be a saturated two-stream instability was also seen for the first time in an IEC experiment. Computational predictions of 2-grid confinement using OOPIC were quite poor, but modeling of the pressure sensitivity of multi-grid confinement was matched quite well in experiment down to pressures at which the two-stream instability was seen to develop. At these pressures (below ~4e-5 mbar), the 1/e confinement was difficult to clearly distill from the data using the same techniques due to the presence of the instability. An envelope amplitude technique was used to show that a multi-grid Argon ion confinement test at 1.9e-6 mbar had a 1/e confinement time of approximately 400µs, or approximately 33 passes compared to the two grid baseline in which the 1/e confinement time was shown to be approximately 10 passes at best.

5.1.   Contributions of this thesis

This thesis reports on the modeling, design, construction, and testing of the first published multi-grid IEC ion confinement experiment.   The general scaling for non-neutral IEC systems was derived. A useful non-dimensional number for non-neutral IEC systems was proposed. The design and construction of the first multi-grid IEC experiment was reported. A 3-dimensional, multi-grid semi-analytic potential model was

described. The first direct measurements of ion confinement times in a multi-grid IEC device were reported. Computational experiments of particle-in-cell models created in OOPIC were compared to measurements of a physical experiment, and the potential for multi-grid IEC devices to improve ion confinement times was shown both computationally and in experiment. Detection of the computationally predicted two-stream instability at the ion bounce frequency was also reported.

5.2. Suggestions

The current experimental hardware could be used to further these investigations into the confinement properties of multi-grid IEC systems at HV and UHV pressures more effectively if an improved ion source with a much higher pressure in the ionization region than in the rest of the chamber is developed. This type of source could decouple the ion signal strength from the background density which could allow for much more accurate measurements at much lower pressures.   It is also desirable to redesign the ion source to eliminate the slug of ions that is injected when the source is shut down.

It would be interesting to experimentally explore the conditions for the onset of the instability. This type of investigation would be greatly informed by continued theoretical research such as is embodied in the work of McGuire [357].

Because of the scaling of this type of non-neutral IEC device, improved power outputs could be achieved by shrinking the size of the device. The limits to this shrinkage would be imposed by surface flashover considerations, or possibly by cold Fowler-Norheim

emission of electrons from the cathode resulting in rapid loss of efficiency at very small

scale. Such analysis is left to future students.

Appendix: Code

This appendix contains some of critical pieces of code that were generated in order to

produce the computational results reported in this thesis. Code is written for MATLAB

Version 14 and OOPIC Pro Version 1.0. For compactness of this document, only one

version of the OOPIC model is included (GridDiagnostics5.inp).

Matlab Code

For reference I have only included the MATLAB code which was directly used in the Simulated Annealing design routine. Elements of this code are used in other scripts to plot parameters of interest, but the included package is self-sufficient for the SA design process.

Annealit2thengrad.m

```
% Simulated Annealing design script for IEC fusion experiment
% Carl Dietrich 5/31/05

% It is assumed that there are 8 longitude lines and 4 latitude lines of
% even spacing (45 and 36 degree separations), and that the 5th, outermost grid is
% grounded at a radius of 0.25 m.

% Configuration = [Ro Rinjector Rgrid1 Rgrid2 Rgrid3 Rgrid4 Potgrid1 Potgrid2
% Potgrid3 Potgrid4];

clear all
close all

Ro = .01;
Rinjector = .18;
Rgrid1 = .05;
Rgrid2 = .07;
Rgrid3 = .1;
Rgrid4 = .14;
Potgrid1 = -7000;
Potgrid2 = -10000;
Potgrid3 = -4000;
Potgrid4 = -1000;

Configuration = [Ro Rinjector Rgrid1 Rgrid2 Rgrid3 Rgrid4 Potgrid1 Potgrid2 Potgrid3
Potgrid4];

%[xbest,Ebest,xhist]=SA(xo,file_eval,file_perturb,options);
% options     algorithm option flags. Uses defaults, [ ], if left blank
%     (1)     To - initial system temperature - automatically determined if
%             left blank ([]). To should be set such that the expression
%             exp(-E(xo)/To)>0.99 is true, i.e. the initial system is "melted"
%     (2)     Cooling Schedule: linear=1, exponential=[2]
%     (3)     dT Temp. increment, e.g. [dT=0.9] for exp. cooling Tk=dT^k*To,
%             abs. temperature increment for linear cooling (Tk+1=Tk-dT);
%     (4)     neq = equilibrium condition, e.g. number of rearrangements
```

```
%              attempted to reach equilibrium at a given temperature, neq=[5]
%      (5)      frozen condition - sets up SA exit criterion
%               nfrozen = non-integer, e.g. 0.1 SA interprets this numbers as Tmin,
%               the minimum temperature below which the system is frozen.
%               nfrozen = integer ,e.g. 1,2..  SA interprets this as # of successive
%               temperatures for which the number of desired acceptances defined
%               under options(4) is not achieved, default: nfrozen=[3]
%      (6)      set to 1 to display diagnostic messages (=[1])
%      (7)      set to 1 to plot progress during annealing (=[0])

 To=1e2; options(1)=To;
   schedule=2; options(2)=schedule;
   dT=.1; options(3)=dT;
   neq=100; options(4)=neq;
   nfrozen=0.001; options(5)=nfrozen;
   diagnostics=1; options(6)=diagnostics;
   plotflag=1; options(7)=plotflag;

rand('state',sum(100*clock));
tic
[BestConfig,Ebest,xhist]=SAmodCarl(Configuration,'griddesigneval2','PerturbConfig2',o
ptions)
toc
[a b]=size(BestConfig);

PlotConfig2(BestConfig(a,:));
title('Modified SA Results');

coreacceptance = .5;
mingap = .02;
LB(1)=0;
UB(1)=BestConfig(a,3)*sin(pi/8)*coreacceptance;  %max Ro is the first grid radius times
the acceptance
LB(2)=BestConfig(a,5);  % lower bound of Rinj is 3rd grid radius
UB(2)=.25;
LB(3)=BestConfig(a,3);  %1.5*mingap;
UB(3)=(BestConfig(a,4)+BestConfig(a,3))/2 - mingap/2;
LB(4)=UB(3)+mingap;
UB(4)=(BestConfig(a,5)+BestConfig(a,4))/2 - mingap/2;
LB(5)=UB(4)+mingap;
UB(5)=(BestConfig(a,6)+BestConfig(a,5))/2 - mingap/2;
LB(6)=UB(3)+mingap;
UB(6)=.25-mingap;
LB(7)=-10000;
UB(7)=0;
LB(8)=-10000;
UB(8)=0;
LB(9)=-10000;
```

```matlab
UB(9)=0;
LB(10)=-10000;
UB(10)=0;
tic
[NewBestConfig,LowestEnergy] =
fmincon('griddesigneval2',BestConfig(a,:),[],[],[],[],LB,UB)
toc
PlotConfig2(NewBestConfig);
title('FMINCON Gradient Search Results');
% Save results to file:
dumpfilename = strcat('SA_FMINCON_',datestr(now,'mmm-dd-HHMM'));
fid=fopen(dumpfilename,'w');
if fid==-1
   error = 'Unable to open dump file!'
end
fid=fopen('filename','w')
fprintf(fid,'%s \n',num2str(NewBestConfig));
fclose(fid);
```

Griddesigneval2.m

```
% Energy evaluation function for simulated annealing design of multi-grid
% IEC fusion reactor experiment
% Carl Dietrich 5/29/05

% Input is an array
% Configuration = [Ro Rinjector Rgrid1 Rgrid2 Rgrid3 Rgrid4 Potgrid1 Potgrid2
% Potgrid3 Potgrid4];

% It is assumed that there are 8 longitude lines and 4 latitude lines of
% even spacing (45 degree separations), and that the 5th, outermost grid is
% grounded at a radius of 0.2 m.

function Energy = griddesigneval(Configuration)
global rx pot_beam pot_prime_beam pot_dubprime_beam K inj_pot
e=1.602e-19;
epso=8.854e-12;
c=3e8;
% Input the desired grid structure:
r = [Configuration(3) Configuration(4) Configuration(5) Configuration(6) .25]; % grid
radius vector
if r(1)>r(2) | r(2)>r(3) | r(3)>r(4) | r(4)>r(5)
    disp('Warning: Invalid grid configuration!')
    r = r
    Energy = 10000
    return
end
Voltagedesired = [Configuration(7) Configuration(8) Configuration(9) Configuration(10)
0];
n=max(size(Voltagedesired));
solidityfudgefactor = 2.75e-5;
for i=1:n-1
    deltaV(n-i) = -(Voltagedesired(n+1-i)-Voltagedesired(n-i));
    Qins(n-i) = solidityfudgefactor*4*pi*epso*deltaV(n-i)/(1/r(n-i)-1/r(n+1-i));
end
Qins(n)=Qins(n-1);
Qdesired(1)=Qins(1);
for i=2:n
    Qdesired(i) = Qins(i)-Qins(i-1);
end
q = Qdesired./r.^2;%[10.5e-8 -2.1e-7 7.5e-8 0];   % grid charge vector
t = 4;        % number of latitude wires
l = 8;        % number of longitude wires
thickness =.001;% wire thickness
kmax = 32;
mult = kmax/(2*l);
```

```matlab
% Calculate coefficients:
%tic
[Abar, Bbar]=solve_coeff(r,q,t,l,thickness,mult);
%toc
%tic
phi = pi/2;
theta = 0;  %pi/l;
divs = 300;
dr = max(r)/divs;
rx=[0:dr:max(r)];

for i=1:(divs+1)
   if rx(i)<.01
      pot(i) = spherical_potential_norm_posm_bar(r,Abar,Bbar,.01,theta,phi);
   else
      pot(i) = spherical_potential_norm_posm_bar(r,Abar,Bbar,rx(i),theta,phi);
   end
end
edge_ground = -pot(divs+1);
pot = pot+edge_ground;

for i=1:(divs+1)
   if i==1
      pot_prime_wire(i)=0;
   elseif i==divs+1
      pot_prime_wire(i)=(pot(i)-pot(i-1))/dr;
   else
      pot_prime_wire(i)=((pot(i)-pot(i-1))/dr+(pot(i+1)-pot(i))/dr)/2;
   end
end

theta = pi/l;
for i=1:(divs+1)
   if rx(i)<.01
      pot_beam(i) = spherical_potential_norm_posm_bar(r,Abar,Bbar,.01,theta,phi);
   else
      pot_beam(i) = spherical_potential_norm_posm_bar(r,Abar,Bbar,rx(i),theta,phi);
   end
end
pot_beam = pot_beam+edge_ground;
for i=1:(divs+1)
   if i==1
      pot_prime_beam(i)=0;
   elseif i==divs+1
      pot_prime_beam(i)=(pot_beam(i)-pot_beam(i-1))/dr;
   else
```

```
      pot_prime_beam(i)=((pot_beam(i)-pot_beam(i-1))/dr+(pot_beam(i+1)-
pot_beam(i))/dr)/2;
   end
end

for i=1:(divs+1)
   if i==1
      pot_dubprime_beam(i) = 0;
   elseif i==divs+1
      pot_dubprime_beam(i)=(pot_prime_beam(i)-pot_prime_beam(i-1))/dr;
   else
      pot_dubprime_beam(i)=((pot_prime_beam(i)-pot_prime_beam(i-
1))/dr+(pot_prime_beam(i+1)-pot_prime_beam(i))/dr)/2;
   end
end

%%%%%%%%%%%%%%%%%%%%%%%%%%%%%%
K=zeros(size(rx));
% Initial beam envelope conditions
Ro=Configuration(1);
r_inj = Configuration(2);
mi = 40*1.67e-27;   % Argon
inj_pot = spherical_potential_norm_posm_bar(r,Abar,Bbar,r_inj,pi/l,pi/2)+edge_ground;
inj_pot_dtheta =
spherical_potential_norm_posm_bar(r,Abar,Bbar,r_inj,2*pi/l,pi/2)+edge_ground;
dphidtheta=(inj_pot_dtheta-inj_pot)/(pi/l);
if dphidtheta<0
   disp('Reflection region is defocussing => bad design')
   Energy = 10000
   return
end
vtherm=340;
Rprimeo=0;
Rfinal = 0;
Rprimefinal = 0;
no=2e13;
YO = [Ro Rprimeo];
OPTIONS = ODESET('RelTol',1e-4,'AbsTol',1e-8);
for i=1:max(size(rx))
   vi(i)=sqrt(2*e*(abs(pot_beam(i)-inj_pot))/mi)+vtherm;
   gamma(i)= 1/sqrt(1-vi(i)^2/c^2);
   K(i)=e^2*no*Ro^2/(2*epso*mi*vi(i)^2*gamma(i)^3); % perveance
end
if max(isnan(K))
   disp('K is NaN!')
   Energy = 10000
   return
end
```

```
iter = 0;
maxiters = 1000;
acceptance = .8;
while iter<maxiters % & beam envelope is inside acceptance window
   iter = iter+1;
   no = 1.1*no;
   K = K.*1.2;   % since perveance is proportional to density...
   [X Y]=ode45('ode45beamfunc',[0 (r_inj-dr)],YO,OPTIONS);
   [n m]=size(Y);
   [maxR, imaxR]=max(abs(Y(:,1)));
   %Checks:
   if maxR > X(imaxR)*sin(pi/8)*acceptance & X(imaxR)>=r(1)
      break
   end
   for ib=1:4
      if r_inj>r(ib) & interp1(X, Y(:,1), r(ib)*cos(pi/8)) > acceptance*r(ib)*sin(pi/8)
         disp('good break')
         break
      end
   end
end

no = no;
Ro = Ro;

normalizing_factor = (1e14)^2*(.01)^3;  % Approximate density and core size from 2D
OOPIC sims
Energy = normalizing_factor/(no^2*Ro^3) %*V_c^4)
if max(max(isnan(Y)))
   disp('Warning: Solution NaN!')
   Energy = 10000
   return
end
if min(Y(:,1))<0
   disp('Warning: beam envelope crosses R=0!')
   Energy = 10000
end
if max(imag(Y(:,1)))
   disp('Beam envelope has imaginary component!')
   Energy = 10000
end
if iter>=maxiters
   disp('Maximum number of iterations has been exceeded!')
   Energy = 10000
end
```

%toc

PerturbConfig2.m

% Configuration perterbation function for SA design of a multi-grid
% IEC fusion reactor experiment
% Carl Dietrich 5/31/05

% Input is an array
% Configuration = [Ro Rinjector Rgrid1 Rgrid2 Rgrid3 Rgrid4 Potgrid1 Potgrid2
% Potgrid3 Potgrid4];

% It is assumed that there are 8 longitude lines and 4 latitude lines of
% even spacing (45 degree separations), and that the 5th, outermost grid is
% grounded at a radius of 0.25 m.

```
function [NewConfig] = PerturbConfig2(Configuration)
% Start with old configuration:
NewConfig = Configuration;
% Pick the two degrees of freedom to be perturbed
firstchoice = ceil(10*rand);
secondchoice = ceil(10*rand);
while firstchoice==1
   firstchoice = ceil(10*rand);
end
while firstchoice == secondchoice  | secondchoice==1 % ensure that there are 2 perturbed
DOFs
   secondchoice = ceil(10*rand);
end

% If it is necessary to move the grids, move them first (inside out)...
mingap = .02; % minimum radial gap between grids...

if firstchoice == 3 | secondchoice == 3% if we are perturbing the 1st grid
%    if Configuration(4)-mingap <.25/3
%       maxsize=Configuration(4)-mingap;   % can't move beyond the 2nd grid
%       if maxsize<minsize
%          maxsize=Configuration(3);
%       end
%    else
%       maxsize=.25/3;           % or 1/3rd the distance (arbitrary)
%    end
   minsize=.03;              % minimum grid radius is 3 cm
   maxsize=Configuration(4)-mingap;   % can't move beyond the 2nd grid
   NewConfig(3)= minsize+rand*(maxsize-minsize);
   if NewConfig(3)< minsize
     NewConfig(3)=minsize;
   elseif NewConfig(3)>maxsize
     NewConfig(3)=maxsize;
```

```
    end
  R_Grid_1 = NewConfig(3)
end
if firstchoice == 4 | secondchoice == 4% if we are perturbing the 2nd grid
%    if Configuration(5)-mingap<.25/2
%       maxsize=Configuration(5)-mingap;   % can't move beyond the 3rd grid
%    else
%       maxsize=.25/2;           % or 1/2 the distance (arbitrary)
%    end
  maxsize=Configuration(5)-mingap;   % can't move beyond the 3rd grid
  minsize=NewConfig(3)+mingap;    % minimum grid radius is grid 1 + the min gap
  NewConfig(4)= minsize+rand*(maxsize-minsize);
  R_Grid_2 = NewConfig(4)
end
if firstchoice == 5 | secondchoice == 5% if we are perturbing the 3rd grid
%    if Configuration(6)-mingap<.25*.75
%       maxsize=Configuration(6)-mingap;   % can't move beyond the 4th grid
%    else
%       maxsize=.25*.75;          % or 3/4 the distance (arbitrary)
%    end
  maxsize=Configuration(6)-mingap;   % can't move beyond the 4th grid
  minsize=NewConfig(4)+mingap;    % minimum grid radius is grid2 +mingap
  NewConfig(5)= minsize+rand*(maxsize-minsize);
  R_Grid_3 = NewConfig(5)
end
if firstchoice == 6 | secondchoice == 6% if we are perturbing the 4th grid
  maxsize=.25-mingap;           % max size is mingap from the anode
  minsize=NewConfig(5)+mingap;    % minimum grid radius is grid3 plus mingap
  NewConfig(6)= minsize+rand*(maxsize-minsize);
  R_Grid_4 = NewConfig(6)
end

% Now pick focal point and injection point if necessary:
% if firstchoice == 1 | secondchoice == 1% if we are perturbing the focal size
%     % maximum size of Ro (focus) is assumed to be half of the sine of the
%     % pi/8 times the inner grid radius, Rgrid1
%     maxsize=0.5*NewConfig(3)*sin(pi/8);
%     minsize=.003;   % implicit assumption that the focal diameter > 6mm
%     NewConfig(1)= minsize+rand*(maxsize-minsize);
%     Ro = NewConfig(1)
% end
if firstchoice == 2 | secondchoice == 2% if perturbing the injector location
  % Assume the injector must be located outside the third grid and
  % inside the outermost anode grid (which has Ranode=0.25)
  maxsize = 0.25;
  minsize = NewConfig(5);
  NewConfig(2)= minsize+rand*(maxsize-minsize);
  R_injector = NewConfig(2)
```

```
end

% Now perturb the potentials if necessary:
if firstchoice == 7 | secondchoice == 7% if we are perturbing the 1st pot
   maxpot=-5000;
   minpot=-10000;
   NewConfig(7)= minpot+rand*(maxpot-minpot);
   Pot_Grid_1 = NewConfig(7)
end
if firstchoice == 8 | secondchoice == 8% if we are perturbing the 1st pot
   maxpot=-5000;
   minpot=-10000;
   NewConfig(8)= minpot+rand*(maxpot-minpot);
   Pot_Grid_2 = NewConfig(8)
end
if firstchoice == 9 | secondchoice == 9% if we are perturbing the 1st pot
   maxpot=0;
   minpot=-5000;
   NewConfig(9)= minpot+rand*(maxpot-minpot);
   Pot_Grid_3 = NewConfig(9)
end
if firstchoice == 10 | secondchoice == 10% if we are perturbing the 1st pot
   maxpot=0;
   minpot=-5000;
   NewConfig(10)= minpot+rand*(maxpot-minpot);
   Pot_Grid_4 = NewConfig(10)
end


% Never perturb focal point (always constant fraction of inner grid radius)
   % maximum size of Ro (focus) is assumed to be half of the sine of the
   % pi/8 times the inner grid radius, Rgrid1
   maxsize=0.5*NewConfig(3)*sin(pi/8);
   %minsize=.003;   % implicit assumption that the focal diameter > 6mm
   NewConfig(1)= maxsize;  %minsize+rand*(maxsize-minsize);
   Ro = NewConfig(1);
```

PlotConfig2.m

% Energy evaluation function for simulated annealing design of multi-grid
% IEC fusion reactor experiment
% Carl Dietrich 5/29/05

% Input is an array
% Configuration = [Ro Rinjector Rgrid1 Rgrid2 Rgrid3 Rgrid4 Potgrid1 Potgrid2
% Potgrid3 Potgrid4];

% It is assumed that there are 8 longitude lines and 4 latitude lines of
% even spacing (45 degree separations), and that the 5th, outermost grid is
% grounded at a radius of 0.2 m.

```
function Energy = PlotConfig2(Configuration)
global rx pot_beam pot_prime_beam pot_dubprime_beam K inj_pot
e=1.602e-19;
epso=8.854e-12;
c=3e8;
% Input the desired grid structure:
r = [Configuration(3) Configuration(4) Configuration(5) Configuration(6) .25]; % grid
radius vector
if r(1)>r(2) | r(2)>r(3) | r(3)>r(4) | r(4)>r(5)
   disp('Invalid grid configuration!')
   Energy = 10000
   return
end
Voltagedesired = [Configuration(7) Configuration(8) Configuration(9) Configuration(10)
0];
n=max(size(Voltagedesired));
solidityfudgefactor = 2.75e-5;
for i=1:n-1
   deltaV(n-i) = -(Voltagedesired(n+1-i)-Voltagedesired(n-i));
   Qins(n-i) = solidityfudgefactor*4*pi*epso*deltaV(n-i)/(1/r(n-i)-1/r(n+1-i));
end
Qins(n)=Qins(n-1);
Qdesired(1)=Qins(1);
for i=2:n
   Qdesired(i) = Qins(i)-Qins(i-1);
end
q = Qdesired./r.^2;%[10.5e-8 -2.1e-7 7.5e-8 0];   % grid charge vector
t = 4;        % number of latitude wires
l = 8;        % number of longitude wires
thickness =.001;% wire thickness
kmax = 32;
mult = kmax/(2*l);
```

```
% Calculate coefficients:
%tic
[Abar, Bbar]=solve_coeff(r,q,t,l,thickness,mult);
%toc
%tic
phi = pi/2;
theta = 0;  %pi/l;
divs = 300;
dr = max(r)/divs;
rx=[0:dr:max(r)];

for i=1:(divs+1)
   if rx(i)<.01
      pot(i) = spherical_potential_norm_posm_bar(r,Abar,Bbar,.01,theta,phi);
   else
      pot(i) = spherical_potential_norm_posm_bar(r,Abar,Bbar,rx(i),theta,phi);
   end
end
edge_ground = -pot(divs+1);
pot = pot+edge_ground;

for i=1:(divs+1)
   if i==1
      pot_prime_wire(i)=0;
   elseif i==divs+1
      pot_prime_wire(i)=(pot(i)-pot(i-1))/dr;
   else
      pot_prime_wire(i)=((pot(i)-pot(i-1))/dr+(pot(i+1)-pot(i))/dr)/2;
   end
end
figure;
subplot(2,1,1);
plot(rx,pot,'b');
hold on;
theta = pi/l;
for i=1:(divs+1)
   if rx(i)<.01
      pot_beam(i) = spherical_potential_norm_posm_bar(r,Abar,Bbar,.01,theta,phi);
   else
      pot_beam(i) = spherical_potential_norm_posm_bar(r,Abar,Bbar,rx(i),theta,phi);
   end
end
pot_beam = pot_beam+edge_ground;
for i=1:(divs+1)
   if i==1
      pot_prime_beam(i)=0;
   elseif i==divs+1
      pot_prime_beam(i)=(pot_beam(i)-pot_beam(i-1))/dr;
```

```matlab
    else
        pot_prime_beam(i)=((pot_beam(i)-pot_beam(i-1))/dr+(pot_beam(i+1)-
pot_beam(i))/dr)/2;
    end
end

for i=1:(divs+1)
    if i==1
        pot_dubprime_beam(i) = 0;
    elseif i==divs+1
        pot_dubprime_beam(i)=(pot_prime_beam(i)-pot_prime_beam(i-1))/dr;
    else
        pot_dubprime_beam(i)=((pot_prime_beam(i)-pot_prime_beam(i-
1))/dr+(pot_prime_beam(i+1)-pot_prime_beam(i))/dr)/2;
    end
end
plot(rx,pot_beam,'r');
title('Potential v. radius');
legend('Theta = 0 (on grid)','Theta = pi/l (on beampath)');
xlabel('r(m)');
ylabel('Potential (V)');
drawnow;
%%%%%%%%%%%%%%%%%%%%%%%%%%%%%%%%
K=zeros(size(rx));
% Initial beam envelope conditions
Ro=Configuration(1);
r_inj = Configuration(2);
mi = 40*1.67e-27;   % Argon
inj_pot = spherical_potential_norm_posm_bar(r,Abar,Bbar,r_inj,pi/l,pi/2)+edge_ground;
inj_pot_dtheta =
spherical_potential_norm_posm_bar(r,Abar,Bbar,r_inj,pi/l+pi/1000,pi/2)+edge_ground;
dphidtheta=(inj_pot_dtheta-inj_pot)/(pi/1000);
if dphidtheta<0
    disp('Reflection region is defocussing => bad design')
    Energy = 10000
    return
end
vtherm=340;
Rprimeo=0;
Rprimefinal=0;
Rfinal = 0;
no=2e13;
YO = [Ro Rprimeo];
OPTIONS = ODESET('RelTol',1e-4,'AbsTol',1e-8);
for i=1:max(size(rx))
    vi(i)=sqrt(2*e*(abs(pot_beam(i)-inj_pot))/mi)+vtherm;
    gamma(i)= 1/sqrt(1-vi(i)^2/c^2);
    K(i)=e^2*no*Ro^2/(2*epso*mi*vi(i)^2*gamma(i)^3); % perveance
```

```
end
if max(isnan(K))
    disp('K is NaN!')
    Energy = 10000
    return
end
% X=0;
% Xback=0;
% maxR=0;
% imaxR=1;
% maxRback=0;
% imaxRback=1;
% acceptance = .8;
% while Rfinal<Ro & maxR<=acceptance*X(imaxR)*tan(pi/8)&
maxRback<=acceptance*Xback(imaxRback)*tan(pi/8)
%    no = 2*no;
%    K = K.*2;   % since perveance is proportional to density...
%    [X Y]=ode45('ode45beamfunc',[0 (r_inj-dr)],YO,OPTIONS);
%    [n m]=size(Y);
%    Roback = Y(n,1);
%    Rprimeback = Y(n,2);
%    [dphidx dphidy]=gradfield(r_inj-dr,pi/l+atan(Roback/(r_inj-
dr)),Abar,Bbar,r,edge_ground);
%    Omega = atan(dphidy/dphidx);
%    omega_one = atan(Rprimeback);
%    omega_two = 2*Omega - omega_one;
%    Rprimereturn = tan(omega_two);  % mirror reflection off of equipotential
%    [Xback Yback]=ode45('ode45beamfunc',[(r_inj-dr) 0],[Roback
Rprimereturn],OPTIONS);
%    [n m]=size(Yback);
%    Rfinal = Yback(n,1);
%    [maxR, imaxR]=max(Y(:,1));
%    [maxRback, imaxRback]=max(Yback(:,1));
% end
iter = 0;
maxiters = 30;
acceptance = .8;
while iter<maxiters % & beam envelope is inside acceptance window
    iter = iter+1;
    no = 1.1*no;
    K = K.*1.2;   % since perveance is proportional to density...
    [X Y]=ode45('ode45beamfunc',[0 (r_inj-dr)],YO,OPTIONS);
    [n m]=size(Y);
    [maxR, imaxR]=max(abs(Y(:,1)));
    %Checks:
    if (maxR > X(imaxR)*sin(pi/8)*acceptance & X(imaxR)>=r(1))
        break
    end
```

```matlab
   for ib=1:3
      if interp1(X, Y(:,1), r(ib)*cos(pi/8)) > acceptance*r(ib)*sin(pi/8)
         break
      end
   end
end
%toc
no = no
Ro = Ro
%Rprimefinal = Rprimefinal

normalizing_factor = (1e14)^2*(.01)^3;  % Approximate density and core size from 2D
OOPIC sims
Energy = normalizing_factor/(no^2*Ro^3) %*V_c^4)
if  max(max(isnan(Y)))
   disp('Warning: Solution NaN!')
   Energy = 10000
   return
end
if  min(Y(:,1))<0
   disp('Warning: beam envelope crosses R=0!')
   Energy = 10000
end
if max(imag(Y(:,1)))
   disp('Beam envelope has imaginary component!')
   Energy = 10000
end
if iter>=maxiters
   disp('Maximum number of iterations has been exceeded!')
   Energy = 10000
end


subplot(2,1,2);
plot(r_inj,0,'g*');
hold on;
plot(X,Y(:,1),'g');
%plot(Xback,Yback(:,1),'b');
for i=1:max(size(r))
   plot(r(i)*cos(pi/8),r(i)*sin(pi/8),'r*');
end
plot(rx.*cos(pi/8),rx.*sin(pi/8),'r');
labelone=sprintf('Gridline');
labeltwo = sprintf('Outward Beam Envelope for n_c=%3.2E m-3, r_o=%3.2E m',no,Ro);
%labelthree = sprintf('Inward Beam Envelope for n_o=%3.2E m-3, r_o=%3.2E
m',no*vi(1)/vtherm*(Ro/Roback)^2,Roback);
legend('Injection Point',labeltwo,labelone);
```

SAmodCarl.m

% Note: this code is based upon and nearly identical to SA.m developed by Prof. Olivier de Weck
function [xbest,Ebest,xhist]=SAmodCarl(xo,file_eval,file_perturb,options);
% [xbest,Ebest,xhist]=SA(xo,file_eval,file_perturb,options);
%
% Single Objective Simulated Annealing (SA) Algorithm
%
% This function is a generic implementation of the single objective
% Simulated Annealing (SA) algorithm first proposed by Kirkpatrick,
% Gelatt and Vecchi. The algorithm tries to improve upon an initial
% configuration, xo, by evaluating perturbed configurations. When the
% system reaches the "frozen" state, the algorithm stops and the best
% configuration and search history are returned. The user can choose
% from one of two cooling schedules: linear or exponential.
%
% Input:
% xo   initial configuration of the system (a row vector)
% file_eval   file name (character string) of configuration evaluator;
%   assumes that E='file_eval'(x) is a legitimate function
%   call; set up function such that (scalar) output E will be
%   minimized.
% file_perturb file name (character string) of configuration perturbator;
%   assumes that xp='fname_perturb'(x) is a legitimate function
%   call. This function creates a "neighboring" configuration.
% options   algorithm option flags. Uses defaults, [ ], if left blank
%   (1)   To - initial system temperature - automatically determined if
%   left blank ([]). To should be set such that the expression
%   exp(-E(xo)/To)>0.99 is true, i.e. the initial system is "melted"
%   (2)   Cooling Schedule: linear=1, exponential=[2]
%   (3)   dT Temp. increment, e.g. [dT=0.9] for exp. cooling Tk=dT^k*To,
%   abs. temperature increment for linear cooling (Tk+1=Tk-dT);
%   (4)   neq = equilibrium condition, e.g. number of rearrangements
%   attempted to reach equilibrium at a given temperature, neq=[5]
%   (5)   frozen condition - sets up SA exit criterion
%   nfrozen = non-integer, e.g. 0.1 SA interprets this numbers as Tmin,
%   the minimum temperature below which the system is frozen.
%   nfrozen = integer ,e.g. 1,2.. SA interprets this as # of successive
%   temperatures for which the number of desired acceptances defined
%   under options(4) is not achieved, default: nfrozen=[3]
%   (6)   set to 1 to display diagnostic messages (=[1])
%   (7)   set to 1 to plot progress during annealing (=[0])
%
% Output:
% xbest   Best configuration(s) found during execution - row vector(s)
% Ebest   Energy of best configuration(s) (lowest energy state(s) found)

```
% xhist      structure containing the convergence history
%   .iter    Iteration number (number of times file_eval was called)
%   .x       current configuration at that iteration
%   .E       current system energy at that iteration
%   .T       current system temperature at that iteration
%   .k       temperature step index k
%   .C       specific heat at the k-th temperature
%   .S       entropy at the the k-th temperature
%   .Tnow    temperature at the k-th temperature step
%
% User Manual (article):   SA.pdf
%
% Demos:       SAdemo0 - four atom placement problem
%              SAdemo1 - demo of SA on MATLAB peaks function
%              SAdemo2 - demo of SA for Travelling Salesman Problem (TSP)
%              SAdemo3 - demo of SA for structural topology optimization
%              SAdemo4 - demo of SA for telescope array placement problem
%
% dWo,(c)  MIT 2004
%
% Ref: Kirkpatrick, S., Gelatt Jr., C.D. and Vecchi, M.P., "Optimization
% by Simulated Annealing", Science, Vol. 220, Number 4598, pp. 671-680, May
% 1983

% dump file added by Carl Dietrich 6/1/05
dumpfilename = datestr(now,'mmm-dd-HHMM')
fid=fopen(dumpfilename,'w');
if fid==-1
   error = 'Unable to open dump file!'
end
%%%%

%check input
if ~isempty(options)
   To=options(1);
   schedule=options(2);
   dT=options(3);
   neq=options(4);
   nfrozen=options(5);
   diagnostics=options(6);
   plotflag=options(7);
else
   % set all options to default
   % To - set initial system temperature
   eval(['Eo=' file_eval '(xo);']);
   To=abs(-Eo/log(0.99));   % set initial temperature such that probablility of
   % accepting an inferior solution is initially equal to 0.99
   schedule=2;
```

```matlab
    dT=0.9;   % this is the ratio dT=(T_i+1/T_i) for geometrical cooling
    neq=5;   % number of rearrangements accepted at a given T
    nfrozen=3;  % if neq hasn't been reached at nfrozen successive
    % temperatures the system is considered frozen and the SA exits
    diagnostics=1; % display messages
    plotflag=0; %plot convergence
end
%
nmax=neq*round(sqrt(max(size(xo)))); % nmax - maximum number of steps at one
temperature, while
%                          trying to establish thermal equilibrium
%
if nfrozen==round(nfrozen)
    % nfrozen is integer - look for nfrozen successive temperatures without
    % neq acceptances
    Tmin=0;
else
    Tmin=nfrozen; nfrozen=3;
end




% Step 1 - Show initial configuration
if diagnostics==1
disp('Initial configuration: ')
xo
end

% Step 2 - Evaluate initial configuration
eval(['Eo=' file_eval '(xo);']);
counter=1;
xnow=xo; Enow=Eo; nnow=1;
xhist(nnow).iter=counter;

xhist(nnow).x=xo;
xhist(nnow).E=Enow;
xhist(nnow).T=To;
%  still need to add .S      current entropy at that iteration
xbest=xnow;
fprintf(fid,'%s \n',num2str(xbest));
Ebest=Enow;
Tnow=To;
if diagnostics==1
    disp(['Energy of initial configuration Eo: ' num2str(Eo)])
end

if plotflag
    figure(99)
```

```matlab
      semilogy(counter,Enow,'k*');    %plot(counter,Enow,'k*');
      hold on
      semilogy(counter,Enow,'mo')      %plot(counter,Enow,'mo')
      xlabel('Iteration Number')
      ylabel('System Energy')
      legend('current configuration','new best configuration')
      title('SA convergence history')
      lastbest=counter;
      drawnow
  end

  frozen=0;  % exit flag for SA
  naccept=1; % number of accepted configurations since last temperature change
  Tlast=1;   % counter index of last temperature change
  k=1;       % first temperature step
  ET=[];     % vector of energies at constant system temperature

  % start annealing
  while (frozen<nfrozen)&(Tnow>Tmin)

  %Step 3 - Perturb xnow to obtain a neighboring solution

  if diagnostics
      disp(['Counter: ' num2str(counter) ' Temp: ' num2str(Tnow) ' Perturbing
  configuration'])
  end

  eval(['xp=' file_perturb '(xnow);']);

  %Step 4 - Evaluate perturbed solution
  eval(['Ep=' file_eval '(xp);'])
  counter=counter+1;

  %Step 5 - Metropolis Step

  dE=Ep-Enow; % difference in system energy
  PdE=exp(-dE/Tnow);
  if diagnostics
      disp(['Counter: ' num2str(counter) ' Temp: ' num2str(Tnow) ' P(dE)= ' num2str(PdE)])
  end

  %Step 6 - Acceptance of new solution
  if dE<=0 % energy of perturbed solution is lower , automatically accept
      nnow=nnow+1;
      xnow=xp; Enow=Ep;
      xhist(nnow).iter=counter;
      xhist(nnow).x=xp;
      xhist(nnow).E=Ep;
```

```matlab
    xhist(nnow).T=Tnow;
    naccept=naccept+1;
   if diagnostics
   disp(['Counter: ' num2str(counter) ' Temp: ' num2str(Tnow)  ' Automatically accept
better configuration (downhill)'])
   end

else
   % energy of perturbed configuration is higher, but might still accept it
   randomnumber01=rand;
   if PdE>randomnumber01
     nnow=nnow+1;
     xnow=xp; Enow=Ep;
     xhist(nnow).iter=counter;
     xhist(nnow).x=xp;
     xhist(nnow).E=Ep;
     xhist(nnow).T=Tnow;
    if diagnostics
     disp(['Counter: ' num2str(counter) ' Temp: ' num2str(Tnow)  ' Accepted inferior
configuration (uphill)'])
     end

   else
      % keep current configuration
      xnow=xnow;
      Enow=Enow;
     if diagnostics
      disp(['Counter: ' num2str(counter) ' Temp: ' num2str(Tnow)  ' Kept the current
configuration'])
     end
   end
end
     ET=[ET; Enow];
     if plotflag
     figure(99)
     semilogy(counter,Enow,'k*'); %plot(counter,Enow,'k*');
     drawnow
     end


if Enow<Ebest
   % found a new 'best' configuration
   Ebestlast=Ebest;
   Ebest=Enow;
   xbest=xnow;
   fprintf(fid,'%s \n',num2str(xbest));
   if diagnostics
```

```matlab
        disp(['Counter: ' num2str(counter) ' Temp: ' num2str(Tnow)  ' This is a new best
configuration'])
    end
    if plotflag
      figure(99)
      semilogy(counter,Enow,'mo'); %plot(counter,Enow,'mo');
      semilogy([lastbest counter],[Ebestlast Enow],'m-');  %plot([lastbest
counter],[Ebestlast Enow],'m-');
      lastbest=counter;
      drawnow
    end
elseif Enow==Ebest
    same=0;
    for ib=1:size(xbest,1)
      if xbest(ib,:)==xnow
         if diagnostics
        disp(['Counter: ' num2str(counter) ' Temp: ' num2str(Tnow)  ' Found same best
configuration'])
         end
       same=1;
       end
    end

    if same ==0
      Ebestlast=Ebest;
      Ebest=Enow;
      xbest=[xbest ; xnow];
       if diagnostics
         disp(['Counter: ' num2str(counter) ' Temp: ' num2str(Tnow)  ' Found another best
configuration'])
       end
     if plotflag
      figure(99)
      semilogy(counter,Enow,'mo'); %plot(counter,Enow,'mo');
      semilogy([lastbest counter],[Ebestlast Enow],'m-');  %plot([lastbest
counter],[Ebestlast Enow],'m-');
      lastbest=counter;
      drawnow
     end
    end
end

%Step 7 - Adjust system temperature
Told=Tnow;
if (naccept<neq)&(counter-Tlast)<nmax
    if diagnostics
      disp(['Counter: ' num2str(counter) ' Temp: ' num2str(Tnow)  ' Need to reach
equilibrium at this temperature'])
```

```matlab
    end
    % continue at the same system temperature
elseif (naccept<neq)&(counter-Tlast)>=nmax
    if diagnostics
        disp(['Counter: ' num2str(counter) ' Temp: ' num2str(Tnow)  ' System nearly frozen'])
    end

    Eavg=mean(ET);
    Evar=mean(ET.^2);
    C=(Evar-Eavg^2)/Tnow^2;     % specific heat
    S=log(nmax*length(unique(ET))/length(ET));
    xhist(k).k=k;
    xhist(k).C=C;
    xhist(k).S=S;
    xhist(k).Tnow=Tnow;


    frozen=frozen+1;
    Tlast=counter;
    naccept=0;


    switch schedule
        case 1
            % linear cooling
            Tnow=Tnow-dT;
             if Tnow<0
                 frozen=nfrozen; %system temperature cannot go negative, exit
             end
        case 2
            % exponential cooling
             Tnow=dT*Tnow;
        case 3
             Tindex=Tindex+1;
             if Tindex>size(Tuser,1)
                 frozen=nfrozen; % have run through entire user supplied cooling schedule
             else
             Tnow=Tuser(Tindex,1);
             neq=Tuser(Tindex,2);
             end
        otherwise
             disp('Erroneous cooling schedule choice - option(2) - illegal')
    end


    k=k+1;

  if plotflag
```

```matlab
    figure(98)
    hist(ET); Nh=hist(ET); Nh=max(Nh);
    hold on
    semilogx([Eavg Eavg]',[0 Nh+1],'k--')   %plot([Eavg Eavg]',[0 Nh+1],'k--')
    text(Eavg, Nh+1, ['T=' num2str(Told,2)])
    xlabel('Energy')
    ylabel('Occurences')
    drawnow
 end
  ET=[];

 elseif (naccept==neq)
   if diagnostics
     disp(['Counter: ' num2str(counter) ' Temp: ' num2str(Tnow)  ' System reached
equilibrium'])
   end

   Eavg=mean(ET);
   Evar=mean(ET.^2);
   C=(Evar-Eavg^2)/Tnow^2;     % specific heat
   S=log(nmax*length(unique(ET))/length(ET));
   xhist(k).k=k;
   xhist(k).C=C;
   xhist(k).S=S;
   xhist(k).Tnow=Tnow;


   Tlast=counter;
   naccept=0;

   switch schedule
     case 1
       % linear cooling
       Tnow=Tnow-dT;
        if Tnow<0
           frozen=nfrozen; %system temperature cannot go negative, exit
        end
     case 2
       % exponential cooling
        Tnow=dT*Tnow;
     case 3
       % user supplied cooling
        Tindex=Tindex+1;
        if Tindex>size(Tuser,1)
           frozen=nfrozen; %have run through entire user supplied cooling schedule
        else
        Tnow=Tuser(Tindex,1);
        neq=Tuser(Tindex,2);
```

```
                end

            otherwise
                disp('Erroneous cooling schedule choice - option(2) - illegal')
        end


      k=k+1;

    if plotflag
        figure(98)
      hist(ET); Nh=hist(ET); Nh=max(Nh);
      hold on
      semilogx([Eavg Eavg]',[0 Nh+1],'k--')   %plot([Eavg Eavg]',[0 Nh+1],'k--')   %([Eavg
Eavg]',[0 Nh+1],'k--')
      text(Eavg, Nh+1, ['T=' num2str(Told,2)])
      xlabel('Energy')
      ylabel('Occurences')
      drawnow
    end

    ET=[];
   end

end %while (frozen<nfrozen)&(Tnow>tmin)

fprintf(fid,'%s \n',num2str(xbest));
fclose(fid);
% Reached end of SA
 if plotflag
      figure(97)
      k=k-1;
      for ind=1:k
        S(ind)=xhist(ind).S;
        C(ind)=xhist(ind).C;
        Tnow(ind)=xhist(ind).Tnow;
      end

        plot([1:k],C,'bo')
        hold on
        plot([1:k],S,'ms')
        plot([1:k],log(Tnow),'kd')
        legend('C-specific heat','S-entropy','ln(T)-temperature')
        xlabel('Temperature Step')
        title('Simulated Annealing Evolution')
        plot([1:k],C,'b-')
        plot([1:k],S,'m-')
        plot([1:k],log(Tnow),'k-')
```

```
        drawnow

    end

    if diagnostics
        disp(['Counter: ' num2str(counter) ' Temp: ' num2str(Tnow)  ' System frozen, SA
ended'])
        disp(['Best configuration: '])
        xbest
        disp(['Lowest System Energy: ' num2str(Ebest) ])
    end
```

Solve_coeff.m

% Matlab function to calculate the coefficients of the potential
% structure around multiple charged, concentric, spherical grids.
% Written by: Carl Dietrich, 8/6/04

% Inputs: r (radius vector of grids), q (charge/length on grids -- same size
% as r), t (number of latitude lines), l (number of longitude lines),
% acc (the accuracy needed -- typically .05). NOTE: the r vector must have
% increasing radii with index and the charges in q correspond to the
% respective r indices.
% thickness is the wire thickness
% mult = kmax/(2*l)
% Outputs: A and B are 3d matrices of the coefficients for phi.
% The first dimension specifies the region of validity in radius.
% There will be n+1 regions. The second dimension is k and the
% third dimension is m (2k+1). In the exact expression, k = inf
% but in this model k is truncated to a finite integer determined
% by the the required accuracy specified with the input 'acc'.

function [Abar, Bbar]=solve_coeff(r,q,t,l,thickness,mult)

kmax = 2*mult*l;
stddevs_per_wirethickness = 2;
numstddevs = 4; % 4 sigma = 0.9999366 of total

% Check inputs:
if size(r)~=size(q)
    error('Radius vector and charge vector must be the same length!');
end
if t<1
    error('There must be at least one latitude line!');
end
if l<2
    error('There must be at least two longitude lines!')
end
if min(r)<thickness
    error('Geometry error: wires too big!');
end
% Constants:
epso = 8.854e-12;
% Add in Ray's precalced integral:
load IPkm
% Find number of grids
n = max(size(r));
% Calc effective wire thickness
eff_thickness = numstddevs/stddevs_per_wirethickness*thickness; %pi/l*r(1)

```matlab
% Calculate number of standard deviations per numerical integration
%numstddevs = eff_thickness/thickness*stddevs_per_wirethickness
divs=8; %50 %50 %100 % divisions per guassian (divs per eff_wire_thickness)
% Initialize A and B
Abar = zeros(n+1,kmax+1,kmax+1);
Bbar = zeros(n+1,kmax+1,kmax+1);
RHS = zeros(n+1,kmax+1,kmax+1);
int = zeros(kmax+1,kmax+1);
%wait = waitbar(0,'Pre-calculating integrals for spherical potential solution...');

% Pre-Calc integral over phi for all k and m
for k=0:kmax
    %waitbar(k/kmax,wait);
    for m=0:k
        int(k+1,m+1) = IPkm(k+1,m+1);
    end
end
%close(wait);
%wait = waitbar(0,'Calculating coefficients for spherical potential solution...');
for b=1:n
    for k=0:kmax
        %waitbar(k/kmax*b/n,wait);
        %if k==0 | rem(k,2)==0   % assumes north-south symmetry
          for m = 0:k
            RHS(b,k+1,m+1) = 0;
            %%%%%%%%%%%%%%%%%%%%%%%%%%%%%%%%%%
            % loop over longitude lines:
            sumint=0;
            for j=1:l
                % sum of numerical integrals over cosmtheta
                inttwo=0;
                theta=2*pi*j/l-eff_thickness/r(b)/2;
                dtheta = eff_thickness/r(b)/divs;
                for i=1:divs
                    inttwo=inttwo+gsinc(theta-
2*pi*j/l,eff_thickness,r(b),numstddevs)*cos(m*theta)*dtheta;
                    theta=theta+dtheta;
                end
                sumint=sumint+inttwo;
            end
            RHS(b,k+1,m+1) = RHS(b,k+1,m+1)+int(k+1,m+1)*sumint;
            % Calculate right hand side sum over latitude lines if m = 0
            if m == 0
                sumint=0;
                for j=1:t
                    integ=0;
                    phi=pi*j/(t+1)-eff_thickness/r(b)/2;
                    dphi=eff_thickness/r(b)/divs;
```

```matlab
            for i=1:divs
                L=legendre(k,cos(phi),'norm');
                integ=integ+L(1)*gsinc(phi-
pi*j/(t+1),eff_thickness,r(b),numstddevs)*sin(phi)*dphi;
%legendre(0,cos(phi),'norm')*g(phi,thickness,r(b))*sin(phi)*dphi;
                phi=phi+dphi;
            end
            sumint=sumint+integ;
          end
          RHS(b,k+1,m+1) = RHS(b,k+1,m+1) + 2*pi*sumint;
        end

      end   % close m loop
     %end % close if k is even check
   end     % close k loop
end     % close b loop

for k=0:kmax
   for m=0:k
      % Calculate coefficients:
      Abar(n+1,k+1,m+1)=0;
      Bbar(1,k+1,m+1)=0;
      for i=1:n
        if i>1
          Abar(n+1-i,k+1,m+1)=Abar(n+1-i+1,k+1,m+1)*(r(n+1-i)/r(n+1-i+1))^(k) +
q(n+1-i)/thickness/(2*(2*k+1)*pi*epso)*RHS(n+1-i,k+1,m+1)*r(n+1-i); %r(n+1-i)^k
        else
          Abar(n+1-i,k+1,m+1)= q(n+1-i)/thickness/(2*(2*k+1)*pi*epso)*RHS(n+1-
i,k+1,m+1)*r(n+1-i);
        end
        if i<n
          Bbar(i+1,k+1,m+1)=(Bbar(i,k+1,m+1) +
q(i)/thickness/(2*(2*k+1)*pi*epso)*RHS(i,k+1,m+1)*r(i)) *(r(i)/r(i+1))^(k+1);
        else
          Bbar(i+1,k+1,m+1)=(Bbar(i,k+1,m+1) +
q(i)/thickness/(2*(2*k+1)*pi*epso)*RHS(i,k+1,m+1)*r(i));
        end
      end
   end
end
%close(wait);
```

spherical_potential_norm_posm_bar.m

```
% spherical_potential.m
%
% This is a Matlab function to calculate the potential at a given position
% described in spherical coordinates (r, theta, phi) where r is the radius,
% theta is the longitude angle (0-2*pi), and phi is the co-latitude (0-pi).
% Written by: Carl Dietrich 8/6/04

% Inputs: A and B are the coefficient matrices as calculated by the
% function 'phi_coefficients.m'. The other inputs are described above.

% Output: This function outputs the scalar electrostatic potential at the
% specified postition.

function pot = spherical_potential_norm_posm_bar(rvect,Abar,Bbar,r,theta,phi)
[nmag,kmag,mmag] = size(Abar);
n = nmag-1;
i=1;
if r>rvect(max(size(rvect)))
   i = max(size(rvect));
else
   while r>rvect(i)
      i=i+1;
   end
end


pot = 0;
for k = 0:(kmag-1)
   if k==0 | rem(k,2)==0     %only even ks contribute (assumes n-s symmetry)
      LP = legendre(k,cos(phi),'norm');
      for m = 0:k
          pot = pot+(Abar(i,k+1,m+1)*(r/rvect(i))^k+Bbar(i,k+1,m+1)*(r/rvect(i))^(-k-
1))*LP(m+1)*cos(m*theta); %/((-1)^m*sqrt((k+1)/2*factorial(k-m)/factorial(k+m)))
      end
   end
end
```

OOPIC Code

```
GridDiagnostics5.inp
{
GridDiagnostics4.inp -- turns off injection at low density and removes
absorbing injector
GridDiagnostics1.inp -- based on canofworms13b, removed other injectors
canofworms13b -- off axis argon injection at 3.2uA, nonabsorbing
injector
 canofworms5 mess with grid potentials (4 was shrunk size)
 canofworms3 move emitters in and to lower potential
 canofworms2 lower voltages for experiment, July 10, seems to work
 astalk11.inp   add a pihi diagnostic
 astalk9.inp  add in 3rd and 4th stalk
 astalk8.inp  add in 2nd stalk for other grids
 astalk7 addin a user-defined diagnostic
 astalk6 add in fourth grid
 astalk5 add in a third grid
 astalk4 add in a second grid
 astalk3 go back to ions
 astalk2  add a stalk and fix grid shift problem, also implement
electron injection
 alt9c  add additional anode grids near diagonals
 alt9b  turn off diagonal injection, add secondary conditions to dielec
regions
 alt9 use an 80 by 80 grid with electrodes on angles
 alt6 change this file for each case
 alt5  alternative grid config, begin initial matrix, base case, Aug.
26, 2003
 ver20 add in dielectric regions inside grid boxes
 ver19 alternate grid structure.....
 ver15 addi in other six grids, SHOWS AWESOME FOCUSING ABILITY
 ver14 add in second additional grid
 ver13 expand to a 40x40 grid, traditional IEC version
 ver6 add solid grids
 ver5 add pre-loaded ions
 ver4 add variables
 ver3 adopt quarter config,20x20
 ver2 adopt electroninduced ionization,verify reflections
 ver1 adapt plasma ignition for cylindrical IEC
}
Variables
{
 anode = 0 //anode wall potential in volts
 gridA = -7500 //trapping grid ptoential in volts
 gridB = -10000 //cathode grid potential in volts
 gridC = -5000 //pinching grid near cathode
 gridD = -2000 //pinching grid near anode
 //gridE = 4000 //pinching grid near anode

 curr = 20e-6    //gun currents in Amps
// idrift = 2e7    //electron injection velocity, to penetrate 100keV
field about 1 cm
 idrift = 3e2   // used for ion injection velocity  about 100 eV for D
secprob = .8       //1   //0
```

```
 wght = 1e5  //5e6   //particle weighting
 gdm = 1 //emitter cell size
 dem = 25 //diagonal emitter location
 oem = 35 //orthogonal emitter location
 dFAC = 0  //turn diagonal injection on or off
 oFAC = 1  //turn orthogonal injection on or off

 pulseduration = 1e-5 //2e-3  // ion gun pulse duration

 A1 = 10 //initial x-position of gridA
 A2 = 4  //initial y-position of gridA
 B1 = 15
 B2 = 6
 C1 = 20
 C2 = 8
 D1 = 27
 D2 = 11
 E1 = 30
 E2 = 12
 F1 = 37  //anode grid position
  F2 = 15
 G1 = 34  //additional anode grid segments
 G2 = 22
 H1 = 30  //additional anode grid segments
 H2 = 27


}
Region
{
Grid
{
 J = 80
 x1s = 0.0
 x1f = 0.4
 n1 = 1.0
 K = 80
 x2s = 0.0
 x2f = 0.4
 n2 = 1.0
 Geometry = 1
}
Control
{
 dt = 5.0E-9
 ElectrostaticFlag = 1
 BoltzmannFlag = 0
}
MCC
{
 gas = Ar    //H
 pressure = 3e-8 //3e-6
 eSpecies = electrons
 iSpecies = ions
 collisionFlag = 1
}
Species
{
```

```
        name = electrons
        m = 9.11E-31
        q = -1.6e-19
 particleLimit = 2e6
 collisionModel = 1
 supercycle = 50
}
Species
{
        name = ions
        m = 6.68e-26 // Argon
        q = 1.6e-19  // single ionization
 particleLimit = 2e6
 collisionModel = 2
}
//////////////////////////////////ION
GUN://////////////////////////////////////
EmitPort  //left emitter , vertical
{
 speciesName = ions
 j1 = 40-oem
 k1 = 40 - 2*gdm //37 //40 - gdm
 j2 = 40-oem
 k2 = 40 //38 //40 + gdm
 normal = 1

 I = curr*oFAC
 a1=1
 a0=0
 trise=0
 tpulse = pulseduration // cut off the injection after this much time
 tfall=0

 v1drift = idrift
 v2drift = 0
 np2c = wght
 Secondary
 {
  secondary = secprob
  secSpecies = ions
  iSpecies = ions
 }
}
// Now make sidewalls of ion gun:
Dielectric
{
 QuseFlag = 1
 j1 = 0
 k1 = 40
 j2 = 40 - oem
 k2 = 40
 normal = 1
}
Dielectric
{
 QuseFlag = 1
 j1 = 0
 k1 = 40 - 2*gdm
```

```
 j2 = 40 - oem
 k2 = 40 - 2*gdm
 normal = -1
}


/////////////////////////////////////////////
Stalk://///////////////////////////////

Dielectric  //left side of middle STALK
{
 QuseFlag = 0
 j1 = 38
 k1 = 0
 j2 = 39
 k2 = 0
 normal = 1
}
Dielectric  //right side of middleSTALK
{
 QuseFlag = 0
 j1 = 41
 k1 = 0
 j2 = 42
 k2 = 0
 normal = 1
}
Dielectric  //left side of 2nd STALK
{
 QuseFlag = 0
 j1 = 36
 k1 = 0
 j2 = 37
 k2 = 0
 normal = 1
}
Dielectric  //right side of 2nd STALK
{
 QuseFlag = 0
 j1 = 43
 k1 = 0
 j2 = 44
 k2 = 0
 normal = 1
}

Dielectric  //left side of 3rd STALK
{
 QuseFlag = 0
 j1 = 34
 k1 = 0
 j2 = 35
 k2 = 0
 normal = 1
}
Dielectric  //right side of 3rd STALK
{
 QuseFlag = 0
```

```
  j1 = 45
  k1 = 0
  j2 = 46
  k2 = 0
  normal = 1
 }
Dielectric  //left side of 4th STALK
 {
  QuseFlag = 0
  j1 = 32
  k1 = 0
  j2 = 33
  k2 = 0
  normal = 1
 }
Dielectric  //right side of 4th STALK
 {
  QuseFlag = 0
  j1 = 47
  k1 = 0
  j2 = 48
  k2 = 0
  normal = 1
 }
////////////////////////////////////////////////////
ANODE://////////////////////////
Equipotential  //Anode Walls
 {
  C = anode  //top wall
  Segment
   {
   j1 = 0
   k1 = 80
   j2 = 80
   k2 = 80
   normal = -1
   }
// Segment  //bottom wall
// {
// j1 = 0
// k1 = 0
// j2 = 80
// k2 = 0
// normal = 1
// }
  Segment  //bottom right wall     //must adjust for stalks
   {
   j1 = 0
   k1 = 0
   j2 = 32
   k2 = 0
   normal = 1
   }
  Segment  //bottom left wall  //must adjust for stalks
   {
   j1 = 48
   k1 = 0
   j2 = 80
```

```
k2 = 0
normal = 1
}

Segment  //left wall
{
j1 = 0
k1 = 0
j2 = 0
k2 = 80
normal = 1
}
Segment  //right wall-top
{
j1 = 80
k1 = 0
j2 = 80
k2 = 80
normal = -1
}

//  segments for anode grid 1
Segment  //top wall
{
j1 = 40 + F1
k1 = 40 + F2 + 1
j2 = 40 + F1 + 1
k2 = 40 + F2 + 1
normal = 1
}
Segment  //bottom wall
{
j1 = 40 + F1
k1 = 40 + F2
j2 = 40 + F1 + 1
k2 = 40 + F2
normal = -1
}
Segment //right wall
{
j1 = 40 + F1 + 1
k1 = 40 + F2
j2 = 40 + F1 + 1
k2 = 40 + F2 + 1
normal = 1
}
Segment // left wall
{
j1 = 40 + F1
k1 = 40 + F2
j2 = 40 + F1
k2 = 40 + F2 + 1
normal = -1
}

//  segments for anode grid 2
Segment  //top wall
{
```

172

```
j1 = 40 + F2
k1 = 40 + F1 + 1
j2 = 40 + F2 + 1
k2 = 40 + F1 + 1
normal = 1
}
Segment  //bottom wall
{
j1 = 40 + F2
k1 = 40 + F1
j2 = 40 + F2 + 1
k2 = 40 + F1
normal = -1
}
Segment //right wall
{
j1 = 40 + F2 + 1
k1 = 40 + F1
j2 = 40 + F2 + 1
k2 = 40 + F1 + 1
normal = 1
}
Segment // left wall
{
j1 = 40 + F2
k1 = 40 + F1
j2 = 40 + F2
k2 = 40 + F1 + 1
normal = -1
}

//  segments for anode grid 3
Segment  //top wall
{
j1 = 40 - F2
k1 = 40 + F1 + 1
j2 = 40 - F2 - 1
k2 = 40 + F1 + 1
normal = 1
}
Segment  //bottom wall
{
j1 = 40 - F2
k1 = 40 + F1
j2 = 40 - F2 - 1
k2 = 40 + F1
normal = -1
}
Segment //right wall
{
j1 = 40 - F2
k1 = 40 + F1
j2 = 40 - F2
k2 = 40 + F1 + 1
normal = 1
}
Segment // left wall
{
```

173

```
j1 = 40 - F2 - 1
k1 = 40 + F1
j2 = 40 - F2 - 1
k2 = 40 + F1 + 1
normal = -1
}

//  segments for anode grid 4
Segment  //top wall
{
j1 = 40 - F1
k1 = 40 + F2 + 1
j2 = 40 - F1 - 1
k2 = 40 + F2 + 1
normal = 1
}
Segment  //bottom wall
{
j1 = 40 - F1
k1 = 40 + F2
j2 = 40 - F1 - 1
k2 = 40 + F2
normal = -1
}
Segment //right wall
{
j1 = 40 - F1
k1 = 40 + F2
j2 = 40 - F1
k2 = 40 + F2 + 1
normal = 1
}
Segment // left wall
{
j1 = 40 - F1 - 1
k1 = 40 + F2
j2 = 40 - F1 - 1
k2 = 40 + F2 + 1
normal = -1
}
//  segments for anode grid 8
Segment  //top wall
{
j1 = 40 + F1
k1 = 40 - F2
j2 = 40 + F1 + 1
k2 = 40 - F2
normal = 1
}
Segment  //bottom wall
{
j1 = 40 + F1
k1 = 40 - F2 - 1
j2 = 40 + F1 + 1
k2 = 40 - F2 - 1
normal = -1
}
Segment //right wall
```

```
{
j1 = 40 + F1 + 1
k1 = 40 - F2
j2 = 40 + F1 + 1
k2 = 40 - F2 - 1
normal = 1
}
Segment // left wall
{
j1 = 40 + F1
k1 = 40 - F2
j2 = 40 + F1
k2 = 40 - F2 - 1
normal = -1
}

//  segments for anode grid 7
Segment  //top wall
{
j1 = 40 + F2
k1 = 40 - F1
j2 = 40 + F2 + 1
k2 = 40 - F1
normal = 1
}
Segment  //bottom wall
{
j1 = 40 + F2
k1 = 40 - F1 - 1
j2 = 40 + F2 + 1
k2 = 40 - F1 - 1
normal = -1
}
Segment //right wall
{
j1 = 40 + F2 + 1
k1 = 40 - F1
j2 = 40 + F2 + 1
k2 = 40 - F1 - 1
normal = 1
}
Segment // left wall
{
j1 = 40 + F2
k1 = 40 - F1
j2 = 40 + F2
k2 = 40 - F1 - 1
normal = -1
}

//  segments for anode grid 6
Segment  //top wall
{
j1 = 40 - F2
k1 = 40 - F1
j2 = 40 - F2 - 1
k2 = 40 - F1
normal = 1
```

```
}
Segment   //bottom wall
{
j1 = 40 - F2
k1 = 40 - F1 - 1
j2 = 40 - F2 - 1
k2 = 40 - F1 - 1
normal = -1
}
Segment //right wall
{
j1 = 40 - F2
k1 = 40 - F1
j2 = 40 - F2
k2 = 40 - F1 - 1
normal = 1
}
Segment // left wall
{
j1 = 40 - F2 - 1
k1 = 40 - F1
j2 = 40 - F2 - 1
k2 = 40 - F1 - 1
normal = -1
}

//  segments for anode grid 5
Segment   //top wall
{
j1 = 40 - F1
k1 = 40 - F2
j2 = 40 - F1 - 1
k2 = 40 - F2
normal = 1
}
Segment   //bottom wall
{
j1 = 40 - F1
k1 = 40 - F2 - 1
j2 = 40 - F1 - 1
k2 = 40 - F2 - 1
normal = -1
}
Segment //right wall
{
j1 = 40 - F1
k1 = 40 - F2
j2 = 40 - F1
k2 = 40 - F2 - 1
normal = 1
}
Segment // left wall
{
j1 = 40 - F1 -1
k1 = 40 - F2
j2 = 40 - F1 - 1
k2 = 40 - F2 - 1
normal = -1
```

```
}

//top right diagonal anode grid segments, 1-4
//  segments for anode grid G, top right lower
Segment  //top wall
{
j1 = 40 + G1
k1 = 40 + G2 + 1
j2 = 40 + G1 + 1
k2 = 40 + G2 + 1
normal = 1
}
Segment  //bottom wall
{
j1 = 40 + G1
k1 = 40 + G2
j2 = 40 + G1 + 1
k2 = 40 + G2
normal = -1
}
Segment //right wall
{
j1 = 40 + G1 + 1
k1 = 40 + G2
j2 = 40 + G1 + 1
k2 = 40 + G2 + 1
normal = 1
}
Segment // left wall
{
j1 = 40 + G1
k1 = 40 + G2
j2 = 40 + G1
k2 = 40 + G2 + 1
normal = -1
}
//  segments for anode grid G, top right upper
Segment  //top wall
{
j1 = 40 + G2
k1 = 40 + G1 + 1
j2 = 40 + G2 + 1
k2 = 40 + G1 + 1
normal = 1
}
Segment  //bottom wall
{
j1 = 40 + G2
k1 = 40 + G1
j2 = 40 + G2 + 1
k2 = 40 + G1
normal = -1
}
Segment //right wall
{
j1 = 40 + G2 + 1
k1 = 40 + G1
j2 = 40 + G2 + 1
```

```
k2 = 40 + G1 + 1
normal = 1
}
Segment // left wall
{
j1 = 40 + G2
k1 = 40 + G1
j2 = 40 + G2
k2 = 40 + G1 + 1
normal = -1
}
//  segments for anode grid H, top right lower
Segment  //top wall
{
j1 = 40 + H1
k1 = 40 + H2 + 1
j2 = 40 + H1 + 1
k2 = 40 + H2 + 1
normal = 1
}
Segment  //bottom wall
{
j1 = 40 + H1
k1 = 40 + H2
j2 = 40 + H1 + 1
k2 = 40 + H2
normal = -1
}
Segment //right wall
{
j1 = 40 + H1 + 1
k1 = 40 + H2
j2 = 40 + H1 + 1
k2 = 40 + H2 + 1
normal = 1
}
Segment // left wall
{
j1 = 40 + H1
k1 = 40 + H2
j2 = 40 + H1
k2 = 40 + H2 + 1
normal = -1
}
//  segments for anode grid H, top right upper
Segment  //top wall
{
j1 = 40 + H2
k1 = 40 + H1 + 1
j2 = 40 + H2 + 1
k2 = 40 + H1 + 1
normal = 1
}
Segment  //bottom wall
{
j1 = 40 + H2
k1 = 40 + H1
j2 = 40 + H2 + 1
```

```
k2 = 40 + H1
normal = -1
}
Segment //right wall
{
j1 = 40 + H2 + 1
k1 = 40 + H1
j2 = 40 + H2 + 1
k2 = 40 + H1 + 1
normal = 1
}
Segment // left wall
{
j1 = 40 + H2
k1 = 40 + H1
j2 = 40 + H2
k2 = 40 + H1 + 1
normal = -1
}

//top LEFT diagonal anode grid segments, 1-4
//  segments for anode grid G, top LEFT lower
Segment  //top wall
{
j1 = 40 - G1
k1 = 40 + G2 + 1
j2 = 40 - G1 - 1
k2 = 40 + G2 + 1
normal = 1
}
Segment  //bottom wall
{
j1 = 40 - G1
k1 = 40 + G2
j2 = 40 - G1 - 1
k2 = 40 + G2
normal = -1
}
Segment //right wall
{
j1 = 40 - G1 - 1
k1 = 40 + G2
j2 = 40 - G1 - 1
k2 = 40 + G2 + 1
normal = -1
}
Segment // left wall
{
j1 = 40 - G1
k1 = 40 + G2
j2 = 40 - G1
k2 = 40 + G2 + 1
normal = 1
}
//  segments for anode grid G, top LEFT upper
Segment  //top wall
{
j1 = 40 - G2
```

```
k1 = 40 + G1 + 1
j2 = 40 - G2 - 1
k2 = 40 + G1 + 1
normal = 1
}
Segment  //bottom wall
{
j1 = 40 - G2
k1 = 40 + G1
j2 = 40 - G2 - 1
k2 = 40 + G1
normal = -1
}
Segment //right wall
{
j1 = 40 - G2 - 1
k1 = 40 + G1
j2 = 40 - G2 - 1
k2 = 40 + G1 + 1
normal = -1
}
Segment // left wall
{
j1 = 40 - G2
k1 = 40 + G1
j2 = 40 - G2
k2 = 40 + G1 + 1
normal = 1
}
//  segments for anode grid H, top LEFT lower
Segment  //top wall
{
j1 = 40 - H1
k1 = 40 + H2 + 1
j2 = 40 - H1 - 1
k2 = 40 + H2 + 1
normal = 1
}
Segment  //bottom wall
{
j1 = 40 - H1
k1 = 40 + H2
j2 = 40 - H1 - 1
k2 = 40 + H2
normal = -1
}
Segment //right wall
{
j1 = 40 - H1 - 1
k1 = 40 + H2
j2 = 40 - H1 - 1
k2 = 40 + H2 + 1
normal = -1
}
Segment // left wall
{
j1 = 40 - H1
k1 = 40 + H2
```

180

```
j2 = 40 - H1
k2 = 40 + H2 + 1
normal = 1
}
//  segments for anode grid H, top LEFT upper
Segment  //top wall
{
j1 = 40 - H2
k1 = 40 + H1 + 1
j2 = 40 - H2 - 1
k2 = 40 + H1 + 1
normal = 1
}
Segment  //bottom wall
{
j1 = 40 - H2
k1 = 40 + H1
j2 = 40 - H2 - 1
k2 = 40 + H1
normal = -1
}
Segment //right wall
{
j1 = 40 - H2 - 1
k1 = 40 + H1
j2 = 40 - H2 - 1
k2 = 40 + H1 + 1
normal = -1
}
Segment // left wall
{
j1 = 40 - H2
k1 = 40 + H1
j2 = 40 - H2
k2 = 40 + H1 + 1
normal = 1
}


//  segments for anode grid G, BOTTOM right lower
Segment  //top wall
{
j1 = 40 + G1
k1 = 40 - G2 - 1
j2 = 40 + G1 + 1
k2 = 40 - G2 - 1
normal = -1
}
Segment  //bottom wall
{
j1 = 40 + G1
k1 = 40 - G2
j2 = 40 + G1 + 1
k2 = 40 - G2
normal = 1
}
Segment //right wall
{
```

```
j1 = 40 + G1 + 1
k1 = 40 - G2
j2 = 40 + G1 + 1
k2 = 40 - G2 - 1
normal = 1
}
Segment // left wall
{
j1 = 40 + G1
k1 = 40 - G2
j2 = 40 + G1
k2 = 40 - G2 - 1
normal = -1
}
//  segments for anode grid G, BOTTOM right upper
Segment  //top wall
{
j1 = 40 + G2
k1 = 40 - G1 - 1
j2 = 40 + G2 + 1
k2 = 40 - G1 - 1
normal = -1
}
Segment  //bottom wall
{
j1 = 40 + G2
k1 = 40 - G1
j2 = 40 + G2 + 1
k2 = 40 - G1
normal = 1
}
Segment //right wall
{
j1 = 40 + G2 + 1
k1 = 40 - G1
j2 = 40 + G2 + 1
k2 = 40 - G1 - 1
normal = 1
}
Segment // left wall
{
j1 = 40 + G2
k1 = 40 - G1
j2 = 40 + G2
k2 = 40 - G1 - 1
normal = -1
}
//  segments for anode grid H, BOTTOM right lower
Segment  //top wall
{
j1 = 40 + H1
k1 = 40 - H2 - 1
j2 = 40 + H1 + 1
k2 = 40 - H2 - 1
normal = -1
}
Segment  //bottom wall
{
```

```
j1 = 40 + H1
k1 = 40 - H2
j2 = 40 + H1 + 1
k2 = 40 - H2
normal = 1
}
Segment //right wall
{
j1 = 40 + H1 + 1
k1 = 40 - H2
j2 = 40 + H1 + 1
k2 = 40 - H2 - 1
normal = 1
}
Segment // left wall
{
j1 = 40 + H1
k1 = 40 - H2
j2 = 40 + H1
k2 = 40 - H2 - 1
normal = -1
}
//  segments for anode grid H, BOTTOM right upper
Segment  //top wall
{
j1 = 40 + H2
k1 = 40 - H1 - 1
j2 = 40 + H2 + 1
k2 = 40 - H1 - 1
normal = -1
}
Segment  //bottom wall
{
j1 = 40 + H2
k1 = 40 - H1
j2 = 40 + H2 + 1
k2 = 40 - H1
normal = 1
}
Segment //right wall
{
j1 = 40 + H2 + 1
k1 = 40 - H1
j2 = 40 + H2 + 1
k2 = 40 - H1 - 1
normal = 1
}
Segment // left wall
{
j1 = 40 + H2
k1 = 40 - H1
j2 = 40 + H2
k2 = 40 - H1 - 1
normal = -1
}
```

```
//BOTTOM LEFT diagonal anode grid segments, 1-4
//  segments for anode grid G, BOTTOM LEFT lower
Segment  //top wall
{
j1 = 40 - G1
k1 = 40 - G2 - 1
j2 = 40 - G1 - 1
k2 = 40 - G2 - 1
normal = -1
}
Segment  //bottom wall
{
j1 = 40 - G1
k1 = 40 - G2
j2 = 40 - G1 - 1
k2 = 40 - G2
normal = 1
}
Segment //right wall
{
j1 = 40 - G1 - 1
k1 = 40 - G2
j2 = 40 - G1 - 1
k2 = 40 - G2 - 1
normal = -1
}
Segment // left wall
{
j1 = 40 - G1
k1 = 40 - G2
j2 = 40 - G1
k2 = 40 - G2 - 1
normal = 1
}
//  segments for anode grid G, BOTTOM LEFT upper
Segment  //top wall
{
j1 = 40 - G2
k1 = 40 - G1 - 1
j2 = 40 - G2 - 1
k2 = 40 - G1 - 1
normal = -1
}
Segment  //bottom wall
{
j1 = 40 - G2
k1 = 40 - G1
j2 = 40 - G2 - 1
k2 = 40 - G1
normal = 1
}
Segment //right wall
{
j1 = 40 - G2 - 1
k1 = 40 - G1
j2 = 40 - G2 - 1
k2 = 40 - G1 - 1
normal = -1
```

```
}
Segment // left wall
{
j1 = 40 - G2
k1 = 40 - G1
j2 = 40 - G2
k2 = 40 - G1 - 1
normal = 1
}
//  segments for anode grid H, BOTTOM LEFT lower
Segment  //top wall
{
j1 = 40 - H1
k1 = 40 - H2 - 1
j2 = 40 - H1 - 1
k2 = 40 - H2 - 1
normal = -1
}
Segment  //bottom wall
{
j1 = 40 - H1
k1 = 40 - H2
j2 = 40 - H1 - 1
k2 = 40 - H2
normal = 1
}
Segment //right wall
{
j1 = 40 - H1 - 1
k1 = 40 - H2
j2 = 40 - H1 - 1
k2 = 40 - H2 - 1
normal = -1
}
Segment // left wall
{
j1 = 40 - H1
k1 = 40 - H2
j2 = 40 - H1
k2 = 40 - H2 - 1
normal = 1
}
//  segments for anode grid H, BOTTOM LEFT upper
Segment  //top wall
{
j1 = 40 - H2
k1 = 40 - H1 - 1
j2 = 40 - H2 - 1
k2 = 40 - H1 - 1
normal = -1
}
Segment  //bottom wall
{
j1 = 40 - H2
k1 = 40 - H1
j2 = 40 - H2 - 1
k2 = 40 - H1
normal = 1
```

```
}
Segment //right wall
{
j1 = 40 - H2 - 1
k1 = 40 - H1
j2 = 40 - H2 - 1
k2 = 40 - H1 - 1
normal = -1
}
Segment // left wall
{
j1 = 40 - H2
k1 = 40 - H1
j2 = 40 - H2
k2 = 40 - H1 - 1
normal = 1
}

}

///////////////////////////////// End of ANODE: Start Grid
A//////////////////////

Equipotential  //gridA
{
 C = gridA
 Secondary
 {
  secondary = 1
  secSpecies = electrons
  iSpecies = ions
 }
 //grid 1
 Segment  //top 1
{
j1 = 40 + A1
k1 = 40 + A2 + 1
j2 = 40 + A1 + 1
k2 = 40 + A2 + 1
normal = 1
}
Segment  //bottom 1
{
j1 = 40 + A1
k1 = 40 + A2
j2 = 40 + A1 + 1
k2 = 40 + A2
normal = -1
}
Segment //right 1
{
j1 = 40 + A1 + 1
k1 = 40 + A2
j2 = 40 + A1 + 1
k2 = 40 + A2 + 1
normal = 1
}
```

```
Segment // left 1
{
j1 = 40 + A1
k1 = 40 + A2
j2 = 40 + A1
k2 = 40 + A2 + 1
normal = -1
}
//grid 2
Segment  //top 1
{
j1 = 40 + A2
k1 = 40 + A1 + 1
j2 = 40 + A2 + 1
k2 = 40 + A1 + 1
normal = 1
}
     Segment  //bottom 1
     {
     j1 = 40 + A2
     k1 = 40 + A1
     j2 = 40 + A2 + 1
     k2 = 40 + A1
     normal = -1
     }
     Segment //right 1
     {
     j1 = 40 + A2 + 1
     k1 = 40 + A1
     j2 = 40 + A2 + 1
     k2 = 40 + A1 + 1
     normal = 1
     }
     Segment // left 1
     {
     j1 = 40 + A2
     k1 = 40 + A1
     j2 = 40 + A2
     k2 = 40 + A1 + 1
     normal = -1
     }
     //grid 4
     Segment  //top 1
     {
     j1 = 40 - A1
     k1 = 40 + A2 + 1
     j2 = 40 - A1 - 1
     k2 = 40 + A2 + 1
     normal = 1
     }
     Segment  //bottom 1
     {
     j1 = 40 - A1
     k1 = 40 + A2
     j2 = 40 - A1 - 1
     k2 = 40 + A2
     normal = -1
     }
```

```
Segment //right 1
{
j1 = 40 - A1
k1 = 40 + A2
j2 = 40 - A1
k2 = 40 + A2 + 1
normal = 1
}
Segment // left 1
{
j1 = 40 - A1 - 1
k1 = 40 + A2
j2 = 40 - A1 - 1
k2 = 40 + A2 + 1
normal = -1
}
//grid 3
Segment  //top 1
{
j1 = 40 - A2
k1 = 40 + A1 + 1
j2 = 40 - A2 - 1
k2 = 40 + A1 + 1
normal = 1
}
Segment  //bottom 1
{
j1 = 40 - A2
k1 = 40 + A1
j2 = 40 - A2 - 1
k2 = 40 + A1
normal = -1
}
Segment //right 1
{
j1 = 40 - A2
k1 = 40 + A1
j2 = 40 - A2
k2 = 40 + A1 + 1
normal = 1
}
Segment // left 1
{
j1 = 40 - A2 -1
k1 = 40 + A1
j2 = 40 - A2 -1
k2 = 40 + A1 + 1
normal = -1
}
//grid 8
Segment  //top 1
{
j1 = 40 + A1
k1 = 40 - A2
j2 = 40 + A1 + 1
k2 = 40 - A2
normal = 1
}
```

```
        Segment  //bottom 1
        {
        j1 = 40 + A1
        k1 = 40 - A2 - 1
        j2 = 40 + A1 + 1
        k2 = 40 - A2 - 1
        normal = -1
        }
        Segment //right 1
        {
        j1 = 40 + A1 + 1
        k1 = 40 - A2
        j2 = 40 + A1 + 1
        k2 = 40 - A2 - 1
        normal = 1
        }
        Segment // left 1
        {
        j1 = 40 + A1
        k1 = 40 - A2
        j2 = 40 + A1
        k2 = 40 - A2 - 1
        normal = -1
        }
        //grid 7
        Segment  //top 1
        {
        j1 = 40
        k1 = 40 - A1
        j2 = 40 + A2 + 1
        k2 = 40 - A1
        normal = 1
        }
        Segment  //bottom 1
        {
        j1 = 41
        k1 = 40 - A1 - 1
        j2 = 40 + A2 + 1
        k2 = 40 - A1 - 1
        normal = -1
        }
        Segment //right 1
        {
        j1 = 40 + A2 + 1
        k1 = 40 - A1
        j2 = 40 + A2 + 1
        k2 = 40 - A1 - 1
        normal = 1
        }
//      Segment // left 1
//      {
//      j1 = 40 + A2
//      k1 = 40 - A1
//      j2 = 40 + A2
//      k2 = 40 - A1 + 1
//      normal = -1
//      }
        //grid 5
```

```
        Segment  //top 1
        {
        j1 = 40 - A1
        k1 = 40 - A2
        j2 = 40 - A1 - 1
        k2 = 40 - A2
        normal = 1
        }
        Segment  //bottom 1
        {
        j1 = 40 - A1
        k1 = 40 - A2 -1
        j2 = 40 - A1 - 1
        k2 = 40 - A2 -1
        normal = -1
        }
        Segment //right 1
        {
        j1 = 40 - A1
        k1 = 40 - A2
        j2 = 40 - A1
        k2 = 40 - A2 - 1
        normal = 1
        }
        Segment // left 1
        {
        j1 = 40 - A1 -1
        k1 = 40 - A2
        j2 = 40 - A1 -1
        k2 = 40 - A2 - 1
        normal = -1
        }
        //grid 6
        Segment  //top 1
        {
        j1 = 40
        k1 = 40 - A1
        j2 = 40 - A2 - 1
        k2 = 40 - A1
        normal = 1
        }
        Segment  //bottom 1
        {
        j1 = 39
        k1 = 40 - A1 - 1
        j2 = 40 - A2 - 1
        k2 = 40 - A1 - 1
        normal = -1
        }
//      Segment //right 1
//      {
//      j1 = 40 - A2 + 1
//      k1 = 40 - A1
//      j2 = 40 - A2 + 1
//      k2 = 40 - A1 + 1
//      normal = 1
//      }
        Segment // left 1
```

```
        {
        j1 = 40 - A2 - 1
        k1 = 40 - A1
        j2 = 40 - A2 - 1
        k2 = 40 - A1 - 1
        normal = -1
        }

//add stalk region

        Segment // left stalk
        {
        j1 = 39
        k1 = 0
        j2 = 39
        k2 = 40 - A1 - 1
        normal = -1
        }

        Segment // right stalk
        {
        j1 = 41
        k1 = 0
        j2 = 41
        k2 = 40 - A1 - 1
        normal = 1
        }

        Segment // bottom stalk
        {
        j1 = 39
        k1 = 0
        j2 = 41
        k2 = 0
        normal = 1
        }

}

///////////////////////////////End of grid A: Start Grid
B://///////////////////
// grid B

Equipotential  //gridB
{
        C = gridB
        Secondary
        {
                secondary = 1
                secSpecies = electrons
                iSpecies = ions
        }
        //grid 1
        Segment  //top 1
        {
        j1 = 40 + B1
        k1 = 40 + B2 + 1
        j2 = 40 + B1 + 1
```

```
k2 = 40 + B2 + 1
normal = 1
}
Segment  //bottom 1
{
j1 = 40 + B1
k1 = 40 + B2
j2 = 40 + B1 + 1
k2 = 40 + B2
normal = -1
}
Segment //right 1
{
j1 = 40 + B1 + 1
k1 = 40 + B2
j2 = 40 + B1 + 1
k2 = 40 + B2 + 1
normal = 1
}
Segment // left 1
{
j1 = 40 + B1
k1 = 40 + B2
j2 = 40 + B1
k2 = 40 + B2 + 1
normal = -1
}
//grid 2
Segment  //top 1
{
j1 = 40 + B2
k1 = 40 + B1 + 1
j2 = 40 + B2 + 1
k2 = 40 + B1 + 1
normal = 1
}
Segment  //bottom 1
{
j1 = 40 + B2
k1 = 40 + B1
j2 = 40 + B2 + 1
k2 = 40 + B1
normal = -1
}
Segment //right 1
{
j1 = 40 + B2 + 1
k1 = 40 + B1
j2 = 40 + B2 + 1
k2 = 40 + B1 + 1
normal = 1
}
Segment // left 1
{
j1 = 40 + B2
k1 = 40 + B1
j2 = 40 + B2
k2 = 40 + B1 + 1
```

```
normal = -1
}
//grid 4
Segment  //top 1
{
j1 = 40 - B1
k1 = 40 + B2 + 1
j2 = 40 - B1 - 1
k2 = 40 + B2 + 1
normal = 1
}
Segment  //bottom 1
{
j1 = 40 - B1
k1 = 40 + B2
j2 = 40 - B1 - 1
k2 = 40 + B2
normal = -1
}
Segment //right 1
{
j1 = 40 - B1
k1 = 40 + B2
j2 = 40 - B1
k2 = 40 + B2 + 1
normal = 1
}
Segment // left 1
{
j1 = 40 - B1 - 1
k1 = 40 + B2
j2 = 40 - B1 - 1
k2 = 40 + B2 + 1
normal = -1
}
//grid 3
Segment  //top 1
{
j1 = 40 - B2
k1 = 40 + B1 + 1
j2 = 40 - B2 - 1
k2 = 40 + B1 + 1
normal = 1
}
Segment  //bottom 1
{
j1 = 40 - B2
k1 = 40 + B1
j2 = 40 - B2 - 1
k2 = 40 + B1
normal = -1
}
Segment //right 1
{
j1 = 40 - B2
k1 = 40 + B1
j2 = 40 - B2
k2 = 40 + B1 + 1
```

```
normal = 1
}
Segment // left 1
{
j1 = 40 - B2 -1
k1 = 40 + B1
j2 = 40 - B2 -1
k2 = 40 + B1 + 1
normal = -1
}
//grid 8
Segment  //top 1
{
j1 = 40 + B1
k1 = 40 - B2
j2 = 40 + B1 + 1
k2 = 40 - B2
normal = 1
}
Segment  //bottom 1
{
j1 = 40 + B1
k1 = 40 - B2 - 1
j2 = 40 + B1 + 1
k2 = 40 - B2 - 1
normal = -1
}
Segment //right 1
{
j1 = 40 + B1 + 1
k1 = 40 - B2
j2 = 40 + B1 + 1
k2 = 40 - B2 - 1
normal = 1
}
Segment // left 1
{
j1 = 40 + B1
k1 = 40 - B2
j2 = 40 + B1
k2 = 40 - B2 - 1
normal = -1
}
//grid 7
Segment  //top 1
{
j1 = 40 + B2
k1 = 40 - B1
j2 = 40 + B2 + 1
k2 = 40 - B1
normal = 1
}
Segment  //bottom 1
{
j1 = 40 + B2
k1 = 40 - B1 - 1
j2 = 40 + B2 + 1
k2 = 40 - B1 - 1
```

```
        normal = -1
        }
        Segment //right 1
        {
        j1 = 40 + B2 + 1
        k1 = 40 - B1
        j2 = 40 + B2 + 1
        k2 = 40 - B1 - 1
        normal = 1
        }
//      Segment // left 1      //comment out for stalk
//      {
//      j1 = 40 + B2
//      k1 = 40 - B1
//      j2 = 40 + B2
//      k2 = 40 - B1 - 1
//      normal = -1
//      }
        //grid 5
        Segment  //top 1
        {
        j1 = 40 - B1
        k1 = 40 - B2
        j2 = 40 - B1 - 1
        k2 = 40 - B2
        normal = 1
        }
        Segment  //bottom 1
        {
        j1 = 40 - B1
        k1 = 40 - B2 -1
        j2 = 40 - B1 - 1
        k2 = 40 - B2 -1
        normal = -1
        }
        Segment //right 1
        {
        j1 = 40 - B1
        k1 = 40 - B2
        j2 = 40 - B1
        k2 = 40 - B2 - 1
        normal = 1
        }
        Segment // left 1
        {
        j1 = 40 - B1 -1
        k1 = 40 - B2
        j2 = 40 - B1 -1
        k2 = 40 - B2 - 1
        normal = -1
        }
        //grid 6
        Segment  //top 1
        {
        j1 = 40 - B2
        k1 = 40 - B1
        j2 = 40 - B2 - 1
        k2 = 40 - B1
```

195

```
        normal = 1
        }
        Segment  //bottom 1
        {
        j1 = 40 - B2
        k1 = 40 - B1 - 1
        j2 = 40 - B2 - 1
        k2 = 40 - B1 - 1
        normal = -1
        }
//      Segment //right 1      //comment out for stalk
//      {
//      j1 = 40 - B2
//      k1 = 40 - B1
//      j2 = 40 - B2
//      k2 = 40 - B1 - 1
//      normal = 1
//      }
        Segment // left 1
        {
        j1 = 40 - B2 - 1
        k1 = 40 - B1
        j2 = 40 - B2 - 1
        k2 = 40 - B1 - 1
        normal = -1
        }

//add B-stalk regions
        Segment // right top
        {
        j1 = 42
        k1 = 40 - B1
        j2 = 40 + B2
        k2 = 40 - B1
        normal = 1
        }
        Segment // right bottom
        {
        j1 = 43
        k1 = 40 - B1 - 1
        j2 = 40 + B2
        k2 = 40 - B1 - 1
        normal = -1
        }
        Segment // right right
        {
        j1 = 43
        k1 = 0
        j2 = 43
        k2 = 40 - B1 - 1
        normal = 1
        }
        Segment // right left
        {
        j1 = 42
        k1 = 0
        j2 = 42
        k2 = 40 - B1
```

```
normal = -1
}
Segment // right bottom
{
j1 = 42
k1 = 0
j2 = 43
k2 = 0
normal = 1
}
Segment // left top
{
j1 = 40 - B2
k1 = 40 - B1
j2 = 38
k2 = 40 - B1
normal = 1
}
Segment // left bottom
{
j1 = 40 - B2
k1 = 40 - B1 - 1
j2 = 37
k2 = 40 - B1 - 1
normal = -1
}
Segment // left right
{
j1 = 38
k1 = 0
j2 = 38
k2 = 40 - B1
normal = 1
}
Segment // left left
{
j1 = 37
k1 = 0
j2 = 37
k2 = 40 - B1 - 1
normal = -1
}
Segment // left bottom
{
j1 = 37
k1 = 0
j2 = 38
k2 = 0
normal = 1
}


}

//end of grid B
/////////////////////////////////End of grid B: Start grid
C://///////////////////////
```

```
// grid C

Equipotential  //gridC
{
      C = gridC
      Secondary
      {
            secondary = 1
            secSpecies = electrons
            iSpecies = ions
      }
      //grid 1
      Segment  //top 1
      {
      j1 = 40 + C1
      k1 = 40 + C2 + 1
      j2 = 40 + C1 + 1
      k2 = 40 + C2 + 1
      normal = 1
      }
      Segment  //bottom 1
      {
      j1 = 40 + C1
      k1 = 40 + C2
      j2 = 40 + C1 + 1
      k2 = 40 + C2
      normal = -1
      }
      Segment //right 1
      {
      j1 = 40 + C1 + 1
      k1 = 40 + C2
      j2 = 40 + C1 + 1
      k2 = 40 + C2 + 1
      normal = 1
      }
      Segment // left 1
      {
      j1 = 40 + C1
      k1 = 40 + C2
      j2 = 40 + C1
      k2 = 40 + C2 + 1
      normal = -1
      }
      //grid 2
      Segment  //top 1
      {
      j1 = 40 + C2
      k1 = 40 + C1 + 1
      j2 = 40 + C2 + 1
      k2 = 40 + C1 + 1
      normal = 1
      }
      Segment  //bottom 1
      {
      j1 = 40 + C2
      k1 = 40 + C1
```

```
j2 = 40 + C2 + 1
k2 = 40 + C1
normal = -1
}
Segment //right 1
{
j1 = 40 + C2 + 1
k1 = 40 + C1
j2 = 40 + C2 + 1
k2 = 40 + C1 + 1
normal = 1
}
Segment // left 1
{
j1 = 40 + C2
k1 = 40 + C1
j2 = 40 + C2
k2 = 40 + C1 + 1
normal = -1
}
//grid 4
Segment  //top 1
{
j1 = 40 - C1
k1 = 40 + C2 + 1
j2 = 40 - C1 - 1
k2 = 40 + C2 + 1
normal = 1
}
Segment  //bottom 1
{
j1 = 40 - C1
k1 = 40 + C2
j2 = 40 - C1 - 1
k2 = 40 + C2
normal = -1
}
Segment //right 1
{
j1 = 40 - C1
k1 = 40 + C2
j2 = 40 - C1
k2 = 40 + C2 + 1
normal = 1
}
Segment // left 1
{
j1 = 40 - C1 - 1
k1 = 40 + C2
j2 = 40 - C1 - 1
k2 = 40 + C2 + 1
normal = -1
}
//grid 3
Segment  //top 1
{
j1 = 40 - C2
k1 = 40 + C1 + 1
```

```
j2 = 40 - C2 - 1
k2 = 40 + C1 + 1
normal = 1
}
Segment  //bottom 1
{
j1 = 40 - C2
k1 = 40 + C1
j2 = 40 - C2 - 1
k2 = 40 + C1
normal = -1
}
Segment //right 1
{
j1 = 40 - C2
k1 = 40 + C1
j2 = 40 - C2
k2 = 40 + C1 + 1
normal = 1
}
Segment // left 1
{
j1 = 40 - C2 -1
k1 = 40 + C1
j2 = 40 - C2 -1
k2 = 40 + C1 + 1
normal = -1
}
//grid 8
Segment  //top 1
{
j1 = 40 + C1
k1 = 40 - C2
j2 = 40 + C1 + 1
k2 = 40 - C2
normal = 1
}
Segment  //bottom 1
{
j1 = 40 + C1
k1 = 40 - C2 - 1
j2 = 40 + C1 + 1
k2 = 40 - C2 - 1
normal = -1
}
Segment //right 1
{
j1 = 40 + C1 + 1
k1 = 40 - C2
j2 = 40 + C1 + 1
k2 = 40 - C2 - 1
normal = 1
}
Segment // left 1
{
j1 = 40 + C1
k1 = 40 - C2
j2 = 40 + C1
```

```
        k2 = 40 - C2 - 1
        normal = -1
        }
        //grid 7
        Segment  //top 1
        {
        j1 = 40 + C2
        k1 = 40 - C1
        j2 = 40 + C2 + 1
        k2 = 40 - C1
        normal = 1
        }
        Segment  //bottom 1
        {
        j1 = 40 + C2
        k1 = 40 - C1 - 1
        j2 = 40 + C2 + 1
        k2 = 40 - C1 - 1
        normal = -1
        }
        Segment //right 1
        {
        j1 = 40 + C2 + 1
        k1 = 40 - C1
        j2 = 40 + C2 + 1
        k2 = 40 - C1 - 1
        normal = 1
        }
//      Segment // left 1
//      {
//      j1 = 40 + C2
//      k1 = 40 - C1
//      j2 = 40 + C2
//      k2 = 40 - C1 - 1
//      normal = -1
//      }
        //grid 5
        Segment  //top 1
        {
        j1 = 40 - C1
        k1 = 40 - C2
        j2 = 40 - C1 - 1
        k2 = 40 - C2
        normal = 1
        }
        Segment  //bottom 1
        {
        j1 = 40 - C1
        k1 = 40 - C2 -1
        j2 = 40 - C1 - 1
        k2 = 40 - C2 -1
        normal = -1
        }
        Segment //right 1
        {
        j1 = 40 - C1
        k1 = 40 - C2
        j2 = 40 - C1
```

```
k2 = 40 - C2 - 1
normal = 1
}
Segment // left 1
{
j1 = 40 - C1 -1
k1 = 40 - C2
j2 = 40 - C1 -1
k2 = 40 - C2 - 1
normal = -1
}
//grid 6
Segment  //top 1
{
j1 = 40 - C2
k1 = 40 - C1
j2 = 40 - C2 - 1
k2 = 40 - C1
normal = 1
}
Segment  //bottom 1
{
j1 = 40 - C2
k1 = 40 - C1 - 1
j2 = 40 - C2 - 1
k2 = 40 - C1 - 1
normal = -1
}
//      Segment //right 1
//      {
//      j1 = 40 - C2
//      k1 = 40 - C1
//      j2 = 40 - C2
//      k2 = 40 - C1 - 1
//      normal = 1
//      }
Segment // left 1
{
j1 = 40 - C2 - 1
k1 = 40 - C1
j2 = 40 - C2 - 1
k2 = 40 - C1 - 1
normal = -1
}

//add C-stalk regions
Segment // right top
{
j1 = 44
k1 = 40 - C1
j2 = 40 + C2
k2 = 40 - C1
normal = 1
}
Segment // right bottom
{
j1 = 45
k1 = 40 - C1 - 1
```

```
j2 = 40 + C2
k2 = 40 - C1 - 1
normal = -1
}
Segment // right right
{
j1 = 45
k1 = 0
j2 = 45
k2 = 40 - C1 - 1
normal = 1
}
Segment // right left
{
j1 = 44
k1 = 0
j2 = 44
k2 = 40 - C1
normal = -1
}
Segment // right bottom
{
j1 = 44
k1 = 0
j2 = 45
k2 = 0
normal = 1
}
Segment // left top
{
j1 = 40 - C2
k1 = 40 - C1
j2 = 36
k2 = 40 - C1
normal = 1
}
Segment // left bottom
{
j1 = 40 - C2
k1 = 40 - C1 - 1
j2 = 35
k2 = 40 - C1 - 1
normal = -1
}
Segment // left right
{
j1 = 36
k1 = 0
j2 = 36
k2 = 40 - C1
normal = 1
}
Segment // left left
{
j1 = 35
k1 = 0
j2 = 35
k2 = 40 - C1 - 1
```

```
      normal = -1
      }
      Segment // left bottom
      {
      j1 = 35
      k1 = 0
      j2 = 36
      k2 = 0
      normal = 1
      }


}

//end of grid C
/////////////////////////////////////End of grid C: Start Grid
D://///////////////////////

// grid D

Equipotential  //gridD
{
      C = gridD
      Secondary
      {
            secondary = 1
            secSpecies = electrons
            iSpecies = ions
      }
      //grid 1
      Segment  //top 1
      {
      j1 = 40 + D1
      k1 = 40 + D2 + 1
      j2 = 40 + D1 + 1
      k2 = 40 + D2 + 1
      normal = 1
      }
      Segment  //bottom 1
      {
      j1 = 40 + D1
      k1 = 40 + D2
      j2 = 40 + D1 + 1
      k2 = 40 + D2
      normal = -1
      }
      Segment //right 1
      {
      j1 = 40 + D1 + 1
      k1 = 40 + D2
      j2 = 40 + D1 + 1
      k2 = 40 + D2 + 1
      normal = 1
      }
      Segment // left 1
      {
      j1 = 40 + D1
      k1 = 40 + D2
```

```
j2 = 40 + D1
k2 = 40 + D2 + 1
normal = -1
}
//grid 2
Segment  //top 1
{
j1 = 40 + D2
k1 = 40 + D1 + 1
j2 = 40 + D2 + 1
k2 = 40 + D1 + 1
normal = 1
}
Segment  //bottom 1
{
j1 = 40 + D2
k1 = 40 + D1
j2 = 40 + D2 + 1
k2 = 40 + D1
normal = -1
}
Segment //right 1
{
j1 = 40 + D2 + 1
k1 = 40 + D1
j2 = 40 + D2 + 1
k2 = 40 + D1 + 1
normal = 1
}
Segment // left 1
{
j1 = 40 + D2
k1 = 40 + D1
j2 = 40 + D2
k2 = 40 + D1 + 1
normal = -1
}
//grid 4
Segment  //top 1
{
j1 = 40 - D1
k1 = 40 + D2 + 1
j2 = 40 - D1 - 1
k2 = 40 + D2 + 1
normal = 1
}
Segment  //bottom 1
{
j1 = 40 - D1
k1 = 40 + D2
j2 = 40 - D1 - 1
k2 = 40 + D2
normal = -1
}
Segment //right 1
{
j1 = 40 - D1
k1 = 40 + D2
```

```
j2 = 40 - D1
k2 = 40 + D2 + 1
normal = 1
}
Segment // left 1
{
j1 = 40 - D1 - 1
k1 = 40 + D2
j2 = 40 - D1 - 1
k2 = 40 + D2 + 1
normal = -1
}
//grid 3
Segment  //top 1
{
j1 = 40 - D2
k1 = 40 + D1 + 1
j2 = 40 - D2 - 1
k2 = 40 + D1 + 1
normal = 1
}
Segment  //bottom 1
{
j1 = 40 - D2
k1 = 40 + D1
j2 = 40 - D2 - 1
k2 = 40 + D1
normal = -1
}
Segment //right 1
{
j1 = 40 - D2
k1 = 40 + D1
j2 = 40 - D2
k2 = 40 + D1 + 1
normal = 1
}
Segment // left 1
{
j1 = 40 - D2 -1
k1 = 40 + D1
j2 = 40 - D2 -1
k2 = 40 + D1 + 1
normal = -1
}
//grid 8
Segment  //top 1
{
j1 = 40 + D1
k1 = 40 - D2
j2 = 40 + D1 + 1
k2 = 40 - D2
normal = 1
}
Segment  //bottom 1
{
j1 = 40 + D1
k1 = 40 - D2 - 1
```

```
j2 = 40 + D1 + 1
k2 = 40 - D2 - 1
normal = -1
}
Segment //right 1
{
j1 = 40 + D1 + 1
k1 = 40 - D2
j2 = 40 + D1 + 1
k2 = 40 - D2 - 1
normal = 1
}
Segment // left 1
{
j1 = 40 + D1
k1 = 40 - D2
j2 = 40 + D1
k2 = 40 - D2 - 1
normal = -1
}
//grid 7
Segment  //top 1
{
j1 = 40 + D2
k1 = 40 - D1
j2 = 40 + D2 + 1
k2 = 40 - D1
normal = 1
}
Segment  //bottom 1
{
j1 = 40 + D2
k1 = 40 - D1 - 1
j2 = 40 + D2 + 1
k2 = 40 - D1 - 1
normal = -1
}
Segment //right 1
{
j1 = 40 + D2 + 1
k1 = 40 - D1
j2 = 40 + D2 + 1
k2 = 40 - D1 - 1
normal = 1
}
Segment // left 1
{
j1 = 40 + D2
k1 = 40 - D1
j2 = 40 + D2
k2 = 40 - D1 - 1
normal = -1
}
//grid 5
Segment  //top 1
{
j1 = 40 - D1
k1 = 40 - D2
```

```
j2 = 40 - D1 - 1
k2 = 40 - D2
normal = 1
}
Segment  //bottom 1
{
j1 = 40 - D1
k1 = 40 - D2 -1
j2 = 40 - D1 - 1
k2 = 40 - D2 -1
normal = -1
}
Segment //right 1
{
j1 = 40 - D1
k1 = 40 - D2
j2 = 40 - D1
k2 = 40 - D2 - 1
normal = 1
}
Segment // left 1
{
j1 = 40 - D1 -1
k1 = 40 - D2
j2 = 40 - D1 -1
k2 = 40 - D2 - 1
normal = -1
}
//grid 6
Segment  //top 1
{
j1 = 40 - D2
k1 = 40 - D1
j2 = 40 - D2 - 1
k2 = 40 - D1
normal = 1
}
Segment  //bottom 1
{
j1 = 40 - D2
k1 = 40 - D1 - 1
j2 = 40 - D2 - 1
k2 = 40 - D1 - 1
normal = -1
}
Segment //right 1
{
j1 = 40 - D2
k1 = 40 - D1
j2 = 40 - D2
k2 = 40 - D1 - 1
normal = 1
}
Segment // left 1
{
j1 = 40 - D2 - 1
k1 = 40 - D1
j2 = 40 - D2 - 1
```

```
        k2 = 40 - D1 - 1
        normal = -1
        }

//add D-stalk regions
        Segment // right top
        {
        j1 = 46
        k1 = 40 - D1
        j2 = 40 + D2
        k2 = 40 - D1
        normal = 1
        }
        Segment // right bottom
        {
        j1 = 47
        k1 = 40 - D1 - 1
        j2 = 40 + D2
        k2 = 40 - D1 - 1
        normal = -1
        }
        Segment // right right
        {
        j1 = 47
        k1 = 0
        j2 = 47
        k2 = 40 - D1 - 1
        normal = 1
        }
        Segment // right left
        {
        j1 = 46
        k1 = 0
        j2 = 46
        k2 = 40 - D1
        normal = -1
        }
        Segment // right bottom
        {
        j1 = 46
        k1 = 0
        j2 = 47
        k2 = 0
        normal = 1
        }
        Segment // left top
        {
        j1 = 40 - D2
        k1 = 40 - D1
        j2 = 34
        k2 = 40 - D1
        normal = 1
        }
        Segment // left bottom
        {
        j1 = 40 - D2
        k1 = 40 - D1 - 1
        j2 = 33
```

209

```
        k2 = 40 - D1 - 1
        normal = -1
        }
        Segment // left right
        {
        j1 = 34
        k1 = 0
        j2 = 34
        k2 = 40 - D1
        normal = 1
        }
        Segment // left left
        {
        j1 = 33
        k1 = 0
        j2 = 33
        k2 = 40 - D1 - 1
        normal = -1
        }
        Segment // left bottom
        {
        j1 = 33
        k1 = 0
        j2 = 34
        k2 = 0
        normal = 1
        }


}

//end of grid D
/////////////////////////////////End of Grid D: Start Dieletric
Regions//////////////

//regions for grid A

DielectricRegion  //gridA-1
{
      QuseFlag = 0
      j1 = 40 + A1
      k1 = 40 + A2+1
      j2 = 40 + A1
      k2 = 40 + A2+1
}
DielectricRegion  //gridA-2
{
      QuseFlag = 0
      j1 = 40 + A2
      k1 = 40 + A1+1
      j2 = 40 + A2
      k2 = 40 + A1+1
}
DielectricRegion  //gridA-4
{
      QuseFlag = 0
      j1 = 40 - A1
```

```
        k1 = 40 + A2+1
        j2 = 40 - A1
        k2 = 40 + A2+1
}
DielectricRegion  //gridA-3
{
        QuseFlag = 0
        j1 = 40 - A2
        k1 = 40 + A1+1
        j2 = 40 - A2
        k2 = 40 + A1+1
}
DielectricRegion  //gridA-8
{
        QuseFlag = 0
        j1 = 40 + A1
        k1 = 40 - A2+1
        j2 = 40 + A1
        k2 = 40 - A2+1
}
DielectricRegion  //gridA-7
{
        QuseFlag = 0
        j1 = 40 + A2
        k1 = 40 - A1+1
        j2 = 40 + A2
        k2 = 40 - A1+1
}
DielectricRegion  //gridA-5
{
        QuseFlag = 0
        j1 = 40 - A1
        k1 = 40 - A2+1
        j2 = 40 - A1
        k2 = 40 - A2+1
}
DielectricRegion  //gridA-6
{
        QuseFlag = 0
        j1 = 40 - A2
        k1 = 40 - A1+1
        j2 = 40 - A2
        k2 = 40 - A1+1
}

//Regions for Anode grids

DielectricRegion  //anode grid 1
{
        QuseFlag = 0
        j1 = 40 + F1
        k1 = 40 + F2+1
        j2 = 40 + F1
        k2 = 40 + F2+1
        Secondary
        {
                secondary = 1
                secSpecies = ions
```

```
                iSpecies = ions
        }
}
DielectricRegion   //anode grid 2
{
        QuseFlag = 0
        j1 = 40 + F2
        k1 = 40 + F1+1
        j2 = 40 + F2
        k2 = 40 + F1+1
        Secondary
        {
                secondary = 1
                secSpecies = ions
                iSpecies = ions
        }
}
DielectricRegion   //anode grid 4
{
        QuseFlag = 0
        j1 = 40 - F1
        k1 = 40 + F2+1
        j2 = 40 - F1
        k2 = 40 + F2+1
        Secondary
        {
                secondary = 1
                secSpecies = ions
                iSpecies = ions
        }
}
DielectricRegion   //anode grid 3
{
        QuseFlag = 0
        j1 = 40 - F2
        k1 = 40 + F1+1
        j2 = 40 - F2
        k2 = 40 + F1+1
        Secondary
        {
                secondary = 1
                secSpecies = ions
                iSpecies = ions
        }
}
DielectricRegion   //anode grid 8
{
        QuseFlag = 0
        j1 = 40 + F1
        k1 = 40 - F2+1
        j2 = 40 + F1
        k2 = 40 - F2+1
        Secondary
        {
                secondary = 1
                secSpecies = ions
                iSpecies = ions
        }
```

```
}
DielectricRegion  //anode grid 7
{
      QuseFlag = 0
      j1 = 40 + F2
      k1 = 40 - F1+1
      j2 = 40 + F2
      k2 = 40 - F1+1
      Secondary
      {
            secondary = 1
            secSpecies = ions
            iSpecies = ions
      }
}
DielectricRegion  //anode grid 5
{
      QuseFlag = 0
      j1 = 40 - F1
      k1 = 40 - F2+1
      j2 = 40 - F1
      k2 = 40 - F2+1
      Secondary
      {
            secondary = 1
            secSpecies = ions

            iSpecies = ions
      }
}
DielectricRegion  //anode grid 6
{
      QuseFlag = 0
      j1 = 40 - F2
      k1 = 40 - F1+1
      j2 = 40 - F2
      k2 = 40 - F1+1
      Secondary
      {
            secondary = 1
            secSpecies = ions
            iSpecies = ions
      }
}

//add-in diagonal anode grids

//Regions for Emitters deleted


///////////////////////////////////////End dieletric regions: Start
Diagnostics: //////

Diagnostic
{
       HistMax = 1028
       Comb = 2
       Ave = 0
```

```
        j1 = 0
        k1 = 40
        j2 = 80
        k2 = 40
        VarName = phi
        title = phi at equator
        x1_Label = equator position
        x2_Label = time
}

Diagnostic
{
        HistMax = 1028
        Comb = 2
        Ave = 0
        j1 = 40
        k1 = 40
        j2 = 40
        k2 = 40
        VarName = phi
        title = phi at center position
        x1_Label = time
        x2_Label = phi at center
}

Diagnostic
{
        HistMax = 1028
        Comb = 2
        Ave = 5
        j1 = 0
        k1 = 40
        j2 = 80
        k2 = 40
        VarName = rho
        title = rho at equator
        x1_Label = equator position
        x2_Label = time
}

Diagnostic
{
        HistMax = 1028
        Comb = 2
        Ave = 5
        j1 = 30
        k1 = 30
        j2 = 50
        k2 = 50
        VarName = rho
        title = rho in middle
        x1_Label = x
        x2_Label = y
}

Diagnostic
{
        HistMax = 1028
```

```
        Comb = 2
        Ave = 5
        j1 = 0
        k1 = 45
        j2 = 80
        k2 = 45
        VarName = E2
        title = transverse accelration along midline
        x1_Label = x
        x2_Label = E-transverse
}
}
```

Bibliography

1. W.W. Salisbury, Method and Apparatus for Producing Neutrons. U.S. Patent No. 2,489,436, 29 Nov. 1949.

2. J.L. Tuck, *Proceedings of the Second United Nations International Conference on the Peaceful Uses of Atomic Energy*, **30**:6, 1958.

3. W.C. Elmore, J. L. Tuck, and K. M. Watson, On the Inertial-Electrostatic Confinement of a Plasma. *Physics of Fluids*, **2**:239-246, May-June 1959

4. O.A. Lavrent'ev, *Ukrainskii Fizicheskii Zhurnal*, **8**:440, 1962.

5. O.A. Lavrent'ev, *Ukrainskii Fizicheskii Zhurnal*, **8**:446, 1962.

6. P.T. Farnsworth, Space Charge Device for Producing Nuclear Reactions, Canadian Patent No. 654,306, 18 Dec. 1962.

7. J. Sinnis and G. Schmidt, Experimental Trajectory Analysis of Charged Particles in a Cusped Geometry. *Physics of Fluids*, **6**:841-845, 1963.

8. O.A. Lavrent'ev et al., Plasma Diagnostics: 233. Gosatomizdat. Moscow, USSR, 1963.

9. R. Keller and I.R. Jones, Confinement d'un Plasma par un System Polyedrique à Courant Alternative. *Zeitschrift fur Naturforschung*, **21**:1085-1089, 1966.

10. O.A. Lavrent'ev et al., *Urkainskii Fizicheskii Zhurnal*, **11**:982, 1966.

11. P.T. Farnsworth, Electric Discharge Device for Producing Interactions between Nuclei. U.S. Patent No. 3,258,402, 28 June 1966.

12. C. Barnes and D.A. Dunn, State of the Art of Inertial Electrostatic Containment. ITT Industrial Laboratories. Fort Wayne, Ind. App. VA, 1967.

13. A. Simon, ITT Industrial Laboratory Report, Appendix II, 1967.

14. R.L. Hirsch, Experimental Studies of a Deep, Negative, Electrostatic Potential Well in Spherical Geometry. *Bulletin of the American Physical Society*, **13**:289-290, 1967.

15. D.A. Dunn and C. Barnes, One-Dimensional Computer Experiments on Inertial Confinement. *Bulletin of the American Physical Society*, **13**:290, 1967.

16. R.W. Hockney, Two-Dimensional Computer Experiments on Inertial

Confinement. *Bulletin of the American Physical Society*, **13**:290, 1967.

17. R.L. Hirsch and G.A. Meeks, Review of Inertial Confinement Principles and a Beam-to-Spherical Discharge Experiment. *Bulletin of the American Physical Society*, **13**:290, 1967.

18. R.L. Hirsch, Inertial Electrostatic Confinement of Ionized Fusion Gases. *Journal of Applied Physics,* **38**:4522-4534, October 1967.

19. G.D. Porter, *Some Considerations on the Electrostatic Confinement of Fusion Gases*. PhD Thesis, The Pennsylvania State University, 1968.

20. P.T. Farnsworth, Method and Apparatus for Producing Nuclear-Fusion Reactions. U.S. Patent No. 3,386,883, 4 June 1968.

21. R.L. Hirsch, Experimental Studies of a Deep, Negative, Electrostatic Potential Well in Spherical Geometry. *Physics of Fluids*, **11**:2486-2490, November 1968.

22. T.J. Dolan, *Electrostatic-Inertial Plasma Confinement*. PhD Thesis, University of Illinois at Urbana-Champaign, 1970.

23. O.A. Lavrent'ev, Investigation of an Electromagnetic Trap. AEC report No. AEC-TR-7002 (Rev) 1970.

24. T.J. Dolan, J.T. Verdeyen, B.E. Cherrington, and D.J. Meeker, Electrostatic-Inertial Plasma Confinement. AFOSR Scientific Report AFSOR-70-1656TR, University of Illinois at Urbana-Champaign, 1970.

25. C.W. Barnes, Stanford University Institute for Plasma Research Report No. 344, 1970.

26. R.L. Hirsch and G.A. Meeks, Apparatus for Generating Fusion Reactions. U.S. Patent No. 3,530,497, 22 Sept. 1970.

27. R.L. Hirsch, Apparatus for Generating Fusion Reactions. U.S. Patent No. 3,530,036, 22 Sept. 1970.

28. R.L. Hirsch, Lithium Ion Source in Apparatus for Producing Fusion Reactions. U.S. Patent No. 3,533,910, 13 Oct. 1970.

29. D.A. Swanson, J.T. Verdeyen, and B.E. Cherrington, Experimental Observation of Multiple Potential Wells in an Electrostatic Inertial Confinement Device. *Bulletin of the American Physical Society*, **16**:1221, 1971.

30. D.J. Meeker, B.E. Cherrington, and J.T. Verdeyen, Electron Density in an Inertial Electrostatic Confinement Device. *Bulletin of the American Physical Society*, **16**:1221, 1971.

31. C.W. Barnes, Computer Simulation of the Cylindrical Electrostatic-Inertial Confinement Device. *Bulletin of the American Physical Society*, **16**:1221, 1971.

32. E.H. Klevans and K.M. Hu, Equilibrium Solutions for Electrostatic Confinement of Plasmas. *Bulletin of the American Physical Society*, **16**:1221, 1971.

33. K.M. Hu, *Steady State Solutions of an Ion Injection Spherical Electrostatic Confinement Device with Coexisting Beam and Trapped Particles*. M.S. Thesis, The Pennsylvania State University, 1971.

34. W.M. Black, *Potential Well Formation in an Electrostatic Confinement Device*. PhD Thesis, The Pennsylvania State University, 1971.

35. K.M. Hu, Steady State Solutions of an Ion Injection Spherical Electrostatic Confinement Device with Co-Existing Beam and Trapped Particles. A Paper in Nuclear Engineering, The Pennsylvania State University, 1971.

36. G.D. Porter and E.H. Klevans, Plasma Stability in Bounded Systems with Application to a Two-Stream Instability in Spherical Geometry. *Physics of Fluids*, **14**:428-434, 1971.

37. O.A. Lavrent'ev and V.A. Sidorkin, Authors' Record No. 341416. Discoveries, Inventions, Industrial Standards, Trademarks 33, 1972.

38. O.A. Lavrent'ev et al., Gas Discharge in a Spherical Diode. *Urkainskii Fizicheskii Zhurnal*, **17**:143, 1972.

39. T.J. Dolan, J.T. Verdeyen, B.E. Cherrington, and D.J. Meeker, Electrostatic-Inertial Plasma Confinement. *Journal of Applied Physics*, **43**:1590-1600, 1972.

40. R.L. Hirsch, Electrostatic Containment in Fusion Reactors. U.S. Patent No. 3,664,920, 23 May 1972.

41. W.H. Grush, *Electron Density Measurement of an Electrostatically-Confined, Spherically Symmetric, Helium Plasma Using a Microwave Cavity Resonance Shift Technique*. M.S. Thesis, Pennsylvania State University, 1973.

42. G. Imel, *A Theoretical Model of a Spherical Electrostatic Confinement Device*. M.S. Thesis, The Pennsylvania State University, 1973.

43. D.A. Swanson, B.E. Cherrington, and J.T. Verdeyen, Multiple Potential-Well Structure Created by Electron Injection in Spherical Geometry. *Applied Physics Letters*, **23**:125-126, 1973.

44. D.J. Meeker, J.T. Verdeyen, and B.E. Cherrington, Measurement of Electron Density in a Cylindrical Inertial Electrostatic Plasma Confinement Device. *Journal of Applied Physics*, **44**:5347-5355, 1973.

45. W.J. Robinson, and R.J. McKeon, Spectroscopic Data from Spherical Plasmas Formed By Radial Ion Injection. 1973. Unpublished.

46. C.W. Barnes, Computer Simulation of Electrostatic Inertial Confinement. *Stanford University Report* AD-763826, 1973.

47. D.A. Swanson, B.E. Cherrington, and J.T. Verdeyen, Potential Well Structure in an Inertial Electrostatic Plasma Confinement Device. *Physics of Fluids*, **16**:1939-1945, November 1973

48. W.M. Black and J.W. Robinson, Measuring Rotationally Symmetric Potential Profiles with an Electron-Beam Probe. *Journal of Applied Physics*, **45**:2497-2501, 1974.

49. A.L. Gardner, Studies of Charge-Particle Distributions in an Electrostatic Confinement System. Washington, DC, U.S. Atomic Energy Commission Final Report C00-2180-7, 1974.

50. K.M. Hu and E.H. Klevans, On the Theory of Electrostatic Confinement of Plasmas with Ion Injection. *Physics of Fluids*, **17**:227-231, January 1974.

51. W.M. Black and E.H. Klevans, Theory of Potential-Well Formation in an Electrostatic Confinement Device. *Journal of Applied Physics*, **45**:2502-2511, June 1974.

52. D.A. Swanson, *Theoretical Study of a Spherical Inertial Electrostatic Plasma Confinement Device*, Ph.D. Thesis, University of Illinois at Urbana-Champaign, 1975.

53. A.L. Gardner, D.M. Hatch, A.I.Y. Chan, and R.P. Evans, Measurements on a Spherical Electrostatic Confinement System Employing Six Ion Guns. *Annals of the New York Academy of Sciences*, **251**:179-189, 8 May 1975.

54. B.E. Cherrington, J.T. Verdeyen, and D.A. Swanson, Recent Developments in Electrostatic Confinement—Theoretical. *Annals of the New York Academy of Sciences*, **251**:139-151, 8 May 1975.

55. C.W. Barnes, Computer Simulation of Electrostatic Confinement of Plasmas. *Annals of the New York Academy of Sciences*, **251**:370-380, 8 May 1975.

56. J.T. Verdeyen et al., Recent Developments in Electrostatic Confinement— Experimental. *Annals of the New York Academy of Sciences*, **251**:126-138, 8 May 1975.

57. O.A. Lavrent'ev, Electrostatic and Electromagnetic High-Temperature Plasma Traps. *Annals of the New York Academy of Sciences*, **251**:152-178, 8 May 1975.

58. E.H. Klevans, Theoretical Models of Electrostatic Confinement Experiments.

Annals of the New York Academy of Sciences, **251**:190-212, 8 May 1975.

59. T. Consoli, Review of Electrostatic and Electromagnetic Confinement Experiments Made at the French AEC. *Annals of the New York Academy of Sciences*, **251**:322-345, 8 May 1975.

60. Yu.S. Azovskii et al., Generation and Focusing of Ions from a Source with Distributed Parameters, *Report 76-9* (Institute of Physics and Technology, Ukrainian Academy of Sciences, Kharkov), 1976.

61. O.A. Lavrent'ev et al., *Zhurnal Tekhnicheskoi Fiziki*, **46**:1282-1284, 1976.

62. G.H. Miley, *Proceedings of the 2nd Topical Meeting on the Technology of Controlled Nuclear Fusion*. American Nuclear Society, 119, 1976.

63. A.L. Gardner, Studies of Charge-Particle Distributions in an Electrostatic Confinement System. ERDA Tech. Report, January 1976.

64. B. Edwards, *Ion Convergence in Inertial-Electrostatic Devices*. Ph.D. Thesis, University of Illinois, 1979.

65. R.W. Conn et al., Alternate Fusion Fuel Cycle Research. In *Plasma Physics and Controlled Nuclear Fusion Research 1980*, International Atomic Energy Agency, Vienna, 1981, **2**:621-631.

66. M. Hayashi, Institute of Plasma Physics Reports IPPJ-AM-19, 1981.

67. D. Baxter and G. Stuart, The Effect of Charge Exchange on Ion Guns and Application to Inertial-Electrostatic Confinement Devices. *Journal of Applied Physics*, **53**:4597-4601, 1982.

68. J.R. McNally, Jr., Physics of Fusion Fuel Cycles. *Nuclear Technology/Fusion*, **2**:9-28, January 1982.

69. R.W. Bussard, Final Report: DARPA/BMI Study of Advanced Energy Sources and Systems: New Alternatives for Tactical Applications(U), Vol.1, A New Method for Control of Charge Particle Interactions(U). PSR/Eaton Report 1709, Final Report, QRI Program Contract No. DAAH01-84-0005, Battelle Columbus Div. for DARPA, DoD, Pacific Sierra Research, 31 December 1986.

70. *Proceedings, Minicourse on Fusion Applications in Space*, American Nuclear Society Topical Meeting on Fusion Technology, Salt Lake City, UT, 9 Oct. 1988.

71. R.W. Bussard et al., Preliminary Research Studies of a New Method for Control of Charged Particle Interactions. Report 1899, Pacific-Sierra Research, 30 Nov. 1988. Contract No. DNA001-87-C-0052, revised March 1989.

72. R.W. Bussard, Method and Apparatus for Controlling Charged Particles. U.S.

Patent No. 4,826,646, 2 May 1989.

73. G.H. Miley, J. Nadler, T. Hochberg, Y. Gu, O. Barnouin, Inertial-Electrostatic Confinement of Fusion Plasma. *Bulletin of the American Physical Society*, **35**:2138, 1990.

74. J. Nadler, T. Hochberg, Y. Gu, O. Barnouin, G.H. Miley, Design of the University of Illinois Intertial-Electrostatic Confinement (IEC) Device. *Bulletin of the American Physical Society*, **35**:2138, 1990.

75. K. Maffei, J. Lovberg, and R. Jacobsen, Operating Parameters for the DTI/SCIF Device. *Bulletin of the American Physical Society*, **35**:2138, 1990.

76. O. Barnouin, G. Miley, J. Nadler, Y. Gu, and T. Hochberg, Ion Guns for Inertial-Electrostatic Confinement (IEC) Device. *Bulletin of the American Physical Society*, **35**:2138, 1990.

77. R.W. Bussard, Fusion as Electric Propulsion. *Journal of Propulsion and Power*, **6**:567-574, 1990.

78. G.H. Miley, J. Nadler, T. Hochberg, O. Barnouin, and Y. Gu, An Approach to Space Power. *Vision-21 Symposium*, Cleveland, OH, 2-4 April 1990. NASA conf. publ. 10059, p. 141.

79. G.H. Miley, J.H. Nadler, Y.B. Gu, and O. Barnouin, Electrostatic-Inertial Plasma Confinement. *IEEE International Conference on Plasma Science*, IEEE Conference Record-Abstracts, 126-127, May 1990.

80. Y. Gu and G. Miley, Biased Probe for Plasma Diagnostics in Spherical Electrostatic-Inertial Plasma Confinement. *Review of Scientific Instruments*, **61**:2902-2904, October 1990.

81. J.A. Lovberg, K.C. Maffei, and R.A. Jacobsen, SCIF Diagnostics Suite. *Bulletin of the American Physical Society*, **36**:2318, 1991.

82. J.H. Nadler, G.H. Miley, Y. Gu, and T. Hochberg, Advantages of Inertial-Electrostatic Confinement Fusion. *Fusion Technology*, **20**:850, 1991.

83. K.C. Maffei, J.A. Lovberg, and R.A. Jacobsen, Initial Operation of the Directed Technologies SCIF Device. *Bulletin of the American Physical Society*, **36**:2318, 1991.

84. K.E. King and R.W. Bussard, EKXL: A Dynamic Poisson-Solver for Spherically-Convergent Inertial-Electrostatic Confinement Systems. *Bulletin of the American Physical Society*, **36**:2319, 1991.

85. N.A. Krall, K. Wong, and V. Stefan, Theory of Physics Phenomena in the Polywell[TM] Plasma Confinement Geometry. *Bulletin of the American Physical*

Society, **36**:2319, 1991.

86. R.W. Bussard and K.E. King, Phenomenological Modelling of Polywell^{TM}/SCIF Multi-Cusp Inertial-Electrostatic Confinement Systems. *Bulletin of the American Physical Society*, **36**:2319, 1991.

87. K. King and R.W. Bussard, EKXL: A Dynamic Poisson-Solver for Spherically-Convergent Inertial-Electrostatic Confinement Systems. Energy/Matter Conversion Corporation Report, EMC2-1191-03, EMC2, Manassas, VA, 1991.

88. G.H. Miley, Dense Core Plasma in an Inertial-Electrostatic Confinement Device. *1991 U.S.-Japan Workshop on Nuclear Fusion in Dense Plasmas*, Austin, TX, 1991.

89. R.W. Bussard, Some Physics Considerations of Magnetic Inertial-Electrostatic Confinement: A New Concept for Spherical Converging-Flow Fusion. *Fusion Technology*, **19**:273-293, March 1991.

90. G.H. Miley et al., Inertial-Electrostatic Confinement: An Approach to Burning Advanced Fuels. *Fusion Technology*, **19**:840-845, May 1991.

91. G.H. Miley et al., Computer Simulation of Electrostatic Well Formation in Spherical Inertial-Electrostatic Plasma (SIEC) Confinement. *IEEE Conference Record — Abstracts, 18th IEEE International Conference on Plasma Science*, 168, 3-5 June 1991.

92. J. Javedani, Y. Yamamoto, G.H. Miley, Development of a Novel Neutron Source with Applications in Calibration and Monitoring. *Bulletin of the American Physical Society*, **37**:1581, 1992.

93. J.H. Nadler, G.H. Miley, Y. Gu, and T. Hochberg, Characterization of an Inertial-Electrostatic Confinement Glow Discharge (IECGD) Neutron Generator. *Fusion Technology*, **21**:1639-1643, 1992.

94. K.E. King and R.W. Bussard, Particle Trapping and Electron Two-Stream Instability in IEC Systems. *Bulletin of the American Physical Society*, **37**:1581-1582, 1992.

95. R.A. Nebel et al., Inertial-Electrostatic Confinement Studies. *Bulletin of the American Physical Society*, **37**:1582, 1992.

96. R.W. Bussard et al., Ion-Acoustic Waves and Ion Wave Group Trapping in IEC Systems. *Bulletin of the American Physical Society*, **37**:1582, 1992.

97. S.K. Wong, N.A. Krall, Potential Well Formation by Injection of Electrons with Various Energy Distributions into a Sphere or Slab. *Physics of Fluids B*, **4**:4140-4152, 1992.

98. Y. Gu and G.H. Miley, Virial Theorem Limitation to Spherical Electrostatic Inertial Confinement Fusion (SEIC). *Bulletin of the American Physical Society*, **37**:1581, 1992.

99. Y. Yamamoto and G.H. Miley, Comparison of Analytic and Numerical Simulation Solutions for Spherical Inertial Electrostatic Confinement (SEIC) of a Deuterium Fusion Reaction Plasma. *Bulletin of the American Physical Society*, **37**:1581, 1992.

100.   J.H. Nadler, *Space-Charge Dynamics and Neutron Generation in an Inertial-Electrostatic Confinement Device*. PhD Thesis, University of Illinois at Urbana-Champaign, 1992.

101.   R.A. Nebel et al., Inertial-Electrostatic Confinement Studies, *Proceedings of the International Sherwood Fusion Theory Conference*, 1D13, 6 April 1992.

102.   R.W. Bussard and K.E. King, Potential Density Distributions in Inertial-Electrostatic Confinement Systems. *Proceedings of the International Sherwood Fusion Theory Conference*, 1D12, 6 April 1992.

103.   M. Rosenberg and N.A. Krall, The Effect of Collisions in Maintaining a Non-Maxwellian Plasma Distribution in a Spherically Convergent Ion Focus. *Physics of Fluids B*, **4**:1788-1794, July 1992.

104.   N.A. Krall, The Polywell: A Spherically Convergent Ion Focus Concept. *Fusion Technology*, **22**:42-49, August 1992.

105.   J.H. Nadler, Y. Gu, and G.H. Miley, Potential Profile Measurements Based on a Collimated Proton Detector in a Spherical Electrostatic-Inertial Plasma Confinement (SEIC). *Review of Scientific Instruments*, **63**:4810-4812, October 1992.

106.   R.W. Bussard and L.W. Jameson, PBAL: A Code for Power Balance Analyses in EXL/IXL Inertial-Electrostatic Fusion Systems. Reported in *Inertial-Electrostatic-Fusion: IEF*, presented to the EPRI Fusion Panel (review), 15 Oct. 1992, Washington, DC.

107.   S. Dean, R. Gross, R. Krakowski, et al., Report to EPRI on the Inertial Electrostatic Fusion Project. Electric Power Research Institute, Palo Alto, CA, 2 Nov. 1992.

108.   R.W. Bussard, Method and Apparatus for Creating and Controlling Nuclear Fusion Reactions. U.S. Patent No. 5,160,695, 3 Nov. 1992.

109.   L. Turner and D.C. Barnes, The Brillouin Limit and Beyond: A Route to Inertial Electrostatic Confinement of a Single-Species Plasma. *Physical Review Letters* **70**:798, 1993.

110.   R.W. Bussard, The QED Engine System: Direct-Electric Fusion-Powered Rocket Propulsion Systems. *Proceedings of the 10th Symposium on Space Nuclear Power and Propulsion*, AIP Conference Proceedings **271**:1601-1611, 1993.

111.   R.W. Bussard, IEC Study Report, DOE/LANL 9-XG2-Y5957-1, 1993.

112.   R.W. Bussard, Final Report, NASA/NAS 3-26711, 2 vols., 1993.

113.   G.H. Miley and J.B. Javedani, Development of a Novel Neutron Source with Applications in Calibration and Monitoring. FSL-467, Fusion Studies Laboratory, U. of Illinois, 1993.

114.   L. Turner and D.C. Barnes, Exceeding the Brillouin Limit: A Novel Path to Inertial-Electrostatic Confinement of a Single-Species Plasma. *Proceedings of the 1993 International Sherwood Fusion Theory Conference*, 1D3, 28-31 March 1993.

115.   T.N. Tiouririne et al., Inertial-Electrostatic Confinement Studies. *Proceedings of the 1993 International Sherwood Fusion Theory Conference*, 2C24, 28-31 March 1993.

116.   G.H. Miley et al., Inertial Electrostatic Confinement as a Power Source for Electric Propulsion. *Proceedings of the NASA Vision-21 Conference*, NASA Lewis Research Center, Cleveland, OH, 30-31 March 1993.

117.   S.K. Wong and N.A. Krall, A Nonlocal Theory of Counterstreaming Ion Instability. *Physics of Fluids B*, **5**:1706-1714, June 1993.

118.   A.J. Satsangi et al., Measured Light From an IEC. *IEEE Conference Record – Abstracts, 1993 IEEE International Conference on Plasma Science*, 107, 7-9 June 1993.

119.   G.H. Miley et al., Hydrogen Generation with an Inertial Electrostatic Confinement Power Source. *Proceedings of the First International Conference on New Energy Systems and Conversions*, edited by T. Ohta and T. Homma, Universal Academy Press, Inc., Frontier Science Series #7, 183-188, 27-30 June 1993.

120.   H.D. Froning and R.W. Bussard, Fusion-Electric Propulsion for Hypersonic Flight. *Proceedings of the 29th AIAA/ASME/SAE/ASEE Joint Propulsion Conference*, AIAA Paper No. 93-2611, 28-30 June 1993.

121.   R.W. Bussard and L.W. Jameson, The QED Engine Spectrum: Fusion-Electric Propulsion for Air-Breathing to Interstellar Flight. *Proceedings of the 29th AIAA/SAE/ASME/ASEE Joint Propulsion Conference and Exhibit*, AIAA Paper No. 93-2006, 28-30 June 1993.

122.   G.H. Miley et al., Comments on D-^{3}He IEC Experiments and Reactor

Concepts. *Proceedings of the 2nd Wisconsin Symposium on Helium-3 and Fusion Power*, Madison, Wisconsin, 19-21 July 1993.

123.　　R.W. Bussard and L.W. Jameson, Inertial-Electrostatic-Fusion from D to ^{3}He: A Practical Strategy for Fusion Development. *Proceedings of the 2nd Wisconsin Symposium on Helium-3 and Fusion Power*, Madison, Wisconsin, 19-21 July 1993.

124.　　I.V. Tzonev, Light Intensity Measurement: Mathematical Modeling. *First Specialist Workshop on IEC Fusion*, FSL Report #513, Urbana, IL, 21-24 July 1993.

125.　　A.J. Satsangi and I.V. Tzonev, Light Measurement Experiments. *First Specialist Workshop on IEC Fusion*, 21-24 July, 1993.

126.　　T.J. Dolan, Ion Defocusing in Multicusp Plasma Confinement Systems. *Fusion Technology*, **24**:128-129, August 1993.

127.　　G.H. Miley et al., Conceptual Design for a D-^{3}He IEC Pilot Plant. *Proceedings of the 15th IEEE/NPSS Symposium on Fusion Engineering*, **1**:161-164, 11-15 Oct. 1993.

128.　　R.W. Bussard, L.W. Jameson, and H.D. Froning, The QED Engine: Fusion-Electric Propulsion for Cis-Oort/Quasi-Interstellar (QIS) Flight. Paper IAA.4.1-93-708, *7th Interstellar Space Exploration Symposium, Proceedings of the 44th IAF Congress*, 16-22 Oct. 1993. NASA Document ID 19940034655.

129.　　H.D. Froning et al., Fusion-Electric Propulsion for Aerospace Plane Flight. *Proceedings of the AIAA/DGLR Fifth International Aerospace Planes and Hypersonics Technologies Conference*, AIAA Paper No. 93-5126, 30 Nov. – 3 Dec. 1993.

130.　　A.J. Satsangi et al., Innovative Technology for an Inertial Electrostatic Confinement (IEC) Fusion Propulsion Unit. *Proceedings of the 11th Symposium on Space Nuclear Power and Propulsion*, AIP Conference Proceedings, **301**:1297-1302, 1994.

131.　　C.K. Rowdyshrub et al., Inertial-Electrostatic Confinement Studies. *Bulletin of the American Physical Society*, **39**:1741, 1994.

132.　　G.H. Miley et al., A Gridded D-^{3}He IEC Power Plant. *Proceedings of the 7th International Conference on Emerging Nuclear Energy Systems (ICENES '93)*, edited by H. Yasuda, World Scientific, Signapore, 66-70, 1994.

133.　　G.H. Miley, R.N.J. Javedani, J. Nadler, Y. Gu, A. Satsangi, and P. Deck, Inertial Electrostatic Confinement Neutron/Proton Source. In *Third International Conference on Dense Z-Pinches*, M.Hains and A. Knight, eds., New York, 675-689, AIP Press, 1994.

134. J.F. Santarius, K.H. Simmons, and G.A. Emmert, Modelling Inertial-Electrostatic-Confinement Fusion Devices. *Bulletin of the American Physical Society*, **39**:1740, 1994.

135. K.H. Simmons and J.F. Santarius, Numerical Simulation of Inertial Electrostatic Fusion. *Bulletin of the American Physical Society*, **39**:1740, 1994.

136. L.P. Wainwright et al., The UW Spherical Ion Focus Experiment. *Bulletin of the American Physical Society*, **39**:1740, 1994.

137. L.W. Jameson and R.W. Bussard, EIXL V2.3; A Steady-State Simulation of IEF IXL/EXL Systems. *Bulletin of the American Physical Society*, **39**:1739-1740, 1994.

138. R.W. Bussard and N.A. Krall, Comments on "Ion Defocusing in Multicusp Plasma Confinement Systems." *Fusion Technology*, **25**:228-229, 1994.

139. R.W. Bussard and N.A. Krall, Inherent Characteristics of Fusion Power Systems: Physics, Engineering, and Economics. *Fusion Technology*, **26**:1326-1336, 1994.

140. T.A. Thorson et al., Initial Results from the UW Spherical Ion Focus Experiment. *Bulletin of the American Physical Society*, **39**:1740, 1994.

141. T.J. Dolan, Response to "Comments on 'Ion Defocusing in Multicusp Plasma Confinement Systems.'" *Fusion Technology*, **25**:229, 1994.

142. Y. Gu, J.B. Javedani, G.H. Miley, A Portable Cylindrical Electrostatic Fusion Device for Neutronic Tomography. *Fusion Technology*, **26**:929-932, 1994.

143. Y.B. Gu, J.H. Nadler, G.H. Miley et al., Physics and Effects of Grid-Electric Field Perturbation on Spherical Electrostatic-Inertial Confinement Fusion. *Proceedings of the 21st European Physical Society Conference on Controlled Fusion and Plasma Physics*, 1386-1389, 1994.

144. J.B. Javedani et al., Studies of the IEC Accelerator-Plasma Target Fusion Neutron Source for Activation Analysis, *Bulletin of the American Physical Society*, **39**:1768-1769, 1994.

145. D.C. Barnes, R.A. Nebel et al., Inertial Electrostatic Confinement Experiments at Low Working Pressure, Rep. NTTR-101, prepared under Contract DAAK70-93-C-0038 US Army, Nambe Tech Corp., Santa Fe, NM, 1994.

146. Y. Gu, *Self-Generating Electron-Beam Method for Fusion in a Spherical Electrostatic Inertial Confinement Device*, M.S. Thesis, University of Illinois at Urbana-Champaign, 1994.

147.   R.W. Bussard and L.W. Jameson, Design Considerations for Clean QED Fusion Propulsion Systems. *Proceedings of the 11th Symposium on Space Nuclear Power and Propulsion*, AIP Conference Proceedings, **301**:1289-1296, January 1994.

148.   R.W. Bussard, Preliminary Study of Inertial-Electrostatic-Fusion (IEF) for Electric Utility Power Plants. EPRI Report TR-103394, EPRI Contract RP-8016-12, Report No. EMC2-0693-01, February 1994.

149.   G.H. Miley et al., Innovative Technology for an Inertial Electrostatic Confinement (IEC) Fusion Propulsion Unit. *Proceedings of the 30th AIAA/ASME/SAE/ASEE Joint Propulsion Conference*, AIAA Paper No. 94-3321, 27-29 June 1994.

150.   G.H. Miley et al., The IEC: A Novel Source for Boron Neutron Capture Therapy, *First International Workshop on Accelerator-Based Neutron Sources for Boron Neutron Capture Therapy*, INEL 940976, DWN-AC-19-94, 79-88, 11-14 Sept. 1994.

151.   J.H. Nadler, W. Yoon, and G.H. Miley, The IEC Neutron Generator and Filter Concept for Neutron Capture Therapy. *Proceedings of the 6th International Symposium on Neutron Capture Therapy for Cancer*, 393-398, 31 Oct. – 4 Nov. 1994.

152.   T.J. Dolan, Magnetic Electrostatic Plasma Confinement, *Plasma Physics and Controlled Fusion*, **36**:1539-1593, October 1994.

153.   R.W. Bussard, Physics of IEC for Fusion Reactor Systems, LANL Report 9-XG2-U5957-1, Energy Matter Conversion Company, 31 Dec. 1994.

154.   G.H. Miley et al., Innovative Technology for an Inertial Electrostatic Confinement Fusion Propulsion Unit. *Fusion Energy in Space Propulsion*, edited by Terry Kammash, AIAA Press, Washington, DC, 1995.

155.   G.H. Miley, B.P. Bromley, and Y. Gu, A Novel IEC Plasma Jet Thruster, *Bulletin of the American Physical Society*, **40**:1688, 1995.

156.   I.V. Tzonev, G.H. Miley, R.A. Nebel, A Computational Study of the Convergence of Large Angular Momentum, High Current Ion Beams in an Inertial Electrostatic Confinement (IEC) Device. *Proceedings of the 22nd International Conference on Phenomena in Ionized Gases*, **4**:197-198, 1995.

157.   J. Sved, L. Kulcinski, and G.H. Miley, A Commercial Lunar Helium 3 Fusion Power Infrastructure. *Journal of the British Interplanetary Society*, **48**:55-61, 1995.

158.   J.M. DeMora et al., A Conceptual Design for a BNCT Facility Using an IEC Fusion Source. *Transactions of the American Nuclear Society*, **72**:104, 1995.

159.   T.A. Thorson et al., Initial Results from the Wisconsin Spherically Convergent Ion Focus Experiment. *IEEE Conference Record – Abstracts, 1995 IEEE International Conference on Plasma Science*, 257, 1995.

160.   T.H. Rider, A general critique of inertial-electrostatic confinement fusion systems. *Physics of Plasmas* **2**:1853-1872, 1995.

161.   T.N. Tiouririne and D.C. Barnes, Optimization of SCIF fusion systems, *Bulletin of the American Physical Society*, **40**:1665-1666, 1995.

162.   I.V. Tzonev, R.A. Nebel, K.M. Ling, D.C. Barnes, and G.H. Miley, Double Potential Structures and Inertial Collisional Compression (ICC) Effect in an Inertial Electrostatic Confinement (IEC) Device. *Bulletin of the American Physical Society*, **40**:1666, 1995.

163.   Y. Gu and G.H. Miley, Spherical IEC Device as a Tunable X-Ray Source. *Bulletin of the American Physical Society*: **40**:1851, 1995.

164.   G.H. Miley et al., Experimental and Theoretical Studies of Inertial Electrostatic Confinement. Final Report, DOE/LANL 9-XG2-45958, 1995.

165.   S. DelMedico and G.H. Miley, Studies of Alternate Concepts Fusion: Summary of Progress on Inertial Electrostatic Confinement. Final Report. Rockford Technology Associates, Inc., 1995.

166.   W.M. Nevins, Can Inertial Electrostatic Confinement Work Beyond the Ion-Ion Collisional Time Scale? *Physics of SCIF Workshop*, 12-14 Jan. 1995.

167.   G.H. Miley, Grid Physics, IEC Simulations, and Scaling: U. of Illinois Experiments, Plans and Perspectives. *Physics of SCIF Workshop (Unpublished)*, CONF-950170, Santa Fe, NM, 12-14 Jan. 1995.

168.   R. Moses, Enhancing IEC Performance with Focusing Grids. *Physics of SCIF Workshop (Unpublished?)*, CONF-950170, Santa Fe, NM, 12-14 Jan. 1995.

169.   N.A. Krall, Polywell Experimental Results and Interpretation. *Physics of SCIF Workshop (Unpublished?)*, CONF-950170, 12-14 Jan. 1995.

170.   D.C. Barnes, Penning Trap Concept and Scaling. *Physics of SCIF Workshop (Unpublished?)*, CONF-950170, 12-14 Jan. 1995.

171.   T.H. Rider, Collisional Electron Effects and Power Balance. *Physics of SCIF Workshop (Unpublished?)*, Santa Fe, NM, CONF-950170, 12-14 Jan. 1995.

172.   J.B. Javedani, IEC Triple Grid. *Physics of SCIF Workshop (Unpublished)*, Santa Fe, NM, CONF-950170, 12-14 Jan. 1995.

173.   R.W. Bussard and L.W. Jameson, Inertial-Electrostatic-Fusion Propulsion Spectrum: Air-Breathing to Interstellar Flight. *Journal of Propulsion and Power*, **11**:365-372, March-April 1995.

174.   G.H. Miley, Development of a Novel Neutron Source with Applications in Calibration and Monitoring. Final Report. DOE Contract DEFG02-93ER75873, April 1995.

175.   T.H. Rider, *Fundamental Limitations on Plasma Fusion Systems Not in Thermodynamic Equilibrium*. PhD Thesis. Massachusetts Institute of Technology, June 1995.

176.   B.P. Bromley et al., PDS1 Simulations of IEC Fusion Devices. *IEEE Conference Record – Abstracts, 1995 IEEE International Conference on Plasma Science*, 206, 5-8 June 1995.

177.   I.V. Tzonev, G.H. Miley, and R.A. Nebel, Plasma Physics Simulations of Double Potential Wells in an IEC Device. *IEEE Conference Record – Abstracts, 1995 IEEE International Conference on Plasma Science*, 258, 5-8 June 1995.

178.   J.F. Santarius and K.H. Simmons, Performance of Polywell^{TM} Inertial-Electrostatic Confinement for Applications. *IEEE Conference Record – Abstracts, 1995 IEEE International Conference on Plasma Science*, 258, 5-8 June 1995.

179.   K.H. Simmons and J.F. Santarius, Numerical Simulation of the Polywell Device. *IEEE Conference Record – Abstracts, 1995 IEEE International Conference on Plasma Science*, 258, 5-8 June 1995.

180.   R.J. Fonck, Experimental and Modelling Tests of a Spherically Convergent Ion Focus. *IEEE Conference Record – Abstracts, 1995 IEEE International Conference on Plasma Science*, 266, 5-8 June 1995.

181.   Y. Gu, P. Heck, and G. Miley, Ion Focus Via Microchannels in Spherical Inertial-Electrostatic Confinement and Its Pulsed Experimental Results. *IEEE Conference Record – Abstracts, 1995 IEEE International Conference on Plasma Science*, 266-267, 5-8 June 1995.

182.   Y. Gu, G.H. Miley, and S. DelMedico, Pulsed IEC Neutron Generation. *Proceedings of the 10th IEEE Pulsed Power Conference*, **2**:1500-1505, 3-6 July 1995.

183.   G.H. Miley, The Inertial Electrostatic Confinement Approach to Fusion Power. *Proceedings of the 16th IEEE/NPSS Symposium on Fusion Engineering*, **2**:1419-1422, 30 Sept. – 5 Oct. 1995.

184.   J.M. DeMora, R.A. Stubbers, and R.A. Anderl, Study of Ion Microchannels and IEC Grid Effects using the SIMION Code. *Proceedings of the 16th IEEE/NPSS Symposium on Fusion Engineering*, **2**:1486-1489, 30 Sept. – 5

Oct. 1995.

185.	R.A. Anderl et al., Development of an IEC Neutron Source for NDE. *Proceedings of the 16ᵗʰ IEEE/NPSS Symposium on Fusion Engineering*, **2**:1482-1485, 30 Sept. – 5 Oct. 1995.

186.	R.A. Nebel et al., Inertial Electrostatic Confinement (IEC) Neutron Sources. *Proceedings of the 16ᵗʰ Symposium on Fusion Engineering*, **2**:1229-1231, 30 Sept. – 5 Oct. 1995.

187.	W.M. Nevins, Can Inertial Electrostatic Confinement Work Beyond the Ion-Ion Collisional Time Scale? *Physics of Plasmas*, **2**:3804-3819, October 1995.

188.	B.P. Bromley, K.M. Ling, G.H. Miley, and R.A. Nebel, PIC-MCC Simulations of the IEC Fusion Device. *Bulletin of the American Physical Society*, **40**:1736, November 1995.

189.	I.V. Tzonev, J.M. DeMora, G.H. Miley, Effect of Large Ion Angular Momentum Spread and High Current on Inertial-Electrostatic Confinement Potential Structures. *Proceedings of the 16ᵗʰ IEEE/NPSS Symposium on Fusion Engineering*, **2**:1476-1481, 1996.

190.	M. Ohnishi, Y. Yamamoto, K. Yoshikawa, K. Sato, Multi-potential Well Formation and Neutron Production in Inertial-Electrostatic Confinement Fusion by Numerical Simulations. *Proceedings of the **16**ᵗʰ IEEE/NPSS Symposium on Fusion Engineering*, **2**:1468-1471, 1996.

191.	Y. Gu, M. Williams, R. Stubbers, G.H. Miley, Pulsed Operation of Spherical Inertial-Electricostatic Confinement Device. *Proceedings of the 12ᵗʰ Topical Meeting on The Technology of Fusion Energy*, *Fusion Technology*, **30**:1342-1346, 1996.

192.	T.A. Thorson, *Ion Flow and Fusion Reactivity Characterization of a Spherically Convergent Ion Focus*. PhD Thesis, University of Wisconsin, 1996.

193.	I.V. Tzonev, *Effect of Large Ion Angular Momentum Spread and High Current on IEC Potential Structures*, M.S. Thesis, University of Illinois at Urbana-Champaign, 1996.

194.	A.J. Satsangi, *Light Intensity Measurements of an Inertial Electrostatic Confinement Fusion Plasma*. M.S. Thesis, University of Illinois at Urbana-Champaign, 1996.

195.	G.H. Miley, B.P. Bromley, and Y.B. Gu, A Novel IEC Electric Propulsion Unit for Satellite Applications. *Proceedings of the Space Technology and Applications International Forum 1996*, AIP Conference Proceedings, **361**:1435-1439. 7-13 Jan. 1996.

196.   H. Matsuura, Studies for IEC in FSL/UIUC. FSL Lab Report, 22 March 1996.

197.   G.H. Miley et al., Discharge Characteristics of the Spherical Inertial Electrostatic Confinement (IEC) Device. *XVIIth International Symposium on Discharges and Electrical Insulation in Vacuum*, **2**:654-658, 21-26 July 1996.

198.   G.H. Miley and J. Sved, The IEC, a Plasma-Target-Based Neutron Source, *Proceedings of the ANS Topical Meeting on Industrial Radiation and Radioisotope Measurement Applications*, Raleigh, NC, 6-9 Oct 1996.

199.   M. Ohnishi et al., Correlation Between Potential Well Structure and Neutron Production in Inertial Electrostatic Confinement Fusion. Institute of Advanced Energy Research Report, Kyoto Univeristy, ISSN 1342-3185, 21 Oct. 1996.

200.   G.H. Miley et al., Optimization of IEC Grid Design for Maximum Neutron Production. *Fusion Technology*, **30**:1315-1319, December 1996.

201.   L. Chacón and G.H. Miley, IEC Breeder for D-^{3}He Satellite Systems. *Fusion Technology*, **30**:1320-1325, December 1996.

202.   Y. Yamamoto et al., Preliminary Studies of Inertial-Electrostatic Confinement Fusion Experiments. *Fusion Technology*, **30**:1332-1336, December 1996.

203.   C.H. Williams and S.K. Borowski, An Assessment of Fusion Space Propulsion Concepts and Desired Operating Parameters for Fast Solar System Travel. *Proceedings of the 33rd AIAA/ASME/SAE/ASEE Joint Propulsion Conference and Exhibit*, 1997.

204.   G.H. Miley, The Inertial Electrostatic Confinement Approach to Fusion Power. *Current Trends in International Fusion Research*, edited by Panarella, Plenum Press, New York, 135-148, 1997.

205.   G.H. Miley, Y. Gu, R. Stubbers, J. DeMora, and B. Jurczyk, Research on IEC—A Plasma-Target-Based Neutron Source. *Transactions of the American Nuclear Society*, **77**:505, 1997.

206.   G.L. Kulcinski, J.F. Santarius, and H.Y. Khater, Overview of Neutron/Proton Source Applications from IEC Fusion Devices. *Transactions of the American Nuclear Society*, **77**:507-508, 1997.

207.   J. Sved, The Commercial IEC Portable Neutron Source. *Transactions of the American Nuclear Society*, **77**:504, 1997.

208.   M. Ohnishi, K.H. Sato, Y. Yamamoto, and K. Yoshikawa, Correlation Between Potential Well Structure and Neutron Production in Inertial Electrostatic

Confinement Fusion. *Nuclear Fusion*, **37**:611-619, 1997.

209.   M. Ohnishi, Y. Yamamoto, M. Hasegawa, K. Yoshikawa. Inertial Electrostatic Confinement Fusion Neutron Source R&D and Issues. *Transactions of the American Nuclear Society*, **77**:503, 1997.

210.   R.A. Nebel et al., The Los Alamos Intense Neutron Source. *Transactions of the American Nuclear Society*, **77**:503-504, 1997.

211.   R.A. Nebel et al., The Los Alamos Intense Neutron Source. LA-UR 97-1512, LANL, 1997.

212.   T.J. Dolan, Prospects of Magnetic Electrostatic Plasma Confinement. *Current Trends in International Fusion Research*, edited by Panarella, Plenum Press, New York, 197-209, 1997.

213.   G.H. Miley, B.P. Bromley, and Y. Gu, A Low-Power IEC Thruster for Satellite Applications. *Seventh Advanced Space Propulsion Research Workshop*, NASA Office of Space Access and Technology, JPL, Pasedena, CA, 1997.

214.   B.P. Bromley, *Approximate Modeling of the Inertial Electrostatic Confinement Cylindrical Device*. M.S. Thesis, University of Illinois at Urbana-Champaign, 1997.

215.   B. Jurczyk, *Theory and Development of a Sealed Deuterium-Tritium Inertial Electrostatic Confinement Neutron Generator*, M.S. Thesis, University of Illinois at Urbana-Champaign, 1997.

216.   R.A. Stubbers, Pulsed Power Supply (and Operation) of the Cylindrical Inertial Electrostatic (IEC) Fusion Device. M.S. Thesis, University of Illinois, 1997.

217.   G.H. Miley, A Novel 2.5 MeV D-D Neutron Source. *Journal of Brachytherapy International*, **1**:**1**:111-121, 1997.

218.   T.A. Thorson, R.D. Durst, R.J. Fonck, and L.P. Wainwright, Convergence, Electrostatic Potential, and Density Measurements in a Spherically Convergent Ion Focus. *Physics of Plasmas*, **4**:4-15, January 1997.

219.   Y. Gu and G.H. Miley, Overview of IEC Research. *Proceedings of the DOE Workshop on Innovative Confinement Concepts*, UCLA, 4-6 March 1997.

220.   C.H. Williams and S.K. Borowski, Fusion Propulsion System Survey and Desired Operating Parameters. *Fusion Propulsion Workshop*, MSFC, 25-26 March 1997.

221.   G.H. Miley et al., Progress in IEC Research for Near-Term Thrusters and Future Fusion Propulsion. *Proceedings of the NASA JPL Space Propulsion*

Research Workshop, California, 21 May 1997.

222. H.D. Froning Jr., Roadmap for QED (Quiet Electric Discharge) Engine Research and Development. Work performed under NASA purchase Order No. H28027D for the NASA MSFC, AL, July 1997.

223. R.W. Bussard, System Technical and Economic Features of QED-engine-Driven Space Transportation. *Proceedings of the 33rd AIAA/SAE/ASME/ASEE Joint Propulsion Conference*, AIAA Paper No. 97-3071, 6-9 July 1997.

224. G.H. Miley, Y. Gu, J. M. DeMora, R. A. Stubbers, T. A. Hochberg, J.H. Nadler, and R. A. Anderl, Discharge Characteristics of the Spherical Inertial Electrostatic Confinement (IEC) Device. *IEEE Transactions on Plasma Science*, **25**:733-739, August 1997.

225. G.H. Miley and J. Sved, The IEC—A Plasma-Target-Based Neutron Source. *Applied Radiation and Isotopes*, **48**:1557-1561, October-November 1997.

226. G.H. Miley and J.M. DeMora, Studies of Ion and Electron Beams in a Spherical IEC Device. *Gaseous Electronics Conference*, 7-9 October 1997.

227. L. Chacón, J.M. DeMora, and G.H. Miley, Engineering Issues of Gridded Inertial Electrostatic Confinement Devices. *Proceedings of the 17th IEEE/NPSS Symposium on Fusion Engineering*, **2**:737-740, 6-10 Oct. 1997.

228. L. Chacón, B.P. Bromley, and G.H. Miley, Prospects of the Cylindrical IEC Fusion Device as a Neutron Source. *Proceedings of the 17th IEEE/NPSS Symposium on Fusion Engineering*, **2**:858-861, 6-10 Oct. 1997.

229. B. Jurczyk, Y. Gu, and G.H. Miley, Resonant Ion Driven Oscillation (RIDO) Concept. *Proceedings of the 1997 APS Division of Plasma Physics Meeting*, 17-21 Nov. 1997.

230. B.P. Bromley, L. Chacon, and G.H. Miley, Approximate Modeling of Cylindrical Inertial Electrostatic Confinement (IEC) Fusion Neutron Generator. *Proceedings of the 16th International Conference on the Numerical Simulation of Plasmas*, 191-192, 1998.

231. D.C. Barnes and R.A. Nebel, Stable, Thermal Equilibrium, Large-Amplitude, Spherical Plasma Oscillations in Electrostatic Confinement Devices, *Physics of Plasmas*, **5**:2498-2503, 1998.

232. G.H. Miley et al., Scaling of the Inertial Electrostatic Confinement (IEC) for Near-Term Thrusters and Future Fusion Propulsion. *Proceedings of the 15th Symposium on Space Nuclear Power and Propulsion*, **3**:1373-1375, 1998.

233. L. Chacón and G.H. Miley, Inertial Electrostatic Confinement ^{3}He Breeder for D-^{3}He Satellite Systems. *Fusion Technology*, **33**:182-209, 1998.

234.	M. Ohnishi et al., Study on an Inertial Electrostatic Confinement Fusion as a Portable Neutron Source. *Fusion Engineering and Design*, **42**:207-211, 1998.

235.	R. Nebel and D.C. Barnes, The Periodically Oscillating Plasma Sphere, *Fusion Technology*, **34**:28-45, 1998.

236.	T.A. Thorson et al., Fusion Reactivity Characterization of a Spherically Convergent Ion Focus. *Nuclear Fusion*, **38**:495-507, 1998.

237.	L. Chacón et al., Implicit Bounce-Averaged Fokker-Planck (BAFP) Code to Study the Ion Defocusing in Spherical Inertial Electrostatic Confinement (IEC) Systems. *Proceedings of the 1998 APS Division of Plasma Physics Meeting*, Q7P.23, 1998.

238.	Y. Gu, *Experimental Study of Proton Rate Density in a Spherical Inertial Electrostatic Confinement Fusion Device*. PhD Thesis, Department of Electrical Engineering, University of Illinois at Urbana-Champaign, 1998.

239.	R.W. Bussard and H.D. Froning, System/SubSystem Engineering Interface Considerations and R&D Requirements for IEF/QED Engine Systems, *Proceedings of the Space Technology and Applications International Forum 1998*, AIP Conference Proceedings, **420**, 25-29 Jan. 1998.

240.	G.H. Miley and L. Chacon, Engineering Issues for a Gridded IEC for Fusion Propulsion. *Abstract Proceedings, Ninth Advanced Space Propulsion Research Workshop and Conference*, 11-13 March 1998.

241.	G.H. Miley, Some Near-Term Applications of Fusing Plasmas. *ANS Topical on Fusion Technology*, *Fusion Technology*, **34**:484-488, June 1998.

242.	W.M. Nevins, A. Carlson, N. Rostoker, M. W. Binderbauer, and H.J. Monkhorst, Feasibility of a Colliding Beam Fusion Reactor. *Science*, **281**:307a, 17 July 1998.

243.	G.H. Miley et al., Accelerator Plasma-Target-Based Fusion Neutron Source. *Fusion Engineering and Design*, **42**:461-467, 1 Sept. 1998.

244.	R.A. Nebel, *Summary of the US-Japan Workshop on IEC Neutron Sources*, Los Alamos, 14-15 Sep. 1998.

245.	M. Ohnishi et al., Numerical Studies of Inertial Electrostatic Confinement Fusion Taking Account of Atomic Processes. *Summary of the US-Japan Workshop on IEC Neutron Sources*, 14-15 Sept. 1998.

246.	M. Ohnishi et al., Studies of Inertial Electrostatic Confinement Fusion Neutron Source. *Fusion Technology*, **34**:1071-1075, November 1998.

247.   H. Momota and G.H. Miley, Virtual Cathode in a Spherical Inertial Electrostatic Confinement. *Proceedings of The US-Japan Workshop and The Satellite Meeting of ITC-9 on Physics of High Beta Plasma Confinement in Innovative Fusion System*, NIFS-PROC-41, 95-102, 14-15 Dec. 1998.

248.   D.C. Barnes, Uniform-Density, Spherical Electron Focus. *Physics of Plasmas*, **6**:4472, 1999.

249.   G.H Miley and H. Momota, Criteria for Potential Trap Formation in an IEC. *Bulletin of the American Physical Society*, **44**:**7**:191, 1999.

250.   G.H. Miley and Y. Gu, IEC Neutron Source Development and Potential Well Measurements. *Current Trends in International Fusion Research: Proceedings of the Second Symposium*, 179-195, 1999.

251.   G.H. Miley et al., Issues for Development of Inertial Electrostatic Confinement (IEC) for Future Fusion Propulsion. *Proceedings of the 35th AIAA/ASME/SAE/ASEE Joint Propulsion Conference and Exhibit*, AIAA-99-2140, 1999.

252.   H. Momota and G.H. Miley, Virtual Well Formation in a Spherical Inertial Electrostatic Confinement Device. *Bulletin of the American Physical Society*, **44**:596-597, 1999.

253.   J. Nadler, Inertial-Electrostatic Confinement (IEC) Fusion for Space Propulsion. Final Report. MSFC. NASA Document ID 19990103080, 1999.

254.   J.M. Demora and G.H. Miley, Charge Exchange Modeling in a Spherical IEC Device. *Bulletin of the American Physical Society*, **44**:596, 1999.

255.   L. Chacon, G.H. Miley, D.C. Barnes, Energy Gain Studies of Spherical IEC Devices using the BAFP Code. *Bulletin of the American Physical Society*, **44**:597, 1999.

256.   R.A. Nebel and J.M. Finn, Kinetic Calculation for POPS. *Bulletin of the American Physical Society*, **44**:596, 1999.

257.   R.A. Nebel, D.C. Barnes, R. Bollman, G. Eden, and L. Morrison, The Los Alamos Intense Neutron Source. *Current Trends in International Fusion Research: Proceedings of the Second Symposium*, 411-425, 1999.

258.   J. DeMora, *Cathode Grid Optimization Studies for the Spherical Inertial Electrostatic Confinement Device*. M.S. Thesis, University of Illinois at Urbana-Champaign, 1999.

259.   R. Kusaba, *Numerical Analysis of an Cylindrical Electrostatic Confinement Fusion Device*. M.S. Thesis, Kyoto University, 1999 (in Japanese).

260. G.H. Miley, A D-^{3}He IEC Power Unit for Space Applications. *Proceedings of the Space Technology and Applications International Forum 1999*, edited by M.S. El-Genk, AIP Conference Proceedings, **458**:1327-1332, January 1999.

261. G.L. Kulcinski et al., *Demonstration of D^{3}He Fusion in an Inertial Electrostatic Confinement Device. Fusion Technology Institute*, University of Wisconsin, 29 Jan. 1999.

262. G.H. Miley, A Portable Neutron/Tunable X-Ray Source Based on Inertial Electrostatic Confinement. *Nuclear Instruments and Methods in Physics Research*, **A422**:16-20, 11 Feb. 1999.

263. J.H. Nadler, G.H. Miley, A Breakthrough Fusion Power Unit for Space Applications. Final Report for NASA SBIR Contract #NAS8-99044, Award No. 98-1 04.02-3772, June 1999

264. L. Chacón de la Rosa, *Fokker-Planck Modelling of Spherical Inertial Electrostatic Virtual-Cathode Fusion Systems*. PhD Thesis. University of Illinois at Urbana-Champaign, September 1999.

265. J.H. Nadler, G.H. Miley, M.D. Conventry, M.J. Williams, B.E. Jurczyk, R.A. Stubbers, and Y. Nam, High-Current Pulsed Operation of an Inertial-Electrostatic Confinement (IEC) Device. *Proceedings of the 18th IEEE/NPSS Symposium on Fusion Engineering*, 25-29 October 1999.

266. M. Ohnishi et al., Electron Streaming from Central Core Region in Inertial-Electrostatic Confinement Fusion. *Proceedings of the 18th IEEE/NPSS Symposium on Fusion Engineering*, 213-216, 25- 29 Oct, 1999.

267. G.H. Miley, J.M. DeMora, B.E. Jurczyk, and Martin Nieto, Computational Studies of Collisional Processes in Inertial Electrostatic Glow Discharge Fusion Devices. *Proceedings of the 18th IEEE/NPSS Symposium on Fusion Engineering*, 23-25 October 1999.

268. K. Yoshikawa et al., Real Time Measurements of Strong Localized Potential Profiles Through Stark Effects in the Central Core Region of an Inertial-Electrostatic Fusion Device. *Proceedings of the 18th IEEE/NPSS Symposium on Fusion Engineering*, 27-30, 25- 29 Oct, 1999.

269. R.A. Nebel, Innovative Energy Sources and Advanced Applications—The Los Alamos Intense Neutron Source. *Proceedings of the 18th IEEE/NPSS Symposium on Fusion Engineering*, 31-34, 25- 29 Oct, 1999.

270. R.P. Ashley, G.L. Kulcinski, J.F. Santarius, G. Piefer, K.M. Subramanian, D-^{3}HE Fusion in an Inertial Electrostatic Confinement Device. *Proceedings of the 18th IEEE/NPSS Symposium on Fusion Engineering*, 35-37, 25-29 October 1999.

271.   T.H. Bauer and R.A. Wigeland, An Innovative Accelerator-Driven Inertial Electrostatic Confinement Device Using Converging Ion Beams. *Proceedings of the Eighth International Conference on Nuclear Engineering*, 2000.

272.   J. Sved, Evolution of IEC Fusion Via Commercial Fusionstar Opportunities, *Proceedings of the Eighth International Conference on Nuclear Engineering*, 2000.

273.   M. Nieto, H. Momota, and G.H. Miley, Use of an IEC Device as a Proton Beam Source. *Proceedings of the 8th International Conference on Nuclear Engineering*, 2000.

274.   H. Matsuura, Ion Distribution Function and Radial Profile of Neutron Production Rate in Spherical Inertial Electrostatic Confinement Plasmas. *2nd US-Japan Workshop on IEC Neutron Sources*, 2000.

275.   T. Shirouzu, *Study of an Cylindrical Electrostatic Confinement Fusion Device*. M.S. Thesis, Kyoto University, 2000 (in Japanese).

276.   J. Nadler, G.H. Miley, M. Convertry, and H. Momota, Recent Advances in Inertial-Electrostatic Confinement (IEC) Fusion for Space Power and Propulsion. *Proceedings of the Space Technology and Applications International Forum 2000*, edited by M.S. El-Genk, AIP Conference Proceedings, **504**:1224-1229, 30 Jan. – 3 Feb. 2000.

277.   W.E. Hammond, M.D. Coventry, J. Hanson, I. Hrbud, G.H. Miley, and J.H. Nadler, IEC Fusion: The Future Power and Propulsion System for Space. *Proceedings of the Space Technology and Applications International Forum 2000*, edited by M.S. El-Genk, AIP Conference Proceedings, **504**:1572-1580, 30 Jan. – 3 Feb. 2000.

278.   Y. Gu and G.H. Miley, Experimental Study of Potential Structure in a Spherical IEC Fusion Device. *IEEE Transactions on Plasma Science*, **28**:331-346, February 2000.

279.   M. Ohnishi et al., Beam Optics in Inertial Electrostatic Confinement Fusion. *Review of Scientific Instruments*, **71**:1210-1212, February 2000.

280.   R.A. Nebel and J.M. Finn, Kinetic and Fluid Calculations for the Periodically Oscillating Plasma Sphere. *Physics of Plasmas*, **7**:839-843, March 2000.

281.   H. Momota, G.H. Miley, and J. Nadler, Direct Energy Conversion for IEC Fusion for Space Applications. *Proceedings of the 36th AIAA/ASME/SAE/ASEE Joint Propulsion Conference and Exhibit*, 16-19 July 2000.

282.   J. Nadler, G. Miley, M. Coventry, Y. Nam, and W. Hammond, Inertial Electrostatic Confinement (IEC) for Space Propulsion and Power. *Proceedings of*

the 36th AIAA/ASME/SAE/ASEE Joint Propulsion Conference and Exhibit, 16-19 July 2000.

283.   H. Momota, G.H. Miley, and J. Nadler, Direct Energy Conversion for IEC Propulsions. *National Institute of Fusion Studies*, NIFS-641, August 2000.

284.   G.H. Miley and J. Sved, The IEC Star-Mode Fusion Neutron Source for NAA - Status and Next-Step Designs. *Applied Radiation and Isotopes*, **53**:779-783, 15 Nov. 2000.

285.   H. Matsuura et al., Ion Distribution Function and Radial Profile of Neutron Production Rate in Spherical Inertial Electrostatic Confinement Plasmas. *Nuclear Fusion*, **40**:1951-1954, December 2000.

286.   R.P. Ashley et al., Steady-State D-^{3}He Proton Production in an IEC Fusion Device. *Fusion Technology*, **39**:546-551, 2001.

287.   G.H. Miley, The IEC Device as a Low Cost Student Experiment with a Burning Fusion Plasma. *Bulletin of the American Physical Society*, **46**, 2001.

288.   Y. Iwamoto et al., Preliminary Results of Cylindrical Electrostatic Confinement Experiment. *Fusion Technology*, **39**:552-556, March 2001.

289.   Y. Yamamoto et al., Effect of Electrode Shape on Fusion Reaction Rate in a Cylindrical Electrostatic Confinement Device. *Fusion Technology*, **39**:557-561, March 2001.

290.   K. Masuda et al., Identification of D-D Fusion Reaction by Simultaneous Neutron and Proton Measurements in an Inertial Electrostatic Confinement Fusion Device. *Fusion Technology*, **39**:562-566, March 2001.

291.   J. Khachan et al., Measurements of Ion Energy Distributions by Doppler Shift Spectroscopy in an Inertial-Electrostatic Confinement Device. *Physics of Plasmas*, **8**:1299-1304, April 2001.

292.   H. Matsuura et al., Radial Profile of Neutron Production Rate in Spherical Inertial Electrostatic Confinement Plasmas. *Fusion Technology*, **39**:1167-1173, May 2001.

293.   K. Yoshikawa et al., Strongly Localized Potential Profile Measurements through Stark Effects in the Central Core Region of an Inertial-Electrostatic Fusion Device. *Fusion Technology*, **39**:1193-1201, May 2001.

294.   K. Masuda et al., Performance Characteristics of an Inertial Electrostatic Confinement Fusion device with a Triple-Grid System. *Fusion Technology*, **39**:1202-1210, May 2001.

295.   M. Ohnishi et al., Particle-in-Cell Simulation of Inertial Electrostatic

Confinement Fusion Plasma. *Fusion Technology*, **39**:1211-1216, May 2001.

296.   Y. Yamamoto et al., Effects of Electrode Shape on Performance Characteristics of a Cylindrical Inertial Electrostatic Confinement Fusion Device. *Fusion Technology*, **39**:1188-1192, May 2001.

297.   R.A. Nebel and J.M. Finn, Fluid and Kinetic Stability of Virtual Cathodes for the Periodically Oscillating Plasma Sphere. *Physics of Plasmas*, **8**:1505-1513, May 2001.

298.   K. Yoshikawa et al., Measurements of Strongly Localized Potential Well Profiles in an Inertial Electrostatic Fusion Neutron Source. *Nuclear Fusion*, **41**:717-720, June 2001.

299.   H. Momota and G.H. Miley, Virtual Cathode in a Stationary Spherical Inertial Electrostatic Confinement. *Fusion Science and Technology*, **40**:56-65, July 2001.

300.   M. Daino, *Study for Low Pressure Operating of a Cylindrical Inertial Electrostatic Confinement Fusion Device*. M.S. Thesis, Graduate School of Energy Science, Kyoto University, 2002 (in Japanese).

301.   T. Tadokoro et al., Development of Compact Neutron Generators by Using Ion Sources. *4th US-Japan Workshop on IEC Neutron Sources*, 2002.

302.   G.H. Miley et al., Overview of IEC Theory and Experiments at the University of Illinois. *4th US-Japan Workshop on IEC Neutron Sources*, 2002.

303.   R.P. Ashley et al., Recent IEC Experimental Results at the University of Wisconsin. *4th US-Japan Workshop on IEC Neutron Sources*, 2002.

304.   T. Sakai, K. Noborio, and Y. Yamamoto, Analysis of Discharge Characteristics of the Inertial Electrostatic Confinement Fusion using a Particle Code with Monte Carlo Collision Scheme. *Proceedings of the 19th IEEE/NPSS Symposium on Fusion Engineering*, 209-212, 21-25 Jan. 2002.

305.   K. Masuda et al., Measurement of the Energy Distribution of Fast Excited Atoms by Doppler Shift Spectroscopy in an Inertial-Electrostatic Confinement Fusion Device. *Proceedings of the 19th IEEE/NPSS Symposium on Fusion Engineering,* 434-437, 21-25 Jan. 2002.

306.   H. Momota and G.H. Miley, A Collimator-Converter System for IEC Propulsion. *Proceedings of the Space Technology and Applications International Forum 2002*, edited by M.S. El-Genk, AIP Conference Proceedings, **608**:834-844, 3-7 Feb. 2002.

307.   R. Burton et al., High Performance Manned Interplanetary Space Vehicle Using D-^{3}He Inertial Electrostatic Fusion. *Proceedings of the Space Technology*

and Applications International Forum 2002, edited by M.S. El-Genk, AIP Conference Proceedings, **608**:819-827, 3-7 Feb 2002.

308.   R.W. Bussard, An Advanced Fusion Energy System for Outer-Planet Space Propulsion. *Space Technology and Applications International Forum 2002*, AIP Conference Proceedings, **608**:768-779, 3-7 Feb. 2002.

309.   S.K. Murali, Inertial Electrostatic Confinement Concept Based Fusion Propulsion System for Long-Range Missions Beyond the Heliopause. *ANS Annual Meeting*, 9-13 June 2002.

310.   H. Momota, G.H. Miley, and T. Bauer, NBI Supported SIEC. *5th US-Japan Workshop on IEC Fusion*, University of Wisconsin, 9-10 October 2002.

311.   M. Ohnishi, Overview of the Japanese IEC Program. *5th US-Japan Workshop on IEC Fusion*, 9-10 Oct. 2002.

312.   J.F. Santarius, Modeling D-D Operation of the UW IEC Experiment. *5th US-Japan Workshop on IEC Fusion*, 9-10 Oct. 2002.

313.   G.L. Kulcinski, The United States IEC Program, *5th US-Japan Workshop on IEC Fusion*, 9-10 Oct. 2002.

314.   J.W. Weidner, *The Production of ^{13}N from Inertial Electrostatic Confinement Fusion*, M.S. Thesis, University of Wisconsin, 2003.

315.   R.L. Burton, H. Momota, N. Richardson, Y. Shaban, and G.H. Miley, Fusion Ship II – A Fast Interplanetary Space Vehicle Using Inertial Electrostatic Fusion. *Proceedings of the Space Technology and Applications International Forum 2003*, edited by M.S. El-Genk, AIP Conference Proceedings, **654**:553-562, 2-5 Feb. 2003.

316.   J. Khachan, D. Moore, and S. Bosi, Spatial Distribution of Ion Energies in an Inertial Electrostatic Confinement Device. *Physics of Plasmas*, **10**:596-599, March 2003.

317.   G.H. Miley et al., Experimental Simulation of a Proton Collimator for a Fusion Space Thruster. *NASA/MSFC/JPL/UAH 14th Annual Advanced Space Propulsion Workshop (ASPW 2003)*, Huntsville, AL, 15-17 April 2003.

318.   H. Matsuura et al., Correlation Between Ion/Electron Distribution Functions and Neutron Production Rate in Spherical Inertial Electrostatic Confinement Plasmas. *Nuclear Fusion*, **43**:989-998, September 2003.

319.   K. Yoshikawa et al., Magnetron Discharge Characteristics for Improvement of an Inertial Electrostatic Confinement Neutron/Proton Source. *Fusion Science and Technology*, **44**:529-533, September 2003.

320.   B.B. Cipiti and G.L. Kulcinski, Embedded D-^{3}He Fusion Reactions and Medical Isotope Production in an Inertial Electrostatic Confinement Device. *Fusion Science and Technology*, **44**:534-538, September 2003.

321.   J.W. Weidner et al., Production of ^{13}N via Inertial Electrostatic Confinement Fusion. *Fusion Science and Technology*, **44**:539-543, September 2003.

322.   T. Higashi et al., Preliminary Results of Low Pressure Discharge Experiments of a Cylindrical Inertial Electrostatic Confinement Fusion Device Aimed for a Small Neutron Source. *Fusion Science and Technology*, **44**:544-548, September 2003.

323.   R.P. Ashley et al., Recent Progress in Steady State Fusion Using D-^{3}He. *Fusion Science and Technology*, **44**:564-566, September 2003.

324.   N. Noborio, T. Sakai, and Y. Yamamoto, Investigation of Spatial Distribution of Neutron Production Rate and its Dependency on Pressure in Spherical IECF by One-Dimensional Simulations. *Proceedings of the 20th IEEE/NPSS Symposium on Fusion Engineering*, 328-331, 14-17 Oct. 2003.

325.   K. Masuda et al., Performance Characteristics of an Inertial-Electrostatic Confinement Fusion Device with Magnetron Discharge. *Proceedings of the 20th IEEE/NPSS Symposium on Fusion Engineering*, 628-631, 14-17 Oct. 2003.

326.   K. Tomiyasu et al., Numerical Simulation for UW IEC Device. *6th US-Japan Workshop on IEC Fusion*, 20-21 Oct. 2003.

327.   G.L. Kulcinski et al., Current Directions for the University of Wisconsin IEC Research Program. *6th US-Japan Workshop on IEC Fusion*, 20-21 Oct. 2003.

328.   G. Piefer, Helium Ions Source of D-^{3}He Converged Core Operation. *6th US-Japan Workshop on IEC Fusion*, 20-21 Oct. 2003.

329.   T. Tomizawa et al., Characteristics of the Cylindrical IECF Experiments at Low Gas Pressure Operation. *Summary of the US-Japan Workshop on IEC Neutron Sources*, 20-21 Oct. 2003.

330.   M.J. Park, RF Plasma Ions Sources of Compact Neutron Generators. *6th US-Japan Workshop on IEC Fusion*, 20-21 Oct. 2003.

331.   G.H. Miley, R. Stubbers, J. Webber, H. Momota, Magnetically-Channeled SIEC Array (MCSA) Fusion Device for Interplanetary Missions. *Proceedings of the Space Technology and Applications International Forum 2004*, edited by M.S. El-Genk, AIP Conference Proceedings, **699**:399-405, 8-11 Feb. 2004.

332.   G.H. Miley, Y. Shaban, and Y. Yang, RF Ion Gun Injector in Support of Fusion Ship II Research and Development. *Proceedings of the Space Technology*

and Applications International Forum 2004, edited by M.S. El-Genk, AIP Conference Proceedings, **699**:406-412, 8-11 Feb. 2004.

333.   K. Tomiyasu, *Pulsed Operation of an Inertial Electrostatic Confinement Fusion Device and its Applications*. M.S. Thesis, Tokyo Institute of Technology, 31 Feb. 2004.

334.   B.B. Cipiti, *The Fusion of Advanced Fuels to Produce Medical Isotopes Using Inertial Electrostatic Confinement*, Ph.D. Thesis, University of Wisconsin, May 2004.

335.   S.K. Murali, *Diagnostic Study of Steady State Advanced Fuel (D-D and D-^{3}He) Fusion in an IEC Device*, Ph.D. Thesis, University of Wisconsin, December 2004.

336.   G.H. Miley et al., RF Ion Source-Driven IEC Design and Operation. *Fusion Science and Technology* **47**:1233-1237, May 2005.

337.   J.F. Santarius et al., Overview of University of Wisconsin Inertial-Electrostatic Confinement Fusion Research. *Fusion Science and Technology* **47**:1238-1244, May 2005.

338.   R.F. Radel et al., Implantation of D and He in W-Coated Refractory Carbides. *Fusion Science and Technology* **47**:1250-1254, May 2005.

339.   G.R. Piefer et al., Design of an Ion Source for ^{3}He Fusion in a Low Pressure IEC Device. *Fusion Science and Technology* **47**:1255-1259, May 2005.

340.   A.L. Wehmeyer, R.F. Radel and G.L. Kulcinski, Optimizing Neutron Production Rates from D-D Fusion in an Inertial Electrostatic Confinement Device. *Fusion Science and Technology* **47**:1260-1264, May 2005.

341.   H. Osawa et al., Optimal Position of Ion Source for High Performance of IEC. *Fusion Science and Technology* **47**:1265-1269, May 2005.

342.   H. Osawa et al., Numerical Study on Glow Discharge of IEC Fusion. *Fusion Science and Technology* **47**:1270-1274, May 2005

343.   S. Yoshinaga et al., Fast Neutral Generation by Charge Exchange Reaction and Its Effect on Neutron Production Rate in Inertial Electrostatic Confinement Fusion Systems. *Fusion Science and Technology* **47**:1275-1279, May 2005.

344.   K. Noborio et al., One Dimensional Simulation of an Inertial Electrostatic Confinement Fusion Device at Low Gas Pressure Operation. *Fusion Science and Technology* **47**:1280-1284, May 2005.

345.   Y. Yamamoto et al., Influence of the Electrode Spacing on the

Performance Characteristics of Inertial Electrostatic Confinement Fusion in Low Pressure Operation. *Fusion Science and Technology* **47**:1285-1289, May 2005.

346.   T. Takamatsu et al., Magnetron-Discharge-Based Ion Source for Improvement of an Inertial Electrostatic Confinement Fusion Device. *Fusion Science and Technology* **47**:1290-1294, May 2005.

347.   Y. Ueno et al., Measurement of Ion Energy Distribution in a Cylindrical Inertial Electrostatic Confinement Fusion (C-IECF) Device. *Fusion Science and Technology* **47**:1295-1298, May 2005.

348.   P.J. Shrestha, A Dipole Assisted IEC Neutron Source. Final Report: DOE DE-FG02-04ER86222, May 2005.

349.   R. Thomas, Y. Takeyama, G.H. Miley, H. Momota, and P.J. Shrestha, Dipole-Assisted IEC for Space Propulsion. *Proceedings of the 41st AIAA/ASME/SAE/ASEE Joint Propulsion Conference and Exhibit*, 10-13 July 2005.

350.   R.M. Meyer, S.K. Loyalka, and M.A. Prelas, Potential Well Structures in Spherical Inertial Electrostatic Confinement Devices. *IEEE Transactions on Plasma Science*, **33**:1377-1394, August 2005.

351.   D.L. Book, *NRL Plasma Formulary*, Naval Research Lab, Washington, DC, 2006.

352.   R. Hegerberg, Thorarinn Stefansson, and M.T. Elford, Mearsurement of the Symmetric Charge-Exchange Cross Section in Helium and Argon in the Impact Energy Range 1-10keV. *J.Phys. B: Atomic and Molecular Phys.,* Vol. 11, No. 1, 1978.

353.   Tech-X Corporation, OOPIC Pro Object Oriented Particle-in-Cell Simulation User's Manual, Version 1.0 beta 3, 5621 Arapahoe Avenue, Suite A, Boulder, CO 80305, January 23, 2004.

354.   G. Carter and J.S. Colligon, Ion Bombardment of Solids, Heinemann Educational Books, London (1968).

355.   B. Szapiro and J.J. Rocca, Electron emission from glow-discharge cathode materials due to neon and argon bombardment. *J. Appl. Phys.* **65** (9), 1 May 1989.

356.   G.C. Allen, J.M. Dyke, S.J. Harris, and A. Morris, A Surface Study of the Oxidation of Type 304L Stainless Steel at 600K in Air, *Oxidation of Metals,* Vol. 29, Nos. 5/6, 1988

357.   T. J. McGuire, "Improved Lifetimes and Synchronization Behavior in Multi-grid Inertial Electrostatic Confinement Fusion Devices," MIT Ph.D. Thesis, Aeronautics and Astronautics, February 2007.

358.   J.P.Verboncoeur, A.B.Langdon, and N.T.Gladd, An object-oriented electromagnetic PIC code, *Computer Physics Communications,* **87** (1995) pp 199-211.

359.   D.L.Bruhwiler et.al, Particle-in-cell simulations of plasma accelerators and electron-neutral collisions, *Physical Review Special Topics-Accelerators and Beams,* Vol. 4, 101302, (2001).

360.   S. Humphries Jr., "Charged Particle Beams," John Wiley and Sons, 1990.

361.   http://www.fusor.net/